Università degli Studi di Napoli

Federico II

DOTTORATO DI RICERCA IN INGEGNERIA STRUTTURALE, GEOTECNICA E RISCHIO SISMICO

XXX CICLO

TESI

SOFT GROUTING FOR SEISMIC ISOLATION: Numerical and Physical modelling

Tutor

Prof. Alessandro Flora

Co-Tutor

Prof. Emilio Bilotta

Candidata

Valeria Nappa

Coordinatore

Prof. Luciano Rosati

Summary

CHAPTER 1
SEISMIC ISOLATION SYSTEMS

1. History of Seismic Isolation

A large proportion of the world's population lives in region of seismic hazard, at risk from earthquakes of varying severity frequency of occurrence. Earthquakes cause significant of life and damage to property every year. Many aseismic construction designs and technologies have been developed over the year in attempts to mitigate the effects of earthquakes on buildings, bridges and potentially vulnerable contents. Seismic isolation is a relatively recent, and evolving, technology of this kind. Seismic isolation is a design strategy based on the premise that it is both possible and feasible to uncouple a structure from the ground and thereby protect it from the damaging effect of earthquake motions. This decoupling is achieved by increasing the horizontal flexibility of the system, together with providing appropriate damping. In many applications the seismic isolation system is mounted directly beneath the structure and is referred to as 'base isolation'. The principle in base isolation, as suggested in its name *isolation = the state of being separated, and base = a part that supports from beneath or serves as a foundation for an object or structure* (definition according to Concise Oxford Dictionary), is that of decoupling a structure from its foundation, or in the case of bridges, separating the superstructure from the infrastructure columns or piers. The field of seismic design is a subject that deals primarily with life safety and uncertainty.

The concept of seismic or base isolation as means of earthquake protection seems to be more than 100 years old as reported by Buckle and Mayes (1990) in a review of the history of isolation.

Jacob Bechtold of Munich (Germany) made an application for a U.S. Patent for an Earthquake Proof Building in 1906. His primary claim was for "…An earthquake proof building consisting of a rigid base-plate to carry the building and a mass of spherical bodies of hard material to carry the said base plate freely" (Bechtold, 1906).

Kelly, in an overview paper (Kelly,1986), has described the 1909 patent of Calantarients, a medical doctor from Scarborough, England who proposed "… a method of building to resist the action of earthquakes" which used layers of talc to isolate the walls and floors from ground disturbances. In correspondence to a Chilean colleague, Dr. Calantarients apparently acknowledge the existence of a Japanese system developed 25 years earlier in the late 19th century.

In 1929, Robert Wladislas deMontalk of Wellington, New Zealand filed a patent application for an invention comprising "… a means whereby a bed…is placed and retained between the base of a building and its solid foundation, the (bed) being composed of material which will absorb or minimize shocks thereby saving the building therefrom." (de Montalk, 1932).

These are three examples of almost a hundred known proposals for a seismic isolation system made prior to 1960, but none was ever built.

One historic structure survived to 1973 Tokyo earthquake, and it was the Imperial hotel designed by Frank Lloyd Wright, completed in 1921 (Figure 1.1). This building was founded on a shallow layer of firm soil

that in turn was supported by an underlying layer of mud. Later Wright wrote in his autobiography (Wright, 1977) of the "merciful provision" of soft mud below the upper thick surface layer, which supported the building.

Figure 1.1 Imperial Hotel Tokyo (Japan)

Several unreinforced masonry buildings were only light damaged in 1933 Long Beach earthquake because they were able to slide on their grade beams. At least one masonry house survived the 1976 Tangshan earthquake because it also slid on its foundation (by chance and not because of a purposely conceived foundation behaviour).

For several years now, it has been a question for structural engineers to design earthquake-proof buildings and bridges. Initially, it has been generally thought that building a massive and stiff construction would make it earthquake resistant. But this stiffness or rigidity of the structural elements would lead eventually to a fragile and sudden failure, all in all not complying with the life safety performance criteria and letting inhabitants no time to react in case of an earthquake. Next, the increase of damping, redundancy of buildings, ductility and seismic

energy dissipation were taken into consideration and well implemented throughout the years in seismic building codes.

According to FEMA (Federal Emergency Management Agency) design guidelines, a base isolated structure should have the layout depicted in Figure 1.2.

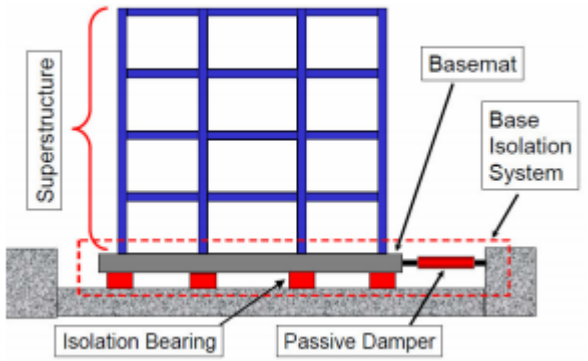

Figure 1.2 Configuration of building structure with Base Isolation System

The 'design earthquake' that the isolation system has to be able to face is specified on the basis of the seismicity of a region, the site conditions and the level of hazard accepted. It must also be recognised that occasionally earthquakes give their strongest excitation at long periods. The likelihood of these types of motions occurring at a particular site can sometimes be foreseen, such as with deep deposits of soft soil which may amplify low-frequency earthquake motions, the old lake bed zone of Mexico City being the best known example. The most important feature of seismic isolation is that its increased flexibility increases the natural period of the structure. Because the period is increased beyond

that of the earthquake, resonance and near-resonance are avoided and the seismic acceleration response is reduced. The benefits of adding a horizontally compliant system at the foundation level of a building can be seen below using an acceleration response spectrum (Figure 1.3).

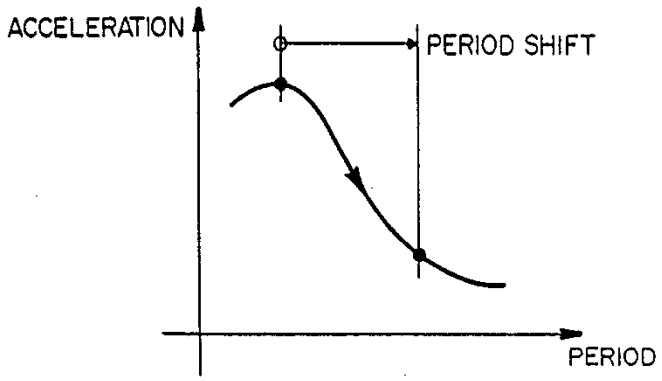

Figure 1.3 Reduction in spectral acceleration

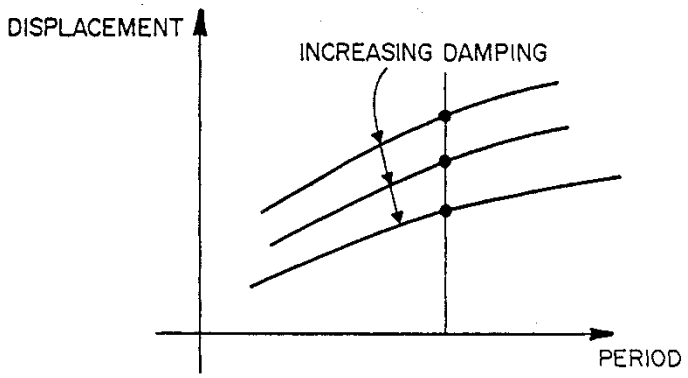

Figure 1.4 Increase in spectral displacement

Increasing the period of the structure reduces the spectral acceleration for typical earthquake shaking. The increased period increases the total displacement of the isolated system (Figure 1.4). Most of the displacement in an isolated building occurs over the height of the isolators and there is generally little deformation in the superstructure. Isolators must be designed to support gravity (and earthquake-induced) loads and accommodate large lateral displacements.

Displacements in isolated structures are often large and efforts are made to add energy dissipation or damping in the isolation system to reduce displacements.

The addition of energy dissipation to the isolation systems serves to reduce displacements in the seismic isolators, which can translate into smaller isolators, reduced costs, etc.

A variety of seismic isolation and energy dissipation devices has been developed over the years, all over the world. The most successful of these devices also satisfy an additional criterion, namely they have a simplicity and effectiveness of design which makes them reliable and economic to produce and install, and which incorporates low maintenance, so that a passively isolated system will perform satisfactorily. Recent seismic isolation devices could be divided into three categories: Laminated Rubber Bearing (LRB), Friction Pendulum System (FPS), and Hybrid Isolation System (HIS). In recent years, the implementation of base isolation systems for the seismic mitigation of buildings has become a common alternative to conventional strengthening measures. It has been estimated that altogether a total of approximately 16,000 structures have been protected in different parts

of the world by seismic isolation, energy dissipation and other anti-seismic systems (Martelli et al. 2012). Most of them are located in Japan, although they are more or less numerous in over 30 other countries.
Some of the largest-isolated buildings in the world are:

- *Sabiha Gökçen International Airport, Istanbul Turkey*

Sabiha Gökçen (*Figure 1.5*) is one of the two international airports in Istanbul, Turkey, which is located near the North Anatolian fault. It was designed by the engineering firm Ove Arup to have 300 base isolator systems that can withstand up to a maximum of 8.0 Mw earthquake. The base isolators can reduce lateral seismic loadings by 80%, which makes it one of the largest seismically isolated structure in the world.

Figure 1.5 Sabiha Gökçen International Airport, Istanbul Turkey (Image Source: Arup)

- *Transamerica Pyramid*

The Transamerica Pyramid (Figure) is an iconic 1970s structure hosted by the Californian city of San Francisco, which sits closely

beside the San Andreas and Hayward faults. In 1989, the Loma Prieta earthquake struck the structure at a magnitude of 6.9 Mw which caused the top story to sway, by almost one foot from side to side, for more than a minute but the building stood tall and undamaged. This earthquake resistance feat can be attributed to the 52-foot-deep steel and concrete foundation that is designed to freely move with seismic loadings. Vertical and horizontal loadings are supported by a unique truss system above the first level with interior frames extending up to the 45th level. The complex combination of these structural systems makes the building resistant to torsional movements and allows large horizontal base shear forces to be absorbed.

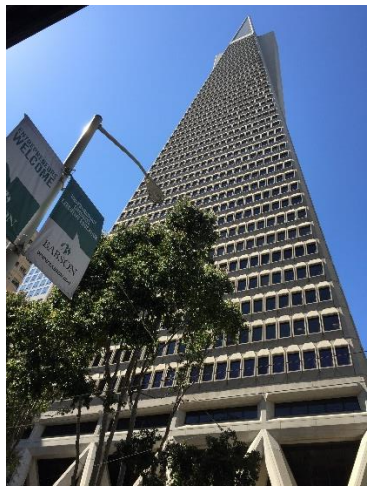

Figure 1.6 Transamerica Pyramid

- *Burj Khalifa*

Burj Khalifa is simply one of the most iconic supertall structures in the world and it's also earthquake resistant (*Figure 1.7*). The structure is

composed of mechanical floors where outrigger walls connect the perimeter columns to the interior walling. By doing this, the perimeter columns are able to contribute support for the lateral resistance of the structure and the verticality of the columns also help with carrying the gravity loads. As a result, Burj Khalifa is exceptionally stiff in both lateral and torsional directions. A complex system of base and foundation design was derived by conducting extensive seismic and geotechnical studies which gave the skyscraper stringent structural measures against earthquakes.

Figure 1.7 Burj Khalifa (Image Source: Burj Khalifa)

- *Taipei 101*

The architectural exterior design, by C.Y. Lee, was inspired by the Asian mentality "we climb in order to see further" (Figure 1.8). Putting aside the architecture, the mind-blowing fact about Taipei 101 is that it houses the biggest tuned mass damper (TMD) in the world (Figure 1.9). It's a gigantic metal ball that counteracts big transient loadings like wind and earthquake to reduce the sway of the supertall tower. The TMD is

supported by hydraulic viscous damper arms and bumper system which function in the same way as a car's shock absorber.

Figure 1.8 Taipei 101 (Image Source: C.Y. Lee)

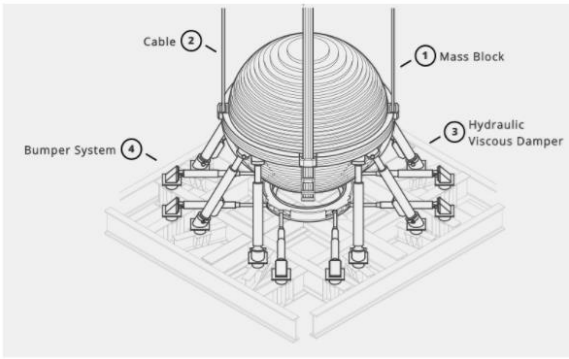

Figure 1.9 Taipei 101's tuned mass damper (Image Source: Taipei 101)

When large forces act upon the tower the TMD sway in the opposite direction bringing the entire building in equilibrium by damping out the transient forces using the ball's mass. This earthquake damper system is located between the 87th floor up until the 92nd level.

- *Philippine Arena*

The Philippine Arena is the world's largest domed arena and is the most amazing earthquake-proof structure. The arena was designed by the Australian architecture firm Populous and the elite engineering firm Buro Happold.

The Philippine plate sits along the Pacific ring of fire, the world's most notorious and active chain of earthquake fault lines. Previous earthquakes in the country has surmounted up to 8.2 Mw and have claimed thousands of lives where the epicentres originate and the seismic activities were also responsible for igniting volcanic eruptions and tsunamis. Philippine Arena's vast stadium roof, spanning 165m in the shortest direction, was engineered to withstand severe transient loadings such as earthquakes, winds, and typhoons.

Figure 1.10 Philippine Arena (Image Source: Philippine Arena*)*

During an earthquake tremor, the lateral loads that generate throughout the structure can be up to 40% of its mass. Buro Happold cleverly responded with an independent base design for the entire structure which means that the main structural body of the arena is isolated from

its base and foundation. The gap between the main structure and base foundation system is composed of lead rubber bearings (LRB) which are a flexible arrangement of materials with high energy dissipation properties. This allows the base and foundation system to freely move with the earthquake force while the top structure remains stationary during dynamic actions.

1.2. Seismic isolation of existing buildings

Techniques have been developed which can be used to insert base isolation under existing buildings with some additional costs, which might be justified especially in the case of historic buildings with an extremely high or even inestimable value (Bailey and Allen 1988; Lignola et al. 2016; Melkumyan, Mihul, and Gevorgyan 2011; Melkumyan 2014; Mezzi, Comodini, and Rossi 2011; Poole and Clendon 1992; Seki et al. 2000).

In countries like Italy, with a high seismic hazard and old or very old towns, where many buildings are hundreds of years old, this is one of the most relevant problems for the protection of both population and cultural heritage (Costanzo et al., 2007). Few historic buildings meet current code seismic requirements for life safety, and most have architecturally significant elements that are threatened by future earthquakes.

In comparison with new buildings, the seismic base-isolation of existing buildings has some specific features. The installation procedure involves cutting out portions of existing masonry walls in the basement level, constructing RC ties under the walls and installing isolation devices. In

a recent study by Lignola and co-authors (Lignola et al. 2016) a novel procedure for the installation of base isolation was presented, in which a special system to uplift the existing structure from its foundations is used. It should be pointed out that not all existing masonry structures are suitable for retrofitting with base isolation. A basement story should be present and the building should not be connected with neighbouring buildings to allow for the construction of a lateral opening, the so called "seismic gap", which facilitates lateral displacements of the isolation layer. In this case dampers may be used along with base isolation devices to limit lateral displacement to a permissible level (Lignola et al. 2016). Moreover, the existing structural walls should not be already heavily deteriorated or damaged in any other way. Another issue is that the isolators behave as concentrated supports under continuous masonry walls, and that the distance between isolators influences the stresses in the walls and supporting tie beams (Mezzi, Comodini, and Rossi 2011). When positioning the isolation devices in layout, care has to be taken also in order to prevent global torsional effects. The problem of optimizing the placement of the centre of stiffness in order to prevent global torsion in the base-isolation layer has already been extensively studied in (Di Sarno et al. 2011; Kilar and Koren 2009; Lee 1980; Pan and Kelly 1983). As of today, existing applications of base isolation to existing masonry buildings are scarce. They generally focus on heritage buildings with strong preservation needs. One of the best known examples is The Salt Lake City and County Building in Salt Lake City, Utah, USA (Bailey and Allen 1988). Another example from the U.S. is The Hearst Memorial Mining Building in Berkeley, California (Davis

and Robertson 2000), while the largest base-isolated masonry buildings are those of the headquarters of the New Zealand Parliament, which is located in Wellington, New Zealand (Poole and Clendon 1992). Other examples include buildings and monuments which are located mainly in Italy, Greece, Japan, and Turkey (Martelli et al. 2012).

The peculiarity of interventions on the heritage is the requirement of respecting the integrity, besides guaranteeing the safety. The concept itself of integrity has many facets and is somewhat elusive; its comprehension, however, is a necessary prerequisite. Its first and most obvious aspect is the formal, or iconic integrity: the external aspect, the image, the original form that should not be altered by the engineering intervention (Viggiani, 2017). Another important facet are the integrity historical integrity and the material integrity. The materials, the construction techniques, the structural scheme are original features of a monument as significant as its appearance and history. Finally, the harmony between a monument or a city and the surrounding wider landscape is another important aspect of the integrity to be preserved (Viggiani, 2017). The use of the isolation system conceived for new structure could be in conflict with the respect of the iconic, historical and material integrity of the monuments.

1.3. Geotechnical seismic isolation systems

An alternative solution to the problem of seismic isolation of existing buildings could be the geotechnical seismic isolation.

Geotechnical Seismic Isolation (GSI) is one of the most recent solutions to protect structures from the destroying effects of earthquakes. A GSI

system can be defined as a seismic isolation system that involves the direct interaction with the natural soil and/or man-made reinforced soil materials, in contrast to the commonly well-known structural seismic isolation system, in which the flexible or sliding interface is positioned between a structure and its foundation.

In the last decades, GSI has been investigated by many researchers such as Yegian and Lahlaf (1992), Kavazanjian et al. (1991), Yegian and Catan (2004), Yegian and Kadakal (2004), Georgarakos et al. (2005), Kirtas et al. (2009) and Kirtas and Pitilakis (2009) and Tsang (2009) who introduced the GSI concept.

Earthquakes generate seismic waves that radiate away from the source and travel through the earth crust, eventually reaching the ground surface and producing shaking, possibly causing damage to existing structures. Such a damage results from the complex soil-foundation-structure interaction mechanisms due either to the transient ground motion, or, in peculiar conditions (loose saturated granular soils), caused by soil liquefaction. The shaking caused by the waves depends on some general characteristics of the earthquake (size and location, and therefore distance from the site to be protected) and on the characteristics of the site, in terms of subsoil conditions and morphology. Soil characteristics play a relevant role in waves propagation, as soil deposits tend to act as "filters" to seismic waves: considering a complex signal, as it is always the case in nature, some frequencies may be attenuated passing through the soils, some may be amplified (Richart et al., 1970; Aki, 1988; Kramer, 1996; Chavez-Garcia, 2011). Nowadays, analytical tools are available to accurately

carry out local seismic amplification analyses taking into account the effects of soil stratigraphy and ground morphology (Lanzo et al., 2011; Evangelista et al., 2011).

The idea supporting the proposed research activity is to control the subsoil filtering action by artificially modifying the mechanical and physical characteristics of a small part of the foundation subsoil underneath the building to be protected. The research is, therefore, aimed to find a completely new and unconventional way to protect, for instance, existing strategic constructions from earthquakes, respecting their integrity in the most possible meaning (structural, artistic, historical): seismic protection will be obtained by adopting a peculiar grouting technique to adequately modify the mechanical and physical properties of a limited volume of soil, far enough from the structure to be protected. In particular, the idea to be developed consists in introducing into the ground (displacing or permeating it, or both) a new grouting mixture able to completely modify the mechanical response of the treated soil to seismic excitation. The proposed unusual soil grouting should be injected in a small portion of the subsoil, at a suitable depth, not directly beneath the structure to be protected. The depth and thickness of grouting have to be optimized on the basis of the soil properties, the characteristics of the building to be protected, and the expected seismic action.

As previously stated, such an approach is best suited for existing structures, since there are nowadays simpler and more practical alternatives to be implemented in the design of new structures. For

existing structures, on the contrary, it is in principle the least invasive and likely the most effective, if properly conceived.

The idea of a "screen barrier" in the ground has been already proposed in literature. For example, different vibration mitigation measures (for vibrations caused by vehicle and rail-bound traffic generally complex and difficult to analyse) can be used near the source, in the soil layers or close to the buildings to be protected, remembering that the most efficient mitigation methods should be proposed at the design stage of a project. Some authors (Chouw, 1992; Kellezi, 2011) have proposed an approach that is thought to isolate building foundations from steady-state or transient soil vibrations by placing a stiff layer, such as an artificial bedrock, under the building's foundation. Vibration at the soil surface depends on the soft layer thickness, its material properties and the frequency content of the dynamic source; the aim is to artificially reduce the wave propagation in the top layer thanks to a virtual rigid base at an appropriate depth (Figure 1.11), because if the excitation frequency is less than the lowest eigen-frequency of the layer, the waves spreading into the layer will be impeded, reducing foundation excitation and structural response (Kellezi, 2011). The dynamic response of buildings can also be improved by installing wave lateral barriers like open, in-filled (walls) or gas cushion trenches (Massarsch, 2004, 2005) close to the vibration source. The most efficient isolation barrier is an open trench in the ground; open or liquid-filled trenches are unfortunately difficult to use in practice, above all in built up areas, also because rain or percolating water can fill up the trench, reducing the impedance difference relatively to the ground significantly (Andersen

and Augustesen, 2009); so light-weight in-filled trenches are generally placed.

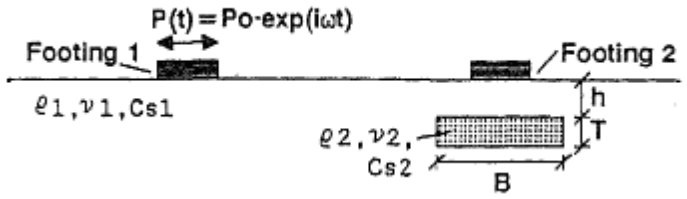

Figure 1.11 Screen barrier for superficial waves

When subjected to compressive stresses due to the lateral earth pressure after installation in the ground, however, these light-weight materials change their dynamic properties and loose much of their vibration isolation effect. As a matter of fact, in order to achieve vibration isolation from artificial vibrations, it is necessary to create an abrupt change of impedance in the ground; density as well as stiffness increase by increasing pressure and so a lateral trench should resist the high lateral earth pressure without changing its impedance. So gas cushions in-filled trenches are also used to create a flexible barrier to great depths, with a very low impedance (low density and low wave velocity). Such barriers are able to resist the later earth pressure, creating a flexible barrier with a vibration isolation capacity comparable to an open trench. As an alternative approach, nowadays soil grouting is sometimes used for earthquake hazard mitigation, but with little or no ability to truly mitigate seismic hazard.

As a matter of fact, during the last years, an increasing number of researchers have been studying treated ground dynamic properties in

order to understand and control the modifications introduced by various treatments to the mechanical and dynamical ground properties (Saxena et al., 1987; Chepkoit and Aggour, 2000; Cai and Liang, 2003; Spencer, 2010). However, these studies have an approach completely different from the one herein proposed, and usually study grouted soils which are stiffer and stronger than the original soil, while this will not be the goal of our research project, whose aim is to introduce a less stiff grouted layer.

In some cases, engineering applications of conventional superficial grouting have been proposed in literature as a mean to mitigate seismic actions, but always considering cemented (and therefore improved) soils in the topmost part of the subsoil. Numerical one-dimensional site response analyses proved that stiffening the uppermost soil layers by grouting reduces the overall ground motion, but has little or no effect on the high-frequency content of the seismic motion transmitted to the surface, which can therefore still be potentially dangerous to stiff massive buildings to be protected (D'Onofrio et al., 1999).

Two-dimensional FEM analyses have proved that the use of vertical stiff barriers of grouted soil may even amplify the seismic acceleration amplitudes due to the internal reflections of waves under the building foundations (Di Prisco and Serra, 1996). In other words, while static vertical and lateral ground displacements may be somehow reduced by the conventional shallow soil grouting techniques, these latter do not guarantee an appropriate mitigation of seismic inertial forces in the buildings.

So, stiffening the uppermost soil by grouting certainly reduces seismically induced ground motion, but may have little or no effect on the energy transmitted to the structure to be protected, which can still be very high and therefore potentially dangerous. So, ground displacements may be somehow reduced by this conventional superficial soil grouting because of increasing soil stiffness, but this does not guarantee that the seismic hazard has been properly mitigated.

The approach proposed in this research is similar to the ones previously exposed for lateral trenches used to preserve from superficial vibrations. In fact, the proposed solution tends to explore the possibility to create a full screen barrier for seismic risk mitigation. Since there are only very few references in literature on this topic (Kirtas and Pitilakis, 2009), this research is innovative and, in case applicable, it would give rise to new activities both in the research and application fields.

The isolation mechanism that this thesis will analyse takes advantage of few experiences reported in literature. One of those is the one reported by Dietz and Woods (2006), who show series of shaking table tests, made to evaluate the seismic response of a caisson modelled at 1/30 scale, using a shear stack (that is a flexible-walled hollow box designed and built to enable geotechnical modelling in conjunction with the shaking table).

The mitigation scheme studied by Dietz and Woods involved the construction of a soft caisson around and beneath an existing foundation, made by inserting a horizontal slip layer at a moderate depth (authors suggests around 10m) and also inserting soft trenches around the foundation (Figure 1.12). The weak layer had a low value of the shear

strength angle, thanks to the use of the roller bearings, which the experimental box sits on, whereas soft trenches (made with cylinders of neoprene) offered negligible shear stiffness.

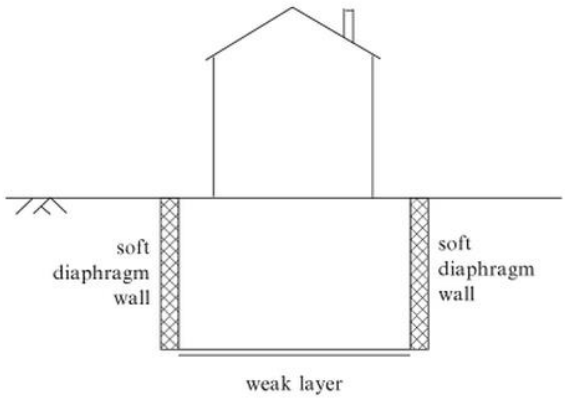

Figure 1.12 Scheme adopted by Wood (2006) for his isolation typology

The shaking table tests, performed by applying different seismic inputs to the system, demonstrated that this isolation scheme, installed within the ground underlying a vulnerable structure, can improve its seismic performance, but the inclusions are successful only when the frequency content of the input motion lies above the resonance frequency of the modified system. Thus, for maximising their benefit and widening their range of application, the stiffness and the friction angle of the whole treated mass should be minimised; this is an important, critical theoretical topic, because the frequency content of the expected earthquake motion is not previously known.

There are several studies on base-isolating low-rise buildings by placing liners beneath the foundation slab, thanks to the slip coefficients that are function of axial load, number of cycles and velocity and that has been

obtained with both standard and modified surfaces. Many authors have studied slip layer beneath a building slab foundation to provide base isolation.

On the basis of shake table tests on sand deposit and analytical tests, Yegian and Kadakal (2004) proposed to place a smooth synthetic material beneath building foundations (Figure 1.13) in order to provide a slip layer by using a geo-textile placed over an ultra-high molecular weight polyethylene sheet. The concept was that the liner placed in a curved shape penetrating the soil profile would dissipate energy through slip displacement (Yegian, 2004), transmitting significantly reduced motions to the overlying isolated soil layer and any structure founded on it. This system is useful in decreasing both peak as well as spectral responses measured at the surface and in the central isolated mass than the motion below the isolating liner, but, as a consequence, slip displacements were recorded along the perimeter of the isolated soil layer. Because of the restoring force, effect of the gravitational weight of the isolated soil layer, the slip displacements are small in the central zone, but, near the edges of the isolated region, it's necessary to study the effects on utilities and similar. Doudomis et al (2002) proposed placing soil layers with low shearing resistance beneath buildings, to let building slip under the action of strong seismic motions (Figure 1.14Figure 1.14). According to the authors, the low shearing layer should be provided by suitable natural materials, such as granular products from rocks containing low friction materials (talc, chlorite, serpentine, etc.) with an adequate strength in compression or high plasticity clays (monmorillonitic clays and similar).

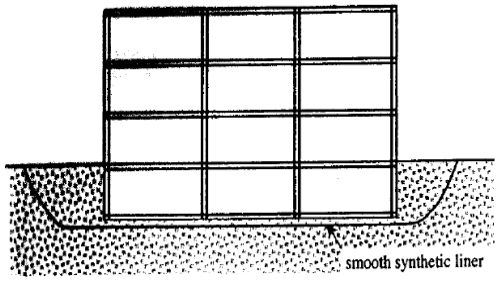

Figure 1.13 Isolating scheme with smooth synthetic material beneath building foundation (Yegian and Kadakal,2004)

The great disadvantages of this system are the doubtful constructability, and the design problems. The coefficient of friction of 0.2 proposed by the authors does not guarantee large force reductions. A similar approach has been made by Taskov et al. (2004). A liquid storage tank whose base has been isolated by the ALSC (is acronym of "Almost Lifted Structure Concept") system has been modelled. In this system, the foundation of the structure is placed on a sliding plate positioned on a recess containing oil under pressure, which has the purpose of lowering the sliding resistance between the foundation and the ground. By using shacking table test, the modified structure is hit by a certain vibration; structure moves with no foundation shear resistance, because this resistance is quite totally decreased by the uplift oil pressure force. The movements are opposed by springs at the sides of the ALSC system, which have to break down the maximum displacements and refocus the foundation to its original position when oscillations end.

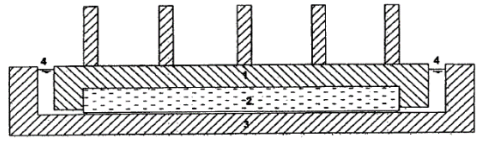

1: Foundation 2: Soil layer 3: Concrete slab 4: Water level

Figure 1.14 Scheme proposed by Doudomis et al. (2002) with an artificial soil layer

Tests with this typology of system have been made on a reduced scale test of the model of St. Nicholas church (Tashkov et al., 2010) (Figure 1.15). The system shows a very effective reduction of input energy transmission and keeps the structure out of resonance within a broad frequency range of the excitation force, deleting bending and shear forces in the main structure and relative story drifts; moreover, this system is not sensitive to vertical excitation component. ALSC system seems to be a good retrofit system, because it does not change the aesthetic appearance of the structure and it is limited to foundation intervention; it is also reversible, because, for coming back to the original condition, oil pressure can be set equal to zero (Figure 1.15). However, it alters the materal and conceptual integrity of the structure, which is as important as the architectonic one (Viggiani, 2017).

On the other hand, an alternative possibility should be to increase the damping of the foundation soil beneath the building to protect. In this sense, rubber soil mixtures (whose acronym is "RSM") placed around the foundation of a building have been proposed (Tsang et al, 2007, 2011; Figure 1.16) for adsorbing seismic energy and exerting a function similar to that of a cushion.

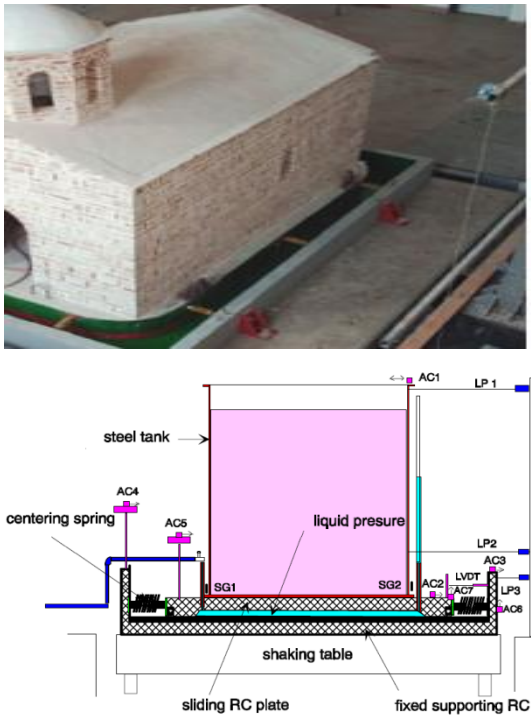

Figure 1.15 St. Nicholas church model to the scale of 1/3.5 tested on the seismic shaking table (a); ALSC instrumentation set up (b)

Rubber has important damping properties used for many years in structural isolating system. According to Tsang (2007), the soil layers surrounding foundation (considered having G=222MPa at a confining pressure of 345kPa; Vs ≈ 350m/s) can be replaced by a medium which is made up of soil mixed with a designed proportion of rubber and sand (G=7,5MPa at a confining pressure of 345kPa; Vs ≈ 90m/s), with both an important increase in damping and a decrease in shear stiffness. Using this system, the authors predict an average reduction of 40÷60% in horizontal accelerations, above all for wider buildings (low to

medium rise buildings) with a remarkable increase in the fundamental structural period. The effectiveness of the proposed RSM system has been shown by a preliminary parametric study using three recorded earthquake ground motions. An important issue that has not been explored is the amount of induced vertical displacements, which could be relevant for a building placed at ground surface.

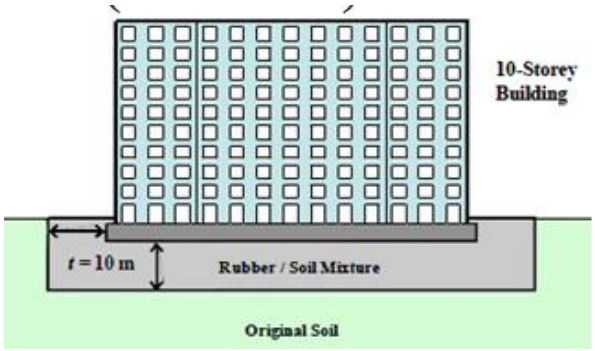

Figure 1.16 RSM system around the foundation of a building (Tsang et al., 2007,2011)

However, the principal topic is not achieved, that is: "How is it possible to apply this method to an existing structure? How could the foundation system be easily modified in order to place such a system?"

In order to answer these questions, the research activity to be carried out should be both theoretical and experimental and should consider the treatment at depth of a thin layer of soil.

In this sense, Kirtas (2009) has studied, numerically and by using centrifuge equipment, the inclusion of different stiff and soft treatments into a soil deposit, considering the presence of a SDOF (Single Degree of Freedom) at ground surface simulating the case of structures with

surface foundations. Actually, he has studied the insertion of horizontal layers beneath the foundation, vertical diaphragms next to the foundation and caissons, which are the combination of two vertical diaphragms and one horizontal layer to form an isolated soil-structure area; any modification of the foundation soil properties may affect the structural response through soil-structure interaction mechanisms in a beneficial or a detrimental way, as reported by Wood (2006). Evaluation of foundation subsoil stiffening and stiff diaphragm intervention effects has revealed that the specific approaches are not efficient in reducing the seismic part of the structural response. On the contrary, the seismic acceleration for several soil-structure combinations could increase after the intervention compared to the initial system, although the adequacy of the methods in soil strength enhancement and excessive settlement reduction is not under question.

In Kirtas (2009) several structural mass and height combinations are examined, since they both enhance soil-structure interaction phenomena leading to different dynamic response. Normalized values of structural mass and height are used according to the expressions:

$$m_{norm} = \frac{m_{str}}{\rho \cdot B^3} \tag{1.1}$$

$$h_{norm} = \frac{h_{str}}{B} \tag{1.2}$$

where:

- m_{str} is the superstructure mass;

- h_{str} is the superstructure height;
- ρ is the soil density;
- B is the characteristic foundation dimension (half the foundation width for strip foundation type).

Results are generally depicted in the frequency domain, introducing the term ‘‘response ratio’’. This is the ratio of the Fourier transform of the response time-histories in selected locations of the modified system to the corresponding response of the initial unmodified system. Thus, values of the response ratio below unity are indicative of the mitigation efficiency of the structural response in the examined frequencies, whereas for ratios exceeding unity it is possible that the intervention has a detrimental effect on the system’s seismic performance.

According to Kirtas (2009) incorporating a short-length soft horizontal layer in the foundation subsoil does not affect significantly the structural seismic response (Figure 1.17, where T_{str} is the SDOF natural period).

Construction of flexible vertical diaphragms next to the foundation could aim at isolating a soil mass underneath the foundation and the superstructure, in order to reduce the induced ground shaking and allow independent oscillation from the surrounding soil. Unlike the previously examined methods, the superstructure acceleration ratio in the case of the ‘‘soft diaphragms’’ presents a wide range of values below unity near the fundamental effective period of the structure, indicating an efficient mitigation of the seismic response (Figure 1.18). The superstructure accelerations in the time-domain (Figure 1.19) for the structure with T_{str}=0.6s and two different excitations verify the mitigation efficiency of the intervention (the excitations are: EQ1with predominant period

between 0.15s÷0.40s and EQ2 with a wide range of frequencies with an important frequency content for T=0.6s÷0.8s, a period range near to the structural effective period).

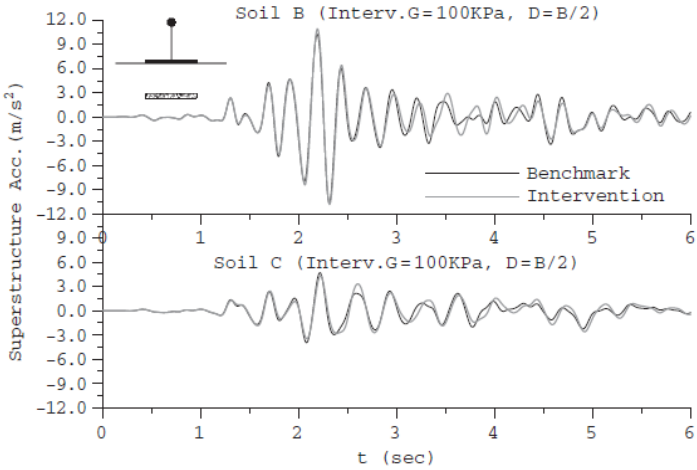

Figure 1.17 Soft horizontal layer: acceleration time-histories (T_{str}=0.2s; m_{nom}=2).

The increase of the dynamic response due to the presence of the proposed system during the EQ1 excitation is of minor importance since the structure is out of resonance with the seismic motion, which is obvious considering the low level of the superstructure acceleration developed in the initial system. On the other hand, applying the EQ2 input motion where resonance phenomena occur, the soft diaphragms induce a significant reduction of structural response. The efficiency of the intervention increases with increasing structural mass, as depicted in both the time and frequency domains.

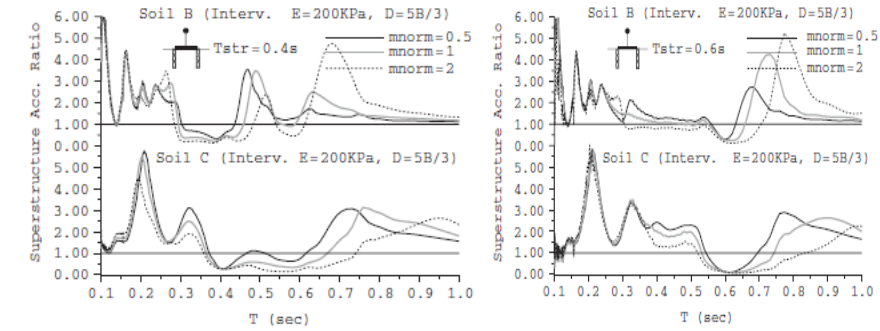

(a) (b)

Figure 1.18 Soft diaphragms: superstructure ratios for Tstr= 0.4s (a) and Tstr=0.6s (b).

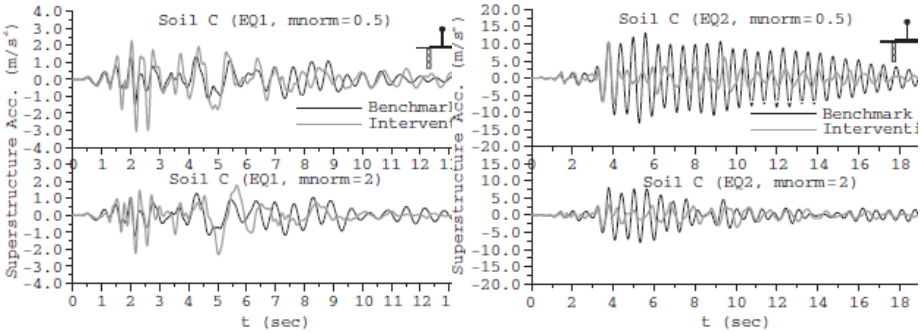

(a) (b)

Figure 1.19 Soft diaphragms: acceleration time-histories for excitations EQ1 (a) and EQ2 (b) (Tstr=0.6s).

Because of the significant deformability of the implemented intervention compared to the initial foundation subsoil conditions, it is reasonable to expect an increase of the seismic displacements of the system. Yet, displacement ratios (Figure 1.20) indicate the possibility of either increased or reduced displacements, depending on the frequency content of the imposed seismic motion. For instance, in the case of EQ1

input motion of low predominant frequency, the displacement of the structure having Tstr=0.6s is only slightly increased (Figure 1.20), confirming the displacement ratio predictions.

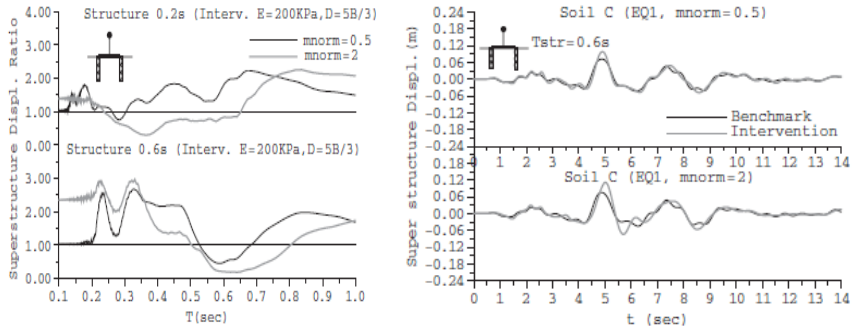

(a) (b)

Figure 1.20 Soft diaphragms: superstructure displacement ratios (a) and corresponding time-histories for EQ1 (Tstr=0.6s).

However, when this layer is combined with flexible diaphragms forming a soft caisson, a reduction of the soil-structure's seismic loading levels could be achieved (Figure 1.21). The dynamic characteristics and especially the fundamental period of this system seem to dominate the response, shifting it to higher periods, out of the frequency content range of common earthquakes. According to authors, significant alteration of the dynamic properties of the system shifts the SDOF response to higher period values, out of the frequency range of common earthquake records, resulting in beneficial effect of the implemented intervention (Figure 1.22). The response ratios in Figure 1.3.12 c and d are plotted for periods up to 2.0s, highlighting the significant modification of the system's dynamic properties.

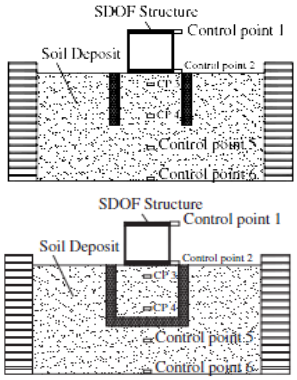

Figure 1.21 Some of the schemes adopted by Kirtas (2009).

The existence of a wide range of ratio values below unity is evident near the fundamental period of the oscillating systems with Tstr=0.2s and 0.6s, indicating a substantial reduction of the structural seismic response. These findings are also verified by the important reduction of the acceleration time-histories at the top of the structure in Figure 1.22. However, according to Kirtas (2009), by considering such a system, increase of the soil deformations and structural displacements are expected and should be handled appropriately considering the specific nature of the implicated materials (Figure 1.23).

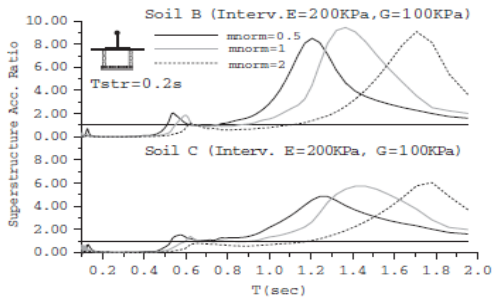

(a)

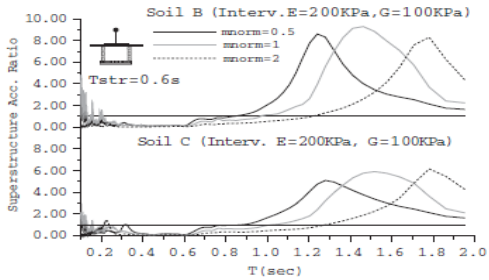

(b)

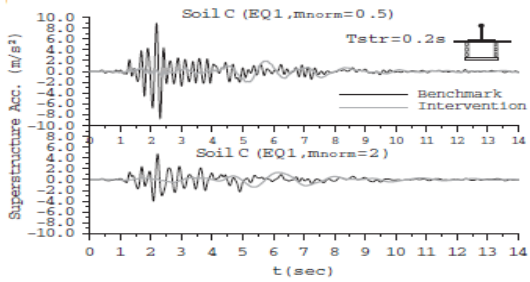

(c)

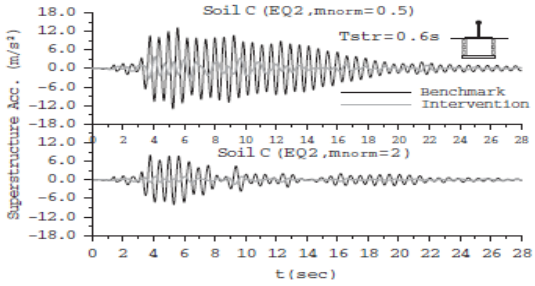

(d)

Figure 1.22 Soft caisson: superstructure ratios for Tstr=0.2s (a) and Tstr=0.6s (b); superstructure acceleration time-histories for Tstr=0.2s (c) and Tstr=0.6s (d) (Kirtas (2009).

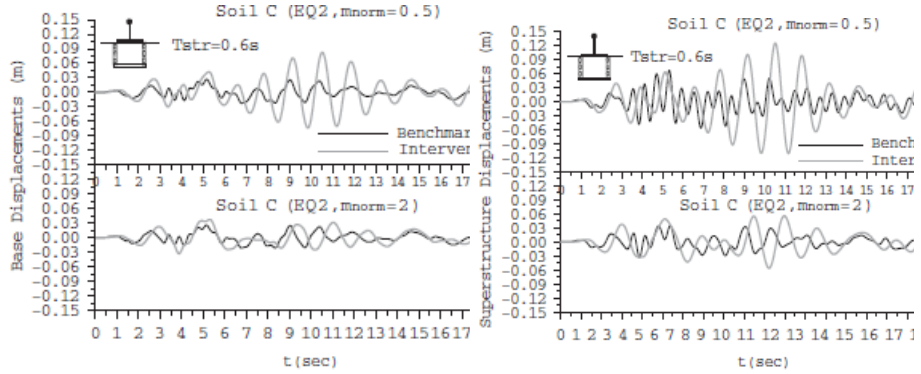

(a) (b)

Figure 1.23 Soft caisson: base (a) and superstructure (b) displacements time-histories

More recently, a GSI solution was applied on bridges (Forcellini, 2017). His paper aims at reproducing the seismic response of bridge configurations on different deformable soil conditions and isolated by a GSI system. The soil has been modelled with nonlinear hysteretic materials and advanced plasticity models. The bridge was modelled as a linear column with the equivalent characteristics of a 1DOF system (Figure 1.1.24). In particular, the mass at the top of the structure represents the deck of the bridge while the stiffness of the 1DOF has been calculated to take into account the presence of the abutments. The study considers the longitudinal direction only. Before the effect of adopting different GSIs with several soil deformability has been studied. The original configuration (without GSI) has been compared with several isolated configurations with different positions of the liner (0.50, 10, 20 and 30 m depth and named GSI1, GSI2, GSI3 and GSI4,

respectively), as shown in Figure 1.1.24 and several bridge configurations has been considered (0.429–0.526–0.674 s).

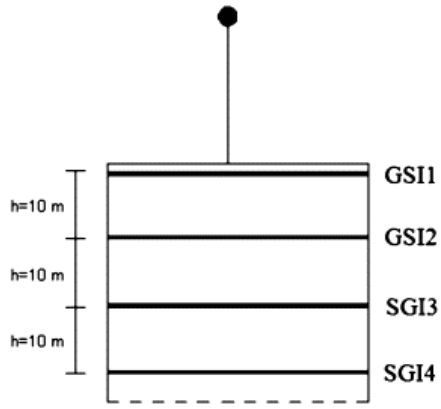

Figure 1.1.24 GSIs applied in the study

After the dynamic analyses have been performed for the configuration on which the improvement has the minor and the major improvement to assess the effects of soil deformability on the structural performance. Five input motions were selected to affect the structure significantly and applied along the longitudinal axis. The isolation reductions have been calculated as the ratio between the peak acceleration at the surface and the PGA for each soil conditions and all the considered input motions. It is possible to assess that the best reduction is achieved for soil A (maximum reduction: 7.78, minimum reduction: 3.82). For soil B and C these values become: 5.52 and 3.22, 3.34 and 2.56 for soil B and C, respectively. In case of soil D (high deformable soil), GSI4 becomes not interesting, since the liner characteristics and soil parameters are similar to each other—the isolation effect is low. The values are 1.54 and 1.10.

A different GSI system was introduced by Mousavi et al. (2016) namely Large Scale Seismic Isolation (LSSI) by which a target zone would be isolated from seismic surface and body waves. Considering the hybrid soil-solid frame, this is done by placing a seismic isolation bearing just below the roof level. The bearing is selected to be an engineered thin pre-saturated liquefiable soil layer through which the roof would be isolated from the lower stories of the dual soil-solid frame. In a large scale view, a fully undrained pre-saturated liquefiable soil layer, as depicted in Figure 1.25, would be able to perform similar to a seismic isolation bearing and satisfy abovementioned requirements. It is crucial to note that the liquefiable layer must be placed in a level surface with minimal slope to avoid pore pressure localization.

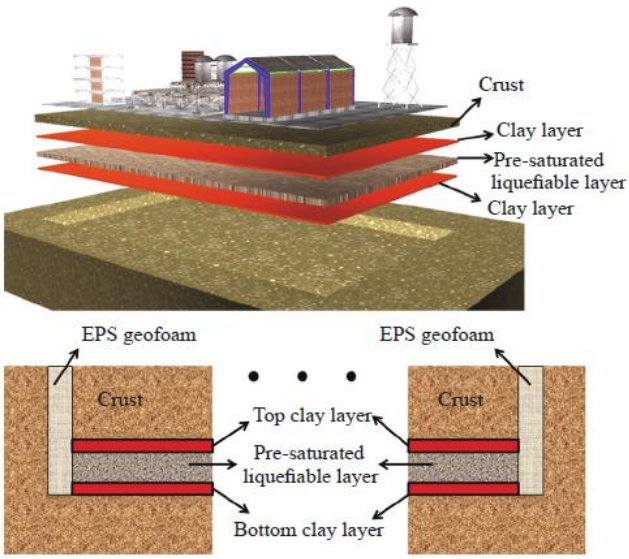

Figure 1.25 Main details of the large seismic isolation (LSSI)

Feasibility and efficiency of LSSI concept has been investigated by available ground motion database through making comparison between recorded accelerations on liquefied soils and those on non-liquefied soils. Some researchers, such as Miyajima et al. (2000) and Kostadinov et al. (2000), have focused on this feature and tried to detect liquefied zones from their corresponding recorded ground accelerations. Miyajima et al. (2000) observed substantial reduction in horizontal components of the ground acceleration due to the occurred liquefaction. Meanwhile, no noticeable change has been reported with regard to the vertical component. Another important characteristic was reduction of the predominant frequencies of the horizontal accelerations.

Figure 1.26 indicates that during liquefaction, horizontal components of the ground acceleration would be decreased while the vertical component remains rather unaffected. Besides, predominant frequencies in liquefied zones are lower than those of non-liquefied zones. All of these observations would be also the case in any seismic isolation technique.

However, it is crucial to note that delayed liquefaction would fail to contribute to the suppression of surface acceleration. The authors aimed to reach an engineered liquefiable soil layer to act as a seismic isolating system. As a result, a liquefiable layer should be engineered to trigger fast liquefaction during the early seconds of an earthquake. This would be accomplished by facilitating pore pressure generation and slowing down its corresponding dissipation. Liquefiable layer of the LSSI should be designed to be able to trigger liquefaction as soon as possible during the design level seismic event. In other words, excess pore water

pressure should be generated fast enough to activate LSSI at the early seconds of the ground motion.

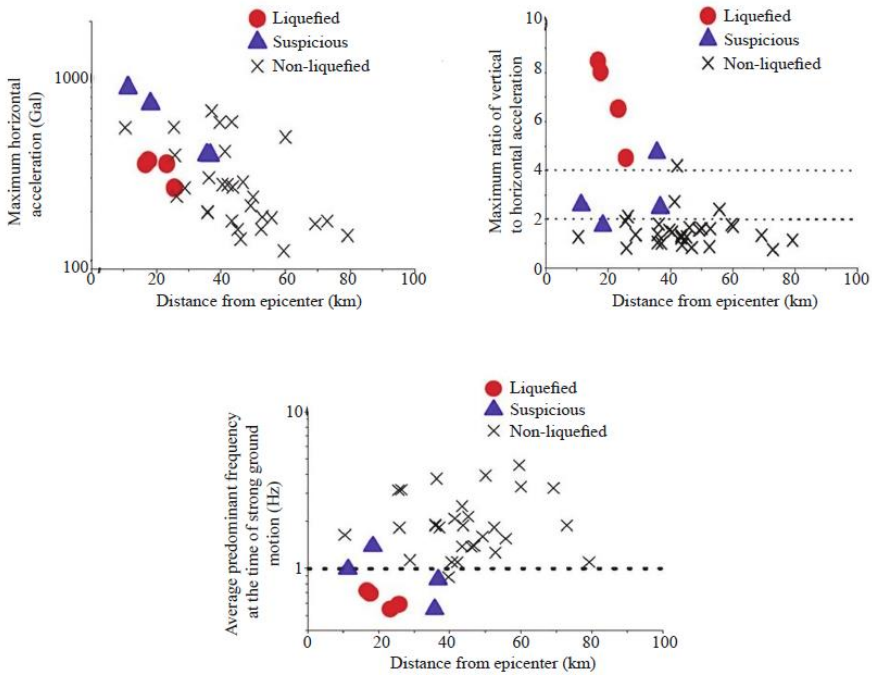

Figure 1.26 Measured ground response on liquefied and non-liquefied soil (Miyajima et al., 2000)

Therefore, an optimum liquefiable layer would be obtained by maximizing of the generated pore pressure at a given strain level and minimizing its corresponding dissipation.

The liquefiable layer is generally of sandy silt, should be very susceptible to liquefaction, and should generate substantial excessive pore water pressure at the early seconds of ground motions. The main role of the upper and lower clay layers is to avoid/postpone pore pressure

dissipation and make the liquefiable layer with minimum shear stiffness and maximum vertical stiffness/strength.

Geofoam sheets also allow large relative displacements between the isolated zone and its neighbouring ground.

The results indicate that LSSI would reduce acceleration spectrum within the short to medium period range, i.e. less than 1s. The contribution of LSSI is more pronounced in stronger ground motions, such as near field ground motions or those with larger return periods.

Generally speaking, after a review of literature cases, the seismic risk mitigation above all for existing and historical buildings seems to be an unresolved problem which allows no completely satisfactory solution. From the ambitious purpose to find a solution for this problem, this research project was developed in the last years.

1.3.1. GSI method proposed and first results

A previous Ph.D. thesis on this topic (Lombardi, 2014) laid the basis for this research project and for the present thesis. In the next section, the results achieved by that thesis are briefly summarized, highlighting advantages and disadvantages of using this kind of *Geotechnical Isolation System*. The GSI method proposed in this research project could be explained by referring to the performance-based design approach; the two key elements for a seismic safety assessment of a building (Figure 1.27) are the seismic demand and the capacity curve.

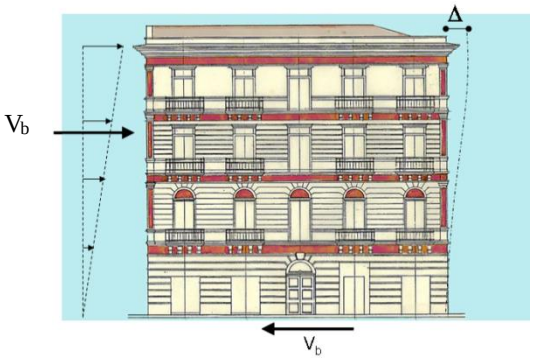

(a)

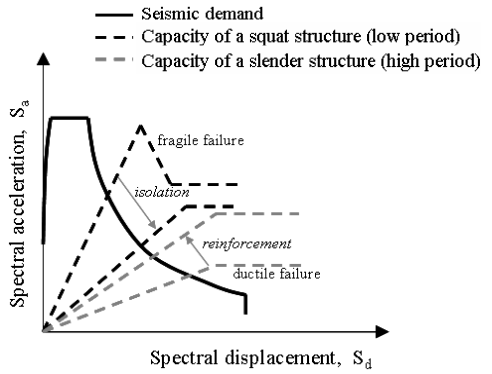

(b)

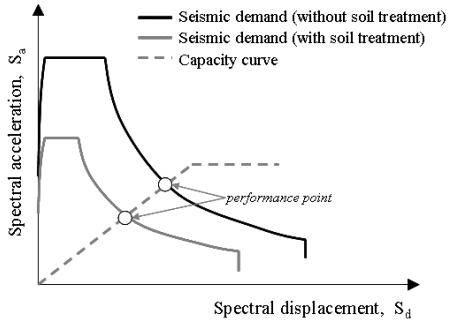

(c)

Figure 1.27 Seismic safety assessment procedure (Lombardi et al. 2013)

This latter is often referred to as a "pushover curve", relating the base shear force V_b, to a reference horizontal displacement Δ, for instance at the top of the building (Figure 1.27). The seismic demand for the pseudo-static analysis of a rigid system can be typically defined in terms of a seismic coefficient (proportional to the design peak ground acceleration a_{max}); for deformable systems, the most conventional way to express it is by using the spectral acceleration Sa(T), the spectral displacement S_d(T), or both (Figure 1.27). For a structure with a given fundamental period, T, S_a(T) and S_d(T) can be viewed as proportional to the above defined shear force and displacement, respectively.

As a consequence, they represent a convenient and synthetic way to analyse seismic demand. S_a(T) and S_d(T) depend on the regional seismic hazard, the seismic site response and the system ductility. The safety assessment can be therefore expressed by comparing demand and capacity, individuating a "performance point" at the intersection of the curves (Figure 1.27). If such a performance point does not exist (i.e. the capacity is lower than the demand, and safety cannot be guaranteed) or it is too close to the limit capacity (i.e. the safety margins are not sufficient or do not respect Codes of Practice specifications), seismic risk mitigation interventions are necessary. In principle, this can be achieved by changing either the capacity curve or the seismic demand, with the final goal to have a performance point with higher safety margins. As previously mentioned, it is common practice to work on the capacity, i.e. on the pushover curve. For new structures, this can be done with base isolation techniques, reducing the fragility and increasing the ductility in the structural capacity, thus shifting the capacity curve to the

right in the plot of Figure 1.27. This is certainly beneficial in terms of safety margins at the performance point, as the limit capacity can be assumed to be similar to that of the less ductile structure without isolation. An alternative is the reinforcement of the structure, obtained by increasing both the stiffness and the strength of the building (Figure 1.27). In such a way, even though the capacity curve is shifted to the left in the plot of Figure 1.27, safety margins may be increased.

In the case of existing constructions and in special case for those having historical value, both this approaches may be incompatible with the above mentioned need to preserve its original state (integrity) (Viggiani, 2017). If neither the building ductility can be increased nor a base isolation system can be adopted, it would be desirable to change the seismic demand. Since seismic demand depends on seismic site response, the only way to change it consists of artificially modifying soil stratification.

The modification can be obtained by grouting activities, and must be designed in order to shrink the seismic demand curve (Figure 1.27), thus resulting into a performance point which, being constant the capacity curve of the building, has larger safety margins against structural failure. Grouting has therefore the function of artificially modifying the mechanism of propagation of the seismic waves in the uppermost part of the subsoil, in such a way to attenuate seismic effects at ground level. Since it may be impossible to reach this goal for any period T, soil treatment has to be tuned to be effective in the range of periods typical of the structures to be preserved. The basic idea of the research work, therefore, is to consider a grouted layer installed at a suitable depth with

a suited shape, by injecting a material with a specific dynamic impedance η much lower than that of the surrounding soil ($\eta=\rho \cdot V_S$, where ρ is the material density and V_S the velocity of shear waves), possibly being able to dissipate part of the incoming seismic energy too. As typical in soil dynamics, the ability of a soil to dissipate energy is usually calculated via the damping ratio D. Since, as previously said, dynamic impedance depends on material density as well, the grouted material may be conceived as having the lowest possible density too. By placing a thin layer with a low dynamic impedance, it is expected that most of the seismically induced effects will concentrate within the layer, and very little will be transmitted to the soil on top. Then, a strongly reduced seismic action will reach the building or the structure to be preserved and smaller or nil damage will occur.

1D and 2D dynamic and static numerical analyses have been performed by Lombardi (2014) in order to study the efficiency of different treatment schemes, whose geometrical and mechanical configurations have been varied with the aim to get an insight on their potentials and limits.

Even though most of the work was focused on numerical simulations of the performance of some possible configurations of the soft caisson, some very preliminary laboratory tests have been carried out on sand mixed with two different industrial products. Their characteristics seemed, at least initially, well suited to the problem under study, because of their either low density or low shear stiffness. The 1D analyses have been carried out using either EERA or NERA, supposing the soil layers

to be horizontally homogenous, horizontally unlimited, and subjected only to a horizontal excitation from the bedrock.

As far as the 1D results are concerned, the insertion of a soft grouted layer at a given depth into the soil deposit is extremely effective in reducing the peak ground accelerations. The maximum acceleration strongly reduces above the soft layer, and such a reduction increases as the impedance ratio between the grouted and the soil layer increases.

In some cases, the insertion of a soft grouted layer may increase the spectral acceleration for large periods, which may be critical for slender structures such as, for instance, tall towers.

2D dynamic analyses were then carried out by Lombardi. The first result obtained was that it is useless to use GSI if the grouted layer does not completely isolate a volume of soil below the foundation to be protected. Whatever the shape of a discontinuous treatment, no effects or detrimental effects are in fact observed. 2D analyses have been then used to study the effects of a soft, continuous caisson having a rectangular section or made of inclined injections on the dynamic response of a soil deposit subjected to the propagation of shear waves.

The 2D dynamic analyses have been carried out using FLAC7. Different geometrical and mechanical configurations of the soft caisson have been considered. In the analyses, the materials have been assumed either linearly elastic or elasto-plastic. In such a way, the relevance of the choice of the constitutive model has been highlighted. Such a choice may be relevant for large amplitude seismic inputs.

As previously said, two different geometrical schemes of the isolated mass have been investigated: a rectangular one, with a horizontal base and vertical sides, and a V-shaped one (Figure 1.28).

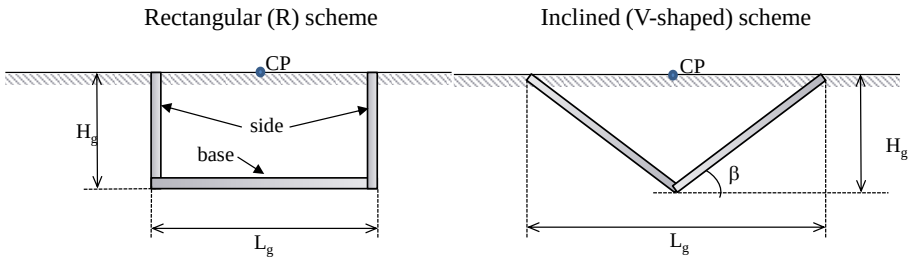

Figure 1.28 Sketches of the geometrical schemes considered in the analyses: rectangular caisson (a), V-shaped caisson (b).

The meshes assumed in the analyses have a horizontal (x) total length of 120 m for the rectangular caisson and of 200 m for the V-shaped one. The thickness of the soil deposit (H_s) has been considered equal to 40, 60 and 80 m, while that of the bedrock (H_b) is always 60 m, for a total height of the model of 100, 120 and 140 m. Ground conditions correspond to those of a dry sand (i.e. no groundwater has been considered) and the analyses are drained. Most of the numerical analyses have been carried out modelling the soil and the bedrock as either elastic or elastic - perfectly plastic (with a Mohr-Coulomb failure criterion) materials. The 2D analyses confirm the 1D observations, with significant differences based on the different signal propagation conditions and on the constraint effect due to the surrounding soil.

In the elastic analyses, it is noted that, varying the geometrical and mechanical configurations of the soft caisson, the lower frequencies are amplified, and the higher ones are reduced. Consistently, when this kind

of mitigation system does not reduce the effects in the zone to be protected, no significant increase of the accelerations outside the caisson are observed.

The beneficial screening effect in terms of acceleration, in the case where it takes place, does not necessarily correspond to an increase in displacements in the soil within the soft caisson. This depends on both the fundamental frequency of the propagated signal and the shear stiffness of the soft layers, especially when the treatment is effective in mitigating seismic effects at ground level

The introduction of a soft caisson, then, modifies the resonance frequencies of the deposit in which it is inserted; if the signal fundamental frequency is close to a natural frequency of the modified deposit, resonance phenomena may occur. Since the soft caisson generally tends, when detrimental, to amplify the lower frequencies, it is confirmed that this system can be effective in reducing the maximum dynamic effects on squat structures, which have lower natural frequencies.

It has been also pointed out that the response of the system depends more on the absolute value of the shear wave velocity $V_{s,g}$ (and therefore its shear stiffness G) of the grouted layers than on the impedance ratio η, and this is somehow an unexpected and certainly original result. In particular, the results presented by Lombardi indicate that both the shear wave velocity of the soft layers and the impedance ratio are relevant parameters in the propagation of the signal through the insulating box, but the former plays a more significant role. To mitigate the seismic risk, it is therefore more convenient the injection of soft layers with a very

low shear wave velocity, whatever the shear stiffness of the surrounding soil. For the sake of simplicity, the existence of a structure at ground level has not been considered in terms of dynamic interaction between the soil and structure behaviour, even though it is expected to play a relevant role. This is certainly a limit of the research at this stage, which has been only partly overcome by this thesis.

By increasing the volumetric stiffness of the grouted layers, the soft caisson is less effective, due especially to the low compressibility of the lateral soft layers which undergo lateral deformation because of vertical shear wave propagation outside the caisson. The higher the compressibility of the lateral layers the larger the decrease in horizontal dynamic actions in the soft caisson.

In the elasto-plastic analyses, two maximum amplitudes (0.05g and 0.5g) of the signals have been considered by Lombardi, in order to check the influence of the plastic behaviour of the natural and treated soil on the effectiveness of the reference soft caisson in filtering and reducing the dynamic effects in the protected soil mass. Two values of the shear strength angle φ'_g were assumed (5° and 15°). In terms of accelerations, it is very interesting to note that the more realistic elasto-plastic model leads to a more efficient behaviour of the isolating caisson for the most critical frequencies. In particular, for such frequencies, even though the signal is not largely reduced, at least it is not as amplified as in the linear elastic analyses

As far as static analyses are concerned, vertical displacements have been calculated taking into account only some schemes for the caisson. Some geometrical and mechanical parameters have been varied, i.e. the length

L_g or the inclination α, the depth H_g, the shear and the volumetric stiffness and the shear resistance of the soft layers. At ground level, a gravity load distribution has been also considered, whose amplitude q_w and length L_s have been varied.

It is noted that, as largely expected, the vertical displacements are increased by assuming a larger value of the distributed load q; furthermore, a smaller load length L_s value determines a reduction in the differential settlements Δw and in the maximum relative rotation β.

By increasing the shear strength angle φ_g', lower vertical settlements w_{max} are calculated. On the other hand, soil shear stiffness does not affect the maximum vertical displacements, which are largely influenced by the volumetric deformations taking place within the horizontal soft layer, and therefore by both the thickness and the volumetric stiffness of the grouted material. The differential displacements Δw and the relative rotations β are significantly influenced by the soft layer stiffness and the shear resistance too.

Moreover, the introduction of soft layers causes a significant reduction of the ultimate bearing capacity of the shallow foundation, which may be unacceptable for structure at ground level to protect. The reduction depends on the value of the shear strength angle of the soft layers: the ultimate load decreases as the shear strength angle decreases.

As previously mentioned, two materials have been tested, in order to look for a potentially suitable soft grout.

The first material is a self-expanding polyurethane insulating foam, essentially a hydrophobic material, resistant to water, chemicals and moisture. Laboratory tests have been carried out to quantify its density

and its shear stiffness when injected to pressures higher than the atmospheric one. The foam has shown a capacity to expand under large confining pressures keeping a very low density. Some resonant column tests have been performed to quantify the shear stiffness at low shear strains as well. Tests results indicate that the polyurethane foam cannot be considered a suitable material for soft layers, because even though it shows a low density even under high pressures, it is rather stiff, having therefore a dynamic impedance which is much larger than the one needed on the base of the results of the numerical analyses.

The second tested material is a super absorbent polymer (SAP), which is a hydrophilic network being able to absorb and retain huge amounts of water or aqueous solutions. The SAP used in this research activity is a polyacrylic acid partial sodium salt. The SAP, previously saturated with distilled or tap water has been mixed with sand, obtaining specimens characterized by different SAP percentages by weight. These specimens have been subjected to a few traditional laboratory tests (direct shear tests, ring tests, oedometer tests, triaxial tests). Even though the extremely low shear stiffness of this jelly material caused a number of difficulties in laboratory activities, starting from the preparation of the specimens, some results could be obtained: increasing the SAP quantities, a significant reduction of both the shear and the volumetric stiffness has been observed, and dynamic impedances similar to the ones suggested by the numerical analyses could be obtained.

Furthermore, the SAP reveals a capacity of swelling under load when saturated. This is an interesting result, because a potential volumetric

expansion of the material, when injected deep into a soil deposit to form a soft layer, could reduce the settlements caused by its low volumetric stiffness.

It has been observed that high values of the shear and volumetric stiffness of the grouted soil are detrimental for the dynamic efficiency of the treatment, but lead to lower vertical displacements. For the soft caisson with a rectangular section, this problem can be partially overcame by using a stiffer horizontal layer and very soft lateral sides. In terms of shear resistance of the soft layers, lower shear strength angles lead to higher efficiencies, but, on the other hand, to larger settlements. The best solution should be certainly conceived to find a smart intersection between the two requirements, which will be a function of the specific structural issue.

Based on these first results, it is obvious that the soft caisson must be designed taking into account also the natural frequency of the structure to be protected, considering the dynamic coupling of the input motion with the subsoil and the building response, whose dynamic interaction with the foundation soil has not been taken into account in this thesis.

1.4. Final remarks

Based on what is reported in the literature and what has been found by Lombardi (2014), the following general conclusions can be drawn:

- the soft barrier needs to be continuous to be effective in cutting the seismic energy in the isolated soil mass;

- the soft barrier cuts the dynamic energy travelling into the soil depending more on the mechanical properties of the soft layers than on its absolute or relative impedance;
- the volumetric stiffness K of the grouted layers plays a relevant role on the effectiveness of the isolating barrier. In the case of a rectangular caisson, the best solution is to have an extremely low value of K on the vertical sides, and a higher one at the base. So doing, the static settlements induced by the creation of the barrier would be reduced. In the case of the V-shaped barrier, this separation is not possible, and the grouted layers have to be as soft as possible;
- as long as the behaviour of the soil under dynamic loading can be modelled as elastic, the barrier has a beneficial effect only for seismic inputs having predominant frequencies higher than that of the isolated mass of soil, having on the contrary detrimental effects for lower frequencies;
- in the case of seismic inputs that induce yielding into the soft layers of the soft caisson, the detrimental effects for the lower frequencies are largely attenuated. This indicates on one hand that the barrier is more and more efficient as the input maximum amplitude is increased, and on the other hand that simple elastic models may overlook this very important aspect. Therefore, there is the need to use constitutive models able to take into account material yielding. The analyses indicate that to this aim an elastic – perfectly plastic model may be sufficient;

- the V-shaped barrier becomes more and more effective as it gets larger (e.g. when its sides have a lower inclination on the horizontal). It is less effective than the rectangular one having the same depth, since the isolated mass is smaller and the filtering effect of the grouted layer is influenced also by the bulk stiffness (eq. 8.b). However, it is still able to reduce the dynamic effects at ground level, at least for input predominant frequencies higher than the natural one of the isolated soil mass.
- In all cases, the reduced value of the shear strength angle in the grouted layers must be considered, to check if it may affect the load bearing capacity of the structure to be protected in an unacceptable way.

REFERENCES

Aki K. (1988). Local site effects on strong ground motion. Earthquake engineering and soil dynamics II: recent advances in ground motion evaluation. *ASCE geotechnical special publication, No.20,* Park City (USA).

Aki K. and Larner K. L. (1970). Surface motion of a layered medium having an irregular interface due to incident plane SH waves. *Journal Geoph. Research., Vol.70.*

Aki K., Richards P. G. (1980). Quantitative Seismology. *W. H. Freeman, San Francisco, California (USA).*

Alterio L. (2012). Seismic vulnerability reduction of monumental building by soils treatment. *Ph.D. Thesis, Università degli Studi di Napoli Federico II (Italia).*

Andersen L., Augustesen A. H. (2009). Mitigation of traffic-induced ground vibration by inclined wave barriers: a three-dimensional numerical analyses. *Proc. 16th International Congress on Sound and Vibration, Krakow (Poland).*

Bailey,J. S., and E. W. Allen. 1988. Seismic isolation retrofitting – salt lake city and county building. *APT Bulletin 20 (2):33–44. doi:10.2307/1494249*

Bard P. Y. (1994) Effects of surface geology on ground motion: recent results and remaining issues. *Proc. 10th European Conference on Earthquake Eingineering, Vienna (Austria), Vol.1.*

Bechtold J., (1907) Earthquake-proof building. *U.S. Patent No. 845, 046*

Bouckovalas G. D., Papadimitriou A. G. (2004). Numerical evaluation of slope topography effects on seismic ground motion. *Proc. 11th Int. Conf. on Soil Dynamics and Earthquake Engineering and 3th Int. Conf. on Earthquake Geotechnical Engineering, Berkeley, California (USA), Vol.2, pp.329-335.*

Buckle I. G. and Mayes R. L. (1990) Seismic Isolation: History, Application, and Performance-A World View. Earthquake Spectra: May 1990, Vol. 6, No. 2, pp. 161-201.

Cai Y., Liang X. (2003) Dynamic properties of composite cemented clay Journal of Zhejiang University. *Journal of Zhejiang University SCIENCE, Zhejiang (China).*

Capotorti F., Monachesi G., Mucciarelli M., Sanò T., Trojani L. (1997). Danneggiamenti ed effetti di sito nel terremoto umbro-marchigiano del settembre 1997. *Ingegneria sismica, Vol.14(3).*

Chang S. W., Bray J. D., Seed R. B. (1996). Engineering Implications of Ground Motions from the Northridge Earthquake. *Bull. Seis. Soc. Am, Vol.86(1), Part B Suppl., pp.270-288.*

Chavez-Garcia F.J. (2011). Site effects due to topography and to soft soil layers: progress made and pending issues. A Personal Perspective. *Proc. 5th International Conf. on Earthquake Geotechnical Engineering – State of the art Lectures, Santiago (Chile).*

Chepkoit K. K. , Aggour M.S. 12 (2000) Dynamic properties of untreated and treated cohesive soils. *Proc. 12th World Conference on Earthquake Engineering Auckland (New Zealand).*

Chouw N., Schmid G. (1992). Building isolation using the transmitting behaviour of a soil layer. *Proc. 10th World Conference on Earthquake Engineering, Madrid (Spain), Vol.4, pp.2519-2524.*

Costanzo A., d'Onofrio A., Lanzo G., Pagliaroli A., Penna A., Puglia R., Santucci De Magistris F., Sica S., Silvestri F., Tommasi P. (2007). Seismic response of historical centers in Italy: selected case studies. *Workshop on 'Geotechnical Earthquake Engineering related to Monuments and Historical Centers', 4th ICEGE, Thessaloniki (Greece).*

Davis HA, Robertson DR (2000). Hearst Memorial Mining Building Seismic Improvements, University of California, Berkeley,

Proceedings of the 12th World Conference on Earthquake Engineering, 30 January – 4 February, Auckland, paper 1636

De Montalk R. W. (1932). Shock absorbing or minimizing means for buildings. *U.S. Patent No. 1,847,120 (New Zealand Patent granted 1929)*

Dietz M.S., Wood D. M. (2006). Shake table testing of a soft caisson for geotechnical seismic retrofit. *Proc. 4th International Conference on Earthquake Geotechnical Engineering, Thessaloniki (Greece).*

Di Prisco G., Serra M. (1996). Modellazione numerica dell'efficacia di interventi di trattamento del sottosuolo per la riduzione del rischio sismico. *Master Degree Thesis, Università degli Studi di Napoli Federico II, Napoli (Italy).*

Di Sarno L., Chioccarelli E. and Cosenza E. (2011) Seismic Response Analysis of an Irregular Base Isolated Building, *Bulletin of Earthquake Engineering, 9(5): 1673-1702. doi: 10.1007/s10518-011-9267-1.*

D'Onofrio A., Mancuso C., Silvestri F. (1999). Reduction of seismic vulnerability by geomaterial attenuation procedures. *Proc. 2nd International Confererence on Earthquake Geotechnical Engineering, Lisboa (Portugal), pp.725-730.*

Doudomis N., Papadopoulos P. Papaliangas T (2002) Low-cost base isolation system on artificial soil layers with low shearing resistance. *Proc. 12th European Conference on Earthquake Engineering, paper reference 661.*

DM 14/1/2008. Norme Tecniche per le Costruzioni. *S.O. n. 30 - Gazzetta Ufficiale della Repubblica Italiana, No. 20 - 4/2/2008.*

Dolce M., Ponzo F.C., Di Cesare A., Arleo G. (2010) Progetto di edifici con isolamento sismico. *IUSS PRESS, Pavia (Italy), pp.215.*

Evangelista L., d'Onofrio A., Santucci de Magistris F., Silvestri F. (2011). Geotechnical characterization of some site interested by

the 2009 L'Aquila earthquake. *Proc. of the 5th Int. Conf. on Earthquake Geotechnical Engineering, Santiago (Chile).*

Faccioli E., Paolucci R. (2005). Elementi di sismologia applicata all'ingegneria. *Pitagora editore, Bologna (Italy), pp.280.*

Forcellini, D. (2017). Assessment on geotechnical seismic isolation (GSI) on bridge configurations *Innov. Infrastruct. Solut. 2: 9. https://doi.org/10.1007/s41062-017-0057-8*

Gazetas G. (1991). Formulas and charts for impedances and embedded foundations. *Journal of Geotechnical Engineering ASCE, Vol.117(9).*

Giovannardi F., Gulsasola A. (2013) Basic isolation: dalle origini ai giorni nostri. *USGS: http://it.calameo.com/read/001671591369645c5959a.*

Gazetas G., Mylonakis G. (1998). Seismic soil-structure interaction: new evidence and emerging issues. *Proc. 3rd Conf. on Geotechnical Earthquake Engineering and Soil Dynamics, Seattle (USA).*

Geli L., Bard P. Y., Jullien B. (1988). The effect of topography on earthquake ground motion: a review and new results. *Bulletin of the Seismological Society of America, Vol.78, pp.42-63.*

Geli L., Bard P.Y., Jullien B. (1988). The effect of topography on earthquake ground motion: a reviewand new results. *Bull. Seism.Soc. Of America, Vol.78(1).*

Georgarakos P., Yegian M.K., Gazetas, G. 2005 In-Ground isolation using geosynthetic liners, *9th World Seminar on Seismic Isolation, Energy Dissipation and Active Vibration Control of Structure. Kobe*

Grant F. S., West G. F. (1965). Interpretation Theory in Applied Geophysics. *McGraw-Hill Book Company, New York, New York (USA), pp.583.*

Housner G. W. (1952). Spectrum intensity of strong-motion earthquakes. *Proc. Symp. on Earthquakes and Blast Effects on Structures, EERI, Univ. of California at Los Angeles, Earthquake Engineering Research Institute, Oakland, California (USA), pp.26–36.*

Idriss I.M. (1990). Influence of local site conditions on earthquake ground motions. *Proc. 4th U.S. Nat. Conf. on Earthquake Engineering, Palm Springs, California (USA), Vol.1.*

Islam Saiful A. B. M. , Jameel M. and Jumaat M.Z. (2011). Seismic isolation in buildings to be a practical reality: Behavior of structure and installation technique. *Journal of Engineering and Technology Research, Vol.3(4), pp.99-117.*

James M Kelly. (1986) Aseismic base isolation: review and bibliography, *In Soil Dynamics and Earthquake Engineering, Volume 5, Issue 4, Pages 202-216, ISSN 0267-7261, https://doi.org/10.1016/0267-7261(86)90006-0.*

James S., Bailey and Edmund W. Allen (1988). Seismic Isolation Retrofitting Salt Lake City and County Building. APT Bulletin, Vol. 20, No. 2, pp. 32-44.

Jibson R. (1987). Summary on research on the effects of topographic amplification of earthquake shaking on slope stability. *Open file Report 87-268, U.S. Geological Survey, Menlo Park, California (USA).*

Kavazanjian, E., Jr., Hushmand, B., and Martin, G.R. (1991). Frictional Base Isolation Using a Layered Soil-Synthetic Liner System. *Proc. 3rd U.S. Conference on Lifeline Earthquake Engineering, ASCE Technical Council on Lifeline Earthquake Engineering Monograph Vol. 4:1139-1151.*

Kellezi L. (2001). Dynamic behavior of a softer layer overlying hard soil / bedrock and vibration reduction. *GEO-Danish Geotechnical Institute, Lyngby (Danmark).*

Kilar, V. and Koren, D. (2010). Simplified inelastic seismic analysis of base-isolated structures using the N2 method. *Earthquake Engng. Struct. Dyn., 39: 967–989. doi:10.1002/eqe.978*

Kirtas E., Rovithis E., Pitilakis K. (2009). Subsoil Interventions Effect on Structural Seismic Response. Part I: Validation of Numerical Simulations. *Journal of Earthquake Engineering, Vol.13(2), pp.155-169.*

Kirtas E., Pitilakis K. (2009). Subsoil Interventions Effect on Structural Seismic Response. Part II: Parametric Investigation. *Journal of Earthquake Engineering, Vol.13(3), pp.328-344.*

Kostadinov MV, Yamazaki F and Sudo K (2000), Comparative Study on the Methods for Detection of Liquefaction from Strong Motion Records, *8th ASCE Specialty Conference on Probabilistic Mechanics and Structural Reliability, University of Notre Dame, IN.*

Kramer S.L. (1996). Geotechnical earthquake engineering. *Prentice-Hall, Upeer Saddle River, New Jersey (USA), pp.653.*

Lanzo G., Silvestri F. (1999). Risposta sismica locale. *Hevelius Edizioni, Benevento, pp.159.*

Lanzo G., Silvestri F., Costanzo A., d'Onofrio A., Martelli L., Pagliaroli A., Sica S., Simonelli A. (2011). Site response studies and seismic microzoning in the middle Aterno Valley (L'Aquila, Central Italy). *Bulletin of Earthquake Engineering, Vol.9(5), pp.1417-1442.*

Lee, D. M. (1980). Base isolation for torsion reduction in asymmetric structures under earthquake loading. *Earthquake Engng. Struct. Dyn., 8: 349–359. doi:10.1002/eqe.4290080405*

Lignola G. P., Di Sarno L., Di Ludovico M., and Prota A. (2016). The protection of artistic assets through the base - isolation of historical buildings: A novel uplifting technology. *Materials and Structures. doi:10.1617/s11527-015-0785-1.*

Lirer S., Flora A., Verdolotti L., Lavorgna M., Iannace S. (2006). Permeation grouting of fine grained pyroclastic soils and rocks. *Ground Improvement, Vol.10, pp.135-177, Thomas Telford Ed., London (Great Britain).*

Lombardi D. (2014). An innovative ground treatment approach for seismic risk mitigation of existing structures. *Ph.D. Thesis, University of Napoli Federico II (Italy).*

Lombardi D., Flora A., Lirer S. (2012). A new approach for reducing seismic hazard on existing buildings by unusual deep soil grouting. *Int. Conf. on Ground Improvement and Ground Control (ICGI 2012), University of Wollongong, Wollongong (Australia).*

Lombardi D., Flora A., Lirer S., Silvestri F. (2012). Interventi di trattamento profondo dei terreni per la mitigazione del rischio sismico: primi risultati. *Incontro Annuale dei Ricercatori di Geotecnica – IARG 2012, Padova (Italy).*

Lombardi, D., Flora, A., Lirer, S., Silvestri F. (2013). An innovative approach for reducing the seismic risk of existing buildings and historic sites. *2nd Int. Symp. on geotechnical engineering for the preservation of monuments and historic sites, Viggiani C., Bilotta E., Flora A, and Lirer S. Editors, Napoli (Italy).*

Lovisolo F., Vitale S. (2006). Povertà, sviluppo e mobilità rurale in Africa Occidentale. *CCTM-Centro Città del Terzo Mondo, Politecnico di Torino, Torino (Italia).*

Martelli A., 2009. Proceedings of International Conference Prohitech09.Rome June 2009 Italy.ICOMOS 1964. The Venice Charter (1964) - International charter for the conservation and restoration of monuments and sites. *Proc. 2nd International Congress of Architects and Technicians of Historic Monuments, Venice. ICOMOS, Int. Council on Monuments and Sites. internet: www.icomos.org/charters/venice_e.pdf*

Martelli A., Clemente P., Saitta F., and Forni M. (2012). Recent worldwide application of seismic isolation and energy dissipation

to steel and other materials structures and conditions for their correct use. *In Behaviour of steel structures in seismic areas: STESSA , ed. F. Mazzolani, and R. Herrera. London, UK: Taylor and Francis Group.*

Massarsch K.R. (2004).Mitigation of Traffic-induced Ground Vibrations. *Proc. 11th international conference on earthquake geotechnical engineering, pp.22–31. Berkeley, California (USA).*

Massarsch K.R. (2005).Vibration isolation using gas-filled cushions. *Proc. Sessions of the Geo-Frontiers Congress, Austin, Texas (USA).*

Melkumyan M., Mihul V., and Gevorgyan E. (2011). Retrofitting by base isolation of existing buildings in Armenia and in Romania and comparative analysis of innovative vs. conventional retrofitting. *In Proc. 3rd International Conf. on Computational Methods in Structural Dynamics and Earthquake Engineering, Corfu Island, Greece.*

Mezzi M., Comodini F., and Rossi L. (2011). A base isolation option for the full seismic protection of an existing masonry school building. *In Proceedings of the Thirteenth International Conference on Civil, Structural and Environmental Engineering Computing, eds. B. H. V. Topping, and Y. Tsompanakis, 1–14. Chania, Crete, Greece: Civil-Comp Ltd.. 6–9 September*

Miyajima M, Kitaura M and Yamamoto M (2000), Detection of Soil Liquefaction Using Strong Ground Motion Records. *12th World Conference on Earthquake Engineering, Auckland.*

Mousavi, S.A., Bastami, M. and Zahrai, S.M. (2016). Large-scale seismic isolation through regulated liquefaction: a feasibility study *Earthq. Eng. Eng. Vib. 15: 579. https://doi.org/10.1007/s11803-016-0350-0*

Naderzadeh A. (2009). Historical Aspects of Seismic Base Isolation Application. *Proc. JSSI 15th Anniversary International Symposium on Seismic Response Controlled Buildings for Sustainable Society, 16-18 Sept. 2009, JSSI, Tokyo (Japan).*

Nikolaou S., Mylonakis G., Gazetas G., Tazoh T. (2001). Kinematic pile bending during earthquakes: analyses and field measurements. *Geotechnique 51(5).*

Pagliaroli A. (2006). Studio numerico e sperimentale dei fenomeni di amplificazione sismica locale di rilievi isolati. *Ph.D. thesis, Università degli Studi di Roma La Sapienza, Roma (Italy).*

Pan, T.-C. and Kelly, J. M. (1983). Seismic response of torsionally coupled base isolated structures. *Earthquake Engng. Struct. Dyn., 11: 749–770. doi:10.1002/eqe.4290110604*

Pitarka A., Irikura K., Iwata T. (1996). Was the basin edge geometry responsilbe for the ground motion amplification in the disaster belt-like zone during January 17, 1995, Kobe (Hyogo-ken Nambu), Japan earthquake? *Proc. International Workshop on Site Response subjected to Strong Earthquake motions, Yokosuka (Japan).*

Poole, R. A., and Clendon J. E. (1992). New Zealand parliament buildings seismic protection by base isolation. *Bulletin of the New Zealand National Society for Earthquake Engineering 25 (3):147–60.*

Rathje E.M., Abrahamson N. A., Bray, J.D. (1998). Simplified Frequency Content Estimates of Earthquake Ground Motions. *Journal of Geotechnical Engineering, Vol.124(2), pp.150-159.*

Richart F.E, Woods R.D. (1970). Vibrations of soils and foundations *Prentice-Hall, Upeer Saddle River, New Jersey (USA).*

Rogriguez-Marek A., Bray D. J., Abrahamson N. A. (1998) A geotechnical seismic site response evaluation procedure. *Proc.*

12th World Conference on Earthquake Engineering (WCEE 2000), Auckland (New Zealand).

Sanchez-Sesma F.J. (1987). Site effects on strong ground motion. *Soil Dynamics and Earthquale Engineering, Vol.6, pp.124-132.*

Sanchez-Sesma F.J. (1990). Elementary soultions for response of a wedge-shaped medium to incident SH and SV waves. *Bull. Seism.Soc.Of America, Vol.80(3).*

Saxena K. S., Avramidis A. S., Reddy K. R. (1987). Dynamic moduli and damping ratio for cemented sand at low strains. *Can. Geotech.Journ. Vol.25, pp.353-368.*

Seed H.B., Murarka J., Lysmer J., Idriss IM (1976). Relationships between maximum acceleration, maximum velocity, distance from source and local site conditions for moderately strong earthquakes. *Bull. Seism.Soc. of America, Vol.66(4).*

Seed, H. B. and Alonso, J. L. (1974). Soil-structure interaction effects in the Caracas Earthquake of 1967. *Report No. 73023, Earthquake Engineering Research Center, Engineering Department, University of California, Berkeley, California (USA).*

Seed H. B. Romo, M. P. Sun, J. J., Lysmer J. (1987). Relationships Between Soil Conditions and Earthquake Ground Motions in Mexico City in the Earthquake of September 19, 1985. *Report No. UCB/EERC-87/15, Earthquake Eng. Res. Center, College of Eng., University of California, Berkeley, California (USA).*

Seki, M., Miyazaki M., Tsuneki Y., and Kataoka K. (2000). A masonry school building retrofitted by base isolation technology. *In Proceedings of the 12th World Conference on Earthquake Engineering, Upper Hutt, N.Z., New Zealand Society for Earthquake Engineering.*

Silvestri, F. (1991). Analisi del comportamento dei terreni naturali in prove cicliche e dinamiche di taglio torsionale. *Ph.D thesis, consorzio tra le Università di Napoli Federico II, Roma La Sapienza, Bari Politecnico (Italy).*

Spencer L. M. (2010). Evaluation of sand treated with colloidal silica gel. *Phd Thesis Georgia Institute of Technology, Atlanta, Georgia (USA).*

Srbulov M. (2008). Simplified analyses with case studies and examples. *Springer ed., Berlin (Germany), pp.263.*

Taskov L., Antimovki A. and Kokalevki M. (2004). Shaking table test of efficiency of ALSC base-isolation system. *Proc. 13th World Conference on Earthquake Engineering Paper No. 785, Vancouver (Canada).*

Taskov L., Manova K., Krstevska L., Garevski M. (2010). Evaluation of efficiency of ALSC floating-sliding base-isolation system based on shake table test and floor response spectra. *Bull. Earthquake Eng (2010), Vol.(8), pp.995-1018.*

Tsang H.H., Lam N.T.K. Yaghmaei-Sabegh S., Sheikh M.N., Indraratna B. (2010). Geotechnical seismic isolation by scrap tire-soil mixtures. *Proc. the 5th international conference on recent advances in geotechnical earthquake engineering and soil dynamics, San Diego, California (USA).*

Tsang H.H., Lo S.H., Neaz Sheikh M. (2012). Seismic isolation for low-to-medium-rise buildings using granulated. *Earthquake engineering and structural dynamics, John Wiley and Sons, Hoboken, New Jersey (USA), Ltd. rubber–soil mixtures: numerical study.*

Tsang H.H. (2009). Geotechnical seismic isolation. Earthquake Engineering: New Research. *Nova Science Publishers, New York (USA), pp.55-87.*

Viggiani C. (2017). Geotechnics and Heritage. *19th International conference on Soil Mechanics and Geotechnical Engineering 17-22 September 2017, Seoul Korea*

Walker B. (1982). Earthquake.Planet Earth. *Time Life Books, pp.153.*

Wood D. M. (2006).Modelling of dynamic soil problems. *Proc. 4th International Conference on Earthquake Geotechnical Engineering – Invited Lectures, Thessaloniki (Greece)*

Wright F.L. (1977). Frank Lloyd Wright - An Autobiography. *Horizon Press*

Wu G., Finn W. (1997). Dynamic Elastic Analyses of pile foundations using finite element method in the frequency domain. *Can. Geotech.Journ., Vol.34(1), pp.34-43.*

Yegian M.K. and Catan M. (2004). Soil Isolation for seismic protection using a smooth synthetic liner. *Journal of Geotechnical and geo-environmental Engineering ASCEE (Nov):1131*.

Yegian M.K., Kadakal U. (2004). Foundation isolation for seismic protection using a smooth synthetic liner. *Journal of Geotechnical and geo-environmental Engineering, Vol.130(11).*

Yegian, M.K., and Lahlaf, A.M. (1992). Dynamic interface shear properties of geomembranes and geotextiles. *Journal of the Geotechnical Engineering, ASCE, Vol. 118, No.5 pp. 760-779*

Zoeppritz K. (1919). Nachrichten von der Königlichen Gesellschaft der Wissenschaften zu Göttingen. *Mathematisch-physikalische Klasse, pp.66-94*

CHAPTER 2

CENTRIFUGE TESTS

2. Introduction

In this chapter the centrifuge tests carried out at the Schofield centre, the geotechnical laboratory of the Cambridge University, were illustrated. Centrifuge tests were designed based on the progress made in the initial stages of the research program (Lombardi, 2014). After a short introduction about the principles of centrifuge modelling, the calibration of the instruments used to perform the tests was described. For a more detailed description of the centrifuge and the instrumentation adopted see the Appendix A. The instrumentation located in the model included accelerometers, air hammer placed at the bottom of the model, MEMs, and LVDTs for the surface settlements measurement. The procedure for the model preparation were explained, including the technique used to realize the soft stratum. Once the models were ready, the centrifuge loading and flight procedure were reported. The interpretation of the results were reported and compared with the numerical results.

2.1. Principles of centrifuge modelling

A centrifuge is essentially a sophisticated load frame on which soil samples can be tested. Geotechnical materials such as soil and rock have nonlinear mechanical properties that depend on the effective confining stress and stress history. A special feature of geotechnical modelling is the necessity of reproducing the soil behaviour both in terms of strength and stiffness. The centrifuge applies an increased "gravitational"

acceleration to physical models in order to produce identical self-weight stresses in the model and prototype. Soil models placed at the end of a centrifuge arm can be accelerated so that they are subjected to an inertial radial acceleration field, which, as far as the model is concerned, acts like a pseudo-gravitational acceleration field.

Scaling laws are relationships that relate the behaviour of the centrifuge model and the prototype. If the same soil is used in the model as in the prototype and if a careful model preparation procedure is adopted whereby the model is subjected to a similar stress history ensuring that the packing of the soil particles is replicated, then for the centrifuge model subjected to an inertial acceleration field of AT times Earth's gravity the vertical stress at depth h_m (where m indicate the model) will be identical to that in the corresponding prototype at depth h_p (where p indicate the prototype) where $h_p=Nh_m$. This is the basic scaling law of centrifuge modelling, that stress similarity is achieved at homologous points by accelerating a model of scale N to N times Earth's gravity.

The most common scale laws (Schofield, 1980) are summarized in Table 2.2.1. The Turner beam centrifuge, used for these tests, was designed by Philip Turner and was built in the workshops of the Department of Engineering at the University of Cambridge. It has a nominal diameter of 10 m and the payload capacity is 1 ton at an operational g level of 150 times earth's gravity. A view of this centrifuge is presented in Table 2.2.1. The two ends of this machine are colour coded blue and red. Although both ends are nominally identical, in regular operations the red end carries the centrifuge models while the blue end carries the counter weight made from steel plates. During

earthquake tests the ends are reversed, that is, the blue end carries the earthquake actuator and the centrifuge model while the red end carries the counterweight.

Table 2.2.1 Scaling laws

	Parameter	Scaling law model/prototype	Units
General scaling laws	Lenght	1/N	m
	Area	$1/N^2$	m^2
	Volume	$1/N^3$	m^3
	Mass	$1/N^3$	$Nm^{-1}s^2$
	Stress	1	Nm^{-2}
	Strain	1	-
	Force	$1/N^2$	N
	Bending moment	$1/N^3$	Nm
	Work	$1/N^3$	Nm
	Energy	$1/N^3$	J
	Seepage velocity	N	ms^{-1}
	Time (consolidation)	$1/N^2$	s
Dynamic events	Time (dynamic)	1/N	s
	Frequency	N	s^{-1}
	Displacement	1/N	m
	Velocity	1	ms^{-1}
	Acceleration	N	ms^{-2}

Centrifuge model test behaviour can be monitored by a variety of instrumentation. Available instrumentation includes not only a wide range of transducers but also visual techniques. Transducers in contact with the centrifuge model should be small and rugged enough to resist

not only their increased self-weight but also mechanical handling during test preparation and disassembly.

Figure 2.1 A view of the Turner beam centrifuge at Cambridge

2.2. Calibration of the instruments

All the instruments are calibrated using a data logger with the software Dasylab 9.0. During the calibration two different Junction boxes are used: one for the accelerometers and the other for the LVDTs.

2.2.1. Piezoelectric accelerometers

The accelerometers are calibrated using a calibrator, which excites the instruments with a sinusoidal input having acceleration amplitude of ±1g. All the calibration factors used in the tests were reported in The calibration factor (CF) was calculated from the equation:

$$CF = \frac{2}{|V_{MIN}| - V_{MAX}}$$

Table 2.2, in which V_{MIN} and V_{MAX} are the maximum and minimum voltage given from the calibration readings. The channel n° 7 of the

Junction box didn't work, for this reason there isn't value in correspondence of that. The calibration factor (CF) was calculated from the equation:

$$CF = \frac{2}{|V_{MIN}| - V_{MAX}}$$

Table 2.2 Calibration of the piezo electric accelerometers

Channel n°	Piezo n°	V_{MIN} [V]	V_{MAX} [V]	Calibration factor [g/V]
1	8131	-0.1461	0.1501	6.752
2	8878	-0.1455	0.1386	7.040
3	8858	-0.1465	0.1498	6.750
4	10176	-0.1703	0.1667	5.935
5	3478	-0.1247	0.1190	8.207
6	8894	-0.1462	0.1381	7.035
7				
8	10218	-0.1211	0.1273	8.052
9	8915	-0.1718	0.1712	5.831
10	8932	-0.1483	0.1456	6.805
11	8904	-0.1478	0.1401	6.947
12	8830	-0.1586	0.1552	6.373
13	8848	-0.1388	0.1265	7.539
14	8888	-0.1576	0.1581	6.335
15	7334	-0.1244	0.128	7.924

2.2.2. LVDT

Prior to use, an LVDT is calibrated by applying known displacements from a screw gauge and its output is measured. The cylindrical body of the LVDT was blocked, instead the metallic stick touched the mini platform and moved with itself. The calibration factor for the LVDT 2 and 037 was shown in Table 2.3 . The calibration factor was determined

for each reading, the similar were used to determine an unique calibration factor, while the others were rejected.

Table 2.3 Calibration of the LVDT instruments

LVDT 2			
Displacements [mm]	Voltage [V]		
0.00	5.326	Calibration factor [mm/V]	
5.02	4.593	6.849	
10.03	3.241	3.706	
15.03	1.846	3.584	
20.00	0.475	3.625	
25.02	-0.926	3.583	3.590
30.04	-2.336	3.560	
35.00	-3.760	3.483	
40.00	-4.952	4.195	
45.01	-5.327	13.360	

LVDT 037			
Displacements [mm]	Voltage [V]		
0	5.2926	Calibration factor[mm/V]	
5	4.4759	6.12	
10.05	3.0522	3.55	
15	1.6294	3.48	
20.01	0.2068	3.52	
24.96	-1.2054	3.51	3.506
29.97	-2.6257	3.53	
34.99	-4.0772	3.46	
39.98	-5.2407	4.29	
44.09	-5.5661	12.63	

2.2.3. MEMS

MEMS devices are able to measure both constant and time-varying accelerations. As a result they can be calibrated by just turning the device upside down and reversing the 1 g component due to the earth's gravity. The results of the calibration were shown in Table 2.4.

Table 2.4 Calibration of the MEMS

M1201			
Direction	Reading (V)	Average (V)	Calibration factor(g/V)
UP	2.5158	2.52285	52.9
	2.5299		
DOWN	2.4805	2.48505	
	2.4896		

V1			
Direction	Reading (V)	Average (V)	Calibration factor(g/V)
UP	2.5315	2.5356	54.9
	2.5397		
DOWN	2.4954	2.4992	
	2.503		

M1202			
Direction	Reading (V)	Average (V)	Calibration factor(g/V)
UP	2.5363	2.5403	58.0
	2.5443		
DOWN	2.5018	2.5058	
	2.5098		

2.3. Materials

2.3.1. Sand

The soil models were made of uniform dry sand, namely HN31 Hostun sand. Table 2.5 reports its properties as know from existing literature (Flavigny, 1990).

Table 2.5 Properties of Hostun sand

Soil	G_s	e_{max}	e_{min}	d_{50} (mm)	d_{10} (mm)	d_{60}/d_{10}
HN31 Hostun Sand	2.65	1.041	0.555	0.335	0.209	1.74

In which Gs is the specific gravity, e is the void ratio and d is the particle diameter. The sand layers were deposited at nominal relative density (D_r) equal to 85%. The relative density was evaluated from expression:

$$D_r = \frac{e_{max} - e}{e_{max} - e_{min}} \quad 2.1$$

In which the relative density was imposed and e calculated from the equation:

$$e = \frac{G_s \cdot m_s}{V} - 1 \quad 2.2$$

where m_s is the weight of the sand poured in the box and V is the internal volume of the box.

2.3.2. Super Absorbing Polymer (SAP)

For the soft layer, the basic idea is to obtain a mixture with mechanical characteristics able to ensure a low dynamic impedance. The adopted material is a super absorbent polymer (SAP), a polymer that can absorb and retain extremely large amounts of a liquid with respect to its own mass. Water-absorbing polymers, which are classified as hydrogels when cross-linked, absorb aqueous solutions through hydrogen bonding with water molecules. A SAP's ability to absorb water is a factor of the ionic concentration of the aqueous solution. In deionized and distilled water, a SAP may absorb 300 times its weight (from 30 to 60 times its own volume) and can become up to 99.9% liquid, but when put into a 0.9% saline solution, the absorbency drops to maybe 50 times its weight. The adopted SAP has granular particles with a diameter less than 1000 microns and a density equal to 0.69gr/ml at environmental temperature. Its configuration after hydration was reported in *Figure 2.2*.

Figure 2.2 SAP material dry and hydrated

The properties are summarized in Table 2.6.

Table 2.6 Main properties of the SAP material

Material	γ (kN/m^3)	ρ (kg/m^3)	V_s(m/s)
SAP	10	1020	30

In the tests SAP and distilled water have been mixed, with a ratio 99.4% by weight of distilled water and 0.6% of SAP. For the centrifuge tests the soft layer was made by using latex balloons filled by hydrated SAP (Figure 2.3). The diameter of the balloons was of about 15 mm. The balloons are supposed not to have any influence on the overall mechanical response of the soft stratum, and were used for the ease of sample preparation.

Figure 2.3 Latex balloons filled with SAP hydrated material

2.4. Model preparation technique

2.4.1. Sand pouring

An automatic sand pourer was used for pluviating the sand in the laminar box, developed at Cambridge. To achieve a specific relative density the

sand needs to be poured from a particular height and at a particular flow rate. The sand is placed in a hopper suspended above the model container. A nozzle was placed at the bottom of the hopper to control the flow rate and the drop height was controlled through the program used to control the equipment. Sand samples of different relative densities are obtained by controlling the drop height and the flow rate through the nozzle. Figure 2.4 presents a schematic diagram of the sand pourer. Figure 2.5 shows the completed automatic sand pourer in Cambridge.

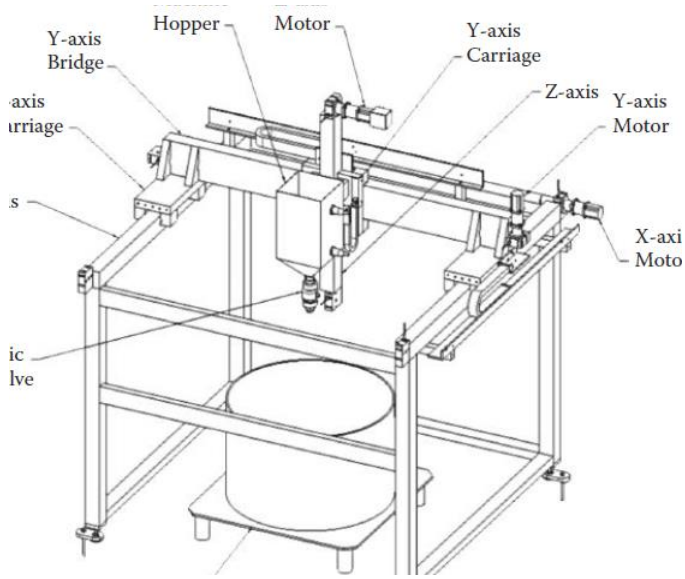

Figure 2.4 Schematic diagram of the automatic sand pourer

The main aim of this device is to have a 3-D traverse of the hopper over the model container. Each of the traverse axes is computer-controlled. In addition to this, there are high- and low-level indicators on the traversing hopper to show the level of the sand.

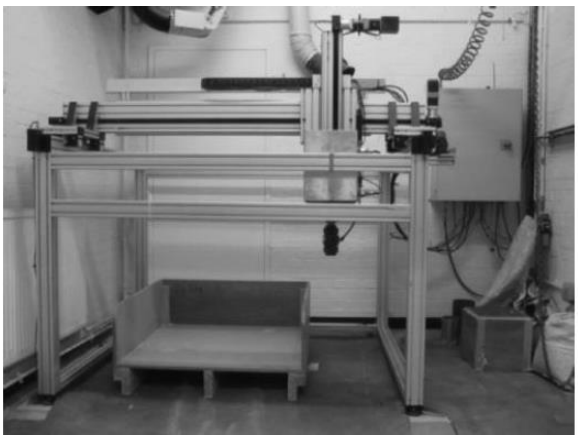

Figure 2.5 Photo of the automatic sand pourer in Cambridge

2.4.2. Centrifuge Model 1

A layout drawing of the first model is shown in Figure 2.6. In the model 1 the soft barrier was horizontal.

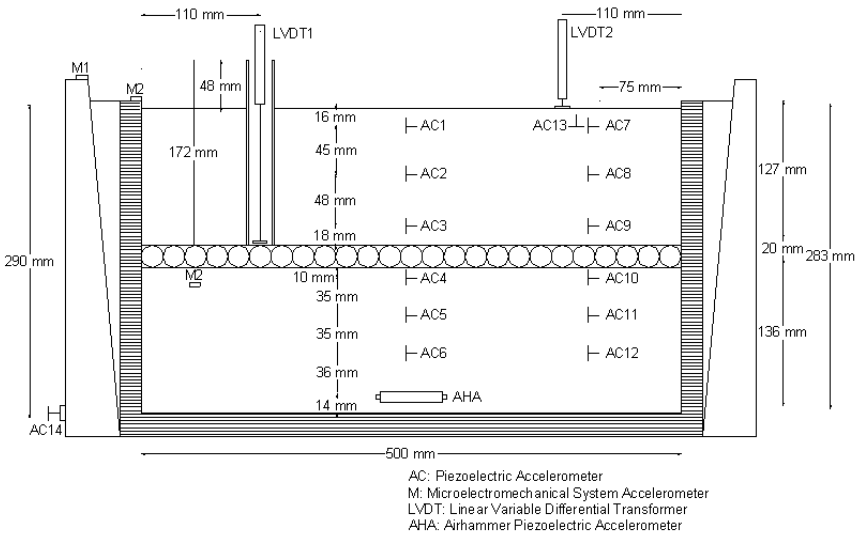

Figure 2.6 Layout of the model 1 (horizontal barrier) with indication of the instrumentation adopted

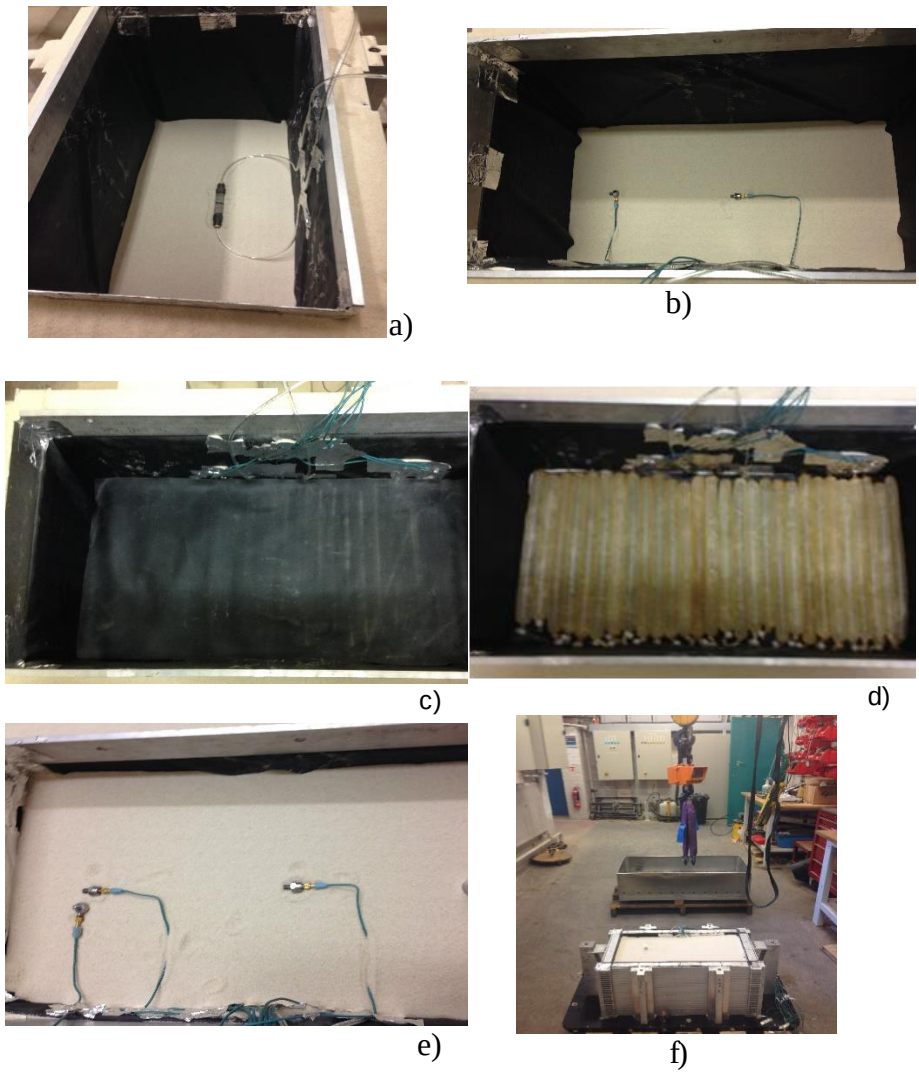

Figure 2.7 Model preparation: a) Positioning Air Hummer b) Positioning horizontal accelerometers, c) thin layers of latex, d) balloons filled with SAP and e) vertical and horizontal accelerometers and small tube for the placement of LVDT f) weighing of the model

The sand layers were deposited at nominal relative density (D_r) equal to 85%. The sand pourer was stopped at desired locations to allow

placement of instruments and balloons. In the first model the balloons were deployed between two thin layers of latex (Figure 2.7).

An air hammer was installed at the bottom of the model and a small hollow tube was placed on the superior layer of latex in order to allow placement of a LVDT as a means of control for the deformation of the soft layer during the spin up. According to the indication of the layout, the accelerometers are placed in the model and photos are taken of every level. When the sand pouring is finished, the total weight of the used sand is measured, in order to calculate a balance of the centrifuge arm.

2.4.3. Centrifuge Model 2

A layout of the model 2 is shown in Figure 2.8. For the creation of the V-shape model (second model), the sand pouring was stopped every 10 mm in order to place the balloons Figure 2.9.

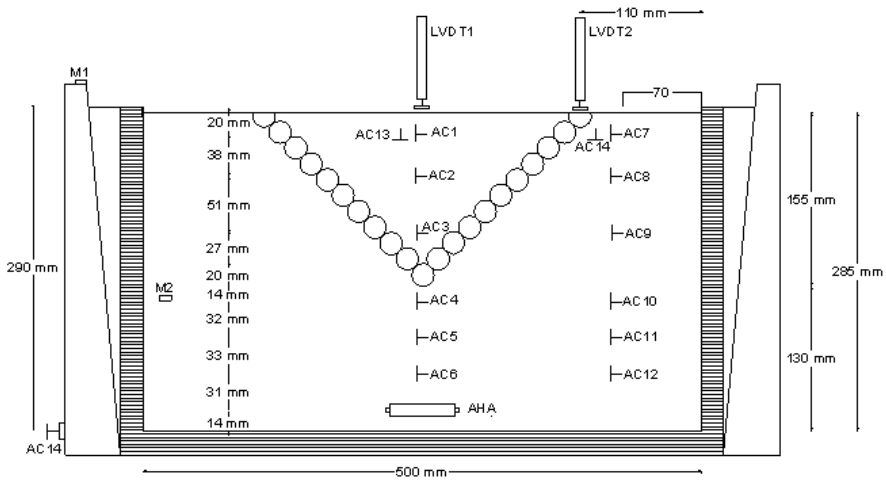

Figure 2.8 Layout of the model 2 (V barrier) with indication of the instrumentation adopted

Also here an air hammer was placed at the bottom of the model. The LVDTs are placed at the centre of the model and outside the V-shaped barrier.

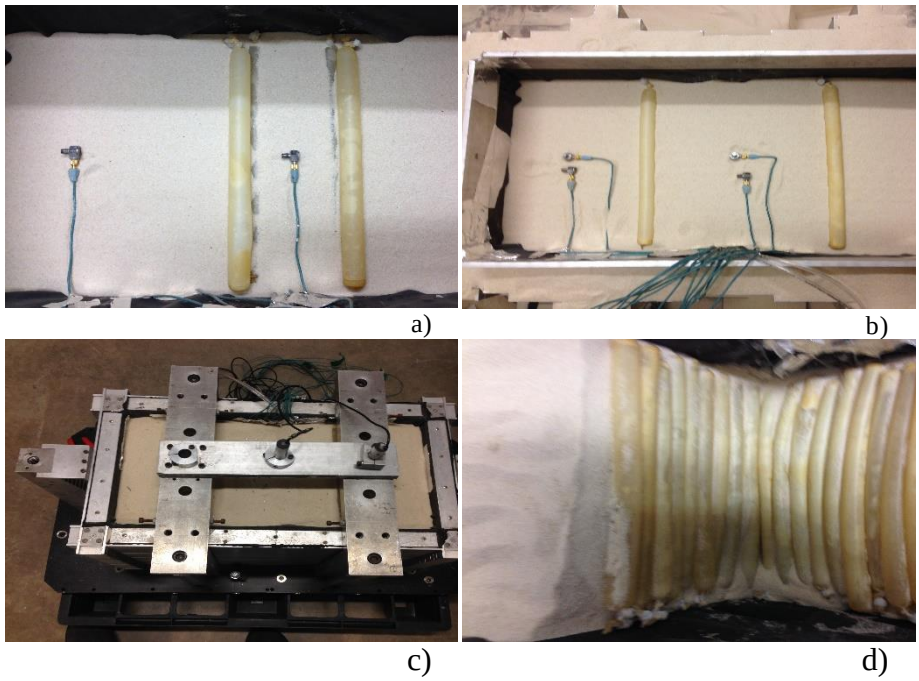

Figure 2.9 Preparation of the second model a) Positioning horizontal accelerometers and some of the balloons, b)vertical and horizontal accelerometers, c) laminar box with LVDT d) V-shape after test

2.4.4. Centrifuge preparation

When the sand pouring is finished, the total weight of the used sand is measured, in order to calculate a balance of the centrifuge arm. The mass of the model is balanced by a counterweight that is placed on an identical swing platform on the other end of the beam. The counterweights are adjusted in each centrifuge test to balance the soil model being tested. The tests are only carried out if the total mass of the package confirm

the calculations. The counterweight is loaded into the centrifuge on the red end and the SAM actuator is installed on the beam on the blue end, then the model is put in the SAM and every cable is connected to the Junction box (Figure 2.10).

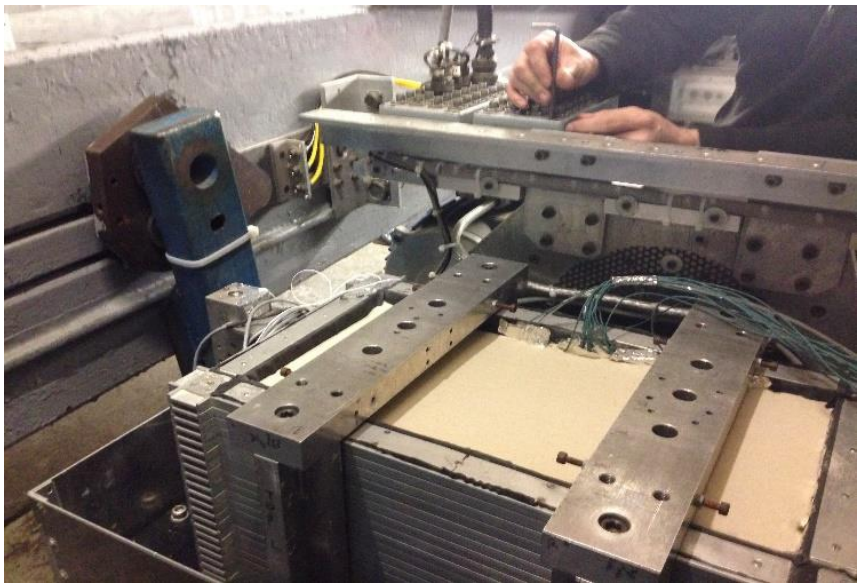

Figure 2.10 Preparation of the test, connection of the cables to the Junction box

All the data were acquired using the software CDAQS, a system that minimizes the noise derived by electrical interference of the SAM system. When the test started the centrifuge is swung up in steps of 10g until 80g. In total two earthquakes were fired at 50g and six at 80g. Table 2.7 shows the values of amplitude, nominal frequency and duration of each signal both at model and prototype scale. It is worth noting that the SAM cannot achieve higher nominal frequencies. In the first model, an LVDT was placed on the soft barrier (Figure 2.6) to evaluate the

settlement of the soft layer due to the increase of self-weight during spin up when the centrifuge was subsequently accelerated in steps of 10g.

Table 2.7Model signals, (bracketed values: values at prototype scale)

Model 1							
Input signal	Gravity level (g)	Frequency (Hz)		Duration (s)		Amplitude (g)	
EQ1	50	50	(1)	0.4	(20)	4.6	(0.09)
EQ2	50	30	(0.6)	0.4	(20)	0.6	(0.01)
EQ3	80	50	(0.625)	0.4	(32)	2.6	(0.03)
EQ4	80	50	(0.625)	0.4	(32)	9.8	(0.12)
EQ5	80	30	(0.375)	0.4	(32)	1.9	(0.02)
EQ6	80	60	(0.75)	0.4	(32)	0.7	(0.01)
EQ7	80	60	(0.75)	0.4	(32)	16.5	(0.21)
EQ8	80	30	(0.375)	0.4	(32)	4.5	(0.06)

Model 2							
Input signal	Gravity level (g)	Frequency (Hz)		Duration (s)		Amplitude (g)	
EQ1	80	50	(0.625)	0.4	(32)	7.4	(0.09)
EQ2	80	50	(0.625)	0.4	(32)	13.4	(0.17)
EQ3	80	30	(0.375)	0.4	(32)	1.3	(0.016)
EQ4	80	60	(0.75)	0.4	(32)	13.2	(0.16)
EQ5	80	60	(0.75)	0.4	(32)	19.1	(0.24)
EQ6	80	30	(0.375)	0.4	(32)	4.5	(0.06)
EQ7	50	50	(1)	0.4	(20)	4.1	(0.08)
EQ8	50	30	(0.6)	0.4	(20)	1.2	(0.025)

2.5. Experimental results

The instruments installed in the model were:

- LVDTs
- Air Hummer
- Piezoelectric accelerometers
- MEMs

2.5.1. LVDT

The LVDT devices measured the settlements w at two different points in each model, during the centrifuge spin up and the following shakings. The swing up data were obtained sampled at 4Hz. The position of the devices was different in the two models, as shown in the insets of Figure 2.6 and Figure 2.8**Errore. L'origine riferimento non è stata trovata.**. In the first model, an LVDT was placed on the soft barrier to evaluate the settlement of the soft layer due to the increase of self-weight during spin up when the centrifuge was subsequently accelerated in steps of 10g until it reached a gravity of 80g. The data given from the swing up readings were showed in the Figure 2.11 and Figure 2.12 for the model 1. The model 1 was subjected to two different flight: both in the first and in second flight the LVDTs showed a similar behaviour, having a similar displacement in each acceleration level. The total settlement was 3 mm during the first flight and 2.5 during the second one.

The densification observed was smaller due to higher value of initial density.

As shown in Figure 2.11 and Figure 2.12, during the spin up, the LVDT 1 (located on the soft layer) showed a slightly larger settlement than the LVDT 2. Since it is reasonable to assume that the deformation of the soft layer is much higher than the one of the sand lying above, the average settlement obtained from the two measurements shown in Figure 2.11 and Figure 2.12 can be used to estimate the change in thickness of the soft layer. The initial thickness of the horizontal barrier is 15 mm, corresponding to 0.75 m and to 1.2 m for gravity levels of 50g

and 80g, respectively. . Under 50 g, before the signals were fired, its thickness is about 12 mm, corresponding to 0.6 m at prototype scale. Under 50 g, before the signals were fired, its thickness is about 12 mm, corresponding to 0.6 m at prototype scale. At this gravity level, two signals were fired, with different nominal frequencies (cf. Table 2.7). Finally, the centrifuge was accelerated to 80g.

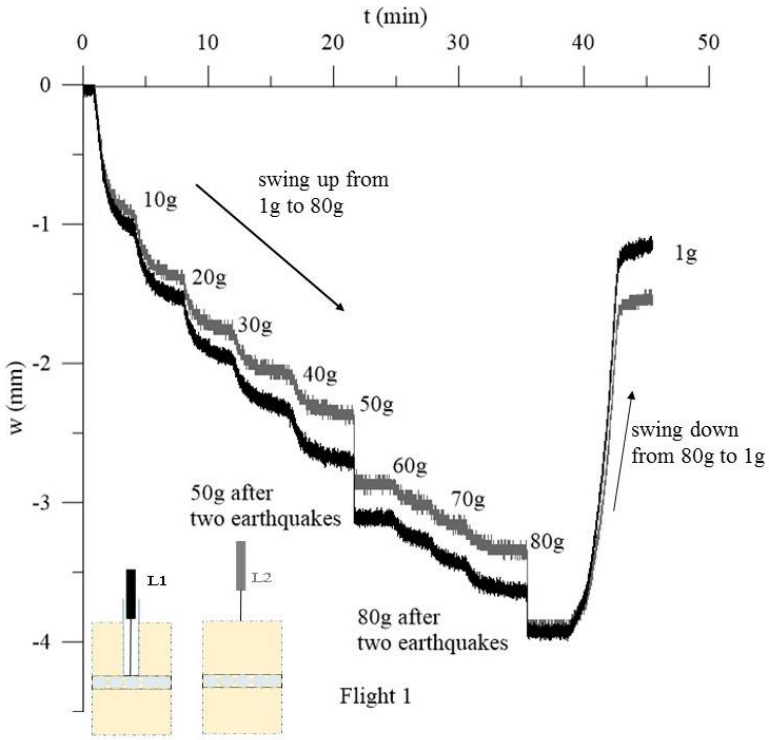

Figure 2.11 LVDTs readings during the swing up (flight 1)

At this new gravity level two signals were fired. According to the LVDT readings, the barrier thickness reduced to about 0.9 m at the prototype scale.

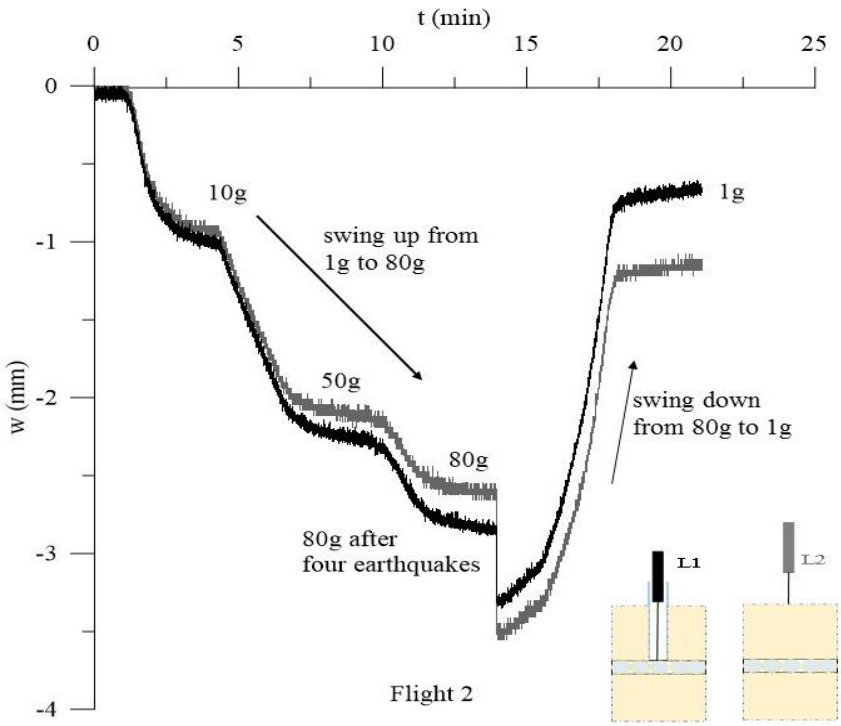

Figure 2.12 LVDTs readings during the swing up (flight 2)

The SAM actuator had autonomy only for five earthquakes: the model was slowed down to 1g and the motor was recharged in order to perform the remaining earthquake in the second flight (cf. Table 4). The data recorded during the dynamic step were plotted against the time sequentially (Figure 2.13). The displacement increased with severity of the input motion. For the earthquake EQ2 (50g) and EQ3 (80g), the displacement recorded was very small corresponding to their low amplitude.

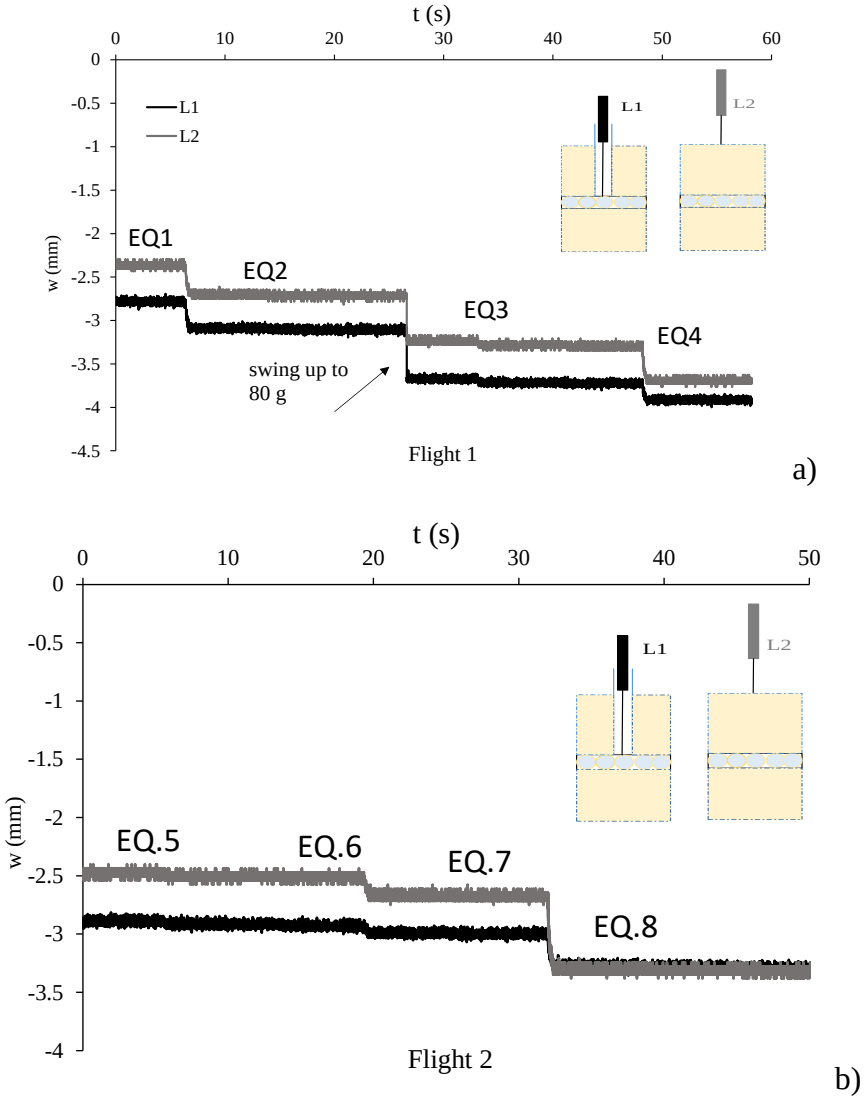

Figure 2.13 Data recorded during the dynamic step by LVDTs a)flight 1 b)flight 2

In the second model, both the displacement transducers were installed at the model ground surface: the LVDT 1 was located at the middle of the model and LVDT 2 along the free field vertical (Figure 2.8). The

model 2 was subjected to two different flight. In the first one only two earthquake were fired, because some of the accelerometers didn't work. For this reason the centrifuge was slowed down to 1 g in order to check the Junction Box. In the second flight, six earthquakes were fired. The recorded settlement was larger within the isolated volume (LVDT 1), especially after that, all the six signals had been fired (Figure 2.14).

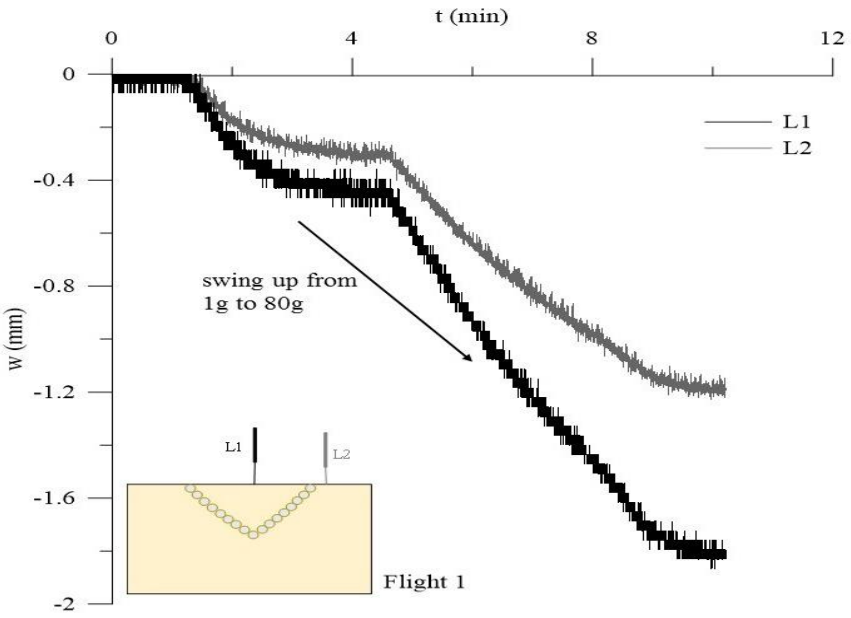

a)

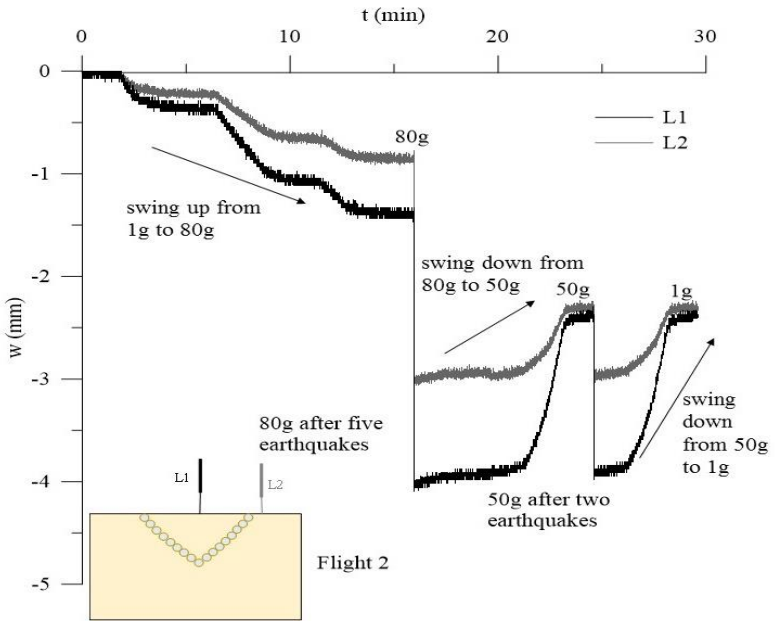

b)

Figure 2.14 LVDTs readings during the swing up: a) flight 1 b) flight 2

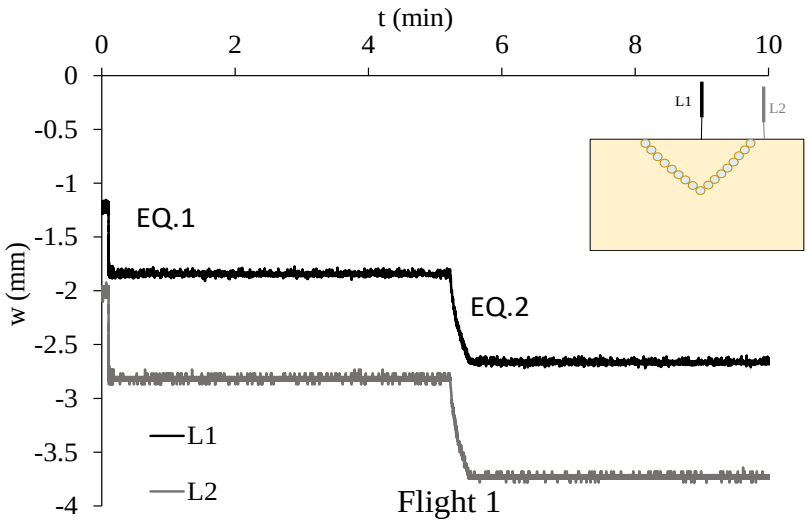

a)

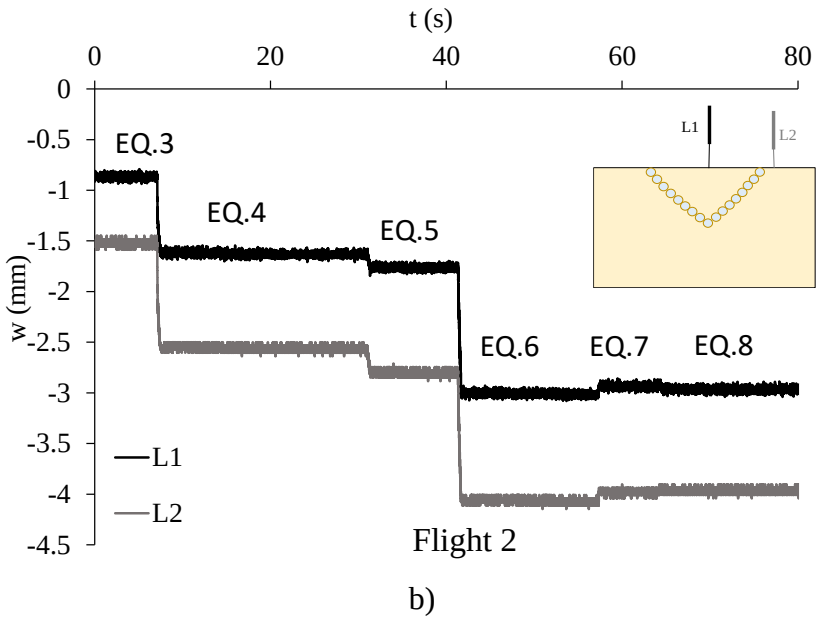

Figure 2.15 Data recorded during the dynamic step by LVDTs a) flight 1 b) flight 2

The recorded displacements during the dynamic phase are shown in Figure 2.15. The displacement increases as the severity of the input motion. From the readings it can be noted an uplift, in correspondence of the earthquake EQ7, between the last earthquake and the centrifuge slowing down to 50g, due to the elastic part of the settlement.

2.5.2. Air Hummer

Shear wave velocity in the ground, V_S, can be used to evaluate in-flight dynamic soil properties in centrifuge models as in situ. The maximum shear modulus, G_{max}, can be computed from the shear wave velocity in accordance with elastic theory:

$$G_{max} = \rho \cdot V_S^2 \qquad 2.3$$

where ρ is the mass density of the soil.

In centrifuge tests, the shear wave velocity, V_S, can be measured by using a miniature air hammer, which operates at strain levels of about 0.03%. Hence V_S, can be obtained by measuring the time, T, required for the wave to travel between two consecutive accelerometers, and the distance, L, between this two. That is:

$$V_S = \frac{L}{T} \qquad 2.4$$

In order to evaluate the shear wave velocity in the sand, the second model has been used, where a free-field vertical array of horizontal accelerometers was available.

The distance between the accelerometers AC4 and AC6 is L=0.07 m and the time lag is T=0.0002 s (L=5.6 m and T=0.016 s at prototype scale), providing a value of V_S=350 m/s, representative of the shear wave velocity at mid-height of the sand layer, hence from eq. 2.10 G_{max}= 202 MPa (Figure 2.16).

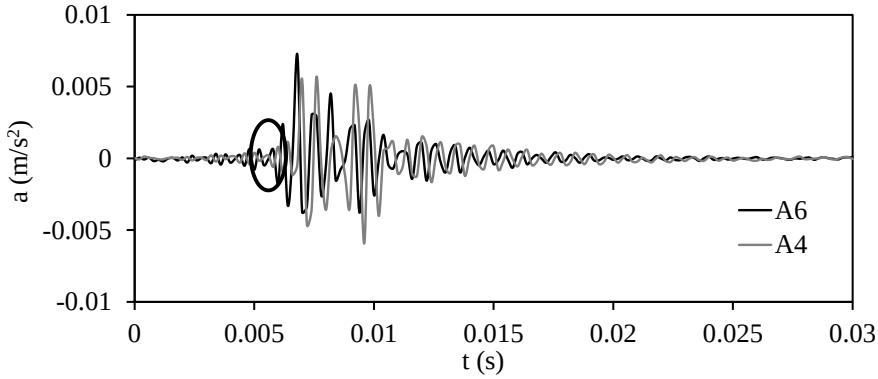

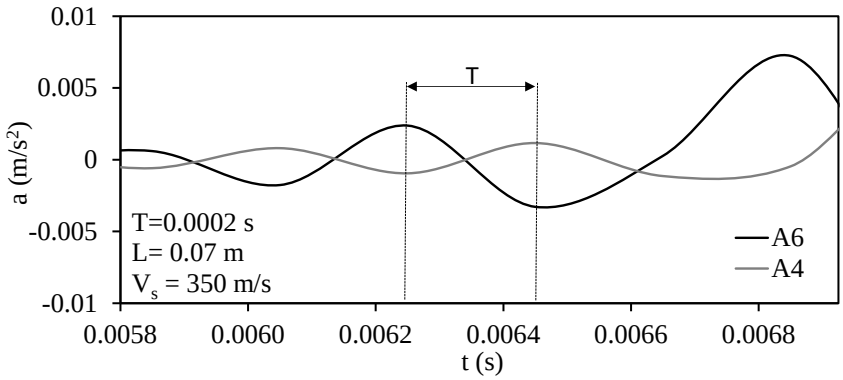

Figure 2.16 Acceleration induced by air hammer pulse: a records at the bottom and at the mid-height (AC6 and AC4); b determination of the travel time of the acceleration wave

Two air hammer tests were performed, at two different gravity levels (50g and 80g). The shear wave velocities measured at a certain depth and at a specific level of g correspond to the shear wave velocity measured at the corresponding prototype depth. Therefore, the prototype V_S profile could be determined.

From the correlation of Hardin and Black (1969) modified for the Hostun sand (Hoque and Tatsuoka, 2004) as:

$$G_{max} = 80 \cdot \frac{(2.17-e)^2}{(1+e)} \cdot \left(\frac{p'}{p_{ref}}\right)^{0.47} \qquad 2.5$$

the profile of G with the depth was obtained, and hence that of the shear wave velocity (Figure 2.17). It can be noted that the experimental data are in good agreement with the literature data.

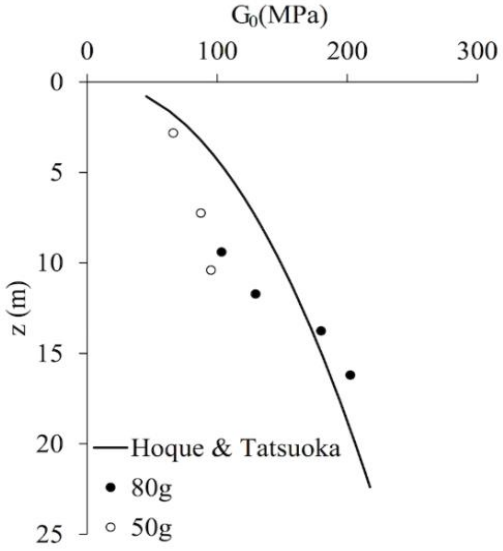

a)

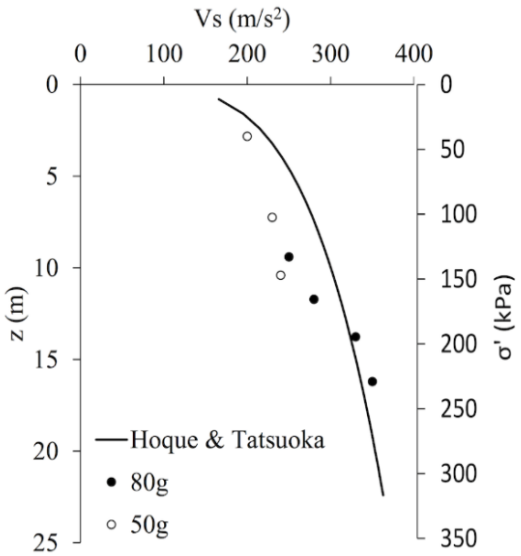

b)

Figure 2.17 a) Shear modulus derived from literature and from air hammer tests; b) corresponding shear wave velocity

By taking advantage of the air hammer, it is also possible to assess the shear wave velocity in the SAP, by applying a similar procedure to the signals recorded by the accelerometers A4 (below) and A3 (above) the soft barrier, as shown in Figure 2.6.

Since this travel time, t, depends not only on the soft barrier ($t_2 = V_{S,2} \cdot L_2$) but also on the sand between the two accelerometers ($t_1 = V_{S,1} \cdot L_1$ and $t_3 = V_{S,3} \cdot L_3$ in Figure 2.18), it is possible to estimate an average shear wave velocity of the barrier as:

$$V_{s,2} = \frac{L_2}{t - \frac{L_1}{V_{s,1}} - \frac{L_3}{V_{s,3}}} \qquad 2.6$$

where $t = t_1 + t_2 + t_3$, and the values of the shear wave velocity of the sand, $V_{S,1}$ and $V_{S,3}$ were estimated both from Figure 2.18.

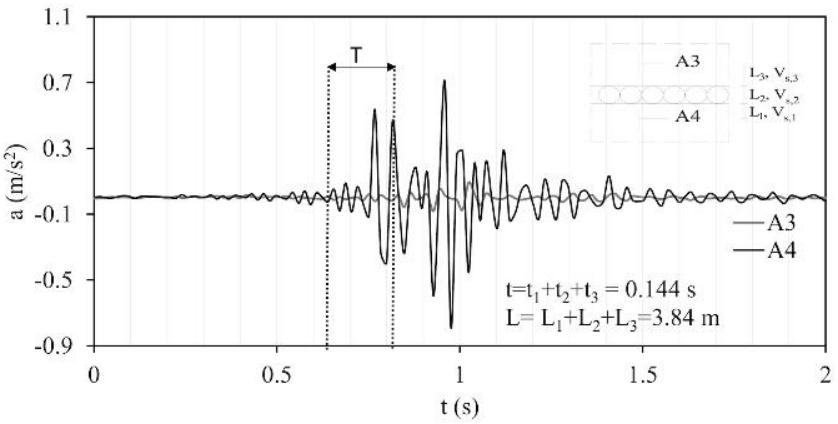

Figure 2.18 Schematic of travel path of the shear wave between accelerometers A4 and A3 and recorded signals at the accelerometers A3 and A4

In order to calculate $V_{s,2}$, the thickness of the soft stratum L_2 has to be known, as shown in §2.9.1. In particular, by assigning to the sand the relevant shear wave velocities $V_{s,1}$ and $V_{s,3}$ (Figure 2.18), a value of $V_{s,2}$=11.8 m/s is computed assuming for the sand the shear wave velocity curve proposed by Hoque and Tatsuoka (2004) and a value of $V_{s,2}$=12.2 m/s is evaluated adopting for the sand the measured shear wave velocity.

2.5.3. Horizontal Piezoelectric accelerometers

Two vertical arrays of six accelerometers each were installed in the first model (horizontal barrier), three above and three below the soft layer. The first array was aligned to the centreline of the model, the second one was located 75 mm away from one side of the box. One of the external accelerometers, located at the base plate (A14 in Figure 2.6), measured the input motion.

In Figure 2.19 the acceleration time histories of the model 1, recorded at the base of the box and the Fourier spectra are shown for the several frequencies investigated in the tests (Table 2.7). The plots shows that the signal applied at the model base was not exactly harmonic: the signal had not constant amplitude and in some cases the signal was not symmetric to the time axis. It may also be noticed that the duration of the shaking events characterized by the smaller amplitudes is generally longer than the nominal value of 0.4 s, due to a known issue of the SAM actuator already observed in previous experimental campaigns (e.g. Lanzano et al., 2012). The 30 Hz signals have a longer duration (EQ2, EQ5, EQ8) because at this frequency a wrong brake operation prevented

an immediate oscillation block. All the acceleration time histories were filtered in a time domain using a 4^{th} order Butterworth type, which was an infinite-impulse-response filter (IIR). The digital filter was a typical "band pass" between the frequencies of 15Hz and 250Hz.

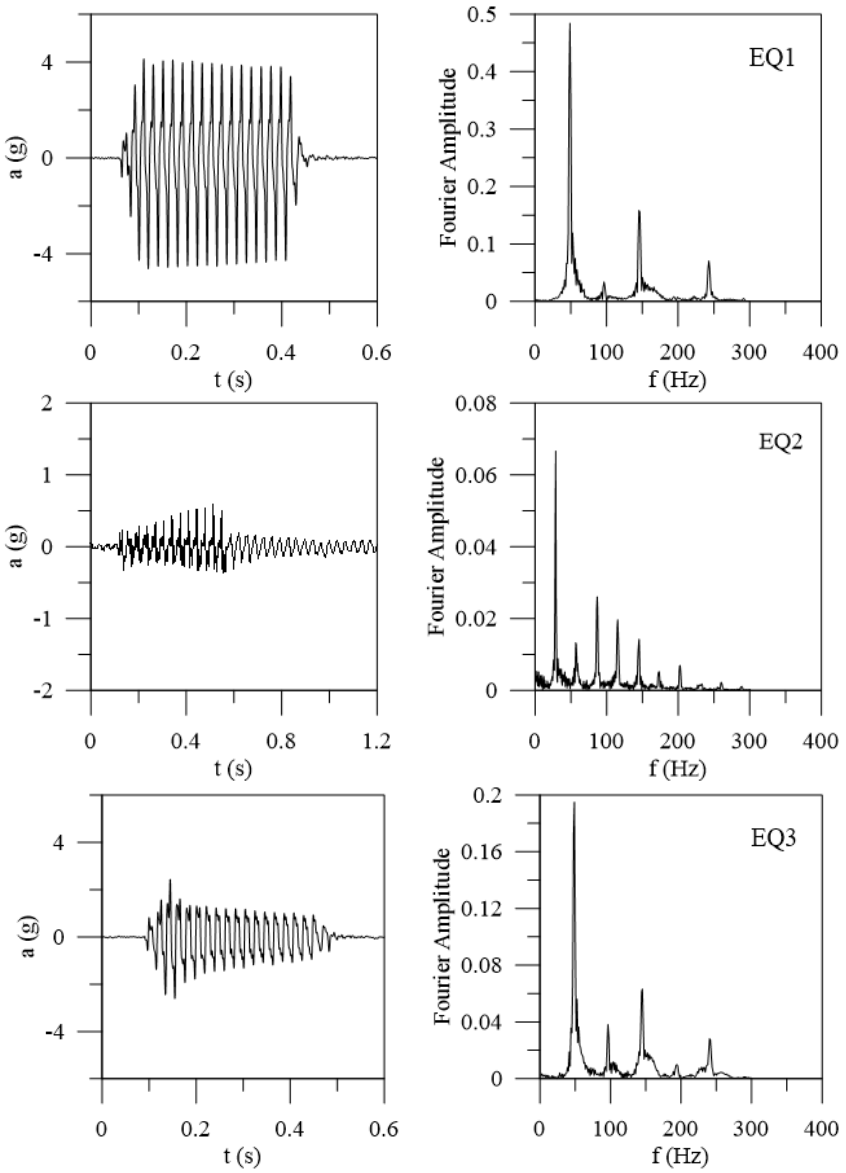

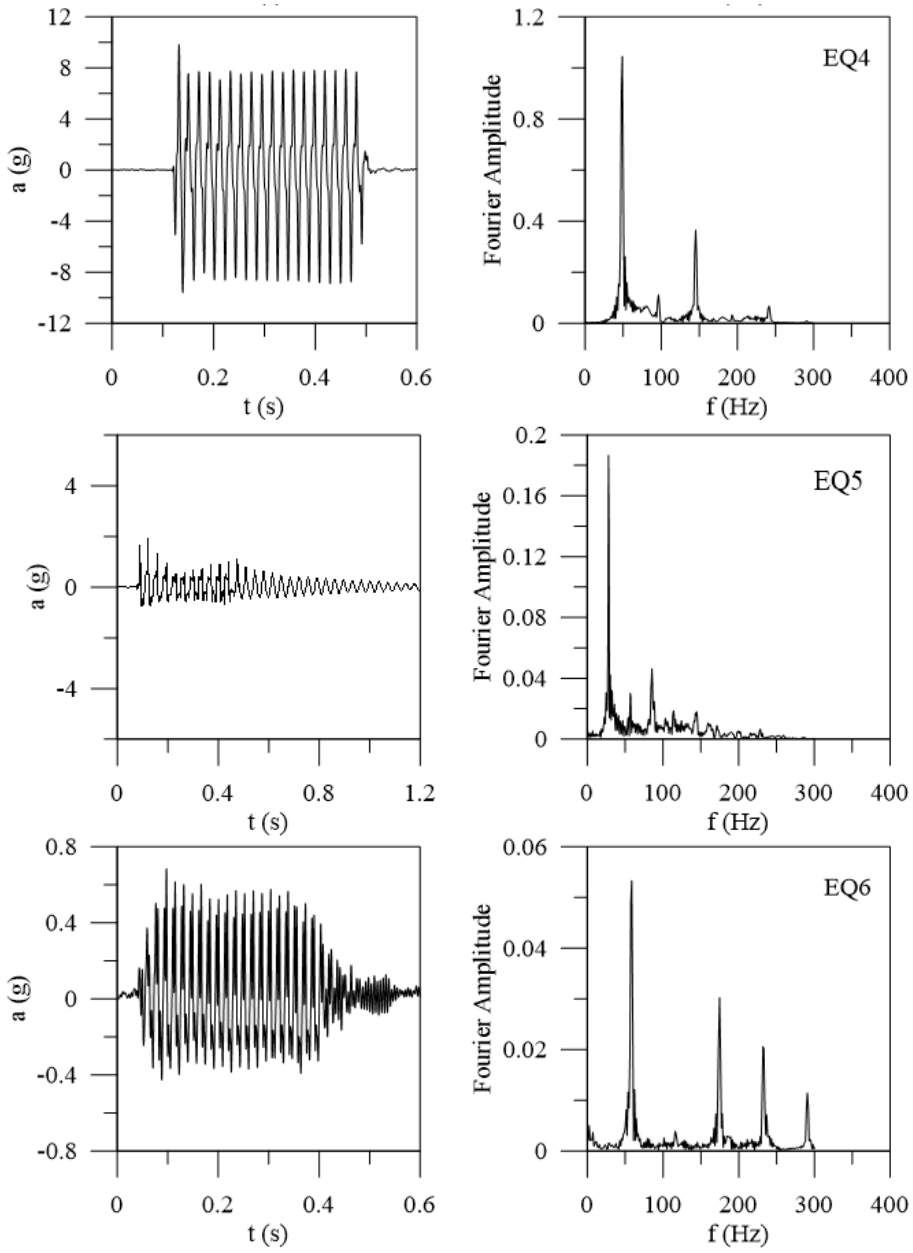
a (g)
t (s)
Fourier Amplitude
f (Hz)
EQ4
EQ5
EQ6

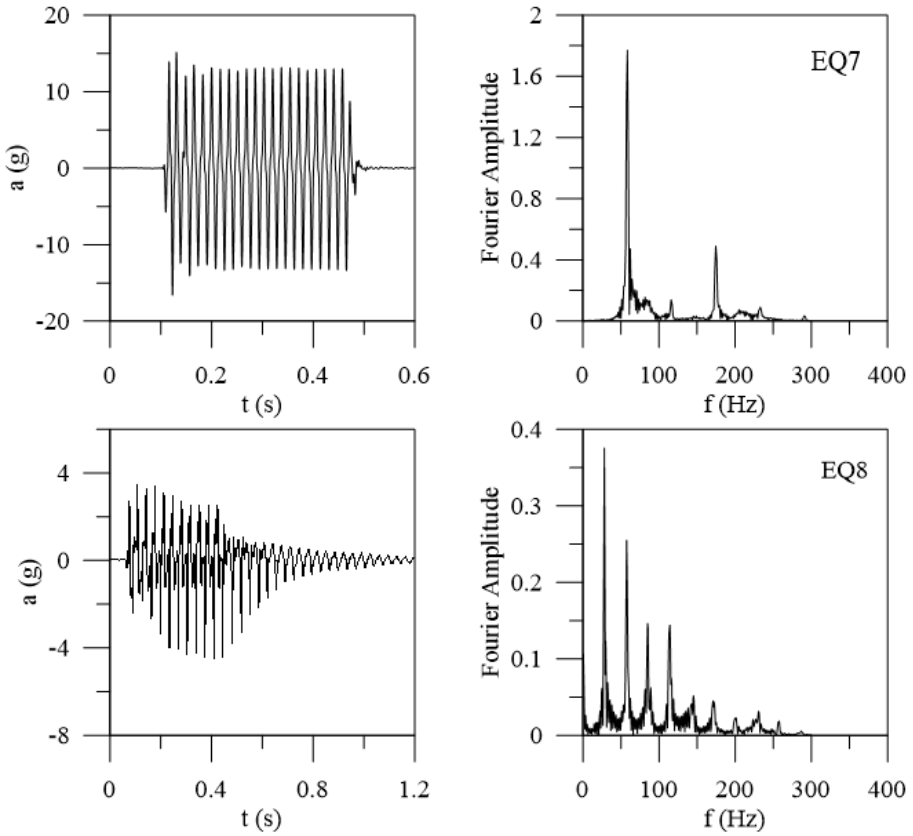

Figure 2.19 Input signals recorded at the model base and respective Fourier spectra

Figure 2.20a and b and Figure 2.21a and b show the acceleration amplification (peak recorded accelerations normalized by the corresponding peak acceleration at the base) at different depths for all signals, obtained from 50g and 80g models, respectively for both of the array. It can be noted that the recorded amplification is higher for the lateral array of the accelerometers, influenced by the side of the laminar box. The acceleration under the soft layer was generally more amplified during weaker excitations. Soon above the barrier attenuation is always

observed, although for the weakest a net amplification is observed in the sand layer above the barrier. On the other hand, in case of stronger events, attenuation always occurred, de-amplification increasing with amplitude of the input signal.

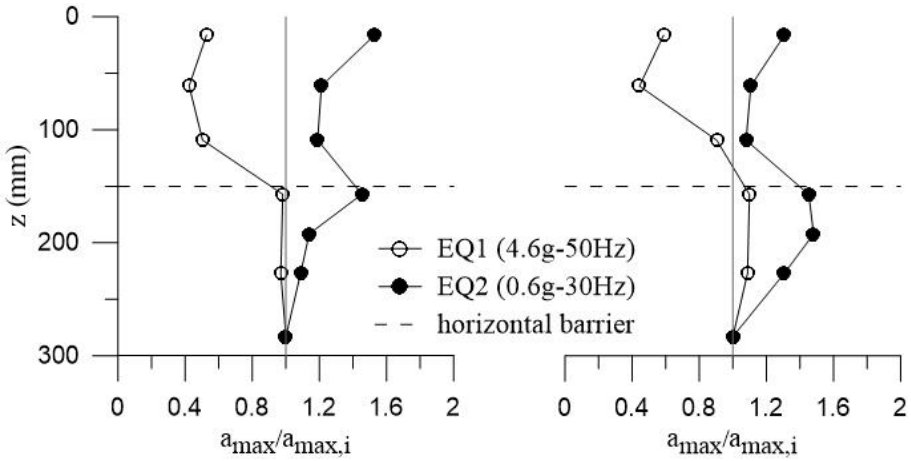

Figure 2.20 Profile of amplification with depth at 50g gravity level: a central array; b lateral array (model 1)

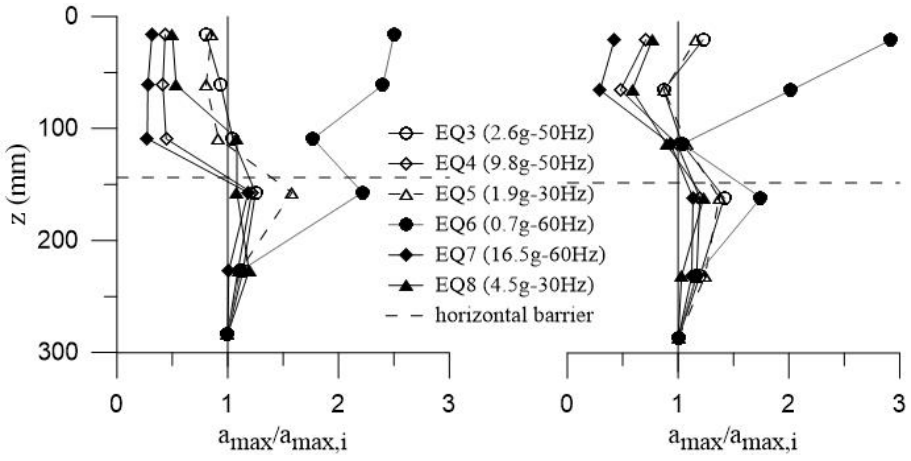

Figure 2.21 Profile of amplification with depth at 80g gravity level: a central array; b lateral array (model 1)

In the model with the V-shaped barrier two arrays of six accelerometers each were also installed: array 1 along the vertical centreline of the model (A1 to A6 in Figure 2.8) and array 2 outside the isolated volume of sand (A7 to A12 in Figure 2.8). Figure 2.22 shows the acceleration amplification ratio at different depths, for all signals at 80g level only, along both arrays. During the test some of piezoelectric accelerometers of array 1 stopped working and for this reason some values are missing in the figure. Hence, in this model an immediate comparison is possible between the results along a vertical line that crosses the soft barrier and another that does not. However, array 2 is not strictly in free-field conditions, since it may be influenced by the presence of the barrier next to it and by the side of the laminar box as shown for the model 1.

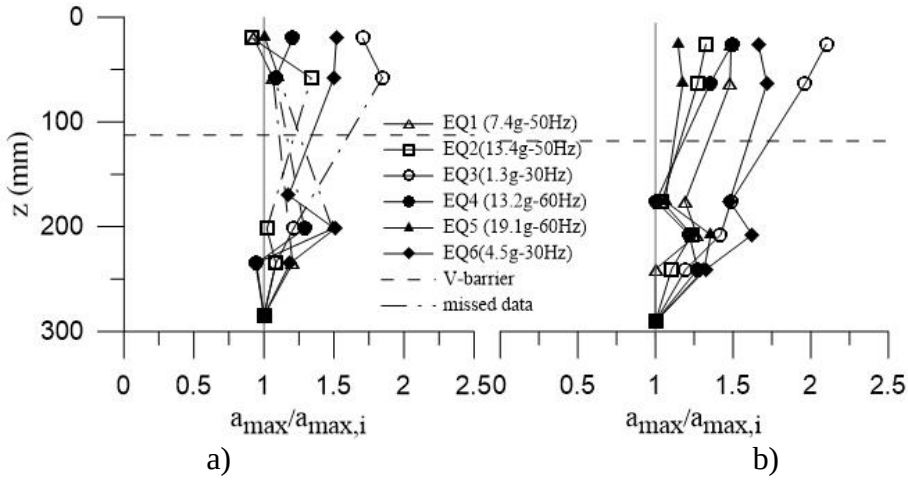

Figure 2.22 Profile of amplification with depth at 80g gravity level: a central array; b lateral array (model 2)

2.5.4. MEMS

The time histories recorded by MEMS M2 (below the barrier) and M3 (on the top surface of the model) for the model 1 are shown in Figure 2.23. There is a good agreement between the results obtained with MEMS and that obtained with piezoelectric accelerometers placed at the same depth. For the model 2 the MEMS devices provides an additional information about free field conditions (Figure 2.24)

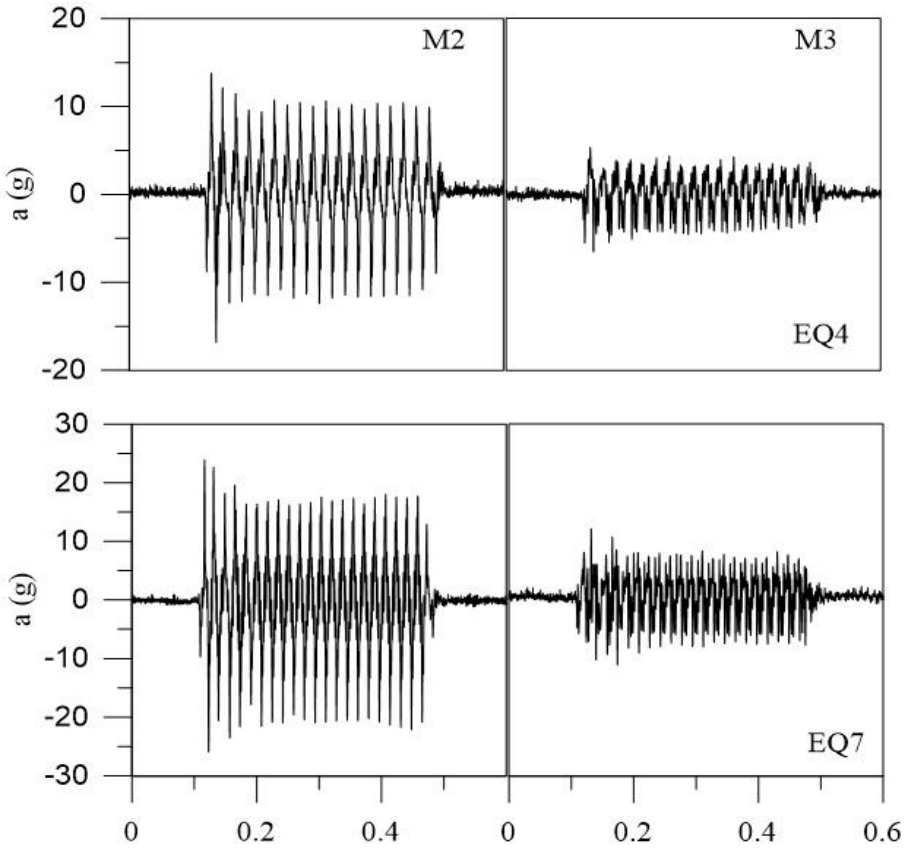

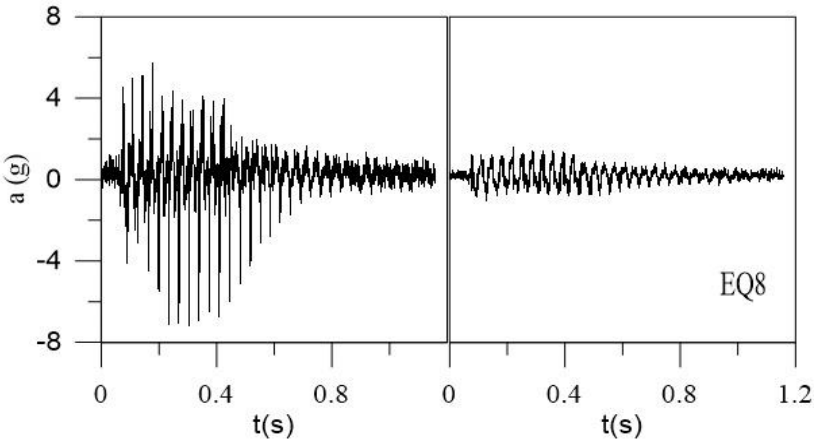

Figure 2.23 Time histories recorded by MEMS in the Model 1

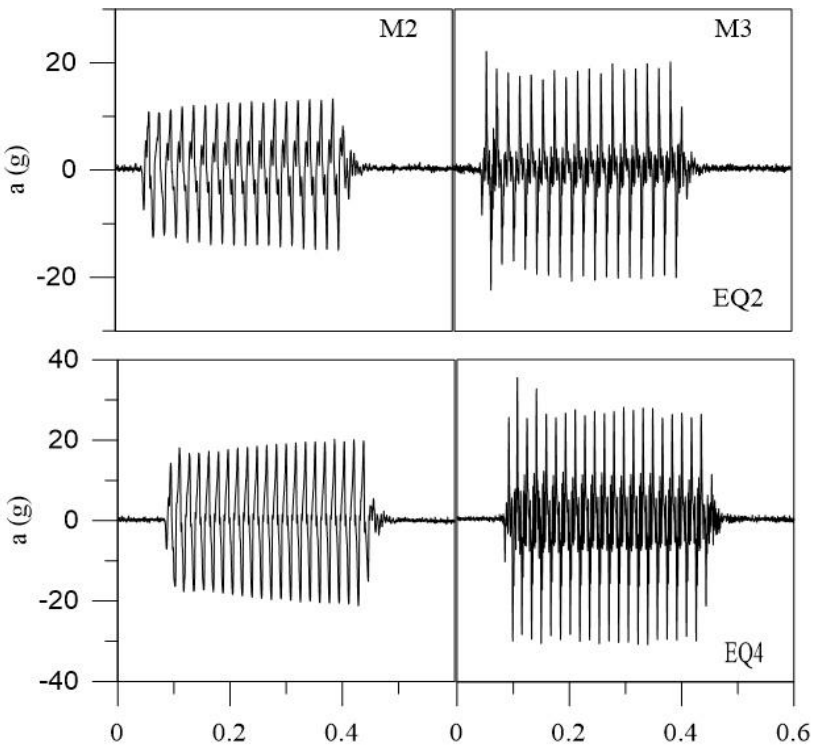

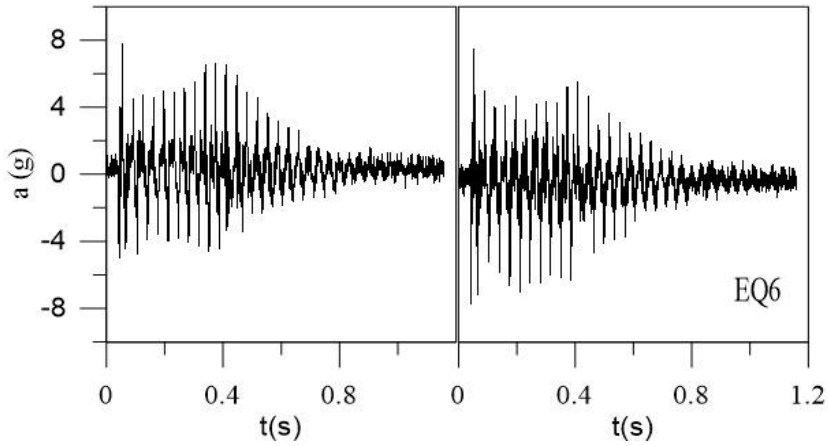

Figure 2.24 Time histories recorded by MEMS in the Model 2

2.5.5. Stress-strain loops

The relative importance of parameters affecting shear modulus and damping were summarised by Hardin and Drnevich (1972a).

Many studies have used cyclic triaxial or resonant column tests to determine these parameters as functions of shear strain and effective stress for various materials, for example, gravels (Seed et al, 1986, Rollins et al, 1998), sands (Wilson, 1988, Kokusho, 1980), loess (Hardcastle and Sharma, 1998) and clays (Idriss et al, 1978, Kokusho et al, 1982, Vucetic and Dobry, 1991). Field studies have also been carried out to investigate stiffness nonlinearity, based on earthquake motions (Chang et al, 1989, Zeghal and Elgamel, 1994, Zeghal et al, 1995). It is not common to see centrifuge data used to develop stress-strain loops, or derive stiffness and damping parameters. Ellis et al (1998) derive modulus and damping of very dense sand saturated with different pore fluids based on centrifuge work carried out in Japan. Teymur and

Madabhushi (2002) generated stress-strain loops to exemplify wavelet techniques and describe boundary effects in centrifuge packages. Pitilakis et al (2004) plotted some first order loops to compare centrifuge and numerical data. Arulnathan et al (2000). With centrifuge testing, there is an added complication of scaling laws. Brennan et al. (2004) reported the procedure to evaluate shear modulus and damping ratio using centrifuge data. In order to estimate the G modulus and the D ratio a set of 3 or more accelerometers should be positioned in every column. From the original shear beam equation, shear stress τ at any depth z may be written as the integration of density ρ times acceleration ü through higher levels (Equation 2.14).

$$\tau(z) = \int_0^z \rho \ddot{u} dz \qquad 2.7$$

The equations proposed by Zeghal and Elgamel (1994) for field measurements utilise acceleration measured at the surface as they deal with site data. In contrast, a reliable surface acceleration is rarely available in centrifuge testing as the instrument needs to be buried to maintain good contact with the soil. A linear fit is therefore recommended between adjacent pairs of instruments, which may be extrapolated from the top pair to the surface (Equation 2.15). If many accelerometers are present, and significant amplification/attenuation is observed, a trapezoidal integration can be used to obtain shear stress. In many centrifuge tests, neither apply. Therefore shear stress is evaluated using Zeghal and Elgamel's expression (Equation 2.15) with the

interpolated surface acceleration obtained from Equation 2.15 with z = 0.

$$\ddot{u}(z) = \ddot{u}_1 + \frac{(\ddot{u}_2 - \ddot{u}_1)}{(z_2 - z_1)}(z - z_1) \qquad 2.8$$

$$\tau(z) = \frac{1}{2}\rho z(\ddot{u}(0) + \ddot{u}(z))$$

Two methods of shear strain calculation are available, a first or a second order expression. Displacement must first be obtained from the acceleration recordings. In order to avoid annoying effects and integration errors due to the unreal variation of the displacements after shaking, it is possible to cut these parts from the signal prior to processing. Acceleration data must be band-filtered prior to integration to produce velocity, and then filtered again before being integrated to displacement u. This is important as low frequency information present in the velocity trace is common and produces a characteristic linearly varying displacement that continues changing after the end of shaking.
A simple first order approximation must be applied (Equation 2.16). This applies for any point between instruments 1 and 2, and as such is more appropriate for the mid-point.

$$\gamma = \frac{(u_2 - u_1)}{(z_2 - z_1)} \qquad 2.9$$

If three instruments are stacked in a soil column then a better, second order approximation may be made (Equation 2.17). This would apply at depth z_i. Equation (2.17) is also part of the Zeghal and Elgamel work.

$$\gamma(z_i) = \frac{\left[(u_{i+1} - u_i)\frac{(z_i - z_{i-1})}{(z_{i+1} - z_i)} + (u_i - u_{i-1})\frac{(z_{i+1} - z_i)}{(z_i - z_{i-1})} \right]}{(z_{i+1} - z_{i-1})} \qquad 2.10$$

In which the index i was relative to the position of the central instruments and i-1 and i+1 to the top and bottom accelerometers. Figure 2.25 shows the differences between these two methods calculated for instance, for model 1 and earthquake 1.

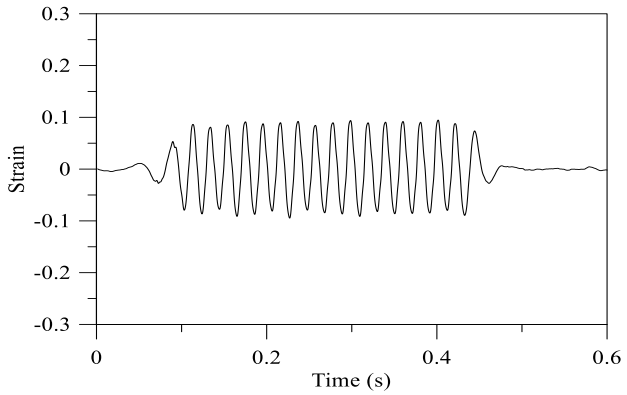

a)

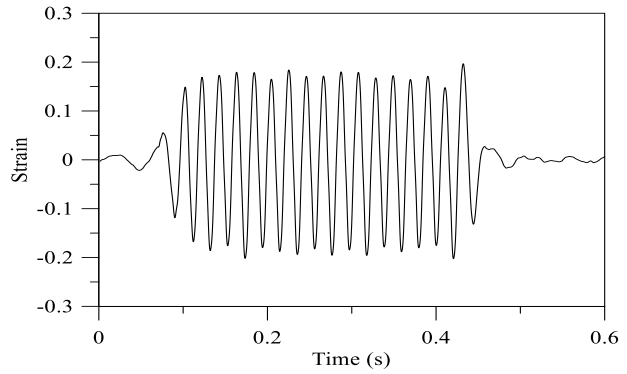

b)

Figure 2.25 strain calculated with a) 1° order b) 2 order

For every instrumented column installed in the model, the shear strains were calculated. Having obtained shear stress and shear strain, a plot of one against the other enables evaluation of shear modulus. Shear modulus and damping ratio mobilized during each signal can be evaluated from stress strain loop as:

$$G(\gamma_{\max}) = \frac{\tau(\gamma_{\max})}{\gamma_{\max}} \qquad 2.11$$

$$D = \frac{W_D(\gamma_{\max})}{4\pi W_E} \qquad 2.12$$

where γ_{max} is the maximum shear strain computed during the signal, $\tau(\gamma_{max})$ is the associated shear stress, W_D is the energy dissipated during one representative stress–strain cycle and W_E is the strain energy

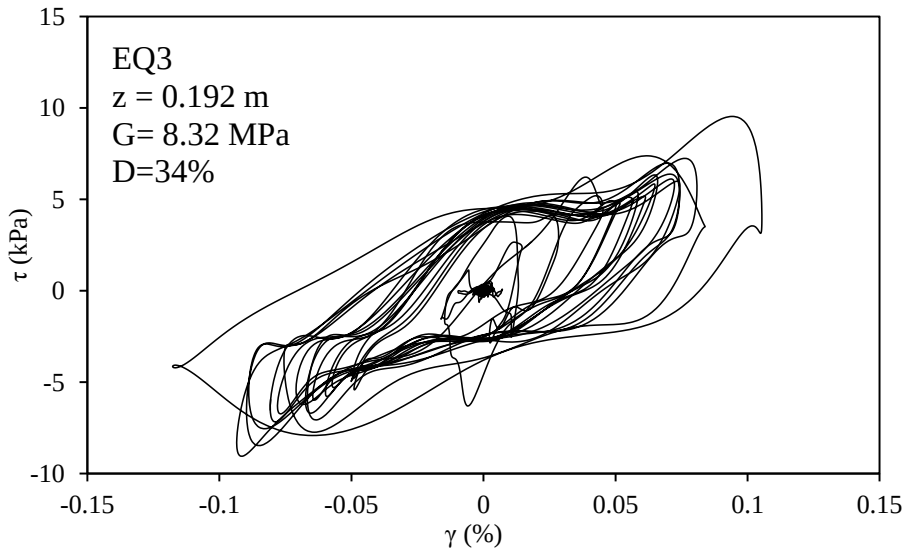

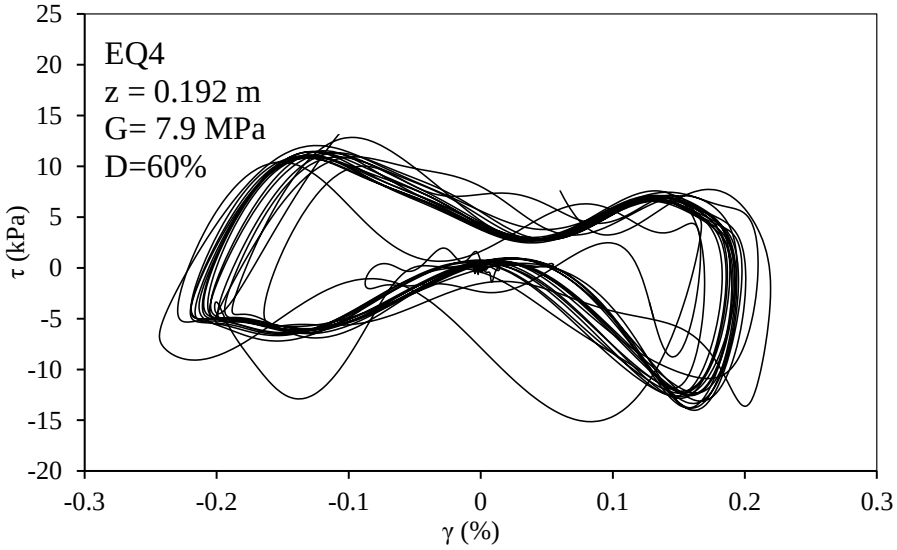

Figure 2.26 Calculation of shear modulus from stress–strain cycles (array 1 of horizontal barrier model)

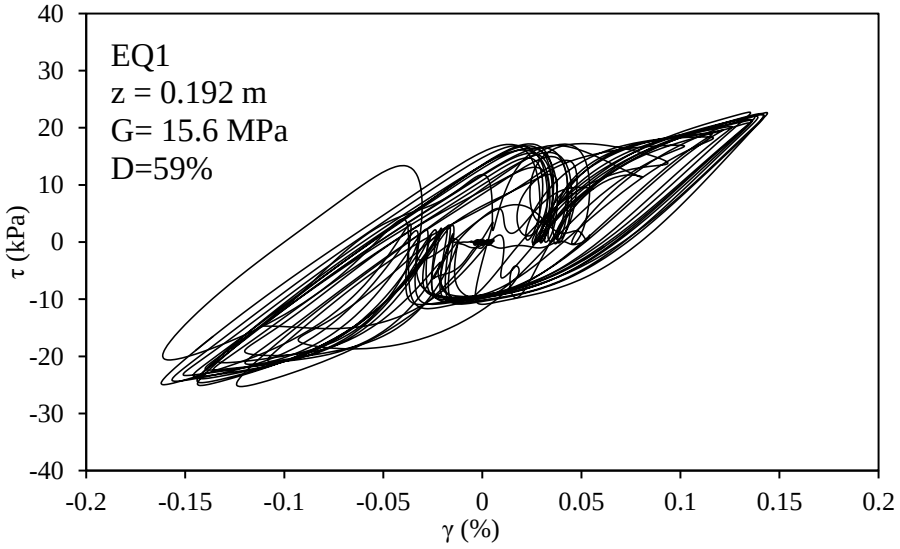

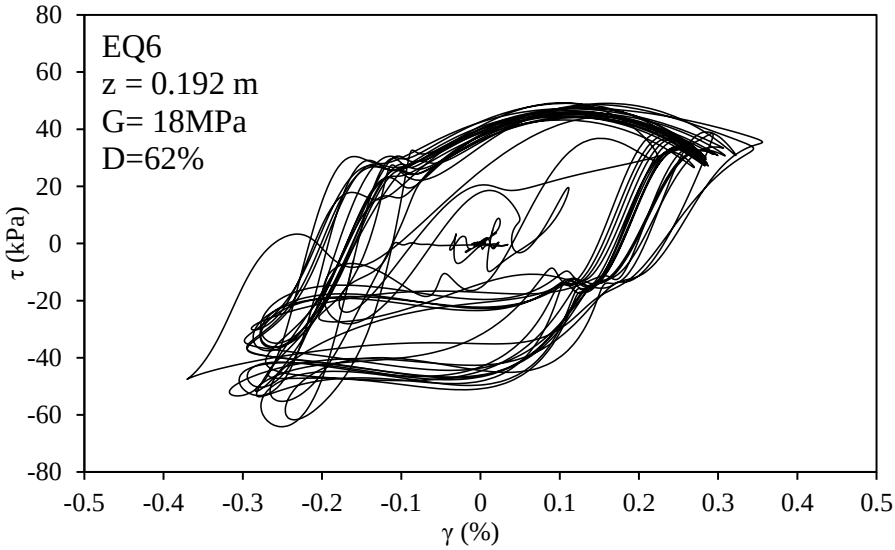

Figure 2.27 Calculation of shear modulus from stress–strain cycles (array 2 of V-shape barrier model)

As an alternative, Brennan et al. (2005) suggested to compute G as the ratio between the difference in maximum and minimum stress applied during a loop and the difference in maximum and minimum strain developed in the same loop. Figure 2.26 shows the stress strain cycle computed during the signals fired at 80 g on the first model with the calculated shear modulus and damping. In the second model (Figure 2.27) it was possible to evaluate the stress strain cycles only along the array 2, due to the malfunctioning of some of the horizontal accelerometers of array 1. Values of shear modulus were derived from the three accelerometers aligned vertically below the soft layer in both the models (A10, A11, A12). These values are compared in Figure 2.28

with the shear modulus degradation curve provided by the empirical relationship proposed by Santos and Correia (2001):

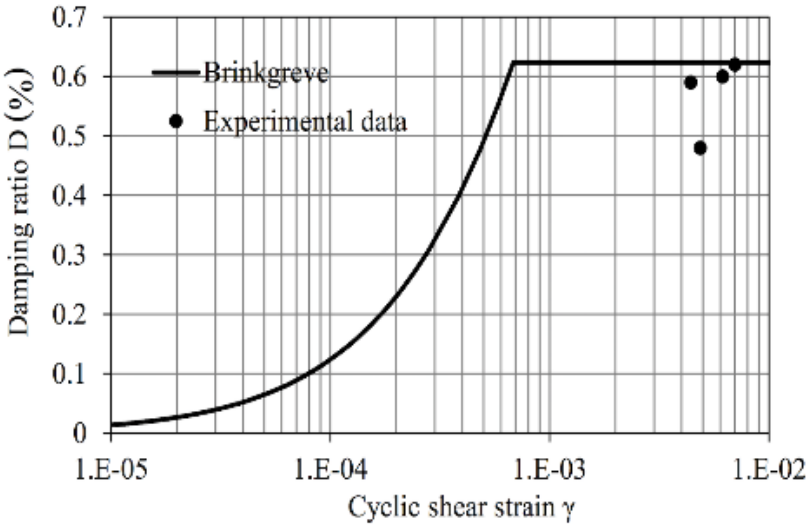

a)

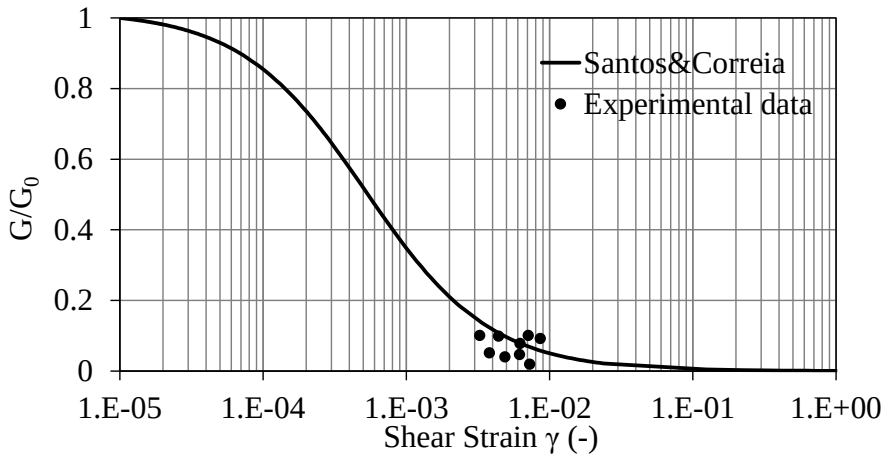

b)

Figure 2.28 Secant shear modulus (a) and damping ratio (b) with cyclic shear strain

$$\frac{G}{G_0} = \frac{1}{1 + a\dfrac{\gamma}{\gamma_{0.7}}} \qquad 2.13$$

where a is equal to 0.385 and $\gamma_{0.7}$ is the shear strain level at which the secant shear modulus is reduced to about 70 % of G_0.

The local hysteretic damping has been calculated with the formulation suggested by Brinkgreve et al. (2007), developed for HS small model in Plaxis. As soon as G_{ur} is reached the damping ratio does not increase further, where G_{ur} is defined as:

$$G_{ur} = \frac{E_{ur}}{2(1+\nu_{ur})} \qquad 2.14$$

where E_{ur} is the Young's modulus for unloading and reloading and ν_{ur} is the unloading/reloading Poisson's ratio.

2.6. Numerical simulation of the centrifuge tests

Numerical simulations of the two centrifuge tests were performed by the FE code Plaxis2D (Brinkgreve et al. 2011). The geometry of both centrifuge models was reproduced. Additionally, the same sand layer without the soft barrier was modelled, to have a reference free-field model for comparison.

2.6.1. PLAXIS 2D software: general features

PLAXIS 2D is a two-dimensional finite element program, developed for the analysis of deformation, stability and groundwater flow in geotechnical engineering. To carry out a finite element analysis using

the PLAXIS 2D program, the first step is to create a two dimensional geometry model composed of points, lines and other components in the x-y plane and specify material properties and boundary conditions. This is done in the first two tabsheets (Geometry modes) of the Input program. The mesh generation and the definition of the calculation phases is done in the last three tabsheets (Calculation modes) of the Input program. The 15-node triangle is the default element. It provides a fourth order interpolation for displacements and the numerical integration involves twelve Gauss point (stress points). The limit of the model area can be assigned according to the domain extension. Once the problem is drawn, the boundary conditions can be assigned by the user, according to the library constraints, or choosing the standard fixities, which is applied automatically according to the analysis type, which can be static or dynamic. Once the geometric and structural settings are defined, distributed (constant or linear) or concentrated loads or displacements, applied in the created internal or external points, can be introduced in the calculation domain. In the Material section the mechanical properties of the soil layers are fixable: the assignable values are the unit weight, the permeability and the stiffness-strength parameters, which are the elastic modulus E, the Poisson ratio ν, the friction angle φ and the cohesion c. Moreover, the stiffness parameters can be defined as linearly variable with depth. For each soil material created can be assigned a constitutive model and the soil behaviour, assignable between drained and un-drained. For each material the interface soil/structure behaviour is defined through the parameter R, which has 1 as a default value, but can be reduced to values almost null.

Once the model features are assigned for each layer and structural element and before the calculation step, the domain is divided in finite elements: the software automatically generates the mesh, without an ordinate structure. In order to get better performance on the analysis results, where the stress variations are very high, the mesh can be more dense, around a model point, line or in a selected region. At the end of Input phase the initial condition is created, performing the generation of pore pressure and effective initial stresses. The initial stress is calculated starting from the K0 ratio, evaluate from the famous Jaky's (1944) relationship $K0=1-sen\varphi$ or manually fixed by the user; the lithostatic conditions can be also generated in the Calculation phase, carrying out a plastic analysis without any loads, displacements and structures activated. After the FE model generation, the effective calculation is carried out, defining the type of analysis required. In the Calculation modulus is assigned the analysis phase, the structures and the soil layers are switched on or off, and the loads and the displacements are activated. The calculation is performed, solving a system of equilibrium and congruence equations in the mesh nodes. The Plaxis code permits the execution of 4 types of FE analysis:

- Plastic
- Consolidation
- Fully coupled flow deformation
- Safety
- Dynamic

The Plastic option is an elasto-plastic deformation analysis; the Consolidation option considers the dissipation with time of pore

pressure increments; the Safety option carries out a stability analysis reducing the strength parameters in order to evaluate a safety factor; the Dynamic option consists in the application of time histories of loads or displacement, corresponding to a point or a line of the model. Before the analysis starting, some relevant mesh points can be selected, in order to know the variation of some parameters with non-geometric parameters. Each calculation phase is divided in steps, in order to carry out the specific analysis in progressive increments of the variable parameters. When the analysis phase is set, the analysis type, the starting phase, the number of steps, the iterative control parameters should be fixed. Once all the phase condition is defined, the calculation process is started; the analysis is performed in sequence, until the soil does not collapse. In the Iteration window, some information of calculation process are showed, including the evolution of the displacement in the selected point, in order to check that the analysis correctly goes forward. Once a FE analysis phase is ended or stopped (manually or automatically due to soil collapse), the results of the calculation can be inspected in the Output modulus. The parameters, which can be displayed in the whole domain, are:

- Total or incremental displacements, velocity and acceleration;
- Total or incremental strain; Cartesian components of total or incremental strain;
- Effective or total stress; Cartesian components of total and effective stresses; total and increments of pore pressure;
- Loads or displacements, stress or strain in the structural elements.

The analysis results was given both as through graphical representation (vectors, contours or shadings) and table lists. The Plaxis user can create a section in the model domain, in order to display the previous listed parameters along the section line (in graph and table form). Concerning the structural elements, the software gives the values of model parameters, but moreover the internal forces in the last calculation steps (hoop load, shear force and bending moment) and the envelops of the previous ones. The Curves modulus is used to obtain non-geometrical variation of the model output parameters (except for the internal forces). In this subprogramme the load or time-displacements curves, the stress-strain ones, the stress or strain paths and the time histories of displacement, velocity or acceleration of the calculation selected points can be displayed and listed. In the mesh nodes, the value of load, displacement, velocity and acceleration are Numerical modelling of soil/tunnel interaction 75 given; from the integration internal nodes the value of stress and strain are obtained. A total of 10 nodes and 10 integration points can be selected in the Calculation phase, which are an important code limitation on the required results. The procedure to perform dynamic analyses is formally similar to the other types of analyses, but needs some explanations about the additive parameters and conditions compared to the other analyses. Moreover the seismic analysis are particular dynamic analysis, in which the waves propagation due to an earthquake should be correctly modelled. In order to perform the seismic shaking of a soil layer, the dynamic loads are applied at the bottom of a bi-dimensional model domain, causing the propagation of the shear waves until the surface of the soil layer. The

use of prescribed displacements permits the application of time histories of displacements, velocity or acceleration during the Calculation phase. In the Calculation phase the equation of the wave propagation are solved in the time domain. The basic equation of the dynamic behaviour is:

$$\underline{\underline{M}}\,\underline{\ddot{u}} + \underline{\underline{C}}\,\underline{\dot{u}} + \underline{\underline{K}}\,\underline{u} = \underline{F} \qquad 2.15$$

in the (2.21), M is the mass matrix, C is the damping matrix, K is the stiffness matrix, F is the load vector and u is the displacement vector. The displacement u, the velocity $\dot{u}$ and the acceleration $\ddot{u}$ can vary with time. The matrix C represents the material damping and it is formulated as a function of the mass and stiffness matrices (Rayleigh damping) as:

$$\underline{\underline{C}} = \alpha_R \underline{\underline{M}} + \beta_R \underline{\underline{K}} \qquad 2.16$$

This limits the determination of damping matrix to the Rayleigh coefficients α_R and β_R.

In order to solve the motion equations, an implicit time integration method is used in the software dynamic implementation, according to the Newmark scheme. With this method, the displacement and the velocity at the point in time t+Δt are expressed respectively as:

$$u^{t+\Delta t} = u^t + \dot{u}^t \Delta t + \left(\left(\frac{1}{2} - \alpha \right) \ddot{u}^t + \alpha \ddot{u}^{t+\Delta t} \right) \Delta t^2 \qquad 2.17$$

$$\dot{u}^{t+\Delta t} = \dot{u}^{t} + \left((1-\beta)\ddot{u}^{t} + \beta\ddot{u}^{t+\Delta t}\right)\Delta t$$

2.18

In above equation Δt is the time step and the coefficient α and β determine the accuracy of the time integration. The default values for the Newmark coefficients are α= 0.25 and β= 0.50 (average acceleration method).

In the case of static deformation analysis, prescribed boundary displacements are introduced at the boundaries of finite element model. For dynamic calculation, the boundaries should in principle be much further away than those for static calculations, because, otherwise, stress waves will be reflected leading to distortion in the computed results. In the Calculation modulus, some parameters should be accurately defined in each dynamic phase in order to perform a correct seismic analysis. The Dynamic Time, expressed in seconds, for each phase should be assigned. The time step used in dynamic calculation is constant and equal to $\delta t = \Delta t / (m \cdot n)$ where Δt is the duration of the dynamic loading, m is the value of Max steps and n is the Number of the sub steps parameter.

2.6.2. Materials and models

The layouts of the three models are shown in Figure 2.29. The Model 1 (horizontal barrier) was taken as reference for the preliminary calibrations of prediction model. The numerical mesh shown in Figure 2.29b was adopted in this case. The soil was characterized by a constitutive model implemented in the Plaxis code, Hardening Soil with

small strain overlay that accounts for strain hardening plasticity and small-strain behaviour of soils (Schanz et al. 1999; Benz et al. 2009).

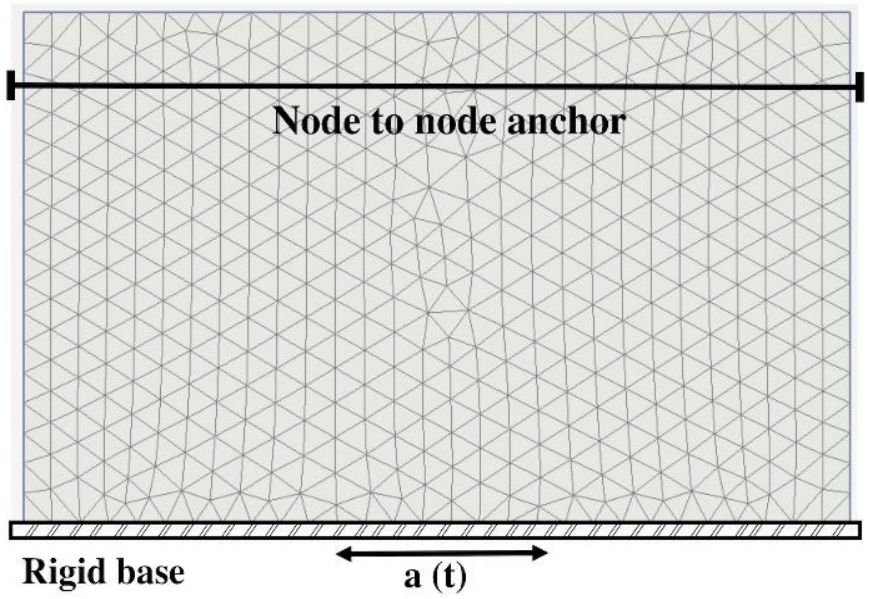

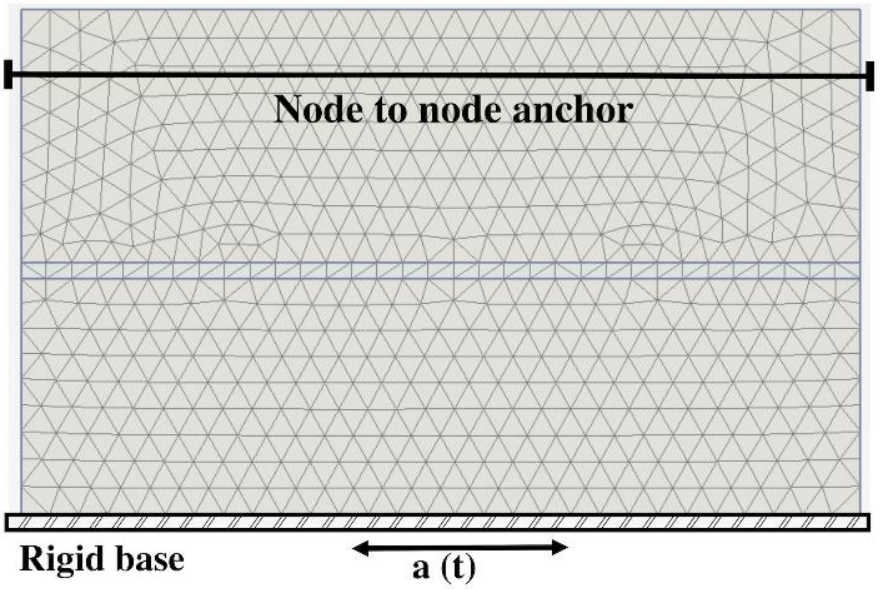

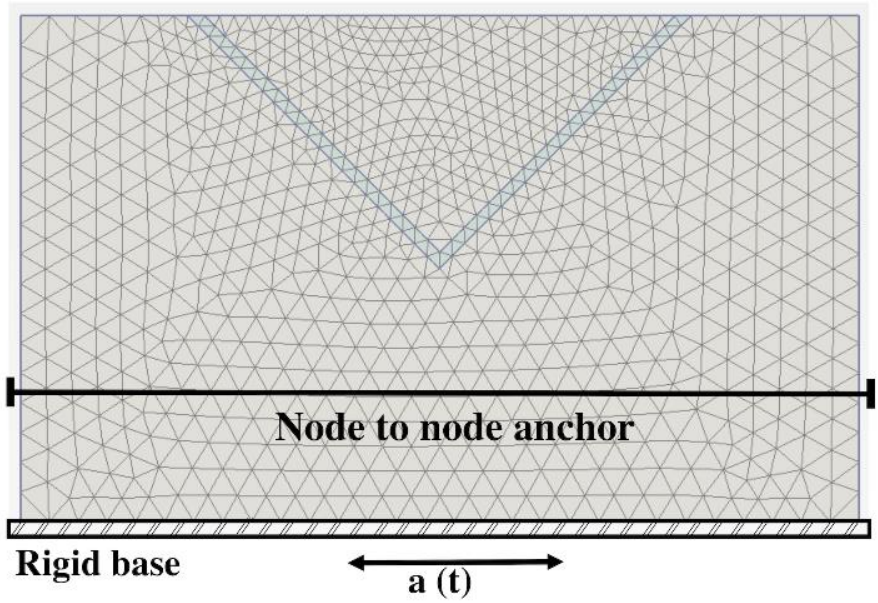

Figure 2.29 Schematic models of the FE mesh, a free field; b horizontal layer; c V-shaped

The model is also able to capture the hysteretic behaviour of sands and the associated hysteretic damping in unloading–reloading cycles. Both stiffness decay and hysteretic damping are crucial in the prediction of the stress–strain behaviour of soil under cycling loading. Two parameters are needed to describe stiffness from very small to medium strains: the initial modulus G_0 and the shear strain level $\gamma_{0.7}$ at which the secant shear modulus is reduced to about 70 % of G_0.

The model parameters for HN31 Hostun sand were extracted from literature (Benz 2007) and they are reported in Table 2.8. The reference pressure p_{ref} is 100 kPa. The value of the parameter E_{0ref} is consistent with the results shown in Figure 2.28.

Table 2.8 Hardening soil small strain parameters adopted for the sand (after Benz 2007)

Parameter	Symbol	Value	Unit
Small strain stiffness	G_{0ref}	202000	kN/m2
Shear strain at 0.7 G0	$\gamma_{0.7}$	0.0002	-
Poisson's ratio	ν	0.25	-
Triaxial compression stiffness	E_{50ref}	30000	kN/m2
Primary oedometer test	E_{oedref}	30000	kN/m2
Unloading/Reloading stiffness	E_{urref}	90000	kN/m2
Reference pressure	p_{ref}	100	kN/m2
Rate of stress-dependency	m	0.55	-
Cohesion	c	0	kN/m2
Friction angle	φ	42	°
Dilatancy angle	ψ	16	°
Stress ratio in primary compression	K_0^{nc}	0.4	-

The small-strain damping of the sand (D_0) was assumed equal to 0.5 %. It was modelled through the Rayleigh formulation, through the coefficients α_R and β_R, estimated using the ‘‘double frequency approach’’ suggested by Park and Hashash (2004). It is worth noting that several procedures can be followed when implementing such an approach. For instance, Amorosi et al. (2010) suggested an iterative procedure, taking into account also the amplification function between the surface and the base level. This seemed necessary to avoid

significant underdamping in the frequency range characterized by an amplification factor larger than one.

Table 2.9 Mohr-Coulomb parameters adopted for the soft barrier

ρ (kg/m3)	G0 (kN/m2)	φ (°)	ν (-)	Vs (m/s)
1020	109	10	0.4	12

Table 2.10 Frequencies used for Rayleigh damping parameters estimations

Model	Input signal	ξ [%]	f1	f2
1	EQ1	0.5	1	3.64
	EQ2		0.6	
	EQ3-EQ4		0.625	
	EQ5		0.375	
	EQ6-EQ7		0.75	
	EQ8		0.375	
2	EQ1-EQ2	0.5	0.625	3.64
	EQ3-EQ4		0.375	
	EQ4-EQ5		0.75	
	EQ6-EQ7		0.375	
	EQ7		1	
	EQ8		0.6	

However, since the Rayleigh formulation was here adopted to model the small-strain damping only (not the hysteretic one at larger strain level), this appeared to be a minor issue.

Hence, the parameters were simply calculated by assuming the Rayleigh damping coincident with the initial damping ratio, D_0, at the predominant frequency of the input signal (f1) (Table 2.7) and at the first natural frequency of the soil layer (f2) (Lanzano et al. 2015), as reported in Table 2.10, where n is the modal damping ratio. The soft barrier was modelled as an elastic-perfectly plastic Mohr-Coulomb material. Its shear strength was determined through shear tests (Flora et al., 2015) while the elastic shear wave velocity was obtained by means of air-hammer pulse tests during the centrifuge flight, as shown in the previous section. The adopted values of parameters are summarized in Table 2.9. The small-strain damping of the barrier (D0) was derived from back-analysis of the experimental results pertaining to EQ1 and EQ2 of the centrifuge model with horizontal layer (Model 1), and it was assumed equal to 2.5%. The recorded time history at the base of the centrifuge container (Figure 2.19) was used as the input motion applied at the bottom boundary of the FE mesh.

Boundary conditions reproduced those of the laminar box used in the tests: periodic boundary at the lateral sides, through displacement restraints between the corresponding nodes, and reflective boundary at the base, through simple supports.

2.6.3. Results: *Horizontal barrier*

The results of the calibration phase is shown in Figure 2.30, for signal 7, for which the largest effectiveness of the barrier was obtained, this indicating an important influence of non-linear behaviour of both the soil and the soft barrier. In the same figure the experimental results are shown for comparison. It can be observed that calculated and recorded acceleration time histories at two different depths and the corresponding Fourier spectra are in good agreement, indicating the soundness of the numerical model.

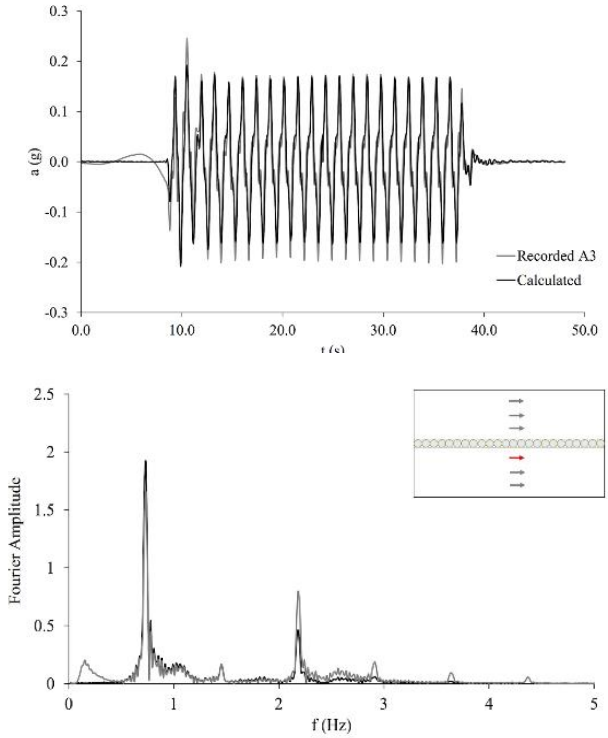

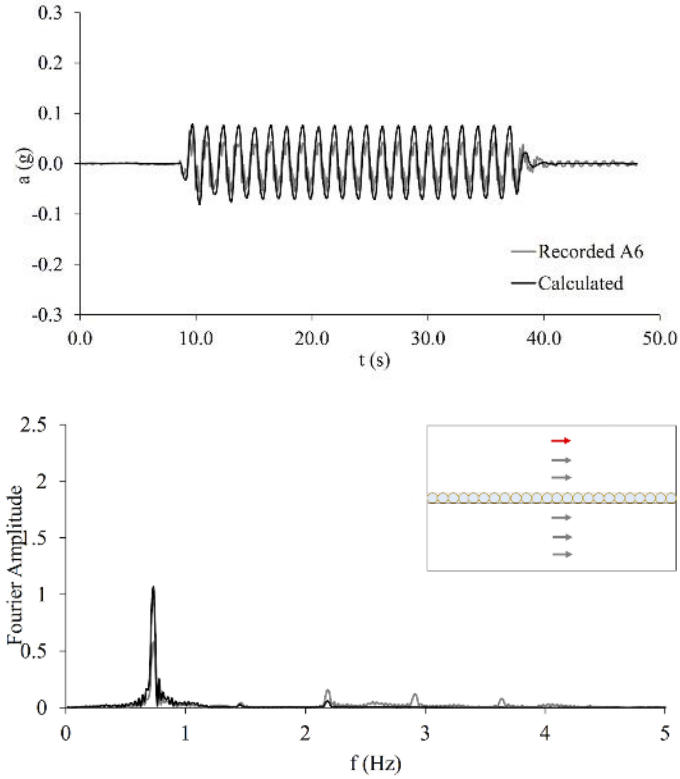

Figure 2.30 Recorded and calculated time histories of acceleration and Fourier spectra

A further confirmation is shown in Figure 2.31. Here the acceleration amplifications at different depths, as measured during EQ4 and EQ7, are compared to the corresponding computed profiles, with and without barrier. Hence, the numerical calculations were performed in free field conditions using the mesh shown in Figure 2.29a. Figure 2.32a and b compare the reference, calculated free-field behaviour with that observed in the centrifuge test performed on the model with the horizontal barrier.

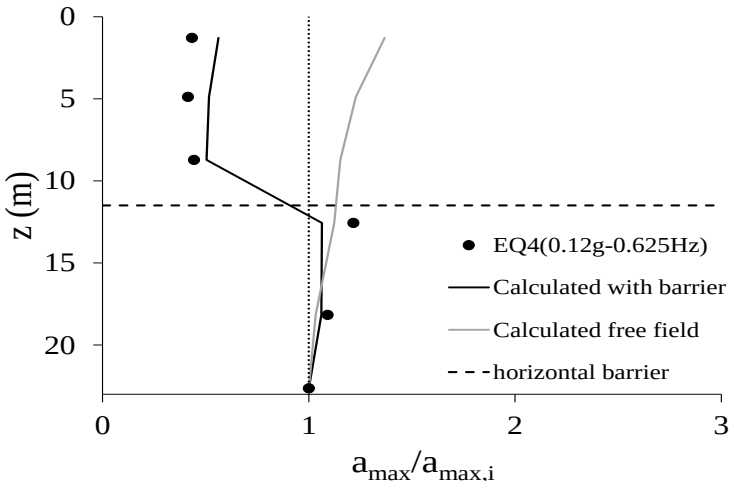

a)

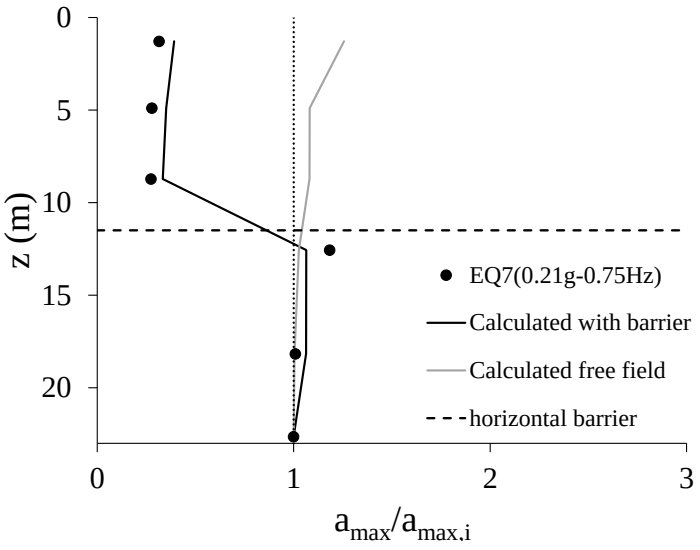

b)

Figure 2.31 Acceleration amplifications at different depths, as measured during EQ4 (a) and EQ7 (b), and corresponding computed profiles, with and without horizontal barrier

The results are compared in terms of an attenuation ratio, defined as the ratio between the maximum acceleration observed at the surface of the model with the horizontal barrier ($a_{max,hb}$) and the maximum acceleration computed without it ($a_{max,ff}$), plotted as a function of the peak input acceleration (Figure 2.32a) and of the input nominal frequency (Figure 2.32b).

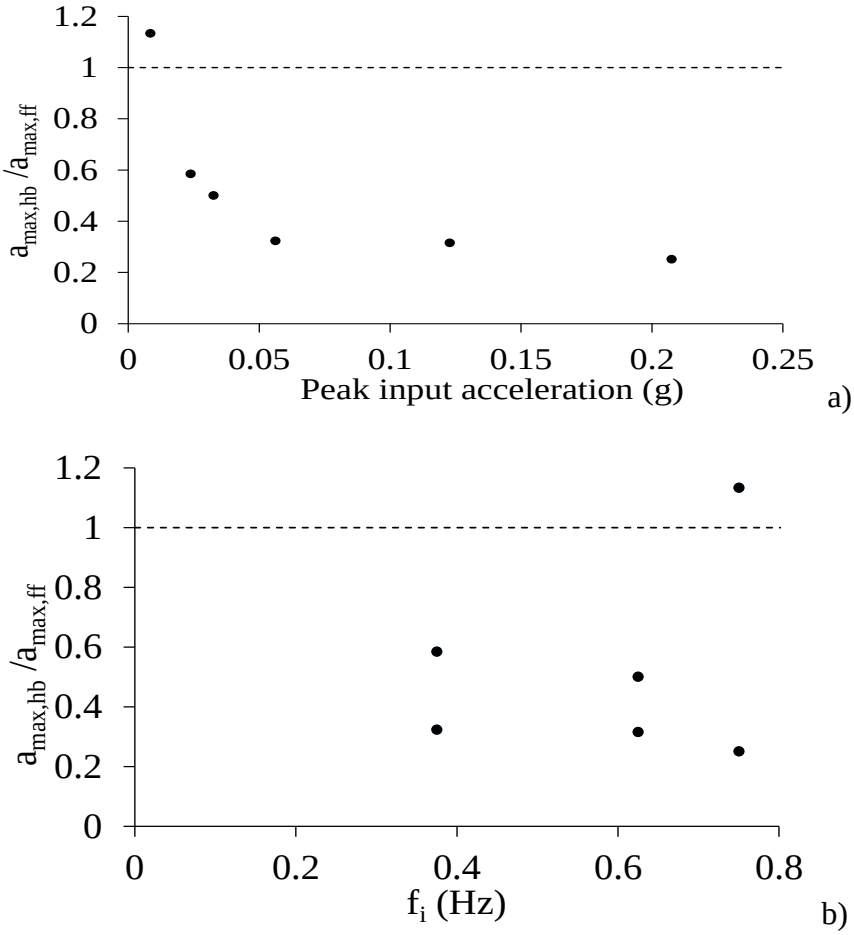

Figure 2.32 Free field versus horizontal barrier: attenuation ratio with the peak input acceleration (a), and with the input frequency (b)

The results confirm that the barrier is generally more effective during strong signals (attenuation ratio lower than 1, in some cases even lower than 0.5).

2.6.4. Results: *V-barrier*

Numerical simulations of the V-shaped barrier model were also carried out, using the mesh of Figure 2.29c. The results achieved for array 2 were hence compared with the results of the reference free-field numerical model. In Figure 2.33 the acceleration amplifications at different depths, as measured during EQ2 and EQ4, are compared to the corresponding computed profiles, with and without barrier. This comparison confirms the ability of the numerical model to predict the experimental results also in the case of V-barrier.

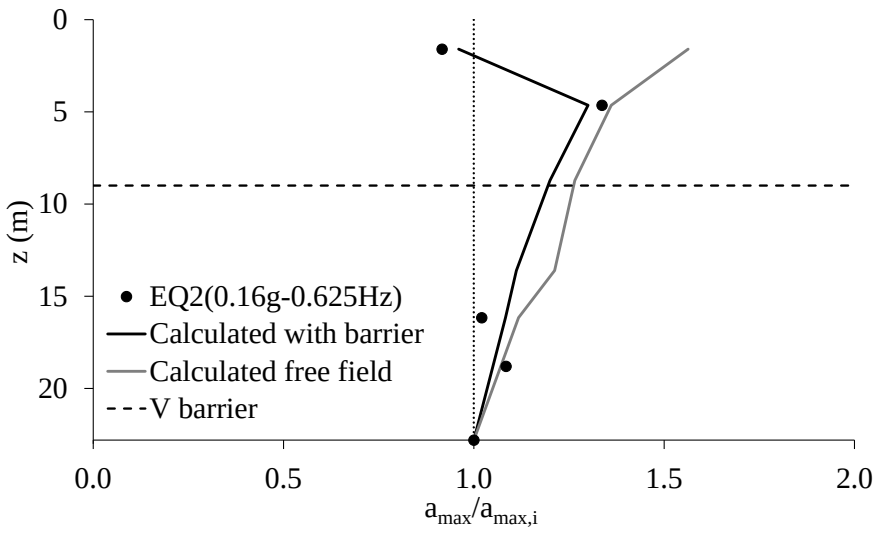

a)

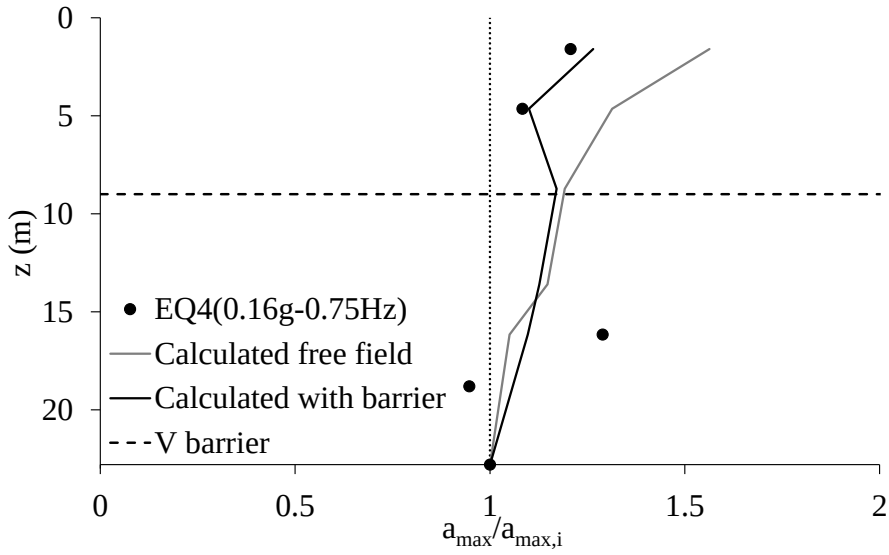

b)

Figure 2.33 Acceleration amplifications at different depths, as measured during EQ2 (a) and EQ4 (b), and corresponding computed profiles, with and without V-shaped barrier

Figure 2.34 shows the results in terms of the ratio between the maximum acceleration at the surface of the model with ($a_{max,Vb}$) and without ($a_{max,ff}$) the V-shaped barrier, plotted as a function of the peak acceleration (Figure 2.34a) and the frequency of the input signal (Figure 2.34b), for all signals at 80 g level. When the input frequency is low the values of the peak acceleration with and without soft barrier are very similar, while by increasing the input frequency the amplification ratio attains values lower than 1, in the range of 0.6–0.8 (Figure 2.34b). However, to properly isolate the frequency effects, input signals of equal

amplitude and different frequencies should be applied. Since this was not the case, no clear frequency effect can be observed in the figure.

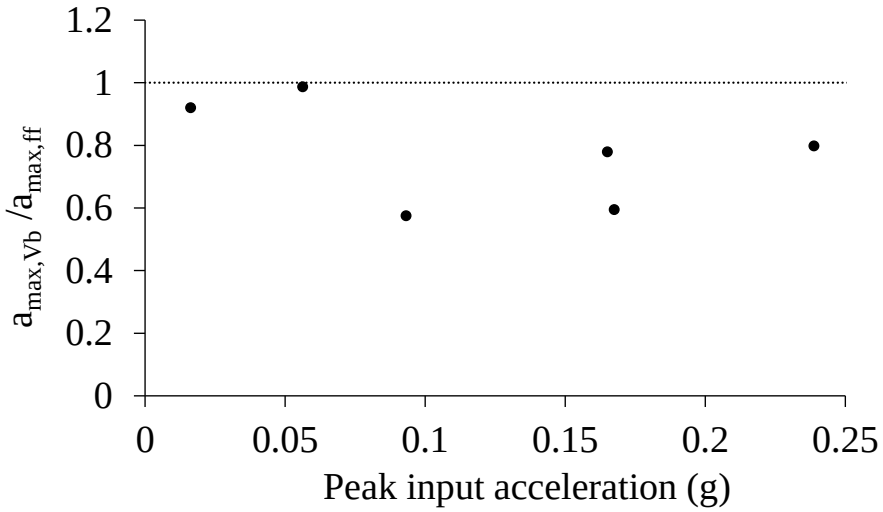

a)

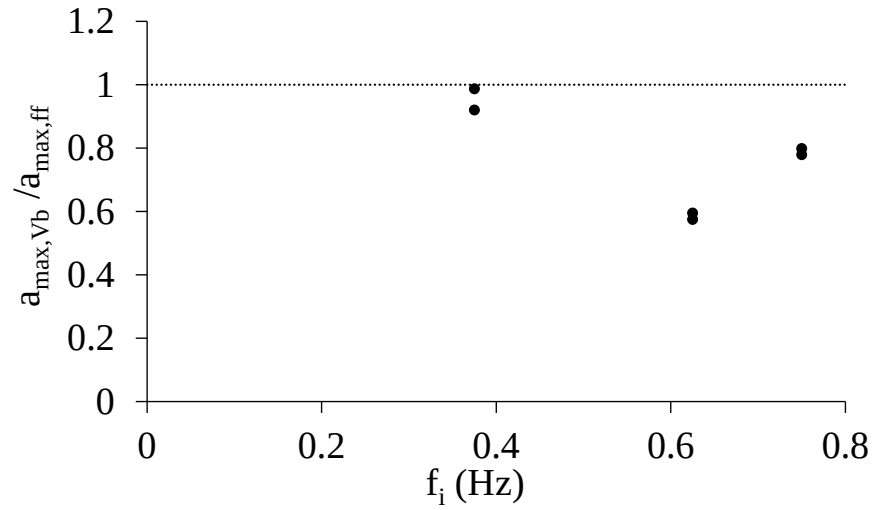

b)

Figure 2.34 Free-field versus V-shaped barrier: attenuation ratio with the peak input acceleration (a), and with the input frequency (b)

Conversely, as input signals of equal frequency characterised by different amplitudes were adopted, the effect of increasing amplitude is evident (Figure 2.34a).

2.7. Final remarks

The two models tested in centrifuge at 50 and 80 g consisted each in a layer of dense Hostun sand, about 280 mm thick, free to be shaken along its main horizontal axis thanks to the adopted container (a laminar box). In the first model a thin horizontal layer made of latex balloons filled with a cross-linked gel was created at about mid-height of the sand layer. In the second, the same balloons were installed to form a V-shaped barrier aimed at isolating a relatively shallow volume of sand.

The experimental results were compared with FE numerical analyses of the same models, carried out also in free field to have a benchmark condition. By validating the FE modelling via the comparison with the experimental results, a robust model has been built, that can be used for carrying out a wider parametric numerical testing.

The experimental results confirm the effectiveness of such soft barriers to reduce amplification in the isolated volume during seismic events, although V-shaped isolating barriers are less effective than a full horizontal barrier. The latter is however rather unfeasible and should only be considered as a reference condition.

Despite the fact that the contrast of impedance between the sand and the barrier decreases because of the decay of sand shear stiffness with large strains, in stronger events the soft barrier shows its highest effectiveness.

This is a clear evidence that yielding plays a beneficial role, and that a low shear strength is needed in the soft layer

REFERENCES

Amorosi A, Boldini D, Elia G (2010) Parametric studies on seismic ground responce by finite element modelling. *Comput Geotech 37:515–528*

Arulnathan, R., Boulanger, R.W., Kutter, B.L. and Sluis, W.K. (2000) New Tool for Shear Wave Velocity Measurements in Model Tests. *Geotechnical Testing Journal. 23(4) p. 444-453.*

Benz T (2007) Small strain stiffness of soil and its numerical consequences. *Ph.d. thesis, Universitat Stuttgart*

Brennan, A.J. (2004) Vertical drains as a countermeasure to earthquake-induced soil liquefaction. *PhD thesis, University of Cambridge, UK.*

Brennan AJ, Thusyanthan NI, Madabhushi SPG (2005). Evaluation of shear modulus and damping in dynamic centrifuge tests. *J Geotech Geoenviron Eng 131(12):1488–1498*

Brinkgreve RB, Kappert JMH, Bonnier PG (2007) Hysteretic damping in a small-strain stiffness model. *Numerical models in geomechanics NUMOG X Pande and Pietruszczak (eds) Taylor and Francis Group, London, ISBN 978-0-415-44027-1*

Brinkgreve RBJ, Swolfs WM, Engine E (2011) PLAXIS user's manual, PLAXIS bv the Netherlands

Chang, C.-Y., Power, M.S., Tang, Y.K. and Mok, C.M. (1989). Evidence of nonlinear soil response during a moderate earthquake. *Proc. 12th ICSMFE, Rio de Janeiro, Brazil. A.A. Balkema publishers. p. 1927-1930.*

Ellis, E.A., Soga, K., Bransby, M.F. and Sata, M. (1998). Effect of pore fluid viscosity on the cyclic behaviour of sands. *Proc. Centrifuge 98 (ed. T. Kimura, O. Kusakabe and J. Takemura), Tokyo, Japan. A.A. Balkema publishers. p. 217-222.*

Flavigny E., Desrues J., Palayer B. (1990). Note Technique le sable d' Hostun "RF". *Rev. Franc. Geotech. N°53 pp. 67-70*

Hardcastle, J.H. and Sharma, S. (1998) Shear modulus and damping of unsaturated loess. *Geotechnical Earthquake Engineering and Soil Dynamics III, ASCE Geotechnical Special Publication 75 p. 178-188*

Hardin BO, Black WL (1969) Closure to vibration modulus of normally consolidated clays. *J Soil Mech. Found Div 95(SM6):1531–1537*

Hardin, B.O., Drnevich, V.P. (1972a). Shear modulus and damping in soils: Measurement and parameter effects. *Journal of Soil Mechanics and Foundations Division, ASCE. 98(6):603-624*

Hoque E., Tatsuoka F. (2004). Effects of stress ratio on small-strain stiffness during triaxial shearing. *Geotechnique, 54 (7):429-439.*

Idriss, I.M., Dobry, R. and Singh, R.D. (1978). Nonlinear behavior of soft clays during cyclic loading. *Journal of the Geotechnical Engineering Division, ASCE. 104(12): 1427-1447.*

Kokusho, T. (1980). Cyclic triaxial test of dynamic soil properties for wide strain range. *Soils and Foundations 20(2): 45-60.*

Kokusho, T., Yoshida, Y. and Esashi, Y. (1982). Dynamic properties of soft clay for wide strain range. *Soils and Foundations 22(4): 1-18.*

Lanzano G, Bilotta E, Russo G, Silvestri F (2015) Experimental and numerical study on circular tunnels under seismic loading. *Eur J Environ Civil Eng 19(5):539–563. doi:10.1080/19648189.2014.893211*

Lanzano G, Bilotta E, Russo G, Silvestri F, Madabhushi SPG (2012) Centrifuge modelling of seismic loading on tunnels in sand. *Geotech Test J 35(6):854–869. doi:10.1520/GTJ104348*

Madabhushi S.P.G. (2014). Centrifuge Modelling for Civil Engineers. *CRC Press, Taylor and Francis*

Madabhushi, SPG and Schofield AN and Lesley S (1998).A new Stored Angular Momentum (SAM) based earthquake actuator. *In: The International Conference Centrifuge 98, 1998-9- to -- pp. 111-116*

Park D, Hashash YMA (2004) Soil damping formulation in nonlinear time domain site response analysis. *J Signal Eng 8:49–274*

Pitilakis, K., Kirtas, E., Sextos, A., Bolton, M.D., Madabhushi, S.P.G. and Brennan, A.J. (2004). Validation by centrifuge testing of numerical simulations for soil- foundation-structure systems. *Proc. 13th World Conf. on Earthquake Engineering, Vancouver, B.C., Canada. Paper no. 2772.*

Rollins, K.M., Evans, M.D., Diehl, N B. and Daily, W.D. (1998). Shear modulus and damping relationships for gravels. *Journal of Geotechnical and Geoenvironmental Engineering, ASCE. 124(5): 396-405*

Santos JA, Correia AG. (2001). Reference threshold shear strain of soil. Its application to obtain an unique strain-dependent shear modulus curve for soil. *In: 15th International conference SMGE, vol 1, Istanbul: Balkema, pp 267–270*

Schanz T, Vermeer PA, Bonnier PG (1999) The hardening soil model: formulation and verification. *In: Brinkgreve RBJ (ed) Beyond 2000 in computation geotechnics. Balkema, Rotterdam, pp 281–290*

Schofield, A. N. (1980). Cambridge geotechnical centrifuge operations, *30 (3), Géotechnique, pp.227–268*

Scott, R.F., (1994). Review of Progress in Dynamic Geotechnical Centrifuge Research. *In: R.J. Ebleher, V.P. Drnevich, and B.L. Kutter, eds. Dynamic Geotechnical Testing II, ASTM STP 1213. San Francisco: ASTM*

Seed, H.B., Wong, R.T., Idriss, I.M. and To kimatsu, K. (1986). Moduli and damping factors for dynamic analyses of cohesionless soils. *Journal of Geotechnical Engineering, ASCE. 112(11): 1016-1032.*

Taylor, R. N. (1995): Geotechnical Centrifuge Technology. *Chapman and Hall, London*

Teymur, B. and Madabhushi, S.P.G. (2002). Shear stress-strain analysis of sand in ESB model container by harmonic wavelet techniques. *Proc. Int. Conf. on Physical Modelling in Geotechnics (ed. R. Phillips, P.J. Guo and R. Popescu), St Johns, NF, Canada. A.A. Balkema publishers. p. 201-206.*

Vucetic, M. and Dobry, R. (1991). Effect of soil plasticity on cyclic response. *Journal of Geotechnical Engineering, ASCE.117(1): 89-107.*

Wilson, J.M.R. (1988). A theoretical and experimental investigation into the dynamic behaviour of soils. *PhD thesis, University of Cambridge, UK.*

Zeghal M, Elgamal A (1994). Analysis of site liquefaction using earthquake records. *J Geotech Eng. doi:10.1061/(ASCE)0733-9410(1994*

Zeghal, M., Elgamel, A.W., Tang, H.T. and Stepp, J.C. (1995). Lotung Downhole Array. II: evaluation of soil nonlinear properties. *Journal of Geotechnical Engineering, ASCE. 121(4): 363-378.*

CHAPTER 3

DYNAMIC AND STATIC PERFORMANCE OF SOFT BARRIERS

3. Introduction

This chapter gives an insight on the static and dynamic performance of soft buried barriers made of a mixture of soil and a Super Absorbing Polymer (SAP) to be used for the mitigation of seismic risk. Centrifuge tests on reduced scale models showed their effectiveness in reducing the ground shaking at surface within an isolated mass of soil. Starting from the back-analysis of the results of the free-field centrifuge tests, a series of numerical analyses have been carried out. A series of different input signals were applied to the base of the numerical model. Each signal was extracted from databases of recorded natural events and a wide range of frequency content, duration and shaking amplitude was covered. The response of a SDOF founded within the isolated ground mass was then observed and commented. Laboratory tests were carried out on sand-SAP mixtures at different relative percentages. The results have been interpreted with reference to the peculiar properties of the two materials (sand and SAP) at the grain scale.

3.2. Laboratory tests on sand – SAP mixtures

The basic idea is creating a barrier with a material with low dynamic impedance. Aiming at this a super absorbent polymer (SAP) was identified. This is a polymer can absorb and retain extremely large amounts of a liquid with respect to its own mass. The ability of the SAP

to absorb water is due to the ionic concentration of the aqueous solution. In deionised and distilled water, a SAP may absorb 500 times its weight and can become up to 99.9% liquid, but when put into a 0.9% saline solution, the absorbency drops to maybe 50 times its weight. The characteristics of the Super Absorbent Polymers depend on their chemical formulation. They can be successfully employed as softening grouts, thanks to their low shear stiffness, which is due to the extremely high water content that the polymers may absorb. A polyacrylic acid partial sodium salt was used and tested in laboratory, pure or mixed with sand in several percentages. The grain-size distributions of the adopted sand (specific gravity Gs= 2.83, uniformity coefficient Cu=1.8) and of dry SAP (dry specific gravity $G_{SAP,d}$=0.69, uniformity coefficient Cu=4) are reported in Figure 3.1.

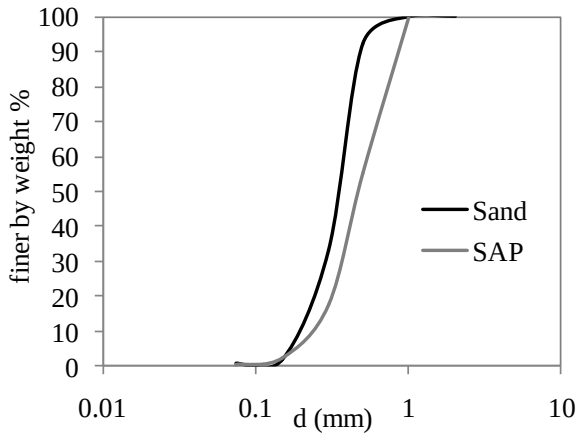

Figure 3.1 Grain size distributions of sand and SAP

Upon contact with water, SAP hydrated specific gravity becomes $G_{SAP,h}$=1.00, and the SAP grains largely increase their volume (Figure

3.2), assuming a gelatinous consistency: hence the single grains show a large distortional deformability and keep a constant volume, similarly to balloons filled with water.

Figure 3.2 SAP grains before and after hydration

Because of this deformability of the hydrated SAP grains, in the case of mixtures with a relevant amount of SAP any attempt to prepare specimens to be tested in the triaxial or torsional shear devices failed. Then, the characterization of sand-SAP mixtures (SGS) had to be based on simpler tests (oedometer tests, direct and ring shear tests, Table 3.1), where the specimens could be prepared under kinematically constrained horizontal conditions (Lombardi 2014). The void ratio reported in Table 3.1 has been calculate

$$e_0 = \frac{G_{SAP,h} \cdot G_s \cdot \gamma_w}{(1-\chi) \cdot G_{SAP,h} + \beta \cdot G_s} \cdot \frac{V}{W} - 1 \qquad 3.1$$

where V and W are respectively the volume and the weight of the specimen, and χ is the percentage of hydrated SAP by weight in the mixture.

Table 3.1 Summary of tests carried out on mixtures at different percentage of hydrated SAP

SAP-sand mixture (SGS)	% SAP by weight (χ)	e_0	Oedometer tests	Direct or ring shear tests	VS,SGS tests	VP,SGS tests
Sand	0	0.40 - 0.80	•	•	•	•
SGS_009	9	0.64	•	•		
SGS_023	23	0.49	•	•		
SGS_033	33	0.16	•	•	•	•
SGS_050	50	-		•	•	
SGS_070	70	-		•		•
SGS_090	90	-		•		
SGS_100	100	-			•	•

This definition is in this case arguable: since the hydrated SAP grains are gelatinous, they are not able to keep their original shape in a mixture and tend to accommodate to the shape of the available void volume, filling it completely. In other words, the interaction with the surrounding grains (either of SAP or sand) is such that, immediately around a single hydrated SAP grain, the local void ratio tends to zero. As a consequence,

the void ratio of a sand-SAP mixture traditionally calculated (3.1) is that pertaining to the sandy part, that is the one related to the voids surrounded by sand grains only. This is certainly the case for a low SAP content, where the mixture matrix is made of sand grains. In this configuration, the SAP grains may be considered as an additional void ratio having the peculiar characteristic of being able to change shape but not volume, like "undrained" voids. Once the SAP content increases and the hydrated SAP grains are the ones building up the governing network in the granular mixture (say for SAP percentage equal or higher than 50%), the void ratio calculated using eq. (3.1) tends to reduce to very low values, because the gelatinous grains leave no voids among them. In such a case, e_0 is close to zero. Because of this, e_0 is not reported in Table 3.1 for χ>0.33.

In Figure 3.3 a schematic view of three possible structures of the mixture are shown.

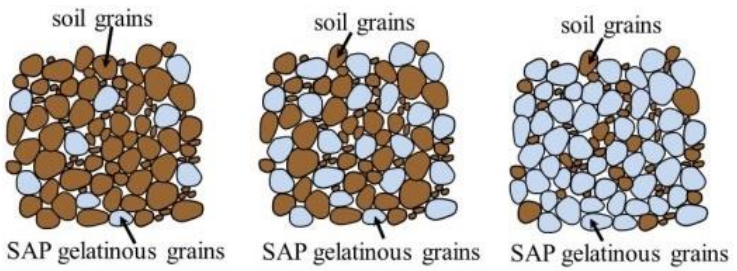

Figure 3.3 Sketches of SAP-soil mixtures with (a) low, (b) medium and (c) high percentage of SAP.

Figure 3.4 shows the measured value of the constant volume angle of shear resistance in direct and ring shear tests.

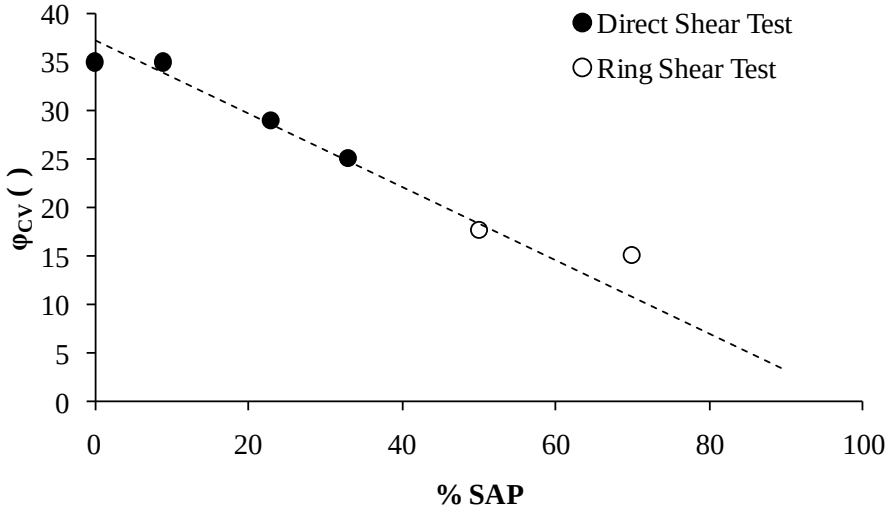

Figure 3.4 Friction angle at constant volume (φ'_{cv}) from shear tests on different SAP/sand mixtures.

Some direct shear tests were carried out (at a constant value of the vertical stress σv=50kPa) in order to give a first assessment of the shear strength of the SAP/sand mixtures. It can be observed that by increasing the SAP content, the shear strength of the mixtures decreases.

Figure 3.5 shows the values of shear and compression wave velocity, V_S and V_P, A series of tests in a large triaxial cell has been made with the aim to measure, in a large specimen, the shear wave velocity (Vs) of the treated soil and, consequently, its shear modulus at small strain levels G_0. The values of the shear waves velocity Vs measured in the triaxial cell are reported in Figure 3.5: as expected, Vs significantly decreases by increasing the SAP percentages. The compression waves velocity

(V_P) of the SAP/sand mixture was measured by means of a non-conventional apparatus. Ultrasonic generators and receiver constitute the instrument used for this purpose. The measured values of V_P are plotted in Figure 3.5 along with the values of Vs previously found. Figure 3.6 shows the values of the Poisson's ratio, ν, corresponding to the measured values of shear and compression wave velocity, V_S and V_P calculated as:

$$\nu = \frac{V_P^2 - 2V_S^2}{2(V_P^2 - V_S^2)} \qquad 3.2$$

It is clear that for low percentage of SAP (30%), the behaviour of sample is close to that of the sand. By increasing the percentage of SAP, the shear wave velocity decreases while the compression wave velocity increases. For a sample made by only SAP, V_P is much higher than Vs and the behaviour of the material is close to that of the water. Such an aspect is furthermore highlighted from the values of Poisson' ratio ν found for the mixtures. Figure 3.6 shows that the values of ν for high percentage of SAP tend to 0.5, and the mixture become incompressible. Interestingly, by increasing the percentage of SAP in the mixture the shear wave velocity (and thus the shear stiffness) keeps reducing, while the compression wave velocity (and thus the oedometric stiffness) after a first reduction tends to increase. The corresponding variation of the Poisson coefficient indicates that, as the SAP content increases, the mixture tends to behave as a material having very high bulk stiffness

(useful to reduce static settlements) and very low shear stiffness (useful for seismic isolation).

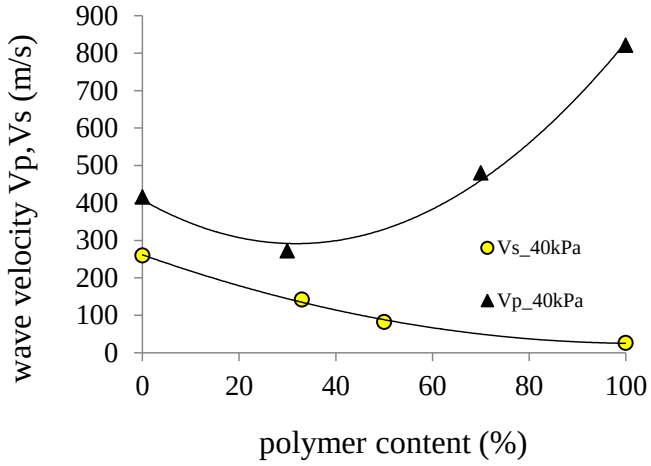

Figure 3.5 Values of shear and compression waves velocity (Vs and VP) of SAP/sand specimens measured at a confining pressure p'=40kPa.

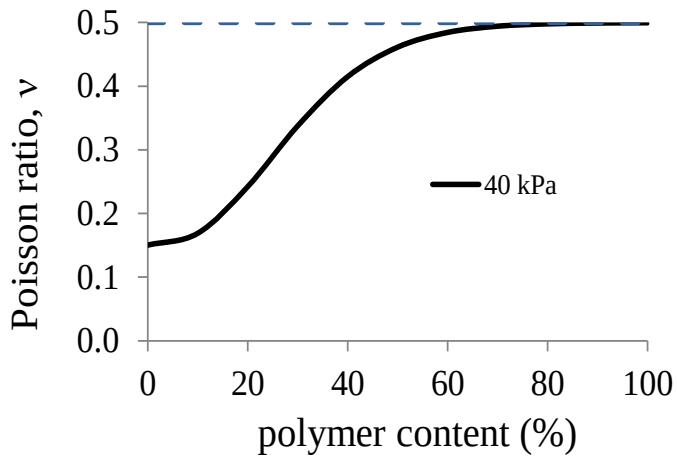

Figure 3.6 Poisson ratio ν for SAP/sand mixtures

In a way, the material behaviour tends to resemble that of water, and is consistent with the physical characteristics of the single hydrated grains, that may be seen as little balloons filled of water.

3.3. Numerical analyses

Numerical simulations were performed by the FE code Plaxis2D (Brinkgreve et al., 2007) (section §2.10.1). The numerical model was calibrated using the results of centrifuge testing on a reduced scale model. Two geometrical schemes (rectangular barrier and V barrier) were analysed with different SAP-sand mixtures (Table 3.2). Some analyses were carried out using the same material for both sides and base of the caisson and others analyses with two different materials, one for the sides and one for the base of the rectangular caisson.

The values adopted for the mechanical properties of the soft layers fall within the range of results of the experimental campaign carried out in laboratory on mixtures of sand with granular hydrophilic polymers (Super Absorbing Polymer, SAP) (section §3.2) that may be used to create soft layers. It is worth noticing that the Super Absorbing Polymer (SAP) is able to reduce the shear stiffness of the treated soil to the very low values needed to have an effective seismic isolation. This is possible because of the ability of the hydrophilic polymer to absorb enormous amounts of water, thus creating a network of gelatinous grains into the grouted soil. In a way, the material behaviour tends to resemble that of water, and is consistent with the physical characteristics of the single hydrated grains, that may be seen as little balloons filled of water.

Looking for possible, future applications, the percentage of polymer in the grouted layers of the soft barrier must be tuned, depending on the specific case. Generally speaking, it should be high enough to achieve the desired reduction of shear stiffness and strength, but not too high, to avoid excessive bulk stiffness that may reduce the effectiveness of the soft barrier, as it will be shown in the parametric analyses. The soft barrier was modelled as an elastic-perfectly plastic Mohr-Coulomb material.

Table 3.2 Parameters adopted for the mixtures

Mixtures				
Sides	Base	φ (°)	V_s (m/s)	ν
SAP100		1	25	0.499
SAP90		3	61	0.496
SAP80		7	92	0.485
SAP70		10	122	0.463
SAP70	SAP100	as the corresponding values above		
SAP60	SAP100			

The soil was characterized by a constitutive model implemented in the Plaxis code, Hardening Soil with small strain overlay that accounts for strain hardening plasticity and small-strain behaviour of soils (Schanz et al. 1999; Benz et al. 2009).

The model is also able to capture the hysteretic behaviour of sands and the associated hysteretic damping in unloading–reloading cycles. Both stiffness decay and hysteretic damping are crucial in the prediction of the stress–strain behaviour of soil under cycling loading. Two parameters are needed to describe stiffness from very small to medium strains: the initial modulus G_0 and the shear strain level $\gamma_{0.7}$ at which the

secant shear modulus is reduced to about 70 % of G_0. The model parameters for HN31 Hostun sand were extracted from literature (Benz 2007) and they are reported in Table 2.8.

3.4. Static analyses

The insertion of a soft barrier in the soil might induce large settlements hence being critical for the static of the building. Therefore static analyses were performed for all the schemes (V-barrier and rectangular barrier) considering a foundation with B=5m. The foundation is modelled as a plate element and the bearing capacity analyses were carried out in displacements control (i.e. incrementally increasing the vertical displacement of the foundation, than calculating the resultant reaction force of the loaded soil underneath it). As a result of the increment of the displacement the soft grout could squirted out and this determines the arrest of the analysis. For this reason, two conditions were examined in the static analyses, in the first one the soft barrier is allowed to move while in the second one a kinematics constraint is inserted in the vertical direction (Figure 3.7).

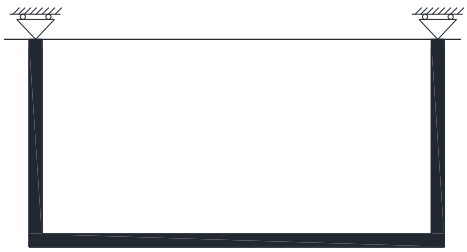

Figure 3.7 Kinematic constraints adopted in static analyses.

3.4.1. V-barrier

All the investigated schemes show a load-displacement curve comparable to that of the foundation without barrier up to a displacement of about 0.1 m and a load of about 2500 kN, with the exception of the scheme SAP100, for which the ultimate bearing capacity was reached for very low settlements, (Figure 3.8).

For displacements higher than 0.1 m, the loading curves depart from the SOIL one, showing much lower bearing capacities. As expected, the higher the SAP content the lower the bearing capacity. The presence of the kinematic constraints does not influence the response of the system obtaining comparable curves for the two static conditions.

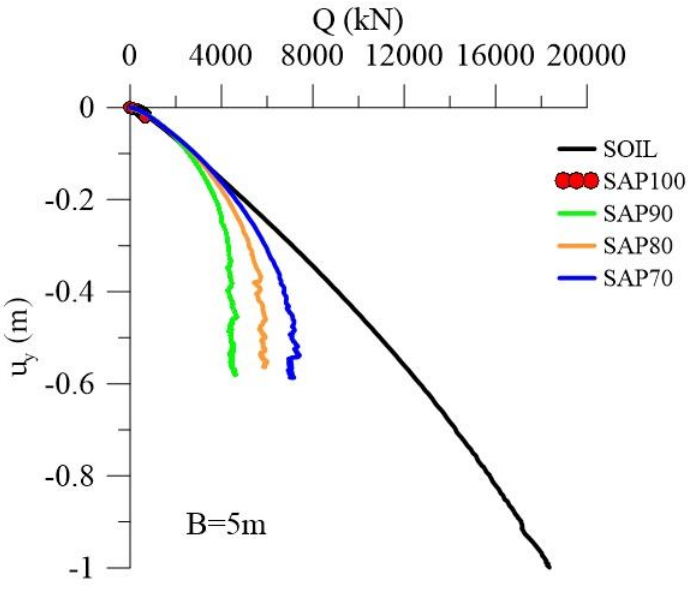

a)

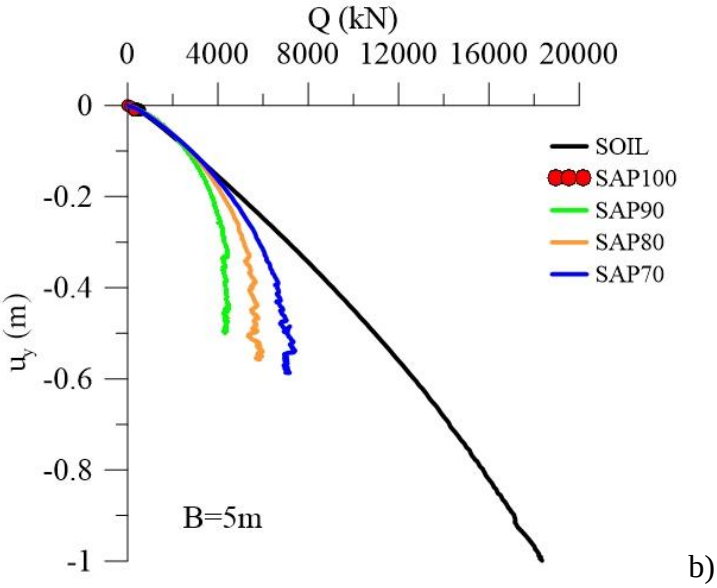

b)

Figure 3.8 Load displacement curves a) free barrier, b) barrier with kinematic constraints

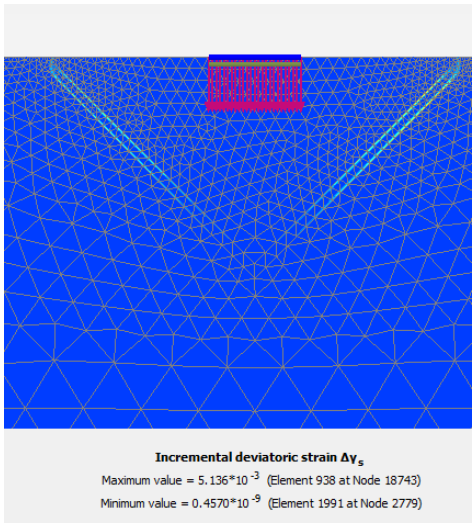

a)

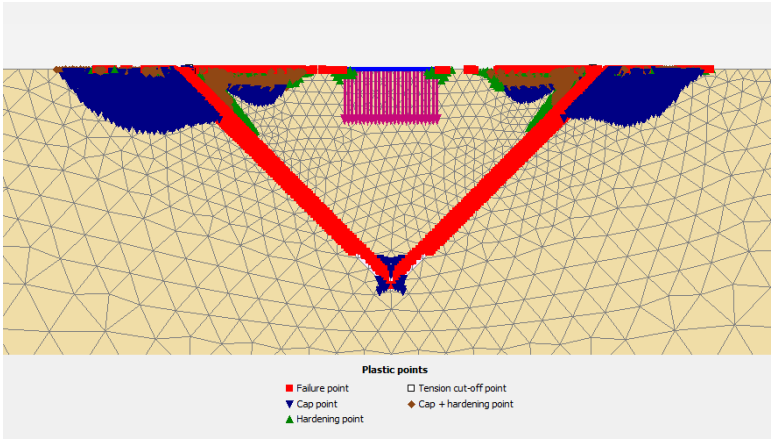

b)

Figure 3.9 a) Incremental deviatoric strains b) plastic points at last step of the analysis

The unacceptable behaviour of the SAP100 model is due to the very low shear strength of the material ($\varphi \approx 1°$), that soon triggers a failure mechanism along the soft barriers. A confirmation is given by Figure 3.9a, that shows shadings of the incremental deviatoric strains, whose maximum values are along the sides of the barrier, and also by Figure 3.9b, that shows the plastic points in the last step of the analysis in which the barrier was completely yielded. The reduction in terms of bearing capacity was of about 90% for SAP100 mixture, and 60% for SAP 70 mixture, as shown in Figure 3.10. A deeper insight on the acceptability of such a reduction will be given in Chapter 5.

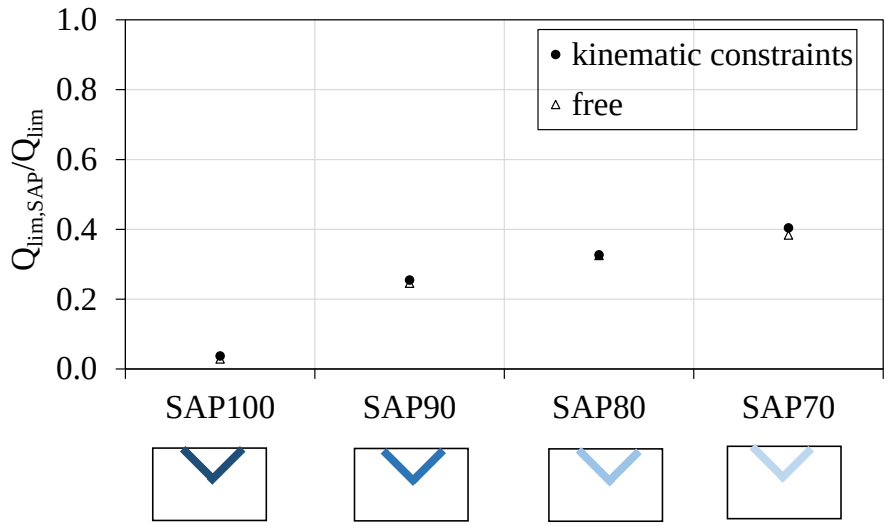

Figure 3.10 Ratio between ultimate bearing capacity with and without barrier for different mixtures analyzed

3.4.2. Rectangular barrier

As reported in Figure 3.11, the rectangular barrier has a better static behavior, if compared with the V shaped one. The reduction of the bearing capacity is of about 90% when the barrier is all made by SAP (SAP100) (Figure 3.12) and it is free to move (without kinematic constraints), while the other schemes show a minor reduction. The introduction of kinematic constraints entail an increment of the bearing capacity for all the barriers made by one material, while does not affect the behavior of the barriers made by two different materials for the base and for the sides (SAP60_100 and SAP7_100). Figure 3.12 shows the plastic points in the last step of the analysis (SAP100) in which the rectangular barrier was completely yielded.

The adoption of a rectangular barrier made by two different materials allows to not using any kind of constraints at the top of the barrier.

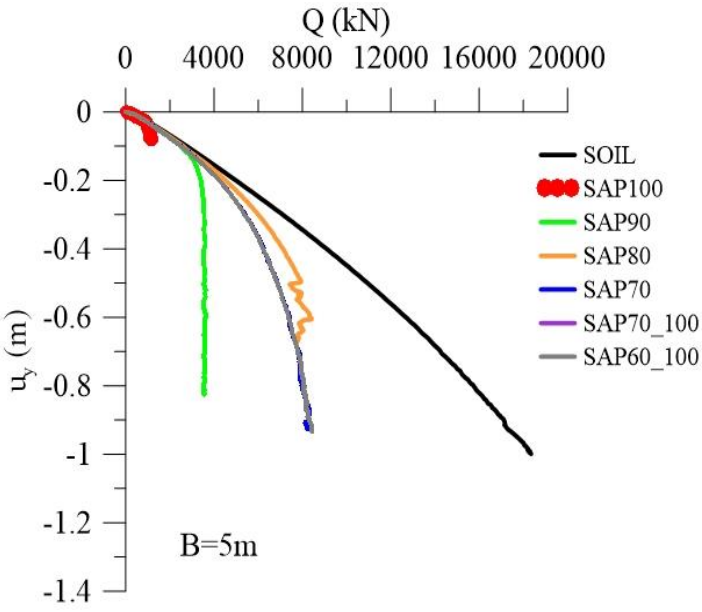

a)

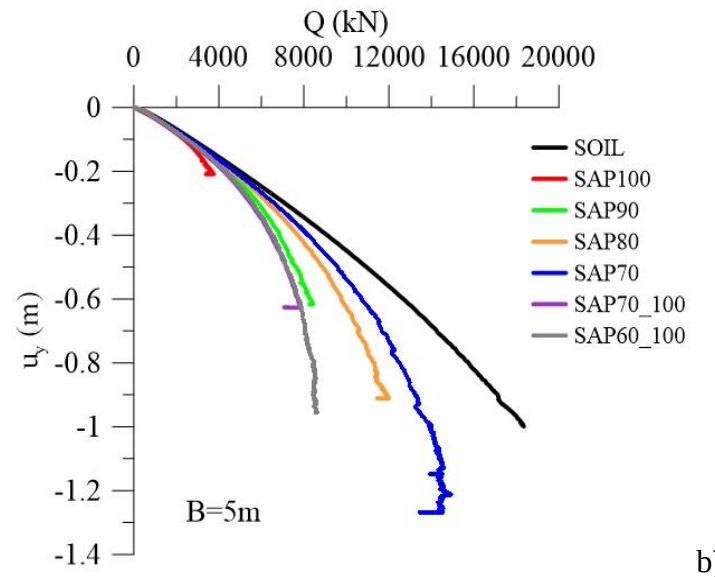

b)

Figure 3.11 Load settlements curves; a) free barrier, b) barrier with kinematic constraints

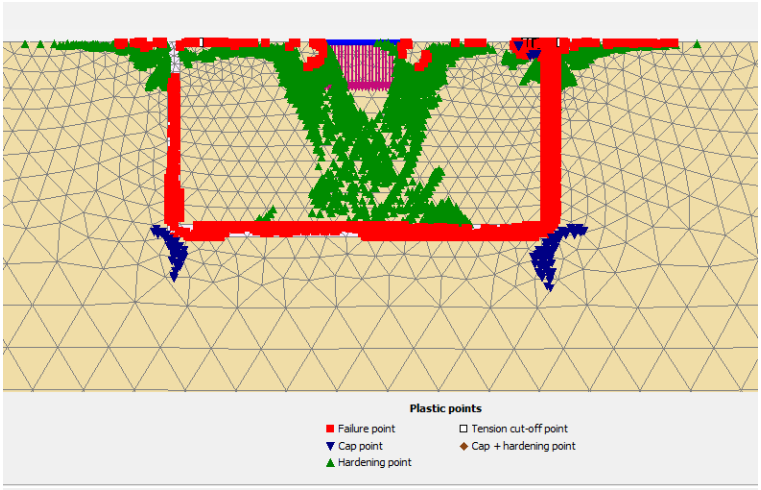

Figure 3.12 Plastic points in the last step of the analysis (SAP100)

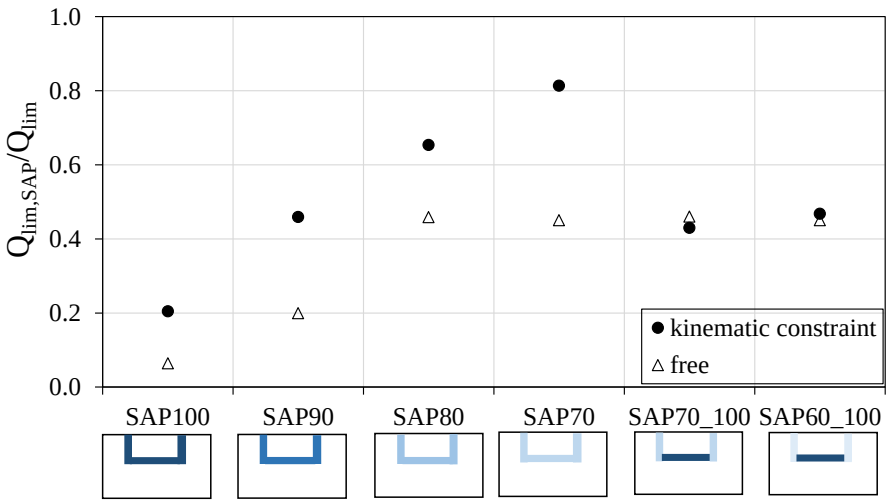

Figure 3.13 Ratio between ultimate bearing capacity with and without barrier for different mixtures analysed

3.5. Dynamic analyses

The mesh adopted in Plaxis2D was shown in *Figure 3.14*.

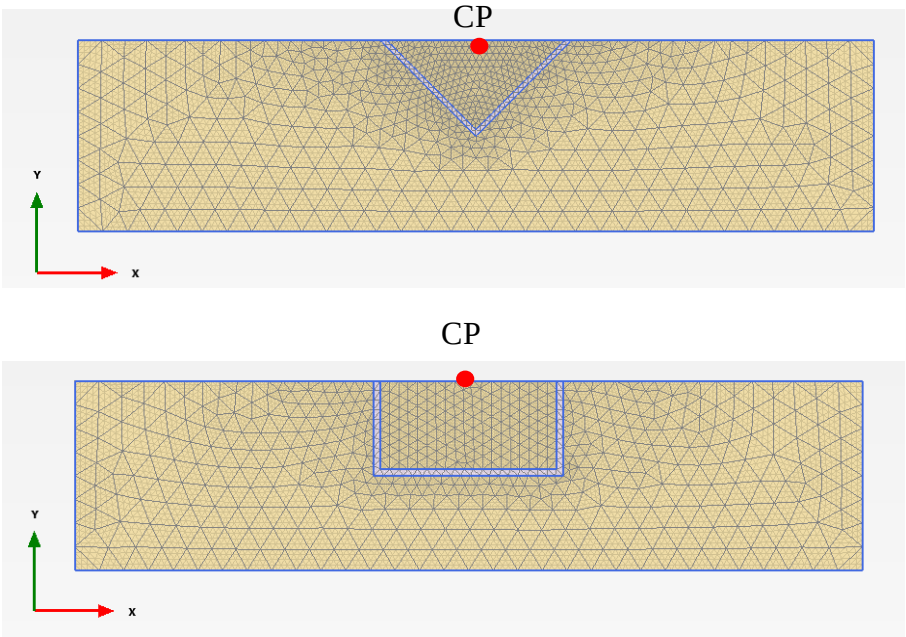

Figure 3.14 Numerical mesh a) V barrier b)rectangular barrier

The results were evaluated in correspondence of the control point CP shown in *Figure 3.14*, in terms of:

- *Ratio between the maximum acceleration in presence of the barrier ($a_{max,SAP}$) and in absence of the barrier (a_{max})*
- *Ratio between the average maximum acceleration in presence of the barrier ($\underline{a}_{max,SAP}$) and in absence of the barrier ($\underline{a}_{max}$)*
- *Ratio between the average Arias Intensity in presence of the barrier ($\underline{IA}_{SAP}$) and in absence of the barrier ($\underline{IA}$)*

Arias Intensity is an important measure of the strength of a ground motion, as it is able to simultaneously reflect multiple characteristics of the motion in question. Arias Intensity (Arias, 1970) describes the cumulative energy per unit weight absorbed by an infinite set of single-degree-of-freedom (SDOF) oscillators having fundamental frequencies uniformly distributed in (0, ∞). The most common representation of the Arias Intensity is recovered for the case of zero damping in the SDOF oscillators:

$$IA = \frac{\pi}{2g}\int_0^{\infty}\left[a(t)^2\right]dt \qquad 3.3$$

where IA is the Arias Intensity in units of length per time, a(t) is the acceleration-time history, and g is the acceleration of gravity.

- *Pseudospectral acceleration (PSA)*

The dynamic equation of motion is given by

$$m\ddot{u} + c\dot{u} + ku = -m\ddot{u}_g \qquad 3.4$$

where $u, \dot{u}, \ddot{u}$ represent the displacement, the velocity and the acceleration of the mass with respect to the base, respectively, c is a damping coefficient and $\ddot{u}_g$ is the input motion. The solution u(t) of a SDOF system subjected to an earthquake is given by Duhamel's integral and its maximum value is used to plot the relative displacement response spectrum. In general, the response spectrum is the locus of the maximum response of SDOF system characterized by different k and subjected to

the same earthquake, for a given damping ratio. The relative displacements response spectrum S_D is given by:

$$S_D = |u|_{\max} \qquad 3.5$$

The absolute pseudospectral acceleration PSA is related to the relative displacement response spectrum according to the following equation:

$$PSA = \omega_0^2 \cdot S_D \qquad 3.6$$

where ω_0 represents the angular frequency of the structure

$$\left(\omega_0 = \sqrt{k/m}\right) \qquad 3.7$$

3.5.1. Input signals

The time histories of acceleration used as base input motions at the bottom boundary of the FE mesh are obtained from different databases (all scaled to the same value of amplitude, that is 0.3g). Table 3.3reports the main characteristics of each record. It is worth noting that the input signals were chosen to cover the broadest possible range of frequency contents (approximately 0.5Hz to 10 Hz). In such a way, the potential beneficial or detrimental effects of the isolating barrier can be better investigated, and its limitations considered.

In Figure 3.15 are reported all input signals adopted in the analyses with the respective Fourier spectra.

Table 3.3 Time histories of acceleration used as input motions in FEA

Database	ID	Name	Date	PGA (m/s^2)	Arias Intensity (m/s)	Predominant period (s)	Predominant frequency (Hz)	Significant Duration (s)
ITACA	146	Campano Lucano	23/11/1980	3.17	1.35	0.2	5.0	38.5
	175	Lazio Abruzzo	07/05/1984	1.23	1.30	0.4	2.5	12
ESD	1635x	South Iceland	17/06/2000	1.53	0.87	0.24	4.2	4.5
	1635y	South Iceland	17/06/2000	1.29	0.73	0.16	6.3	5.8
	1885	Kalamata	13/10/1997	1.15	1.93	0.3	3.3	17.7
	2142x	South Iceland (aftershock)	21/06/2000	1.13	1.23	0.3	3.3	5.3
Japanese Kyoshin Network database	SZO002	Japan	1997	1.67	0.89	0.3	3.3	4.2
	EW83	Kobe	17/01/1995	3.02	1.35	0.08	12.5	15

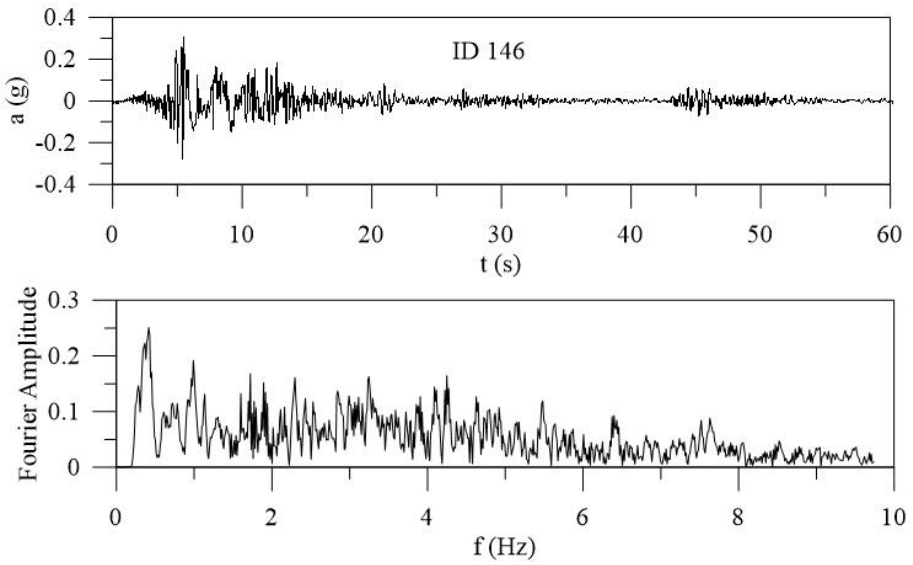

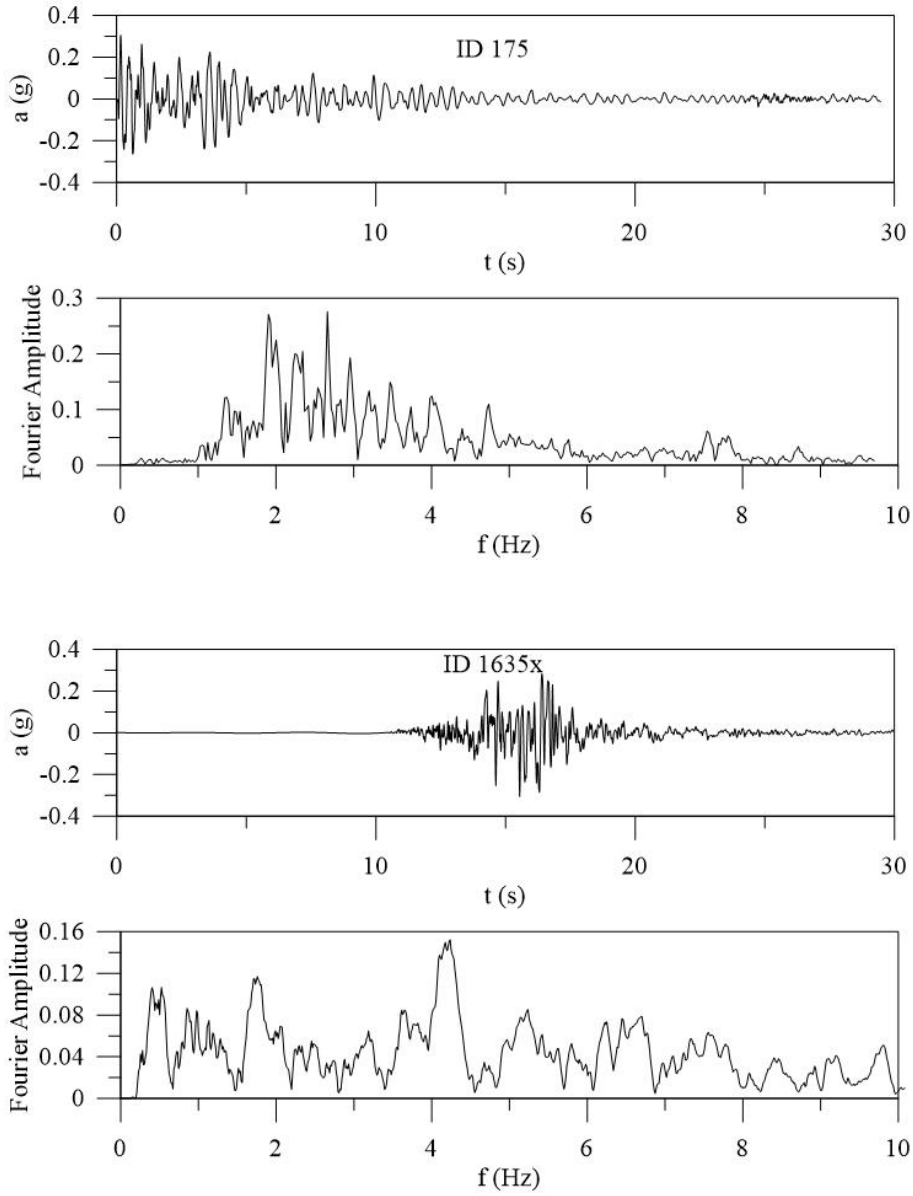
ID 175
a (g)
t (s)
Fourier Amplitude
f (Hz)
ID 1635x
a (g)
t (s)
Fourier Amplitude
f (Hz)

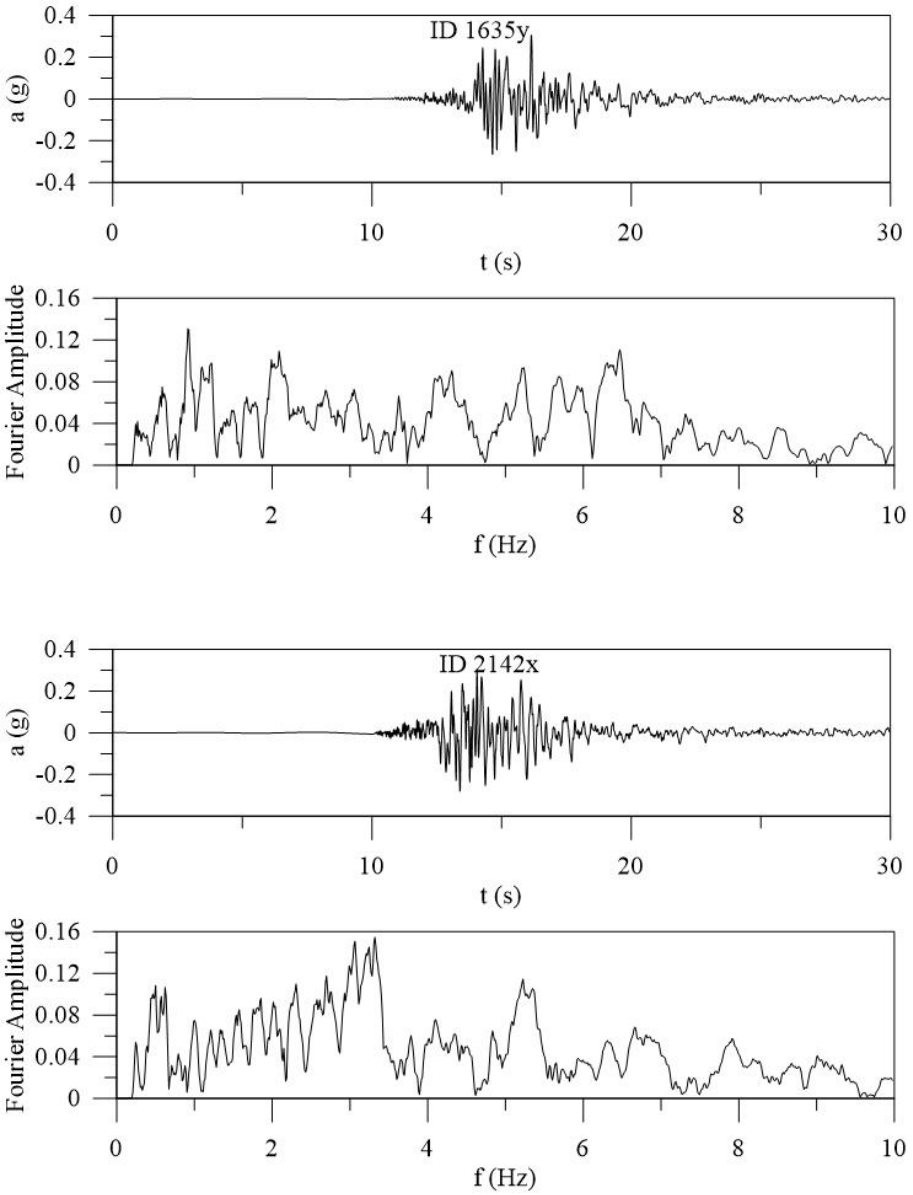
ID 1635y
a (g)
0.4
0.2
0
-0.2
-0.4
0
10
20
30
t (s)
Fourier Amplitude
0.16
0.12
0.08
0.04
0
0
2
4
6
8
10
f (Hz)
ID 2142x
a (g)
0.4
0.2
0
-0.2
-0.4
0
10
20
30
t (s)
Fourier Amplitude
0.16
0.12
0.08
0.04
0
0
2
4
6
8
10
f (Hz)

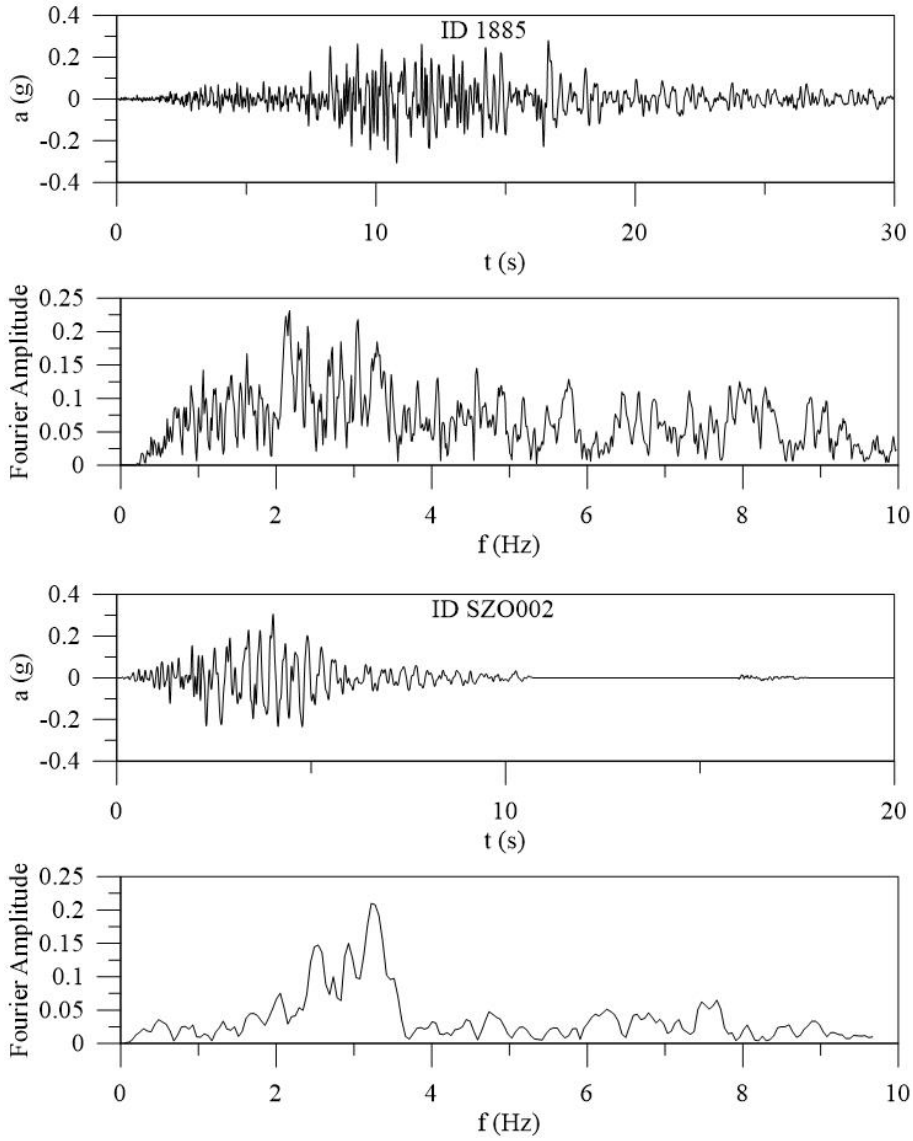
ID 1885
a (g)
t (s)
Fourier Amplitude
f (Hz)
ID SZO002
a (g)
t (s)
Fourier Amplitude
f (Hz)

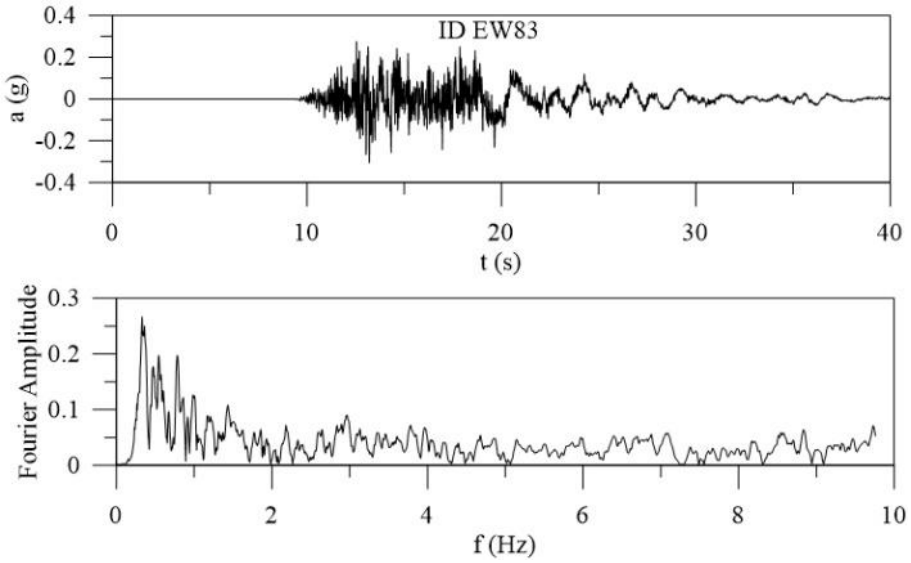

Figure 3.15 Input signals and respective Fourier spectra

3.5.2. Isolated soil mass

The insertion of a soft barrier completely modifies the motion of the protected soil mass. As long as the caisson is soft enough to prevent significant deformations within the isolated soil mass, it is reasonable to assume that such a mass (m) will undergo an almost rigid-body motion. Then, it can be considered as a SDOF system, whose stiffness k is mostly ruled by the soft barrier geometrical and mechanical properties. An approximate evaluation of k can be done with reference to the two schemes reported in Figure 3.16 with reference to a horizontal displacement, considering the contributions on the different sides of the compression stiffness (k_1) and of the shear stiffness of the soft layers (k_2).

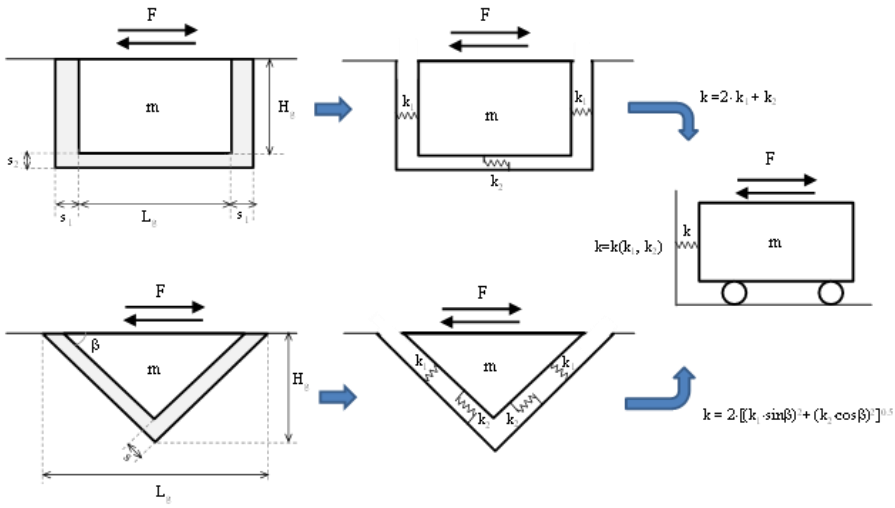

Figure 3.16 Mechanical analogy of the soft caisson with the isolated soil mass as an equivalent SDOF system under the action of cyclic horizontal forces.

Generally speaking, for a layer of length B_g and thickness S the two stiffness parameters k_1 and k_2 are:

$$k_1 = \frac{E_g \cdot B_g}{S} \qquad \textit{compression stiffness} \qquad 3.8$$

$$k_2 = \frac{G_g \cdot B_g}{S} \qquad \textit{tangent stiffness} \qquad 3.9$$

in which G_g is the shear stiffness of the considered soft grouted layer and E_g is the relevant compressive stiffness, that may be the oedometer one if the ratio B_g/S is high and confinement is provided, or the Young modulus in all other cases. With reference to a horizontal shaking action, the equivalent spring stiffness k of the two caissons shown in Figure 3.16 can be computed using eqs. (3.8 and 3.9): for the rectangular

caisson, k is the sum of the compression stiffness k_1 of the soft vertical layers and of the shear stiffness k_2 of the soft base layer, while for the V-shaped caisson it is a simple trigonometric combination of the two. Then:

- rectangular barrier

$$k = 2 \cdot k_{1,side} + k_{2,base} \qquad 3.10$$

- V-shaped barrier

$$k = 2 \cdot \left[k_{1,side}^2 \cdot (\sin\beta)^2 + k_{2,side}^2 \cdot (\cos\beta)^2 \right]^{0.5} \qquad 3.11$$

Then, using eqs. (3.8 and 3.9) into eqs. (3.10 and 3.11) the formulations of k become:

- rectangular barrier

$$k = \frac{2 \cdot E_g \cdot H_g}{S_1} + \frac{G_g \cdot L_g}{S_2} \qquad 3.12$$

- V-shaped barrier

$$k = 2 \cdot \left[\left(\frac{E_g \cdot H_g}{S \cdot \sin\beta} \right)^2 \cdot (\sin\beta)^2 + \left(\frac{G_g \cdot L_g}{2 \cdot S \cdot \cos\beta} \right)^2 \cdot (\cos\beta)^2 \right]^{0.5} = 2 \cdot \left[\left(\frac{E_g \cdot H_g}{S} \right)^2 + \left(\frac{G_g \cdot L_g}{2 \cdot S} \right)^2 \right]^{0.5} \qquad 3.13$$

where H_g and L_g are the depth and width of the caisson, S_1 and S_2 the thicknesses of the lateral and base sides of the rectangular caisson, S the thickness of the sides of the V-shaped caisson and β their inclination on the horizontal (Figure 3.16).

The first natural frequency of a SDOF system depends on the mass m and on the stiffness k as follows:

$$f = \frac{1}{2\pi}\left(\frac{k}{m}\right)^{0.5} \qquad 3.14$$

In the two cases of Figure 3.16 ($m=\rho \cdot H_g \cdot L_g$ for the rectangular caisson, and $m=\rho \cdot H_g \cdot L_g/2$ for the V-shaped one, ρ being the soil density), using eqs. (3.12 and 3.13) eq. 3.14 becomes after trivial passages:

- Rectangular barrier

$$f_{IM} = \frac{1}{2\pi}\left[\frac{1}{\rho}\cdot\left(\frac{2\cdot E_g}{S_1 \cdot L_g} + \frac{G_g}{S_2 \cdot H_g}\right)\right]^{0.5} \qquad 3.15$$

- V barrier

$$f_{IM} = \frac{1}{2\pi}\left\{\frac{4}{\rho^2}\left[\left(\frac{2\cdot E_g}{S \cdot L_g}\right)^2 + \left(\frac{G_g}{S \cdot H_g}\right)^2\right]\right\}^{0.25} \qquad 3.16$$

Even though Eqs. (3.15 and 3.16) are simplified, they highlight the role of some of the involved variables and allow to understand what the expected effect of the creation of the caisson should be. Generally speaking, to have a good isolating effect the natural frequency of the isolated mass of soil must be as low as possible. Thus, eqs. (3.15 and 3.16) say that it is convenient to use grouted layers as soft as possible, as deep as possible and as thick as possible. The latter convenience has a limit due to the need to reduce the static settlements generated by the

creation of the caisson. The real behaviour of the caisson is more complex than shown by eqs. (3.15 and 3.16), mostly because the surrounding soil is not infinitely stiff, hence the stiffness k of the equivalent spring of the isolated mass must depend on it too, likely being lower than the value obtained using eqs. (3.15 and 3.16). The numerical analyses shown in the following have the goal to get an insight into the problem. The frequency f_{IM} of the isolated soil mass calculated through Eq. 3.15 and 3.16 will be used to present the results of these analyses in a more general form.

To check the goodness of the equations proposed, the frequency of the soil mass was also evaluated by means of the software PLAXIS2D, with reference to the schemes reported in Figure 3.17.

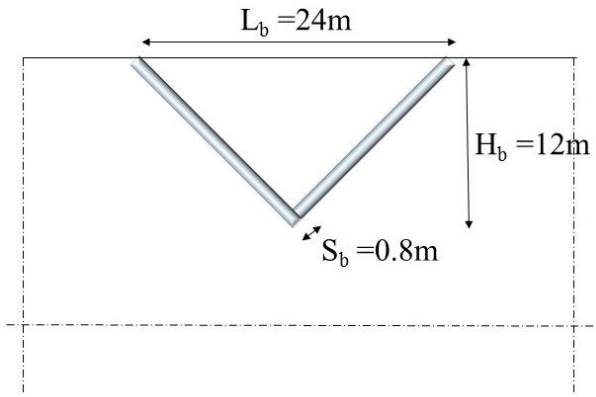

a)

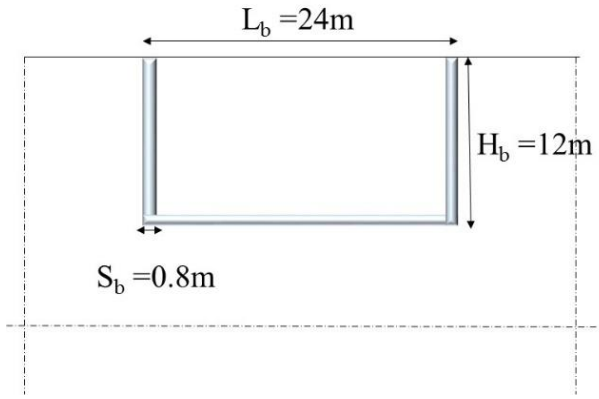

b)

Figure 3.17 Geometrical schemed adopted in Plaxis 2D, a) rectangular barrier b)V barrier

The adopted values of parameters are summarized in Table 3.4.

Table 3.4. Mohr-Coulomb parameters adopted for the soft barrier

ρ (kg/m^3)	G_0 (kN/m^2)	φ (-)	ν (°)	V_s (m/s)
1020	109	5	0.4	12

The frequency evaluated for the model reported in Figure 3.17a was equal to 1.4 Hz while the frequency calculated for the model in Figure 3.17b according to equation (3.16) was equal to 0.9 Hz. The frequency of the isolated masses was also evaluated by means of the software Plaxis2D. A free vibration analysis has been carried out to identify a natural frequency of vibration of the isolated mass. A plastic analysis thereby has been performed with a static force acting laterally at the top left corner of the isolated mass. The soil outside the isolated mass was assumed as rigid in order to avoid an influence on the frequency

evaluated. The next phase was chosen to carry out the free vibration analysis and the calculation for this phase has been allowed to take into account the displacements obtained from the previous phase.

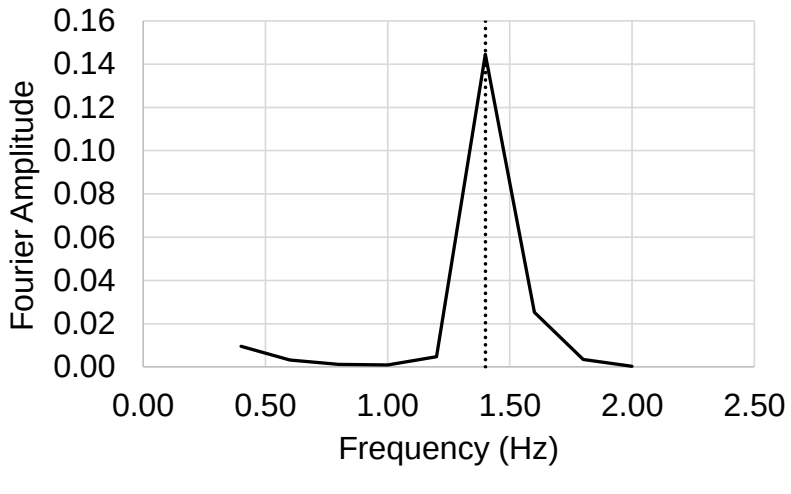

a)

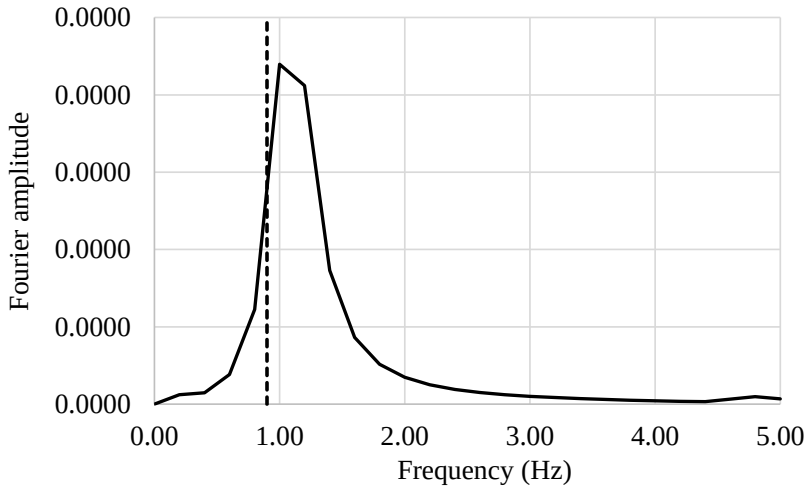

b)

Figure 3.18 Fourier spectra at the top of the isolated mass (the vertical dashed line indicate the frequency obtained by the equations (3.15) and (3.16); a) rectangular barrier b) V barrier

The time history of displacements is obtained at a point situated in correspondence to the static force. The corresponding Fourier transform (Figure 3.18a) clearly shows a peak at frequency 1.4 Hz, confirming the value obtained with expression (3.15) and a peak close to 0.9 for the V barrier (Figure 3.18b)confirming the goodness of the equations.

3.5.3. V-barrier: results of dynamic analyses

The results obtained for the model with V barrier calibrated on the basis of centrifuge test are summarized in the following figures.

Figure 3.19 shows the results in terms of ratio between the maximum acceleration calculated with and without rectangular caisson, for all the input signals considered and for the different mixtures analyzed.

It is evident from the figure that generally the V-barrier loses its efficacy with real signals (many ratios are higher than 1).

To have a complete evaluation of the behaviour of the system under several seismic inputs, the results were also analysed in terms of mean value of accelerations. Figure 3.20 shows synthetically the results in terms of ratio between the average maximum acceleration with and without the barrier obtained for the mixtures analysed. The efficacy of the barrier in terms of ratios is very low, being on average about 10%. Also looking at the results in terms of average Arias Intensity (Figure 3.21), the V barrier seems to be useless, since all values of the ratios IA_{SAP}/IA are equal to one.

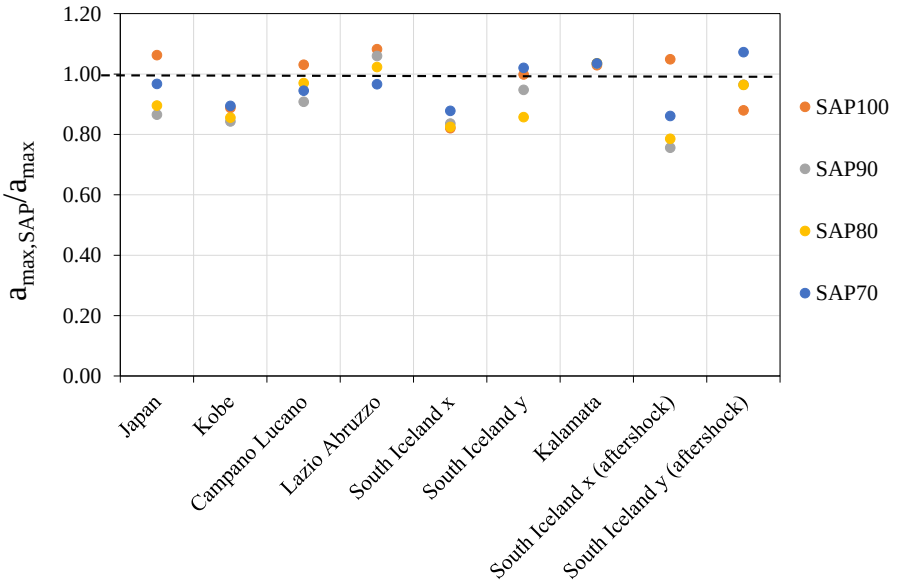

Figure 3.19 Ratio between the maximum acceleration calculated with and without rectangular caisson

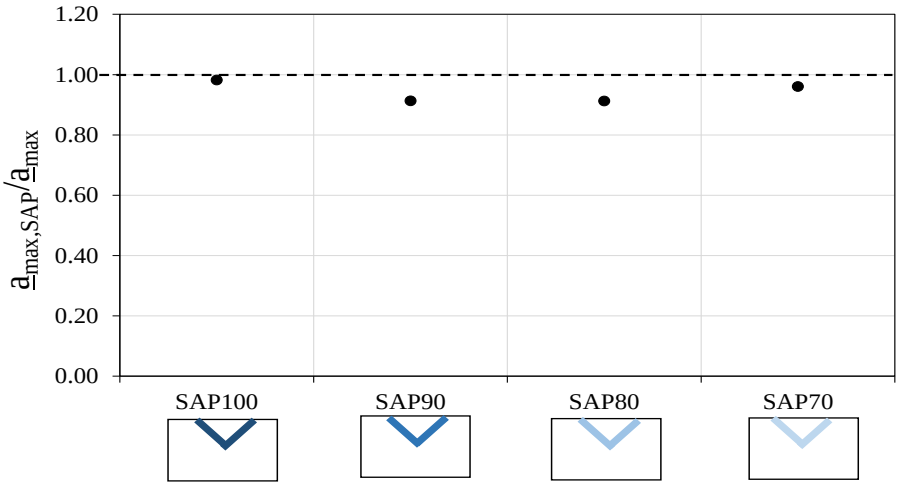

Figure 3.20 Ratio between mean values of acceleration with and without the barrier

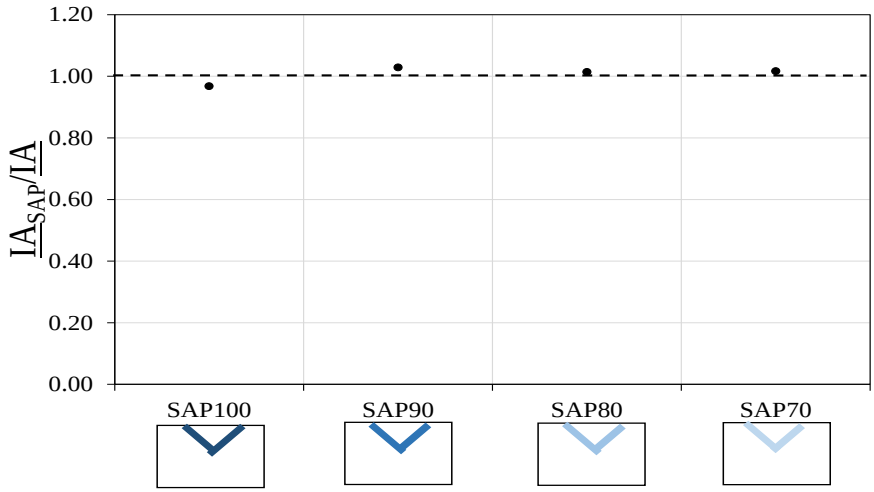

Figure 3.21 Ratio between mean values of Arias Intensity with and without the barrier

The pseudospectral acceleration (PSA) was calculated to give an information on the effect of the insertion of the barrier on a structure.

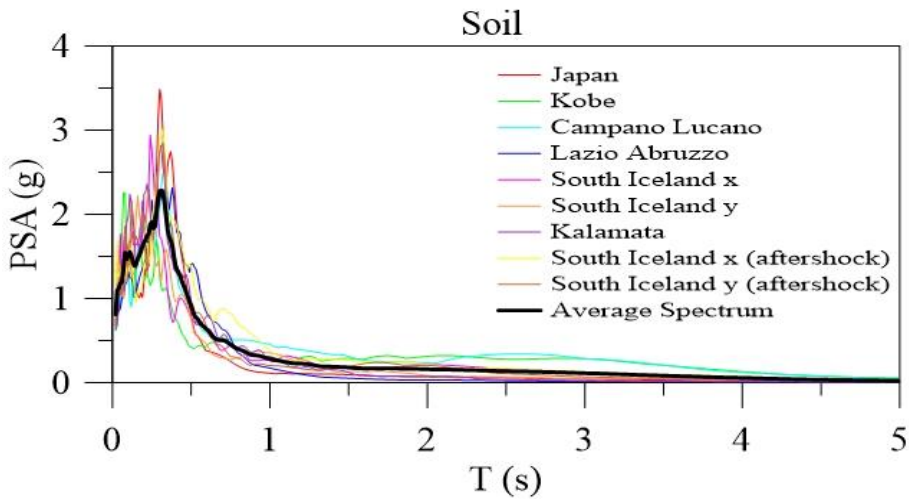

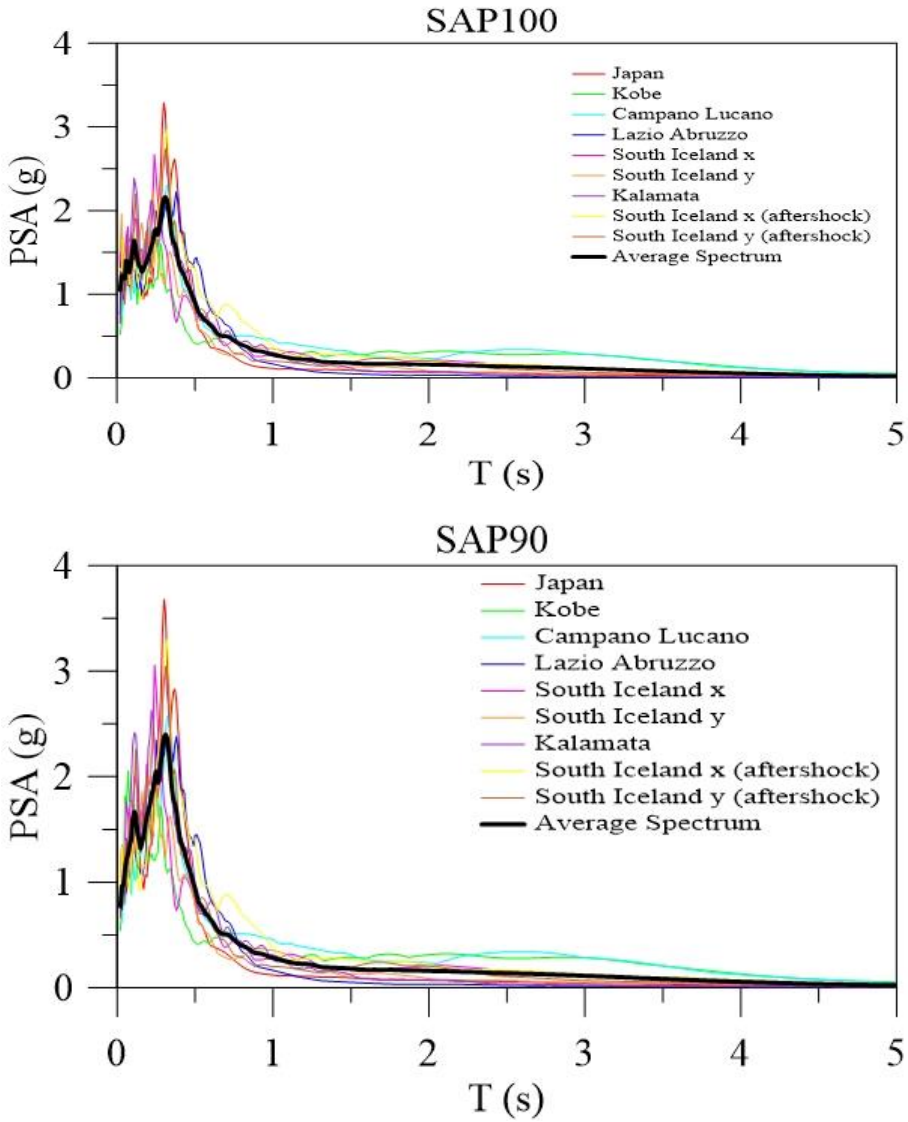
SAP100
PSA (g)
T (s)
Japan
Kobe
Campano Lucano
Lazio Abruzzo
South Iceland x
South Iceland y
Kalamata
South Iceland x (aftershock)
South Iceland y (aftershock)
Average Spectrum
SAP90
PSA (g)
T (s)
Japan
Kobe
Campano Lucano
Lazio Abruzzo
South Iceland x
South Iceland y
Kalamata
South Iceland x (aftershock)
South Iceland y (aftershock)
Average Spectrum

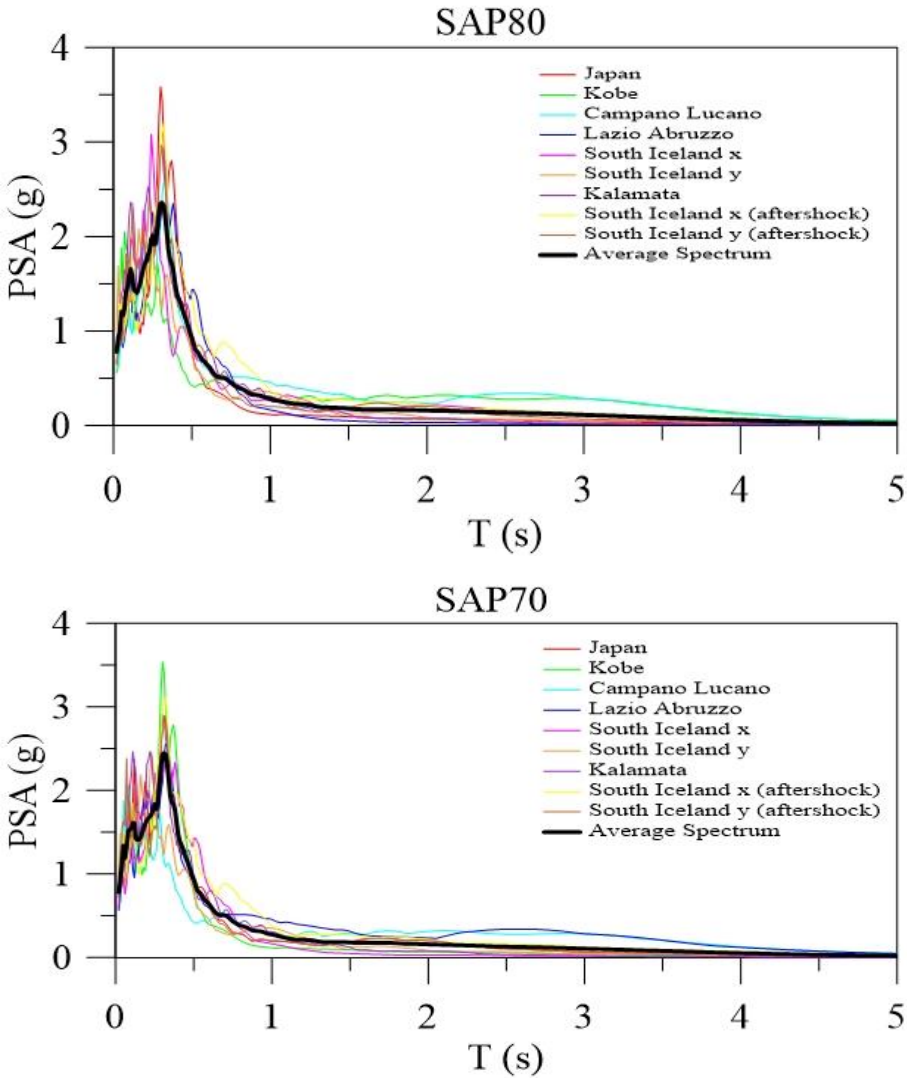

Figure 3.22 Pseudoacceleration spectra calculated for all the mixtures analyzed

Therefore, the PSA were determined for the nine signals and after an average spectrum was derived for the case without barrier and compared

with the average spectrum derived for the case with barrier (Figure 3.22).

The average spectrum (Figure 3.23) obtained in presence of the barrier was perfectly overlapped to that calculated in absence of barrier, confirming the inefficacy of the barrier.

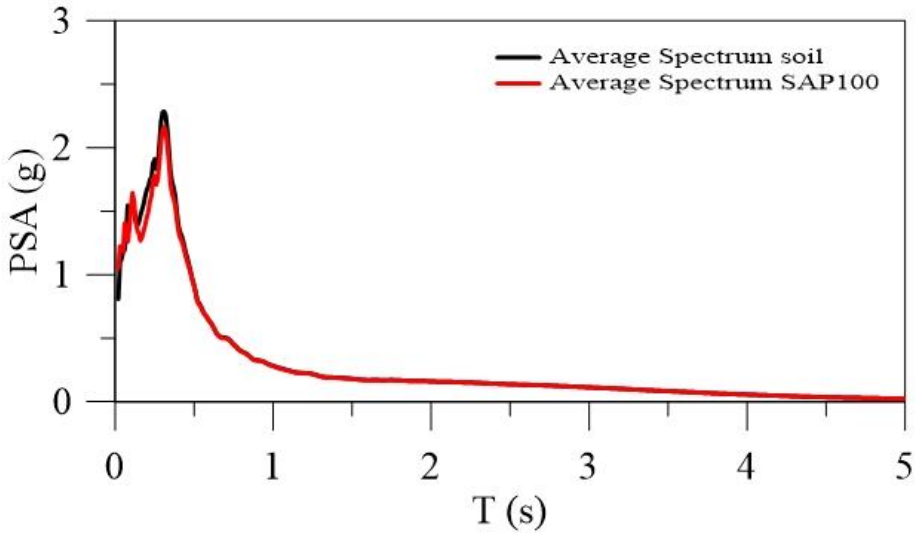

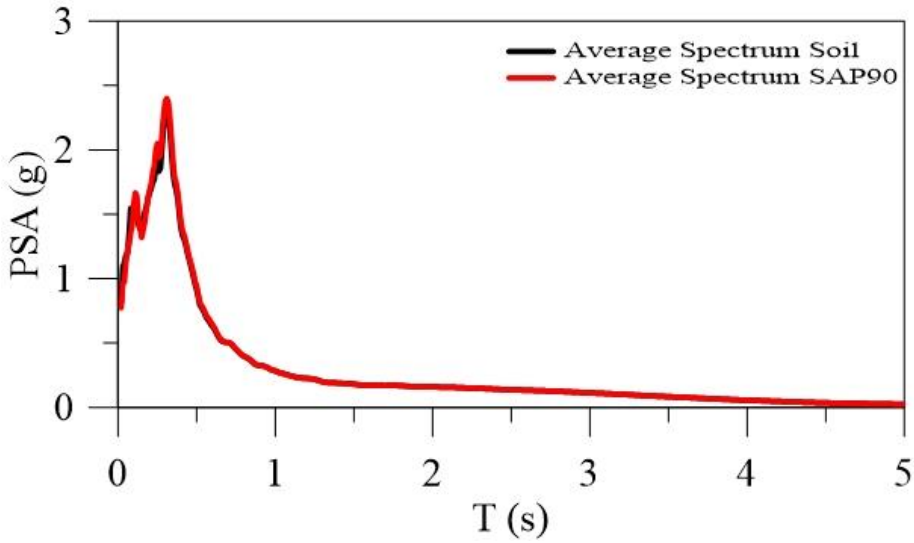

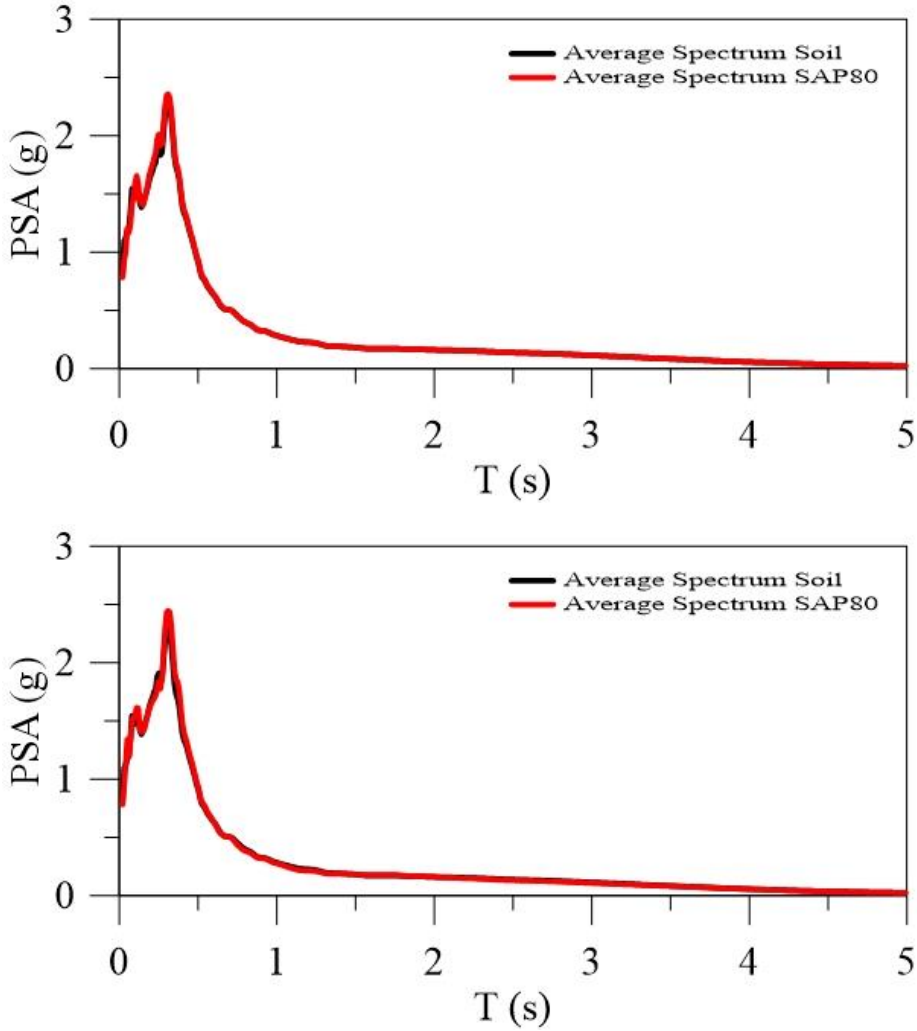

Figure 3.23 Average spectrum with and without the barrier compared for the different mixtures analyzed

3.5.4. Rectangular-barrier: results of dynamic analyses

Figure 3.24 shows the results in terms of ratio between the maximum acceleration calculated with and without rectangular barrier, for all the input signals considered and for the different mixtures analyzed.

The rectangular caisson is fore effective than the V-shaped one. It is evident from the plot that the maximum efficacy was obtained when the caisson was formed by SAP only (SAP100). The efficiency of the barrier decreases as the percentage in SAP decreases. With the SAP70 mixture the barrier became useless (all the ratios are greater than 1). Two more scheme were analyzed, in which the caisson was formed by two different mixture:

- SAP100 on the base
- SAP70 or SAP60 on the sides

These two last schemes seems to be effective in terms of ratio between the maximum acceleration with and without the caisson as shown in figure.

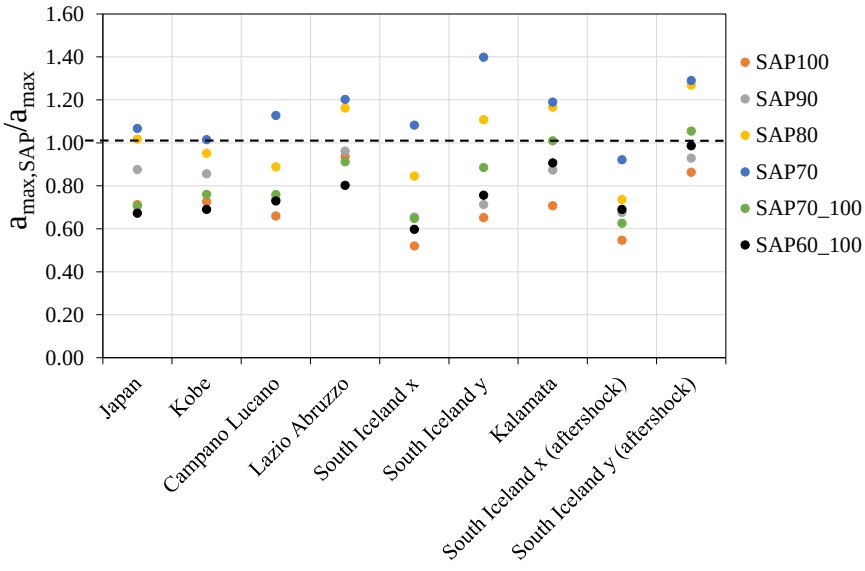

Figure 3.24 Ratio between the maximum acceleration calculated with and without rectangular barrier

To have a complete evaluation of the behaviour of the system under several seismic inputs, the results were also analysed in terms of mean value of accelerations.

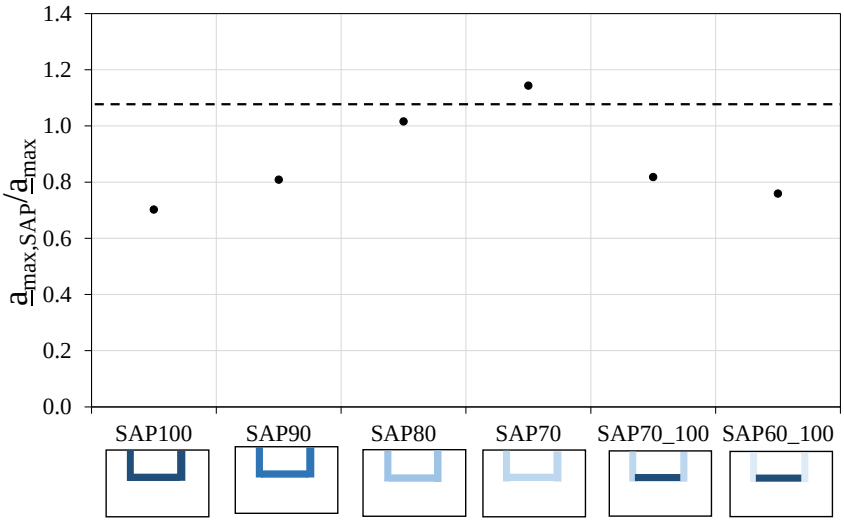

Figure 3.25 shows synthetically the results in terms of ratio between the average maximum acceleration with and without the barrier obtained for the mixtures analysed. It is clear the trend of the average values respect to the scheme examined. The efficacy the decreases as the percentage in SAP decreases. The reduction in terms of acceleration is of about 30% for the SAP100 mixture and for the schemes with two different materials.

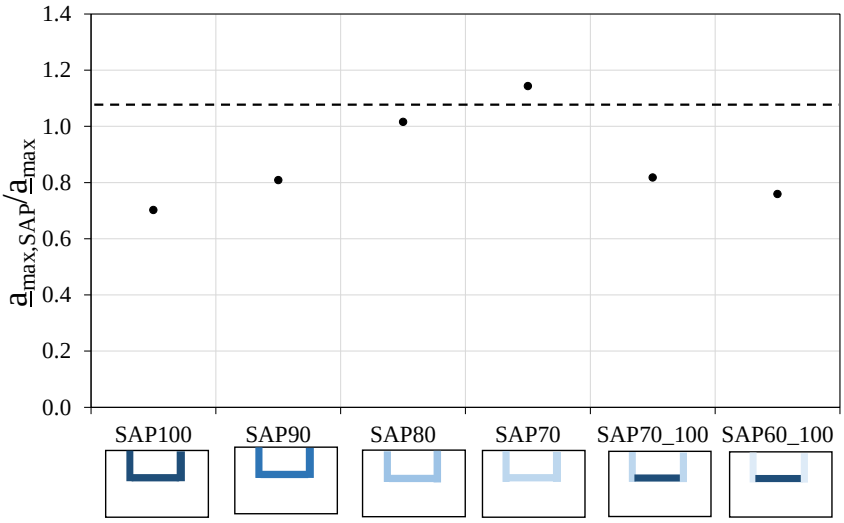

Figure 3.25 Ratio between mean values of acceleration with and without the barrier

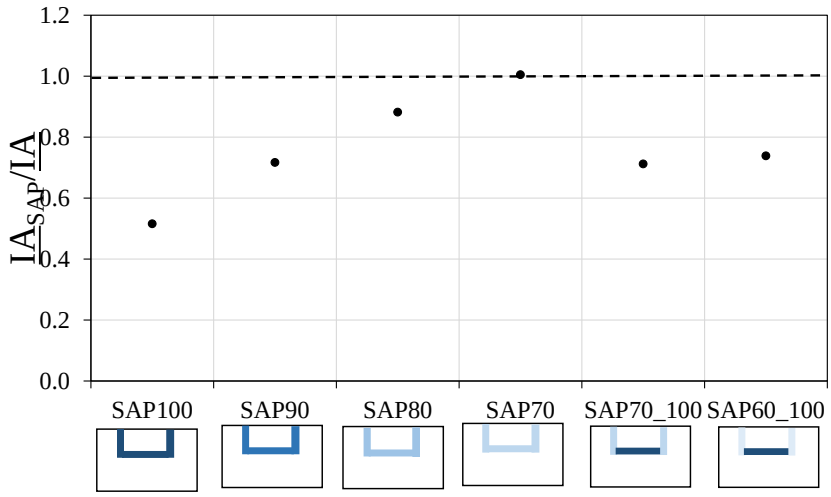

Figure 3.26 Ratio between mean values of Arias Intensity with and without the barrier

Looking now the results in terms of average Arias Intensity, the reduction obtained is of about 50% for the SAP100 mixture, while for

the schemes with two mixtures was obtained the same efficacy (30%) of SAP90 scheme (Figure 3.26).

The pseudospectral acceleration (PSA) was calculated to give an information of the effect of the insertion of the barrier on a structure.

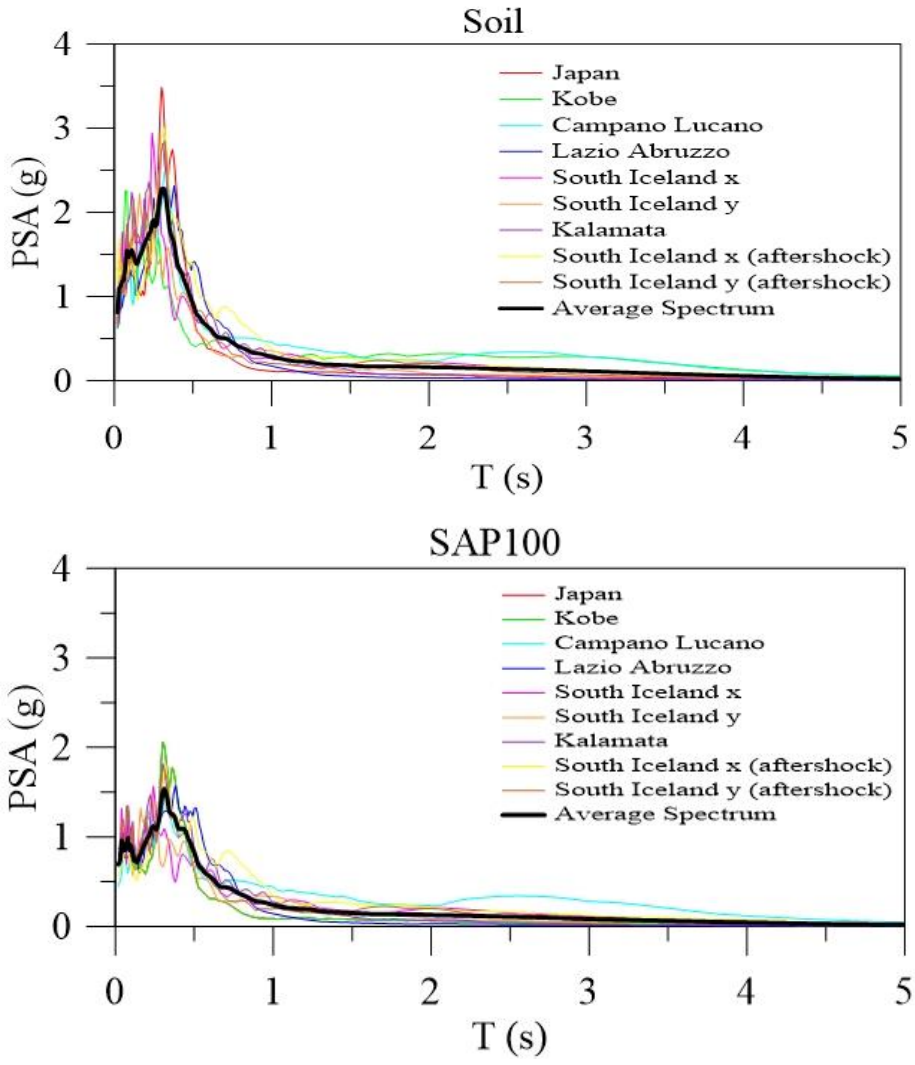

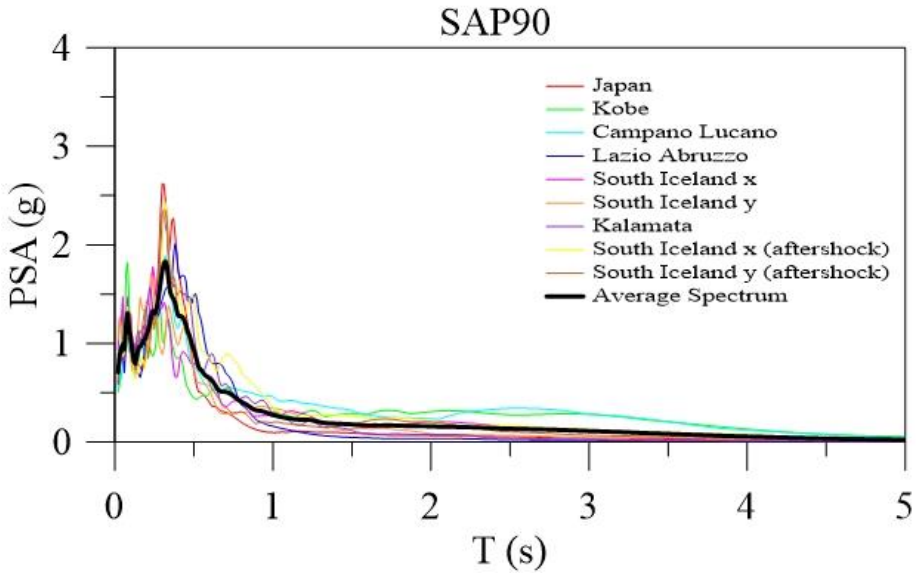
SAP90
PSA (g)
T (s)
Japan
Kobe
Campano Lucano
Lazio Abruzzo
South Iceland x
South Iceland y
Kalamata
South Iceland x (aftershock)
South Iceland y (aftershock)
Average Spectrum

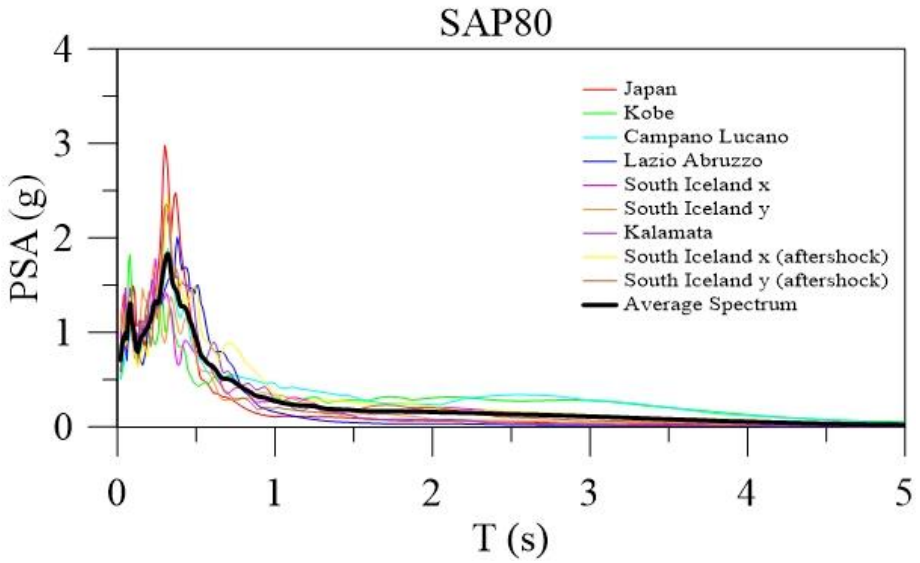
SAP80
PSA (g)
T (s)
Japan
Kobe
Campano Lucano
Lazio Abruzzo
South Iceland x
South Iceland y
Kalamata
South Iceland x (aftershock)
South Iceland y (aftershock)
Average Spectrum

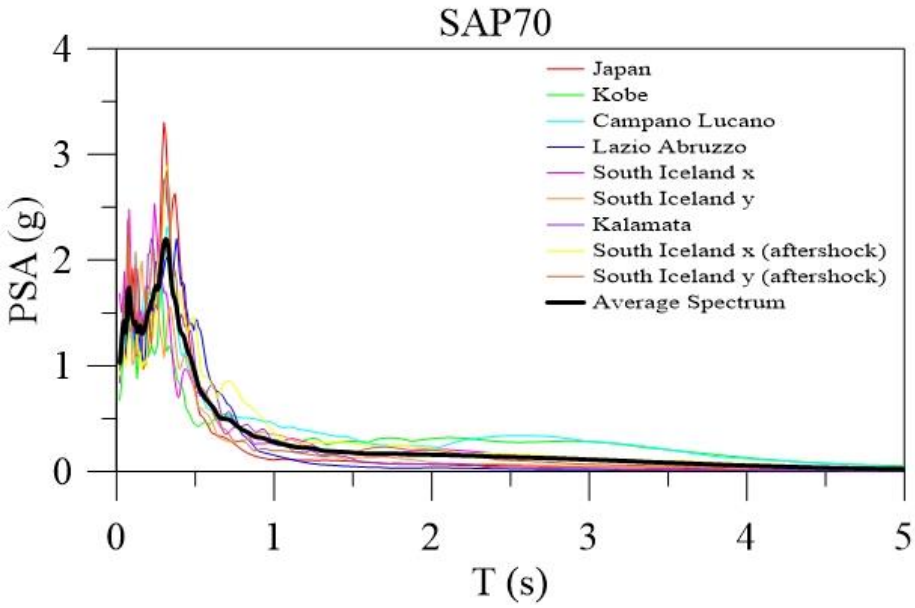
SAP70
PSA (g)
T (s)
Japan
Kobe
Campano Lucano
Lazio Abruzzo
South Iceland x
South Iceland y
Kalamata
South Iceland x (aftershock)
South Iceland y (aftershock)
Average Spectrum

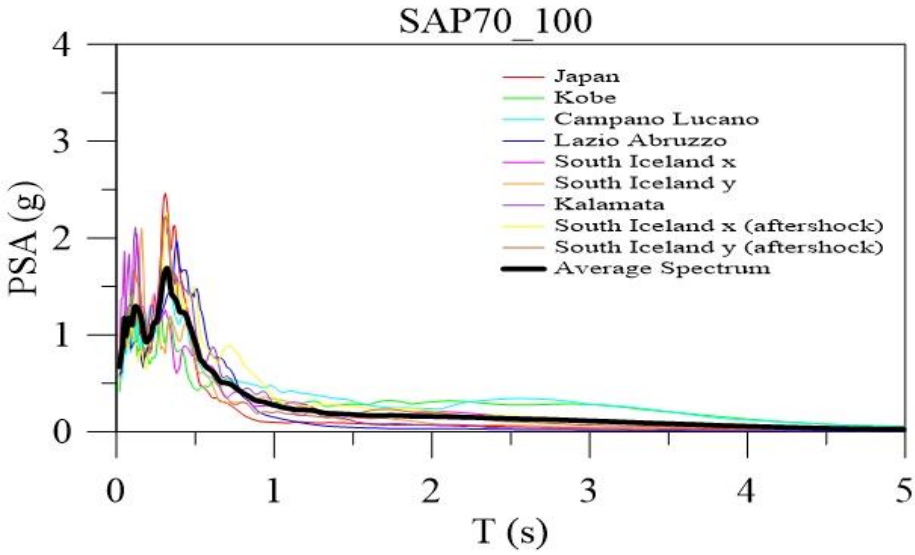
SAP70_100
PSA (g)
T (s)
Japan
Kobe
Campano Lucano
Lazio Abruzzo
South Iceland x
South Iceland y
Kalamata
South Iceland x (aftershock)
South Iceland y (aftershock)
Average Spectrum

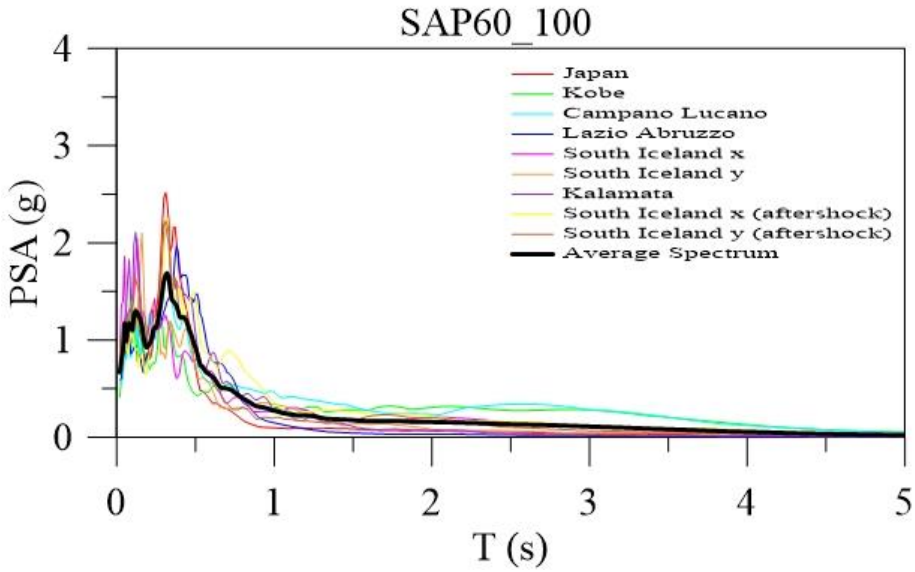

Figure 3.27 Pseudo acceleration spectra obtained for the mixtures analyzed

Therefore, the PSA were determined for the nine signals and after an average spectrum was derived for the case without barrier and compared with the average spectrum derived for the case with barrier (Figure 3.27).

The average spectrum obtained in presence of the barrier keep the same shape of that calculated in absence of barrier but shifted toward minor amplitude of pseudoacceleration for a SDOF period between 0.1 s and 0.5s. The effect of the insertion of the barrier seems to increase the damping of the system. The PSA spectrum confirms the ineffectiveness of the SAP70 mixture, carrying to a worse behaviour of the system.

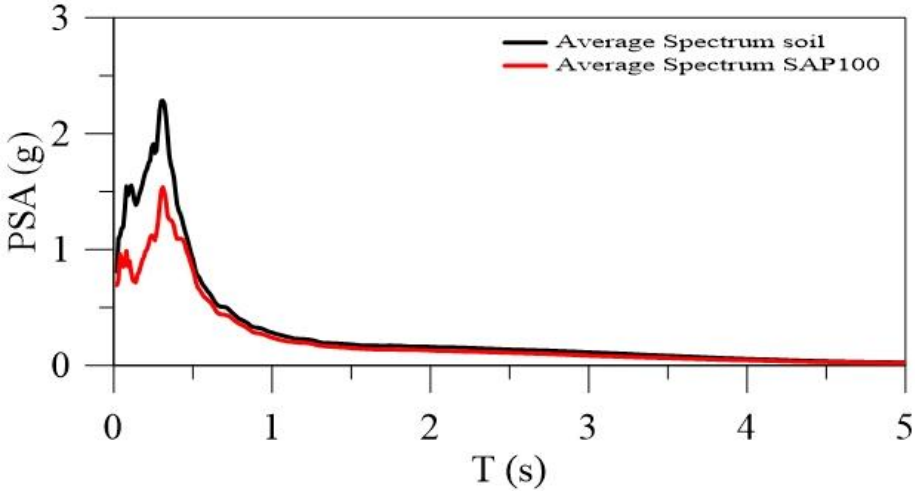
Average Spectrum soil
Average Spectrum SAP100
PSA (g)
T (s)
0
1
2
3
4
5

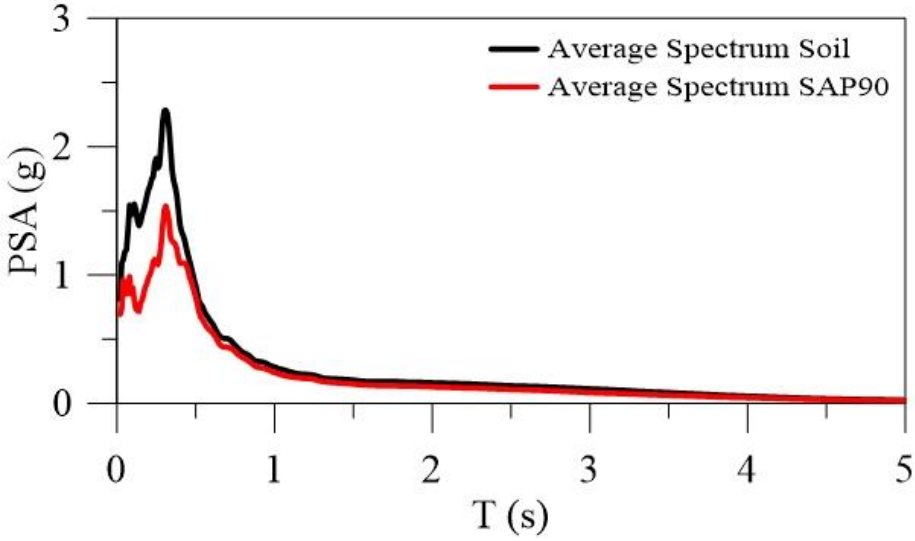
Average Spectrum Soil
Average Spectrum SAP90
PSA (g)
T (s)
0
1
2
3
4
5

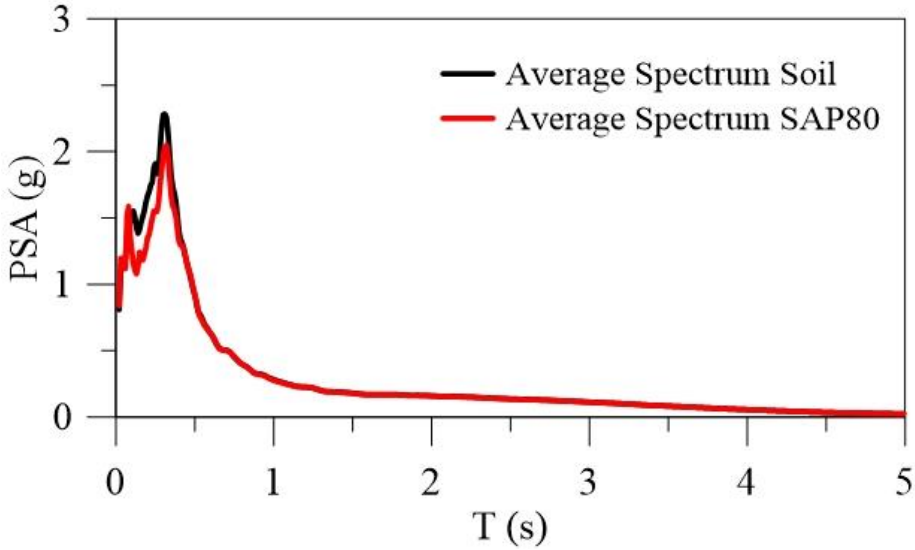
Average Spectrum Soil
Average Spectrum SAP80
PSA (g)
T (s)
0
1
2
3
4
5

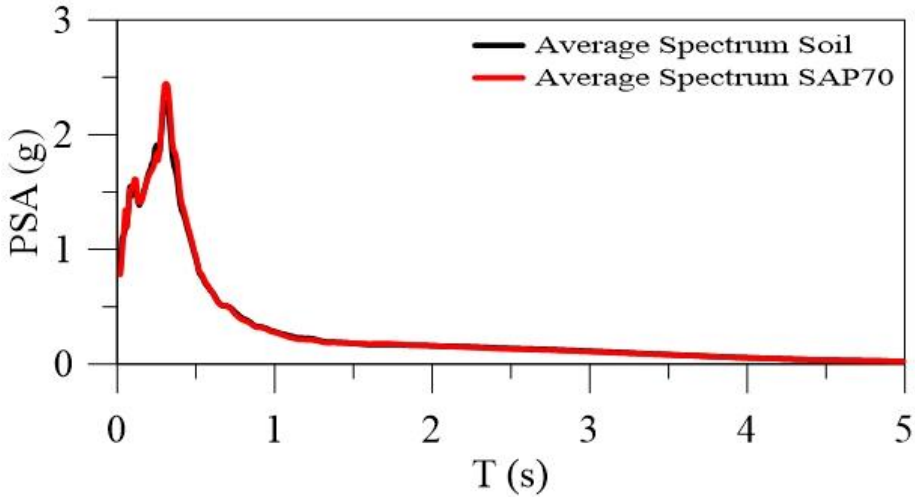
Average Spectrum Soil
Average Spectrum SAP70
PSA (g)
T (s)
0
1
2
3
4
5

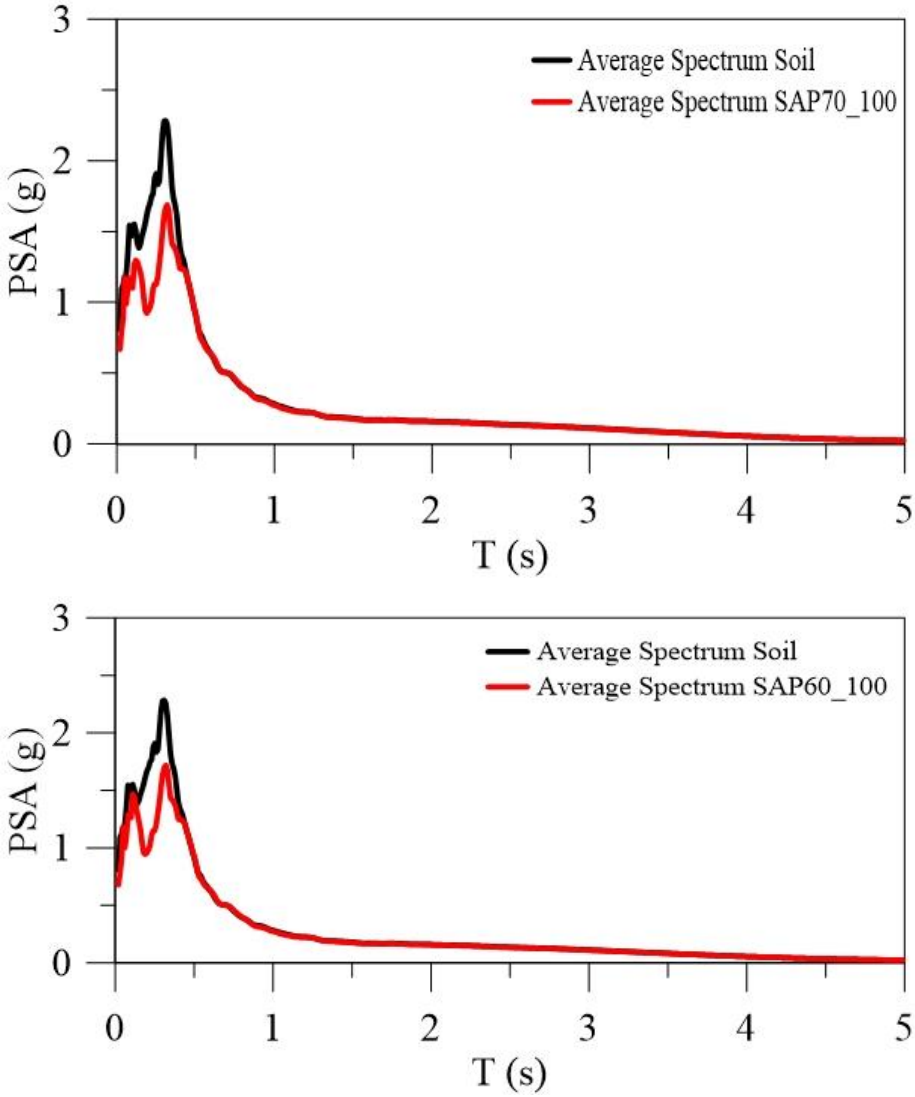

Figure 3.28 Average spectra obtained with the barrier compared with that obtained in absence of the barrier

An additional analysis was carried out considering the presence of a foundation for the SAP100 mixture. The foundation was modelled as a plate element. The results in terms of ratio between the maximum

acceleration obtained with barrier and that obtained without barrier are compared in figure with the reference model without the foundation.

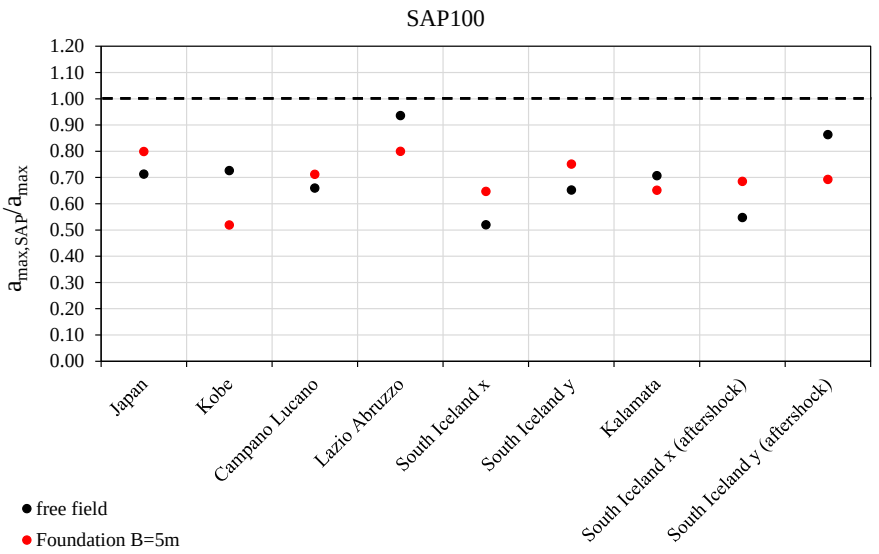

Figure 3.29 Ratio between the maximum acceleration with and without the barrier

The ratios obtained are very similar and the mean values is exactly the same (about 0.7). Therefore, the influence of the foundation can be disregarded in this phase.

3.5.5. Non-continuous rectangular barrier

A non-continuous rectangular barrier was tested to verify if the same results in terms of isolation could be obtained with a non-continuous scheme. The reduction was carried out by cutting the length of the sides L_b from ground level in step of 0.5m until 2 m (Figure 3.30) for which the isolation effect tends to decrease. Figure 3.31 shows the results

obtained in terms of ratio between the average maximum acceleration with and without the barrier obtained for a barrier made by only SAP. In the same figure, also the result obtained for the continuous barrier (SAP100) was reported for comparison.

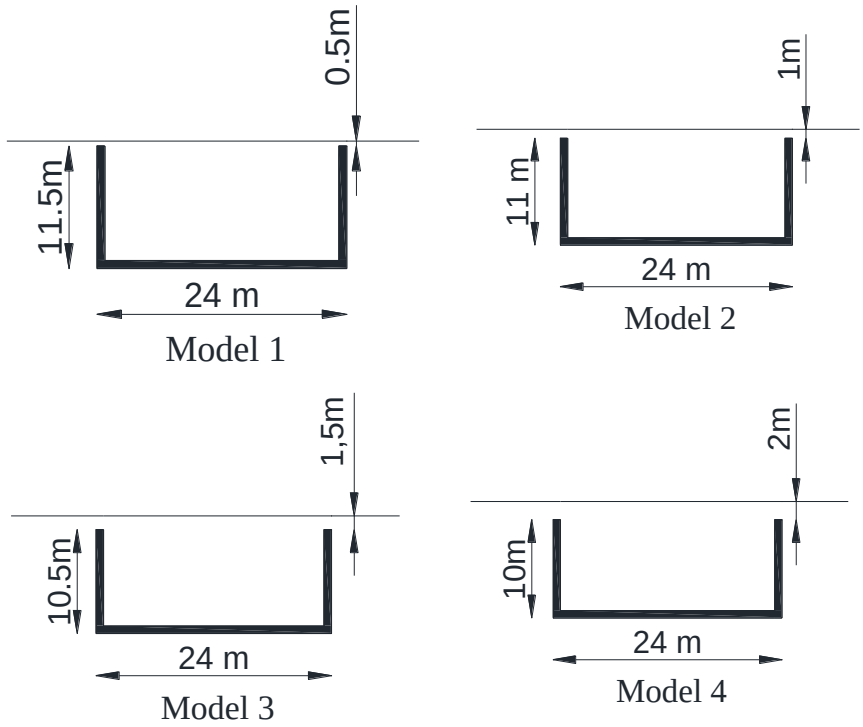

Figure 3.30 Schemes of the non-continuous rectangular barrier

The average remains approximatively constant until a reduction of 1.5m, while from a reduction of 2m a little variation was observed. Therefore a non-continuous barrier could be adopted instead of a continuous barrier.

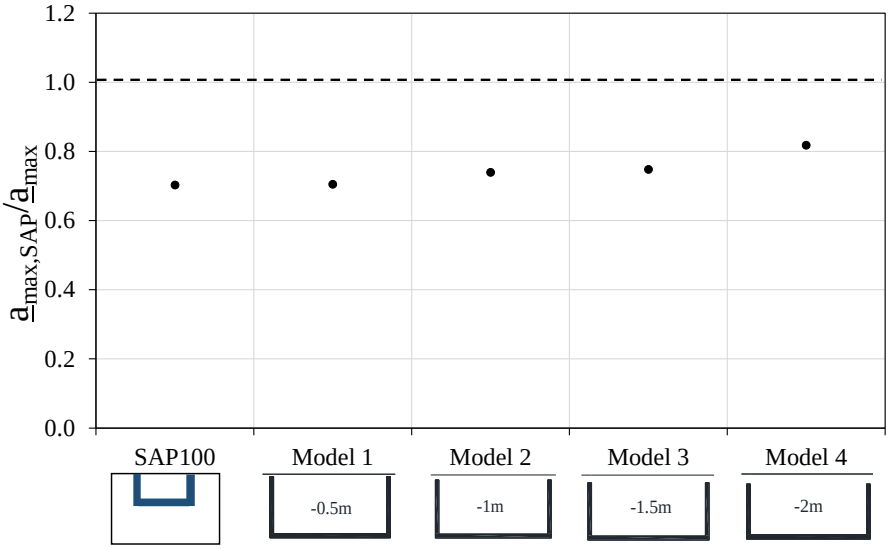

Figure 3.31 Ratio between mean values of acceleration with and without the barrier for non-continuous barrier compared with the continuous barrier

3.6. Final remarks

In this chapter the effect of the insertion of a soft barrier made by different SAP-sand mixtures in the soil, in both static and dynamic conditions was analyzed. The model was calibrated on the centrifuge tests reported in the Chapter 2. Two geometrical configurations of the barrier were modelled (V-barrier and rectangular barrier). The time histories of acceleration used as base input motions at the bottom boundary of the FE mesh are obtained from different databases (all scaled to the same value of amplitude, that is 0.3g). The results of the dynamic analyses are evaluated in terms of maximum accelerations recorded at the top of the model, Arias Intensity and pseudo spectral acceleration. The V-shaped barrier is less effective than the rectangular

one having the same depth, since the isolated mass is smaller and the filtering effect of the grouted layer is influenced also by the bulk stiffness. The V barrier seems to lose its efficacy whit real signals characterized by a high content of low frequencies. The reduction obtained in terms of mean maximum accelerations was of about 10 %. Therefore the use of the V barrier is not recommended. The volumetric stiffness K of the grouted layers plays a relevant role on the effectiveness of the isolating barrier. In the case of a rectangular caisson, the best solution is to have an extremely low value of K on the vertical sides, and a higher one at the base. So doing, the static settlements induced by the creation of the barrier would be reduced. The optimum scheme (both in static and dynamic conditions) is made by two different materials (100% SAP at the base and 60% SAP or 70% SAP along the sides of the rectangular caisson). The rectangular barrier may be of the continuous type or of the non-continuous type by cutting the length of the sides L_b from ground level. The reduction obtained with rectangular barrier was of about 30% obtained for the more feasible mixtures (SAP90 or barrier with SAP100 on the base and SAP70/60 on the sides).

In all cases, the reduced value of the shear strength angle in the grouted layers must be considered, to check if it may affect the load bearing capacity of the structure to be protected in an unacceptable way. Also from the static point of view, the rectangular barrier shows a better behavior than V barrier. The reduction in bearing capacity decreases as the percentage in SAP decreases. Two static conditions were examined, in the first one the barrier is free to move while in the second one a kinematic constraint in vertical direction was inserted to avoid that the

material squirted out as the applied displacement increases. The optimum scheme (both in static and dynamic conditions) is made by two different materials (100% SAP at the base and 60% SAP or 70% SAP along the sides of the rectangular caisson). For it, a reduction of the bearing capacity of about 50% is observed and it is not necessary to introduce a kinematic constraint. However, since many old structures have very large load bearing capacity safety factors, such a reduction may in some cases be not critical, depending on the induced settlements. It is thus argued that, depending on the specific case, the barrier may be adopted with a performance based design.

REFERENCES

Arias A. (1970) A measure of earthquake intensity *R.J. Hansen (Ed.), Seismic Design for Nuclear Power Plants, Massachusetts Institute of Technology Press, Cambridge, MA, pp. 438-483*

Benz T (2007) Small strain stiffness of soil and its numerical consequences. *Ph.d. thesis, Universitat Stuttgart*

Benz T., Vermeer P. A., Schwab R. (2009). *A small-strain overlay model*. International Journal for Numerical and Analytical Methods in Geomechanics, 33, 25-44.

Brinkgreve RB, Kappert JMH, Bonnier PG (2007). Hysteretic damping in a small-strain stiffness model. *Numerical models in geomechanics NUMOG X Pande and Pietruszczak (eds) Taylor and Francis Group, London, ISBN 978-0-415-44027-1*

Lombardi D. (2014) An innovative ground treatment approach for seismic risk mitigation of existing structures, *Ph.D. Thesis, University of Napoli Federico II (Italy).*

Schanz T, Vermeer PA, Bonnier PG (1999). The hardening soil model: formulation and verification. *In: Brinkgreve RBJ (ed) Beyond 2000 in computation geotechnics. Balkema, Rotterdam, pp 281–290*

CHAPTER 4

A MACRO-ELEMENT FOR STATIC ANALYSES OF SOFT BARRIERS

4. Introduction

The scope of this chapter is to present some aspects of the development of a "macro-element" for static soil-structure interaction analyses in presence of soft barrier. Numerical parametric analyses have been carried out in order to study the feasibility of the soft barrier and its geometrical and mechanical properties, which optimize the results both in static and in dynamic field (Chapter 3). The results showed that the barrier could cause a reduction of the bearing capacity of the building to be protected. However, since many old structures have very large load bearing capacity safety factors, such a reduction may in some cases be not critical, depending on the induced settlements.

In order to give an insight on the static performance of soft buried barriers made of a mixture of soil and a Super Absorbing Polymer (SAP) to be used for the mitigation of seismic risk, the macro-element approach is employed. It is assumed that it is possible to formulate directly a relationship between external forces and displacements of a foundation by considering the generalised stress and strain variables, respectively.

The calibration of macro-element parameters requires specific numerical simulation. Numerical parametric analyses were performed to calibrate the macro-element parameters in presence of the soft barrier. Two configuration of the barrier were considered.

The analyses have been carried out by using the commercial code Plaxis2D. The satisfactory predictive capabilities of the macro-element model are finally demonstrated by simulating finite-element tests.

4.2. The concept of macro-element

The concept of soil–structure interaction refers to static and dynamic phenomena mediated by a compliant soil and a stiffer super-structure. Soil–structure interaction is an interdisciplinary field, which lies at the intersection of soil and structural mechanics. Figure 4.1 shows, in a friendly way, the different manner to intend the soil-structure interaction, as reported by Grange (2013). Generally, when a superstructure is analysed by assuming the constrains to be rigid, the procedure is so simplified to nullify the effect of deformability of the foundation soil on the superstructure.

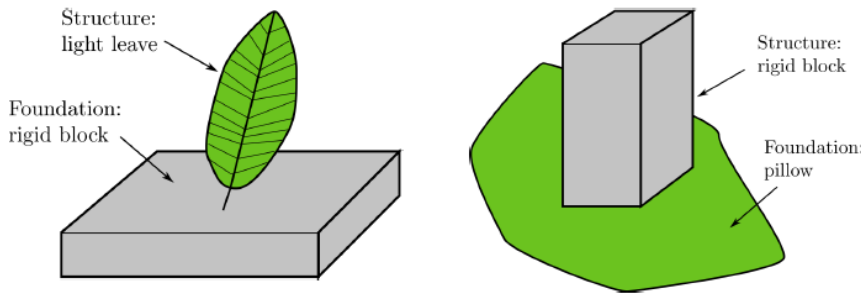

Figure 4.1 Soil structure interaction a) Structural engineer's point of view b) Geotechnical engineer's point of view

In standard analyses, the influence of the foundation/soil system on the mechanical response of the superstructure is taken into account by

introducing a certain number of linear springs, these summarising in a very simple manner the deformability of the foundation soil.

In the field of earthquake engineering, Soil–Structure Interaction (SSI) is a phenomenon that has to be taken into account in order to reproduce correctly the non-linear behaviour of a structure and thus to be able to predict its relative displacements at the top. Simulating SSI involves detailed 3D meshes for the soil and the structure, a big number of degrees of freedom and thus huge computational costs. This is the reason why simplified modelling strategies have extensively been developed during recent years. Among them, the "macro-element" approach consists in condensing all nonlinearities into a finite domain ("close field") and works with generalized variables (forces and displacements) at the centre of the foundation. In that way, it allows considerably decreasing the necessary degrees of freedom of the numerical model. The concept of ''macro-element'' was initially introduced in the context of shallow foundations by Nova and Montrasio (1991). Based on a number of experimental tests performed on a perfectly rigid strip footing resting on a frictional soil and subjected to an eccentric and inclined force, Nova and Montrasio formulated a global elastoplastic model with isotropic hardening for the entire soil–foundation system. The model was written in terms of resultant vertical and horizontal forces and moment acting on the footing normalized by the maximum supported vertical force and was used for the prediction of the footing displacements for quasi static monotonic loading. The rugby-ball-shaped surface of ultimate loads of the system was identified as the yield

surface of the plasticity model. This surface is schematically presented in Figure 4.2.

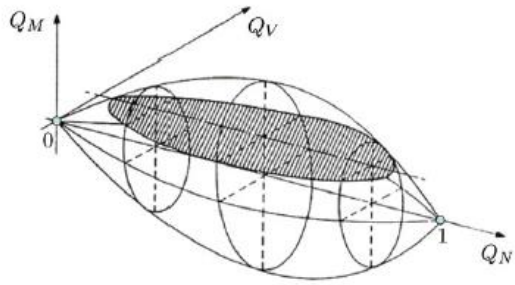

Figure 4.2 Ultimate surface of a footing on sand identified as a plastic yield surface

Other works aimed at extending the applicability of such models to cyclic loading. Pedretti (1998) and subsequently Di Prisco et al (2003). retained the isotropic hardening rule of the Nova and Montrasio model for the case of virgin loading and introduced a hypoplastic bounding surface formulation for the cases of unloading/reloading. In parallel, Paolucci (1997) initiated the use of macro-element models for earthquake engineering applications, whereas Le Pape et al. (1999) and Le Pape and Sieffert (2001) derived macro-element models similar to the Nova and Montrasio model within a thermodynamically consistent framework. An original modelling approach was proposed in the works of Crémer et al. (2001, 2002) in which, two distinct non-linear mechanisms (soil plasticization and footing uplift) are formulated independently, whereas the global footing response is obtained through their coupling. The model was developed for strip footings on cohesive

soils under seismic loading. Uplift was described by a geometric model and soil plasticization by a kinematic and isotropic hardening plasticity model following Prévost (1978). Recently, Grange et al. (2008) modified the plasticity model of Crémer et al. (2001, 2002) for application to circular footings and three-dimensional loading. A model with coupled uplift and soil plasticity has also been presented by Shirato et al. (2008). Similar applications of the concept of "macro-element" have been developed for foundations of offshore platforms subject to quasi-static cycles of loading, as the model by Houlsby and Cassidy (2002). Nova and di Prisco (2003) presented further applications of the macro-element in problems of rock impact on the ground, soil-pipeline interaction problems. In parallel, Muir Wood and Kalasin (2004) presented a macro-element model for the dynamic response of gravity walls.

The "macro-element", viewed simply as a part of the global model, must be described by a "constitutive law" compatible with the rest of the global model elements. This "constitutive law" must be selected in such a way so as to ensure that the response of the system, examined at the meso-scale (i.e. with the macro-element) correctly reproduces the features of the actual response of the model (i.e. at the local scale) that were retained in making the passage from the local to the meso-scale.

To illustrate these ideas, Chatzigogos et al. (2007) presented a simple example from structural engineering. It concerns a steel I-beam as in Figure 4.3a subject to bending moment from the action of a concentrated load at midspan. The "local scale" here refers to the constituent material of the beam, i.e. the steel, which is assumed to be described by an elastic-

perfectly plastic constitutive relationship. The solution of this problem in the "local scale" reveals the creation of a zone of plastic deformations around the central section of the beam. As the load increases, the zone of plastic deformations expands until the completely central section is plasticised. On the inner and outer fibers of the beam the zone of plastic deformations has a finite width b. The beam cannot support any further load increase; it has reached the state of "plastic collapse". The passage to the "meso-scale" is done by considering the "generalized" curvilinear continuous medium as in Figure 4.3b, which coincides with the locus of the neutral axis of the I-beam.

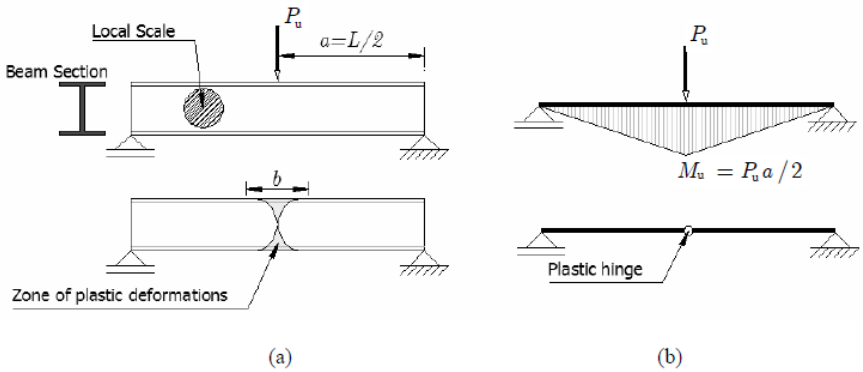

Figure 4.3 An elastic perfectly plastic I-beam subject to pure bending, a) modelling at the local scale; b) modelling at the meso-scale with a plastic hinge as a macro-element

The load increases up to its ultimate value P_u; the bending moment at the centre of the beam equals the moment of plastic collapse M_u of the central beam section and a plastic hinge is created at that point; a mechanism of plastic collapse is created and the beam can support no further load increase. It is obvious that the "plastic hinge" can be viewed

as the macro-element, which actually represents the zone of plastic deformations in the local scale. In passing to the "meso-scale", knowledge about fibres other than the neutral axis is ignored and cannot be retrieved. Moreover, all the non-linearity is lumped at one single point, namely the plastic hinge.

4.2.1. Model formulation

The model was formulated by the definition of generalized forces and displacements, in terms of which "constitutive" equations for macro-element are written. In case of shallow footings, under plane strain conditions, the mechanical interaction can be described in terms of three generalised stresses (the vertical load V, the horizontal load H and the overturning moment M), and three generalised strains (the vertical displacement v, the horizontal displacement u and the rotation θ). Then it is possible to introduce the resultant vertical force V, horizontal force H and moment M acting on the footing and the corresponding displacements v, u and θ in Figure 4.4.

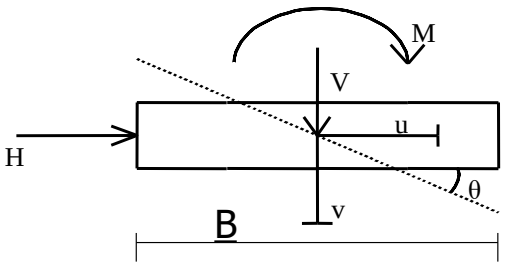

Figure 4.4 Generalised stress and strain variables for shallow foundation

Moreover, it is convenient to work with parameters that are dimensionless, so the ‘‘constitutive’’ equations of the macro-element will be written in terms of the force and displacement parameters normalized according to the following scheme.

$$\underline{Q} = \begin{bmatrix} \xi \\ h \\ m \end{bmatrix} = \frac{1}{V_m} \begin{bmatrix} V \\ H/\mu \\ M/\psi B \end{bmatrix} \qquad \underline{q} = \begin{bmatrix} \eta \\ \varepsilon \\ \zeta \end{bmatrix} = V_m \begin{bmatrix} v \\ \mu u \\ \psi B\theta \end{bmatrix} \qquad 4.1$$

In (5.1), $\underline{Q}$ is the dimensionless generalized force vector, $\underline{q}$ the dimensionless generalized displacement vector, B a characteristic footing dimension, V_m is the maximum centred vertical force supported by the footing, μ and ψ are non-dimensional constitutive parameters. From the definitions (5.1), the expression for the work increment $\dot{W}$ in the dimensionless parameters is written as reported in (5.2) where the total work W in the system is normalized by the characteristic quantity $B \cdot V_m$.

$$\dot{W} = \underline{Q} \cdot \underline{q} = \frac{V \cdot \dot{v} + H \cdot \dot{u} + M \cdot \dot{\theta}}{B \cdot V_m} = \frac{\dot{W}}{B \cdot V_m} \qquad 4.2$$

$$\dot{\underline{Q}} = \underline{\underline{K}} \cdot \dot{\underline{q}} \qquad 4.3$$

Similarly, by introducing the dimensionless generalized tangent stiffness matrix $\underline{\underline{K}}$ by writing the elements of the stiffness matrix are

subjected to the normalization scheme reported in (5.3), where Kij with i, j =V,H,M are the elements of the dimensional tangent stiffness.

$$\underline{\underline{K}} = \frac{1}{V_m}\begin{bmatrix} B\cdot K_{VV} & B\cdot K_{VH} & K_{VM} \\ B\cdot K_{HV} & B\cdot K_{HH} & K_{HM} \\ K_{MV} & K_{MH} & \frac{1}{B}\cdot K_{MM} \end{bmatrix} \qquad 4.4$$

The matrix $\underline{\underline{K}}$ depends on the state of generalized stress $\underline{Q}$, on the direction of the strain increment $\underline{q}$, and on the history of loading.
The structure of the macro-element was presented in Figure 6.

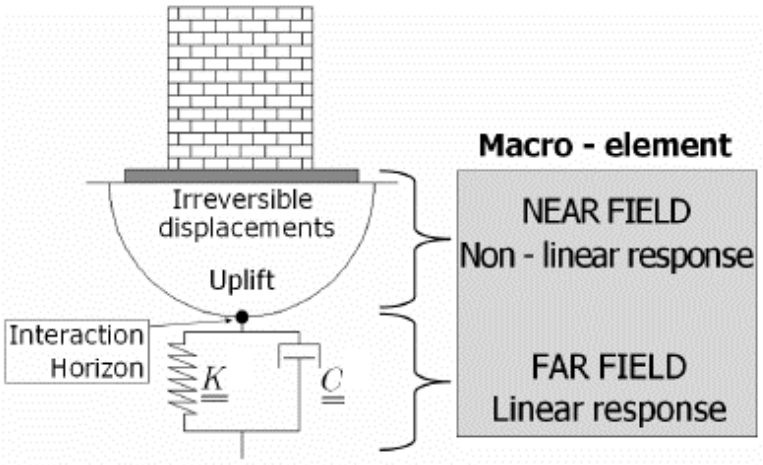

Figure 4.5 Structure of the macro-element (Chatzigogos et al., 2007)

The soil domain is divided in two parts: the far field, which describes the area where the response of the system remains linear, and the near field where all material and geometric non-linearities are lumped.

Accordingly, the response of the far field will be described by the linear part of the constitutive relationship in the macro-element while the response of the near field will correspond to the non-linear part of the established constitutive relationship.

The elastic part of the constitutive law is defined as $\underline{Q} = \underline{\underline{K}}^{el} \cdot \underline{q}^{el}$. For the development of the macro-element, it will be considered that the interaction horizon is reduced to a single point, that coincides with the centre of the footing. The constant elements of the stiffness matrix are identified with the elastic impedances of the foundation. For the case of shallow rigid foundations, it turns out that the coupling terms K_{ij} with $i \neq j$ are negligible and the matrix is diagonal.

The near field response of the system is associated with all the non-linearity generated by the soil-structure interaction phenomena at the soil-footing interface. For the plastic mechanism, a failure criterion, a loading surface and a flow rule are needed.

The model formulated by Nova and Montrasio (1991a) assumed that the constitutive law of the macro element, is rigid-plastic strain-hardening with a non-associated flow rule. It is postulated that there is a loading function f defined as

$$f(Q, \rho_c, \beta) = h^2 + m^2 - \xi^2 \left[1 - \left(\xi / \rho_c\right)\right]^{2\beta} \qquad 4.5$$

The loading function depends on the history through a parameter ρ_c, which in turn depends on plastic generalized strains and on additional parameters:

$$\rho_c = \rho_c(\underline{q}, V_m, R_0, \alpha, \gamma, \mu, \psi) \qquad 4.6$$

where R_0 is the initial stiffness of the foundation under centred vertical load, μ and ψ are constitutive parameters that govern the shape of the failure locus, α and γ control the evolution of the hardening rule. When ρ_c attains its limit value, $\rho_c=1$, the loading function coincides with the failure locus.

The direction of the strain increment $\underline{q}$ when plastic deformation occurs is given by a plastic potential

$$g(\underline{Q}) = \lambda^2 h^2 + \chi^2 m^2 - \xi^2 \left[1 - (\xi/\rho_g)\right]^{2\beta} = 0 \qquad 4.7$$

The parameter ρ_g is a scaling factor, while λ and χ are defined as $\lambda = \mu/\mu_g$ and $\chi = \psi/\psi_g$, with μ_g and ψ_g constitutive parameters. If $\lambda = \chi = 1$ plastic potential and loading function coincide and the flow rule is associated.

The flow rule assumed by Nova and Montrasio is

$$\begin{cases} if \;\; f(\underline{Q}, \rho_c) < 0 \;\rightarrow \dot{\underline{q}} = 0 \;\; \forall \dot{\underline{Q}} \\ if \;\; f(\underline{Q}, \rho_c) = 0 \;\; and \;\; df(\underline{Q}, \rho_c) < 0 \rightarrow \dot{\underline{q}} = 0 \\ if \;\; f(\underline{Q}, \rho_c) = 0 \;\; and \;\; df(\underline{Q}, \rho_c) = 0 \rightarrow \dot{\underline{q}} = \Lambda \dfrac{\partial g}{\partial \underline{Q}} \end{cases} \qquad 4.8$$

The value of plastic multiplier Λ depends on the intensity of the load increment and on the history.

The expression of the failure locus is given by (5.4)

$$F = \left(\frac{M}{\psi \cdot B}\right)^2 + \left(\frac{H}{\mu}\right)^2 - V^2 \cdot \left(1 - \frac{V}{V_m}\right)^{2\beta} \qquad 4.9$$

where β is a parameter that describes the shape of failure locus. The relationship (5.9) in dimensionless form became

$$h^2 + m^2 - \xi^2 \cdot (1-\xi)^{2\beta} = 0 \qquad 4.10$$

Moreover, several authors have been investigating how the failure locus can be affected by different mechanical/geometrical factors, such as the spatial inhomogeneity of soil properties (Gouvernec et al. 2003) or the embedment of the foundation (Bransby et al. 1999; Bransby et al. 2007; Gouvernec 2008). On this point, Gouvernec (2008) confirmed the intrinsically asymmetric shape of the envelope of the cross section (M-H plane), highlighting its marked dependence both on the embedment ratio and the normalized vertical load ξ.

4.3. FE analyses for the calibration of the macro-element

The model presented in the previous section is characterized by nine parameters (V_m, R_0, β, μ, ψ, λ, χ, α, γ). The calibration of model parameters were performed through parametric numerical analyses carried out to by means of the software Plaxis 2D. The system response under static loads was studied, varying the geometry of the barrier. The surfaces of the ultimate load of the systems, with and without soft barriers, were obtained, by performing numerical displacement controlled test.

4.3.1. Parametric analyses: geometrical configurations

Parametric numerical analyses have been performed to better investigate the effect of the insertion of the soft barriers under static loads. The 2D numerical models were analysed with the software Plaxis2D.

Two configuration of the barrier were modelled: rectangular barrier and V-shaped barrier. Both of them are characterized by a depth H_b, a width L_b and a thickness s, as shown in Figure 4.6a and b. The depth H_b was kept constant while the width L_b was varied. In addition, a model without barrier was studied in order to have a reference model (Figure 4.6c).

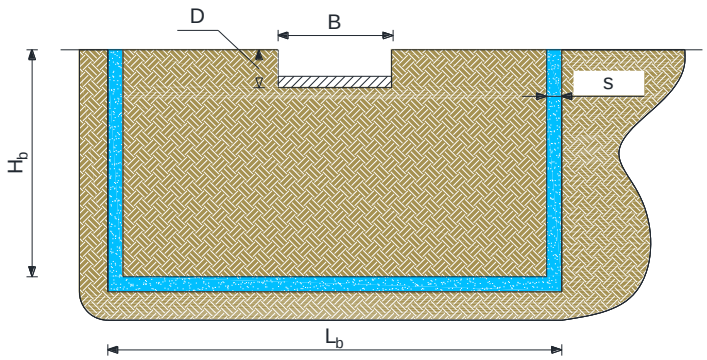

a)

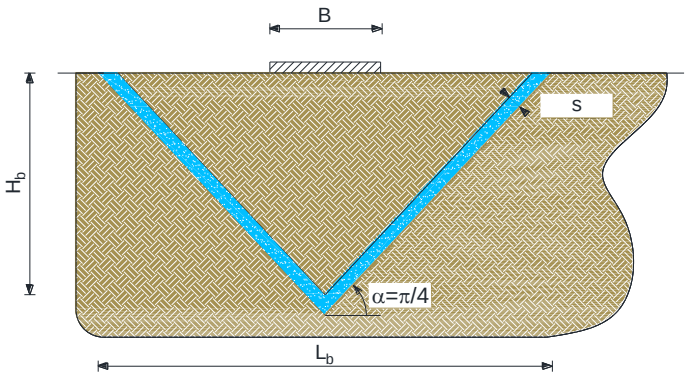

b)

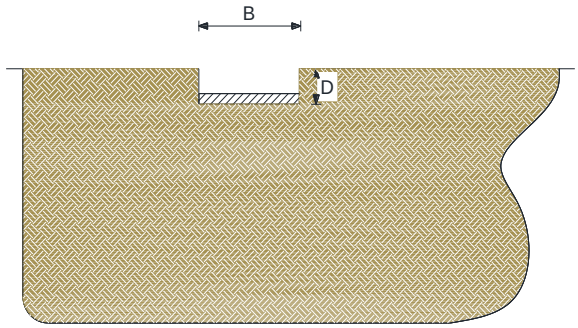

c)

Figure 4.6 Geometrical configuration of the model analysed in parametric analyses, a) rectangular; b) V-shape; c) reference model

A summary of the schemes analysed was reported in Table 4.1.

Table 4.1 Models analysed

Model		Foundation		Soft barrier			
		B	D	H_b	L_b	H_b/B	L_b/B
		m	m	m	m	-	-
Soil	T_D0	6	0	-	-	-	-
	T_D2		2				
Rectangular barrier	R_D0_L12	6	0	12	12	2	2
	R_D0_L24				24		4
	R_D2_L12		2		12		2
	R_D2_L24				24		4
V-barrier	V_D0_L12	6	0	12	12	2	2
	V_D0_L24				24		4

The foundation, lying on Hostun sand (HN31) stratum, was perfectly rigid and it was modelled as a plate element. An interface was introduced at the contact elements between soil and foundation.
Hostun sand is modelled with a fine mesh of finite elements; its constitutive model is Hardening soil with small strain stiffness, already implemented in Plaxis2D. The parameters adopted for the sand are summarized in Table 4.2.

Table 4.2 Parameters adopted for the Hostun sand

G_0^{ref}	202000	kN/m^2
$\gamma_{0.7}$	0.0002	-
ν	0.25	-
E_{50}^{ref}	30000	kN/m^2
E_{oed}^{ref}	30000	kN/m^2
E_{ur}^{ref}	90000	kN/m^2
p^{ref}	100	kN/m^2
m	0.55	-
φ	42	°
ψ	16	°
K_0^{nc}	0.4	-

On the basis of the results presented in Chapter 3 (section §3.2) a mixture of SAP polymer and sand (SAP80, 80% of SAP and 20% of sand in weight) was chosen to create the soft barrier, due to the better behaviour exhibited in static and dynamic condition. The mechanical properties are reported in Table 4.3.

Table 4.3 Mechanical properties adopted for the soft barrier

	φ	V_s	ν
	°	m/s	-
SAP80	7	92	0.485

4.3.2. Failure loci and load-displacements curve

To obtain the failure loci, different load paths were imposed. The load programme includes:

- centred vertical load
- inclined loading (with no overturning moment)
- eccentric loading (with no horizontal load)
- application of a horizontal load and overturning moment at constant centred vertical load
- application of a horizontal load at constant eccentric vertical load

The first load path (centred vertical load) is necessary to determine the maximum centred vertical force supported by the footing V_m.

V-barrier

The insertion of the V-barrier causes a pronounced contraction of the failure surface, as demonstrated in Figure 4.7 for the V-H plane and in *Figure 4.8* for the V-M plane, in which the failure surface obtained for a width of the barrier equal to 24m was compared with the failure surface of the soil model. Since for a foundation of 6m is not conceivable

to realize a barrier wide more than four time the width of the foundation, it is evident that in this condition, a V-barrier is not realisable and the study of the macro-element has been addressed only on the rectangular barrier.

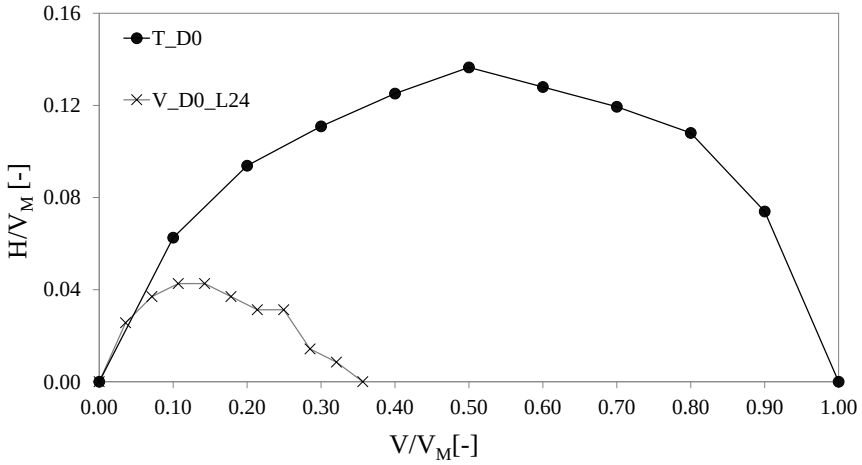

Figure 4.7 Failure locus for inclined load

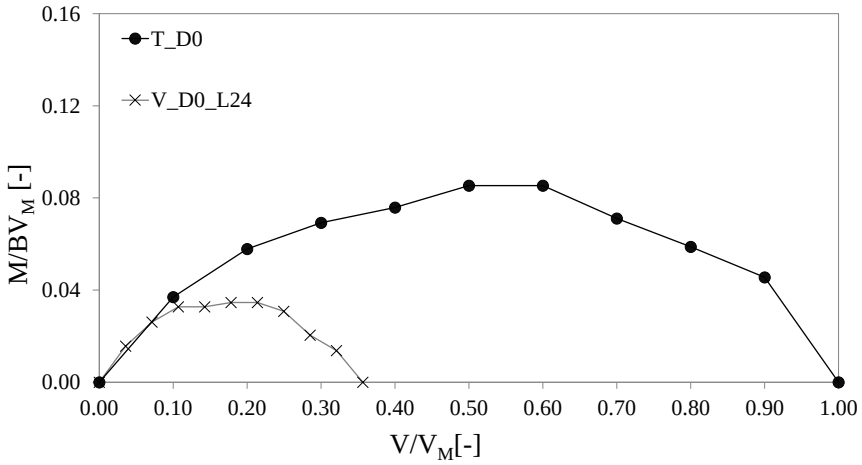

Figure 4.8 Failure locus for eccentric load

Rectangular barrier

Figure 4.9 shows the calculated failure surfaces for inclined centred loading, normalized with respect to the calculated V_m of the model without barrier. Figure 4.9*a* shows the failure surfaces for the model with surface foundation, compared with the model without barrier. It is evident that the failure surface undergoes a contraction, without modify the initial slope, as a consequence of the insertion of the barriers. This contraction increases as the width of the barrier decreases (the sides of the rectangular barrier move close to the foundation). When the barrier is far from the foundation the failure mechanism doesn't intercept the barrier, then the bearing capacity tends to increase. Since for a foundation of 6m is not conceivable to realize a barrier wide more than four time the width of the foundation, it is evident that the variation of this parameter is limited. From Figure 4.9b it can be observed the results of the embedded foundation under inclined load. Especially for lowest value of vertical load, the system can sustain a horizontal load comparable with that of the soil.

The same conclusions were deduced from Fig. 7 that shows the results of the load condition with eccentric load in V-M plane.

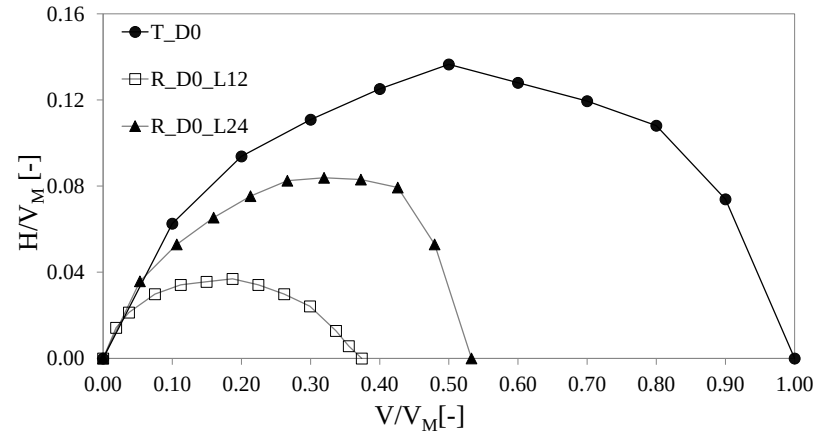

a)

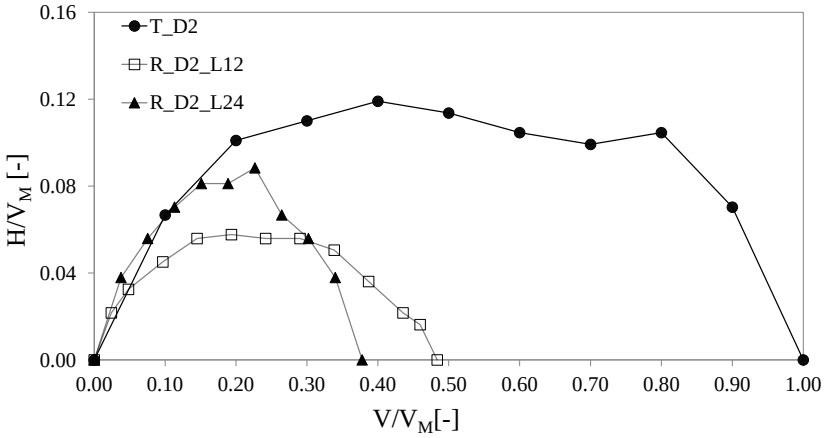

b)

Figure 4.9 Failure locus for inclined load, a) surface foundation; b) embedded foundation

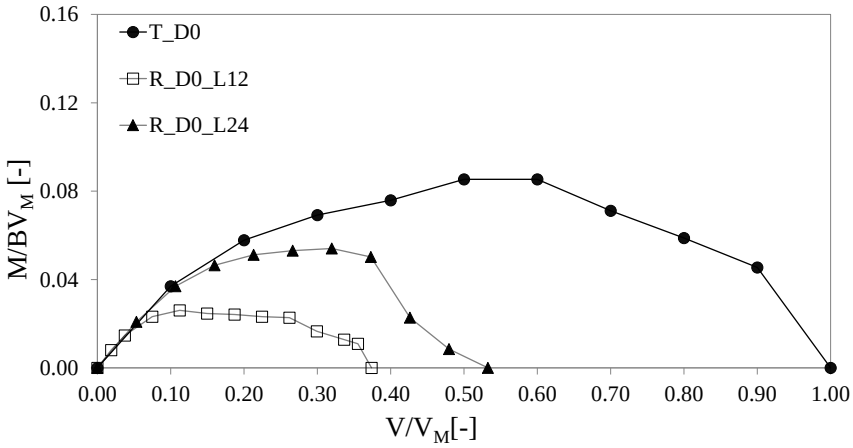

a)

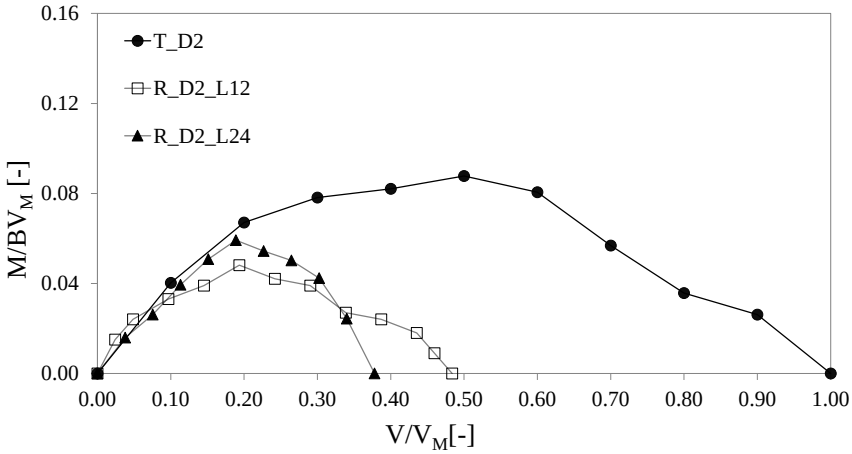

b)

Figure 4.10 Failure locus for eccentric load, a) surface foundation; b) embedded foundation

Finally, the cross section (M-H plane) was determined by application of a horizontal load and overturning moment at constant centred vertical load, and application of a horizontal load at constant eccentric vertical load (*Figure* 4.11). The constant load was chosen equal to $0.3V_m$, to

suppose that in the initial condition (soil without barrier) the safety factor was 3. The failure surfaces confirm the asymmetric shape of the envelope of the cross section (M-H plane), highlighting its marked dependence the normalized vertical load ξ. *Figure 4.11* b shows that there is only a little difference between the failure surfaces in the case of embedded foundation, with the change in width of the barrier.

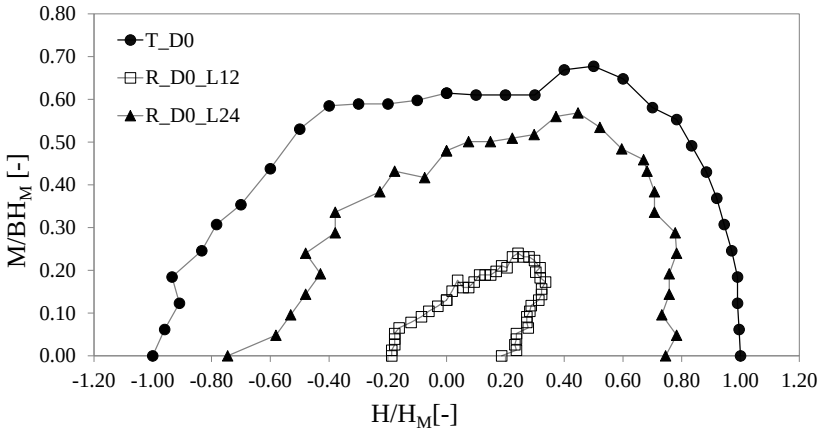

a)

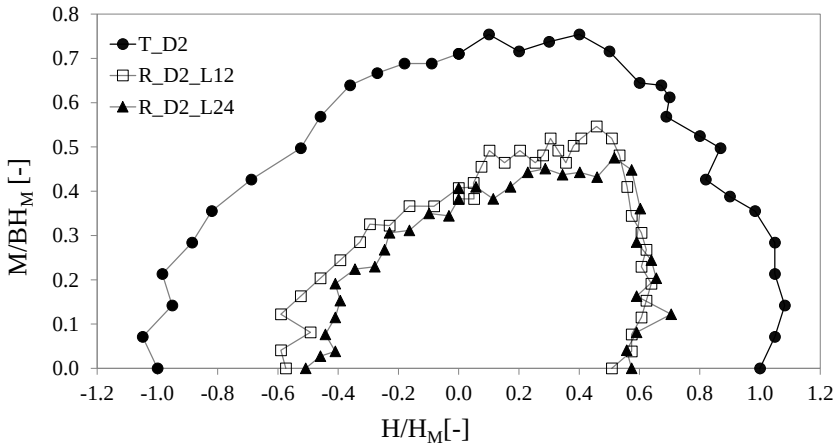

b)

Figure 4.11 V constant sections of the failure locus a) surface foundation; b) embedded foundation

The load displacements curve are calculated to calibrate some of the constitutive parameters of the macro-element. V_m, and R, were determined from the results of the tests with central vertical loading. *Figure 4.12a* shows the results of central vertical loading on surface foundations with different width of the barrier, together with the corresponding model without barrier. *Figure 4.12b* shows the results of central vertical loading on embedded foundations. For both of them (surface and embedded foundation) the initial slope of the load-displacement curve is the same with and without the barrier. For the embedded foundation, the curves are almost overlapped, and then the width of the barrier does not affect substantially the behaviour from this point of view.

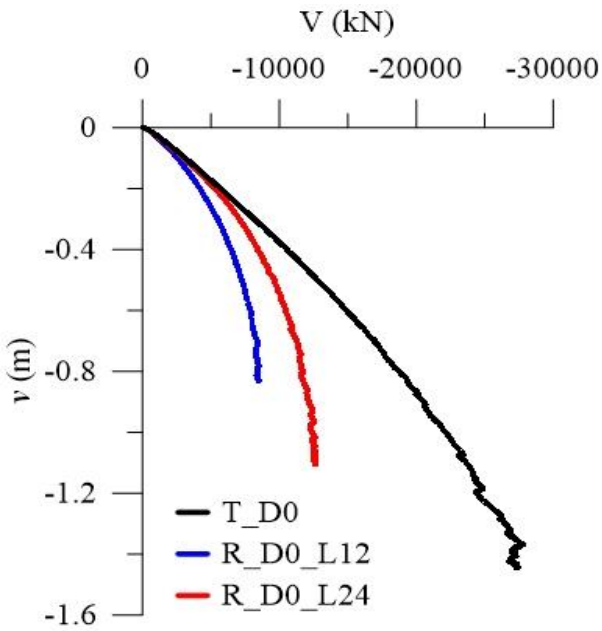

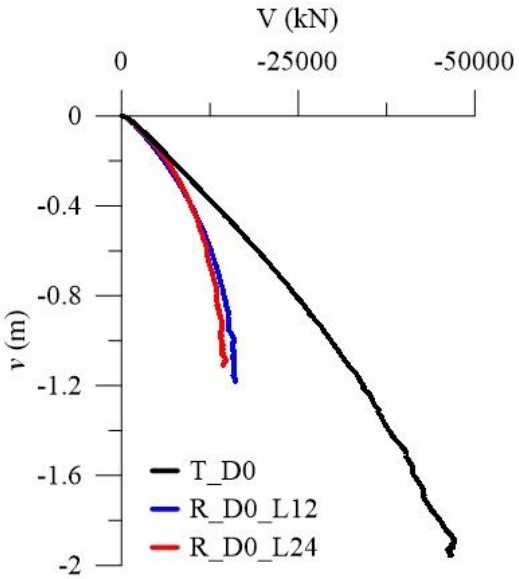

Figure 4.12 Load-displacement curves for centred vertical loading. a)surface foundation; b)embedded foundation

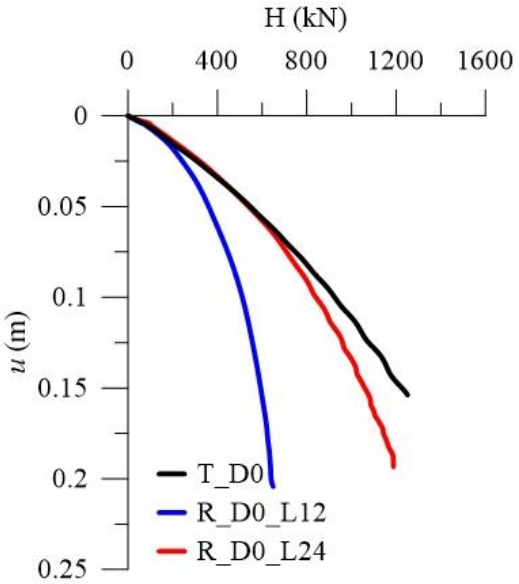

Figure 4.13 Load-displacements curve for inclined load

Figure 4.13 shows the results of a test with an inclined force with V constant and equal to 0.1 V_m (maximum vertical load supported by the soil). These curves are necessary to calibrate the parameter α.
From the construction of the failure loci it is obvious that this kind of seismic isolation is adapt only for the structures having a very large load bearing capacity safety factors, for which such a reduction may in some cases be not critical.

4.3.3. Calibration of the model

To calibrate the parameters V_m and R_0 it is enough to impose a vertical centred load until the failure. The parameter R_0 is independent from the insertion of barrier (*Figure 4.12*), so it is not necessary to calibrate it. To calibrate V_m, parametric analyses were carried out to take into account the feasible geometrical configurations of the rectangular barrier, varying the depth H_b and the width L_b. In Figure 4.14 the values of V_m obtained are reported against the ratio between the width of the barrier L_b and the width of the foundation B, for several depths H_b of the barrier. It can be observed that V_m approach to an asymptote, corresponding to V_m of the natural soil, increasing the width and the depth of the barrier.

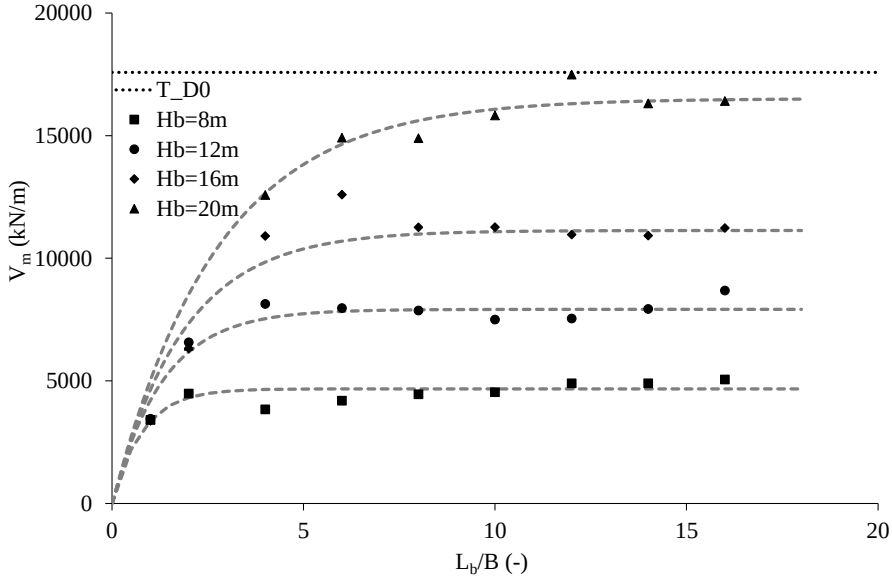

Figure 4.14 V_m obtained varying the geometry of the rectangular barrier

A relation founded on these results was achieved, that allows to calculate analytically the V_m in presence of the barrier known the geometry and V_m of the natural soil (namely in the formula $V_{m,s}$):

$$V_{m(L/B)} = \alpha \cdot V_{m,S} \left[1 - \exp\left(- \frac{R_0 \cdot L_b}{\alpha \cdot V_{m,S} \cdot B} \right) \right] \qquad 4.11$$

where $V_{m,s}$ is the maximum centred vertical force supported by the footing without barrier and α depends on the depth of the barrier, as shown in fig.

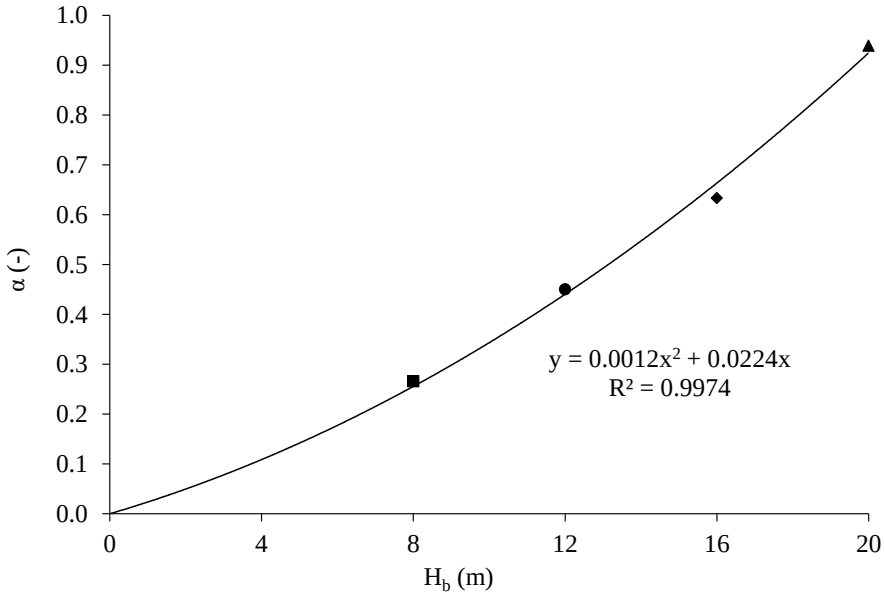

Figure 4.15 Parameters α plotted in correspondence of the depth of the barrier

The parameters μ, ψ and β can be determined from the shape of the failure locus. The parameters μ and ψ give the slope of the tangent of the failure locus at the origin. The insertion of the barrier does not influence the initial slope as shown in *Figure 4.16*, so the μ and ψ adopted are the same for the models with and without barriers. From the *Figure 4.13* the parameter α is calibrated. The other parameters were assumed as suggested by Nova and Montrasio.

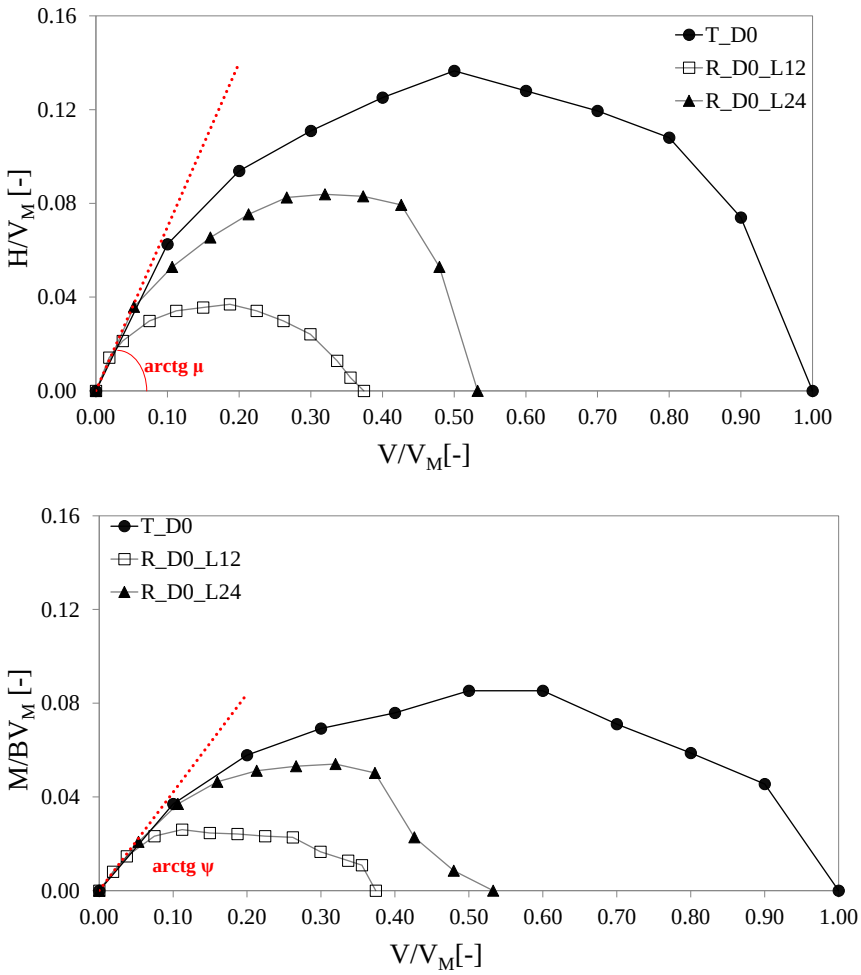

Figure 4.16 Determination of the parameters μ and ψ

4.3.4. Model validation

The validation of the model was carried out by comparing the failure locus and load-displacements curves calculated by FE analyses and that calculated by the macro-element (ME) approach. *Figure 4.17* shows that there is a good accord between the data calculated. *Figure 4.18*

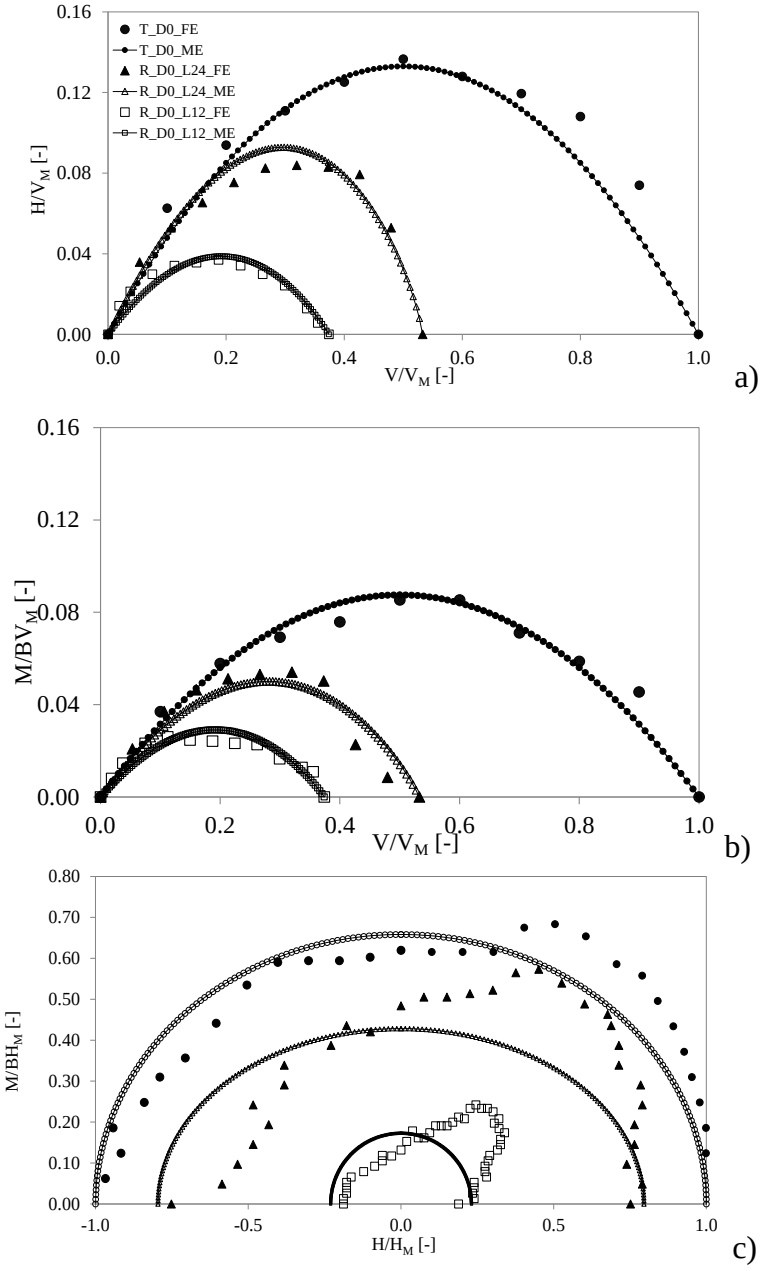

Figure 4.17 Comparison between the FE and ME model

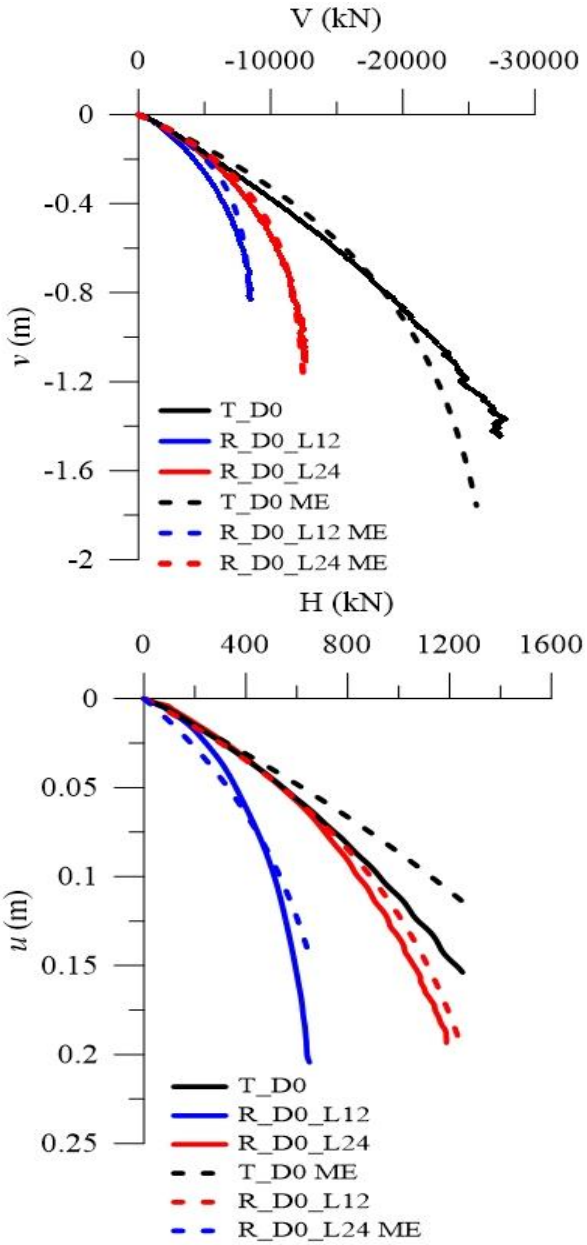

Figure 4.18 Comparison between the load-displacements curves obtained by FE and ME models

The macro-element approach seems to catch the static behaviour of the model also in terms of load-displacements curves *V-v* and *H-u, (Figure 4.18)*. On this basis, it is possible, now to calibrate the dynamic part of the macro-element, to study the behaviour of the soft barrier totally.

4.4. Final remarks

The scope of this chapter is to present a macro-element model for shallow foundations in presence of soft barriers. In Chapter 3 has been shown that the soft barrier could cause a reduction of the bearing capacity of the building to be protected. The aim of the macro-element is to model the near field soil-foundation behaviour. In this concept, the entire soil-foundation system is considered as a one single element located near the foundation area, which is introduced to analyze the non-linear and irreversible behaviour of soil-foundation interaction that can takes place at the near field zone. This theory is expanded by Nova and Montrasio (1991) in a case of shallow strip footing on sand under monotonic loading with an isotropic hardening elasto-plastic law to define the bearing capacity of the foundation in a vertical, horizontal and overturning moment plane. This bearing capacity is defined as a yield surface in a plasticity model. In addition, a kinematic of the system has been introduced by a plastic flow rule. So many factors can have an effect on this capacity.

Numerical parametric analyses were performed to calibrate the macro-element parameters in presence of the soft barrier. The analyses have been carried out by using the commercial code Plaxis2D. To obtain the failure loci, different load paths were imposed. From the construction of

the failure loci it is obvious that this kind of seismic isolation is adapt only for the structures having a very large load bearing capacity safety factors, for which such a reduction may in some cases be not critical. A relation founded on these results was achieved, that allows to calculate analytically the maximum centred vertical force supported by the footing in presence of the barrier. The macro-element approach seems to catch the static behaviour of the model. On this basis, it is possible to calibrate the dynamic part of the macro-element, to considering the soil structure interaction in presence of the soft barrier.

REFERENCES

Bransby M.F., Randolph M.F. (1999), The effect of embedment depth on the undrained response of skirted foundations to combined loading, Soils and Foundations, Vol. 39, No. 4, p. 19-33.

Bransby M.F., Yun G.(2007). The horizontal-moment capacity of embedded foundations in undrained soil, *Canadian Geotechnical Journal, Vol. 44, p. 409-424.*

Chatzigogos C.T., Pecker A., and Salençon J. (2007). Seismic bearing capacity of a circular footing on a heterogeneous cohesive soil, *Soils Found. 47:4, 783–787.*

Crémer C, Pecker A, Davenne L. (2001) Cyclic macro-element for soil-structure interaction: material and geometrical non linearities. *International Journal for Numerical and Analytical Methods in Geomechanics; 25:1257–1284.*

Crémer C, Pecker A, Davenne L. (2002) Modelling of nonlinear dynamic behavior of a shallow strip foundation with macroelement. Journal of Earthquake Engineering; 6(2):175–211.

Di Prisco C, Nova R., Sibilia A. (2003). Shallow footing under cyclic loading: experimental behavior and constitutive modelling. *In Geotechnical Analysis of the Seismic Vulnerability of Historical Monuments, Maugeri M, Nova R(eds). Pàtron:2003; 99–121.*

Gourvenec S. (2008), Effect of embedment on the undrained capacity of shallow foundations under general loading, *Géotechnique, Vol. 58, No. 3, 2008, p. 177-185.*

Gourvenec S., Randolph M.F. (2003). Effect of strength non-homogeneity on the shape of failure envelopes for combined loading of strip and circular foundations on clay, *Géotechnique, Vol. 53, No. 6, 2003, p. 575-586.*

Grange S. (2013) Simplified modelling strategies for soil-structure interaction problems: The macro-element concept. *ALERT*

Doctoral School 2013 Editors: P. Kotronis C. Tamagnini S. Grange pp 195

Grange S, Kotronis P, Mazars J. (2008). A macro-element for a circular foundation to simulate 3D soil-structure interaction. *International Journal for Numerical and Analytical Methods in Geomechanics. 32:1205–1227.*

Houlsby GT, Cassidy MJ. (2002). A plasticity model for the behaviour of footings on sand under combined loading. Géotechnique 52(2):117–129.

Le Pape Y, Sieffert JG, Harlicot P (1999). Analyse non linéaire par macroéléments du comportement des fondations superficielles sous action sismique. *Comptes Rendus Du 5ème Colloque National AFPS. Cachan, France, 19–21 October; 207–214.*

Le Pape Y, Sieffert JG. (2001) Application of thermodynamics to the global modelling of shallow foundations on frictional material. *International Journal for Numerical and Analytical Methods in Geomechanics 2001; 25:1377–1408.*

Nova, R. and Montrasio, L. (1991). Settlements of shallow foundations on sand, *Géotechnique 41(2): 243-256.*

Nova R., di Prisco C., (2003). The Macroelement Concept and its Application in Geotechnical Engineering. *Proceeding of International Symposium FONDSUP 2003. J.-P. Mgnan and Droniuc editors, Paris, Presse ENPC, 1, 389-396.*

Paolucci R. Simplified evaluation of earthquake-induced permanent displacements of shallow foundations. *Journal of Earthquake Engineering 1997; 1(3):563–579.*

Pedretti S. Nonlinear seismic soil-foundation interaction: analysis and modelling method. *PhD thesis, Dpt Ing Strutturale, Politecnico di Milano, 1998.*

Prévost JH. (1978) Anisotropic stress-strain behaviour of clays. *ASCE Journal of Geotechnical Engineering. 116(8):1255–1263.*

Shirato MR, Paolucci R, Kouno T, Nakatani S, Fukui J, Nova R, di Prisco C. (2008). Numerical simulation of model tests of pier-shallow foundation systems subjected to earthquake loads using an elasto-uplift-plastic macroelement. *Soils and Foundations 48(5):693–711.*

Wood M., D., Kalasin, T. (2004). Macroelement for study of dynamic response of gravity retaining walls. *In T. Triantafyllidis (Ed.), Cyclic behaviour of soils and liquefaction phenomena: proceedings of the international conference, Bochum, Germany, 31 March-2 April 2004 (pp. 551-561). London: A. A. Balkema Publishers.*

CHAPTER 5

FIELD TRIALS ON SOFT GROUTING BARRIERS

5. Introduction

Technological interventions into the ground to mitigate the effects of vibrations have been employed in the past, mostly with reference to the effects of anthropic actions (e.g. surface vibrations induced by vehicles and rail-bound traffic). Most of the vibratory energy affecting nearby structures is carried by surface (Rayleigh) waves that propagate in a zone close to the ground surface. In this chapter an additional use of barrier filled with SAP polymer was considered. In particular the capacity of these soft barriers to mitigate the Rayleigh wave energy was investigated. Thus, the usefulness of these wave barriers is directly associated with the proper screening of the Rayleigh wave energy. Field measurements of soft-filled trenches were presented. Vibrodyne is used to produce shear waves in the certain frequency range and seismograph is used to acquire generated values. Two geometrical configuration of the barriers were considered, in the first one the barrier was constructed with an inverted pyramid shape, while in the second one a rectangular trench was created. As a deep rectangular trench is difficult to construct and maintain in practice, trenches with sloping sides have been proposed as an alternative. The screening effectiveness of those barriers is determined from field measurements by comparing site data without barriers. A FEM model was built by means of PLAXIS3D software. The results are compared and discussed.

5.2. Principle of vibration isolation systems

The vibrations due to traffic, piling, blasting, industrial activities, construction and to natural events like earthquakes can potentially damage buildings, disturb people and affect sensitive equipment and technical processes.

Barkan (1962) and Dolling (1965) were the first to report on some field investigations for studying the effectiveness of wave barriers, while these authors as well as Neumeuer (1963) and McNeill et al. (1965) described some successful applications of vibration isolation. The most comprehensive work on the vibration isolation problem was done by Woods (1967, 1968), Richart et al. (1970) and Dolling (1970a, b) who performed extensive field experiments to study the effectiveness of open trenches as Rayleigh wave barriers and provide design recommendations. The energy arising from the traffic is transmitted to the ground through body and surface waves (Woods, 1968). In a homogeneous half space medium, body waves propagate according to a spherical wave front in all directions, whereas surface waves propagate exclusively along the surface separating the two media without spreading through the inside of the earth. Consequently, the geometrical attenuation is greater for body waves than for surface waves. Miller and Pursey (1955) have calculated the distribution of the energy generated by a vertically oscillating disk for the case of an elastic half space with Poisson's ratio equal to 0.25. It appears that 67 percent of the total energy passing through the body of the transmitting medium are due to Rayleigh waves, 26 percent to shear waves, and 7 percent to compression waves. According to Woods (1968), the main problem for

foundation isolation is Rayleigh waves. Their main characteristic is their dispersive propagation pattern. Their amplitude decreases exponentially with depth and most of the energy, which propagates within a narrow zone near the surface, is roughly equal to one wavelength. Some years later, Woods et al. (1974), utilizing holographic interferometry, performed model dynamic tests to study the Rayleigh wave screening effectiveness of several types of rows of cylindrical obstructions or piles. Use of piles in cases of long Rayleigh wavelengths is the only practical solution because construction of very deep trenches required for this kind of waves is impractical. Further experimental (laboratory) studies on the use of piles as isolation barriers were also done by Liao and Sangrey (1978).

Some numerical studies have also been carried out to evaluate vibration-isolation performances of open or filled trenches (Aboudi, 1973; Al-Hussaini and Ahmad 1991, 1996; May and Bolt, 1982; Fuyuki and Matsumoto, 1980; Dasgupta et al. 1986, 1988; Luong, 1994; Kattis et al., 1999a,b; El Naggar and Chehab, 2005; Yeh et al., 1997). The open trench efficiency using the finite/infinite element method in layered soils has been evaluated by Yang and Hung (1997), and Beskos et al. (1986a,b). Plastic diaphragm wall seems also to be an efficient solution (Comina and Foti, 2007). The centrifuge model tested by Davies (1994) has been used for numerical simulation (Wang et al., 2009), with several types of barriers: open trench is the most effective one for blast-induced stress wave but geofoam barrier is more practicable as a permanent protection layer.

According to Woods (1968), wave barriers can be divided into two groups, namely, active and passive isolation systems (Figure 5.1). Barriers placed around the vibratory source are active isolation systems whereas barriers located farther from the source and close to a site where the vibratory amplitude must be reduced are defined as passive isolation systems.

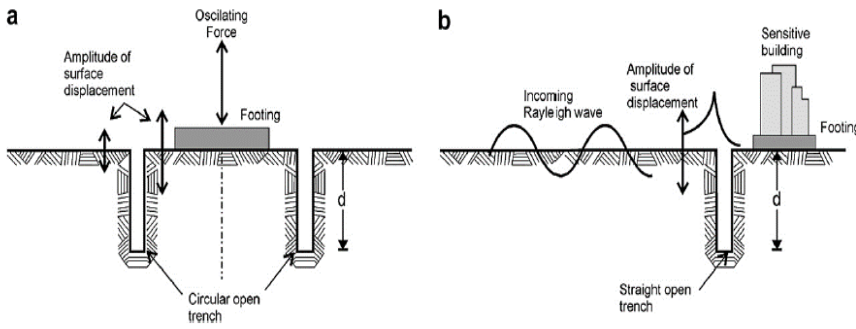

Figure 5.1 Active a) and passive b) isolation systems (Wood, 1968)

Dimensions and material properties are the most important parameters in the efficiency of isolation barriers. Experimental and numerical methods have been used to determine the influence of the geometric parameters for both active and passive isolation systems with open and in-filled barriers. Length L, width w, and depth d of the barrier as well as the distance r from the source are the main geometrical criteria to be considered for the design of isolation systems (Figure 5.2).

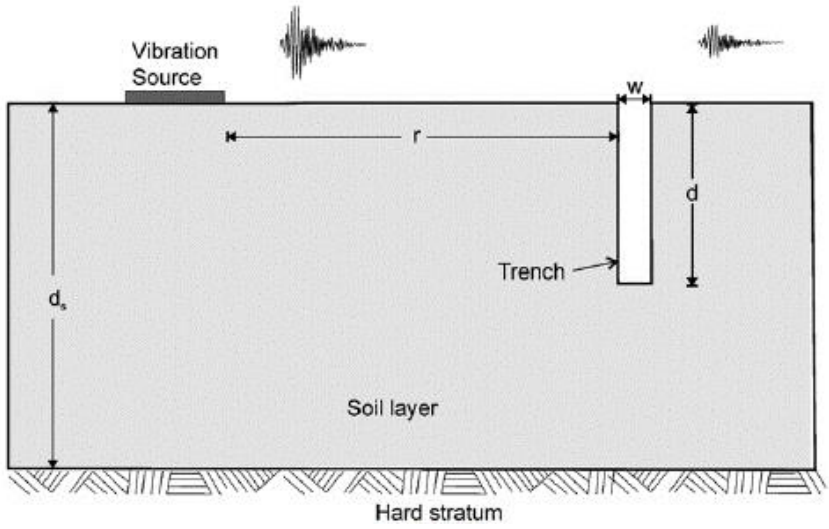

Figure 5.2 Geometrical properties for the design of isolation system

As Rayleigh waves make up the most important part of the traveling energy, and to avoid dependency of the analysis on the exciting frequency, all the geometric parameters are normalized with respect to the Rayleigh wave length λ_R.

Depth is the most important parameter for trench design. In the case of open trenches, the depth must be equal to the surface wavelength. Consequently, the use of open trenches as wave barriers is restricted to small to medium depths in order to minimize soil instability and water table level problems appearing with bigger depths. When the transmitted waves have long wavelengths, open trenches cannot be used as effective wave barriers because of their limited depth (Richart et al., 1970). May and Bolt (1982) have observed that, for an active isolation system, the influence of the distance between barrier and source is practically insignificant. The reduction of acceleration, indeed, is mainly

determined by depth. Contradictory conclusions, on the other hand, are found about the influence of width. Fuyuki and Matsumoto (1980), for example, conclude that the influence of shallow open trench width can be important whereas for Woods (1968) and Segol et al. (1978) width is not a relevant parameter.

Moreover, Woods (1968) suggests that only a small crack or slit would be sufficient to isolate elastic waves.

Trench materials depend on the type of trench, namely, open or in-filled trenches. The results of Beskos et al. (1985), Ahmad and Al-Hussaini (1991), Luong (1994), and Segol et al. (1978) investigations prove that open trenches are more effective wave barriers than infilled trenches. However, because of the open trench wall instability, this method is not very practical. In-filled trenches are more convenient for construction than open trenches. The construction procedure is simple and very little or even no maintenance is required for this type of system. Concrete, bentonite, soil bentonite mixtures are the most common filling materials (Al-Hussaini and Ahmad, 1996). However, other materials such as rubber modified asphalt and EPS have also been used to fill the trench (Zeng et al., 2001; Zhong et al., 2002; Itoh, 2003; Itoh et al., 2005). Massarsch (1991) introduces the concept of the gas cushion barrier using a self hardening cement bentonite. The efficiency study here reveals that the performances are comparable to those obtained with open trenches. Itoh et al. (2005) have conducted centrifuge tests to evaluate the efficiency of barriers made of either aluminium or geofoam. Their conclusion demonstrates that barriers made of geofoam materials are more effective for a wide range of depth values than aluminium

barriers. Furthermore, the aluminium barriers seem to be an ineffective way for reducing vibrations. Wang et al. (2006) have studied the use of geofoam inclusions as wave barriers for the reduction of blast effects. They concluded that the existence of EPS geofoam inclusions affects the attenuation of stress waves in a concrete layer barrier. The impedance ratio (IR) used by geotechnical engineers for distinguishing whether a barrier is soft or hard is introduced here,

$$IR = \frac{\rho_b \cdot V_b}{\rho_s \cdot V_s} \qquad 5.1$$

where ρ_b and ρ_s denote the mass density of the barrier and the soil, respectively, and V_b and V_s the wave velocities of the two. A barrier is soft if IR<1, while it is stiff if IR>1.

The screening effect of the wave barriers can be evaluated using the amplitude reduction ratio A_r defined as the ratio between the vertical displacement amplitude of ground surface with the barrier and the vertical displacement amplitude of ground surface without the barrier.

If one is interested in the response of the soil over some range r beyond the barrier, the average amplitude reduction ratio $\overline{A_r}$ should be used instead:

$$\overline{A_r} = \frac{1}{r}\int A_r(x)\,dx \qquad 5.2$$

Trench barrier efficiency is satisfactory when A_r is lower or equal to 0.25 (Woods, 1968; Richart et al., 1970). This was achieved with a

trench of depth at least 0.6 times the wavelength of Rayleigh waves. Yang and Hung (1997) have conducted a parametric study of the in-filled barrier. The property of the in-filled material is included as one of the parameters of the investigation. Figure 5.3 shows the effect of the impedance ratio IR for in-filled trench.

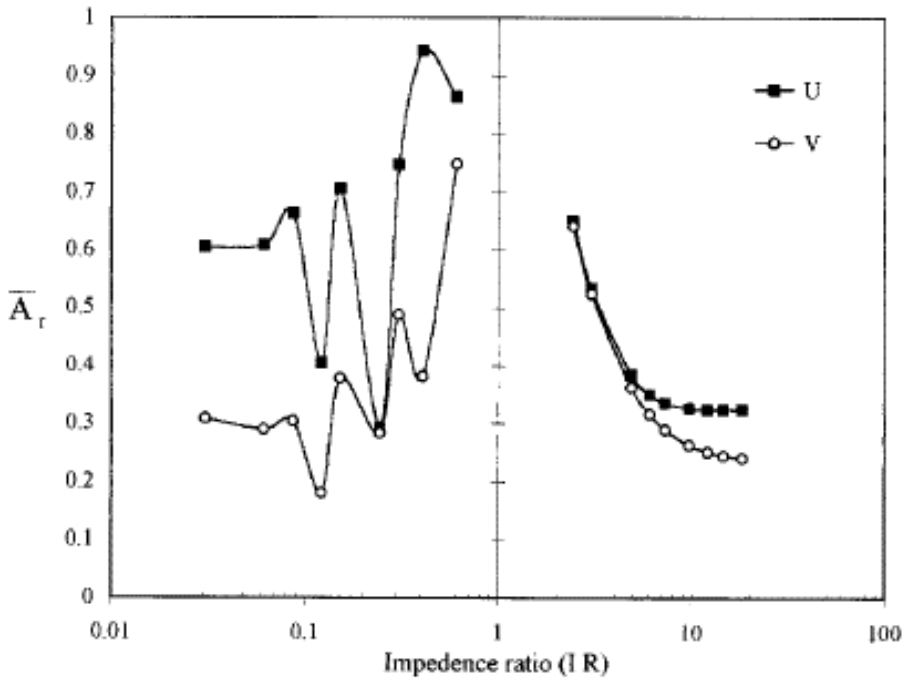

Figure 5.3 Effect of impedance ratio for in-filled trench (Yang and Hung, 1997)

The right-hand part shows the average amplitude reduction ratio $\overline{A}_r$ against the impedance ratio IR for stiffer trenches, i.e., with IR>1 (compared with soil). As can be seen, the increasing of IR can result in improved screening effect. However, a limit of $\overline{A}_r$ 0.32 and 0.24, respectively, is approached for the horizontal and vertical responses, as

the barrier gets harder. In addition, the results obtained for the case with IR<1 for softer trenches have been shown on the left-hand part of Figure 5.3

. Although there is no monotonic decrease of $\overline{A_r}$ as IR decreases for the range IR<1, better screening effect can generally be achieved as the trench become softer in a rough sense.

5.3. Test site investigation

The case study site is in Naples (Italy) (Figure 5.4). Properties of the local soil conditions should be determined to investigate isolation effect of the wave barriers accurately.

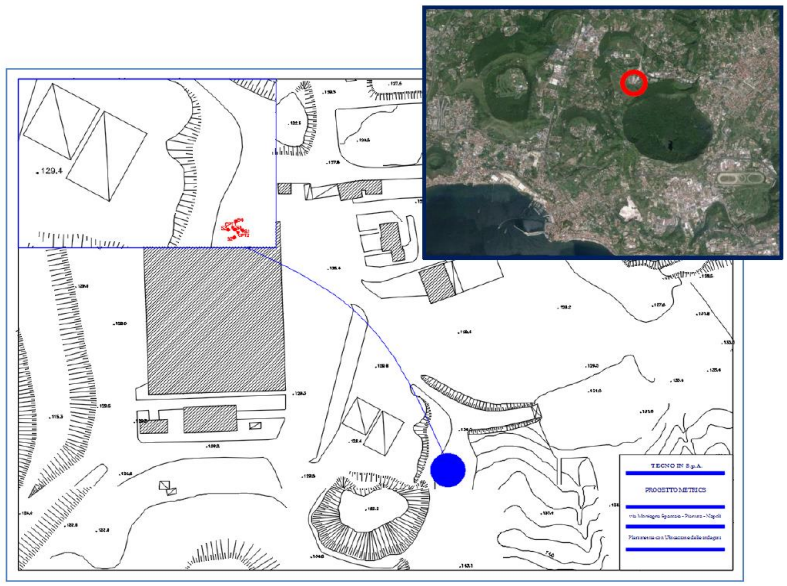

Figure 5.4 Location of test site

Five boreholes were drilled at points close to centre (S5) and four corners of the site (S1, S2, S3, S4), as shown in Figure 5.5. Cone penetration tests (CPT) were realized between boreholes S1 and S2 and between S3 and S4, up a depth of 9 m, to provide a clear view of geotechnical subsurface conditions.

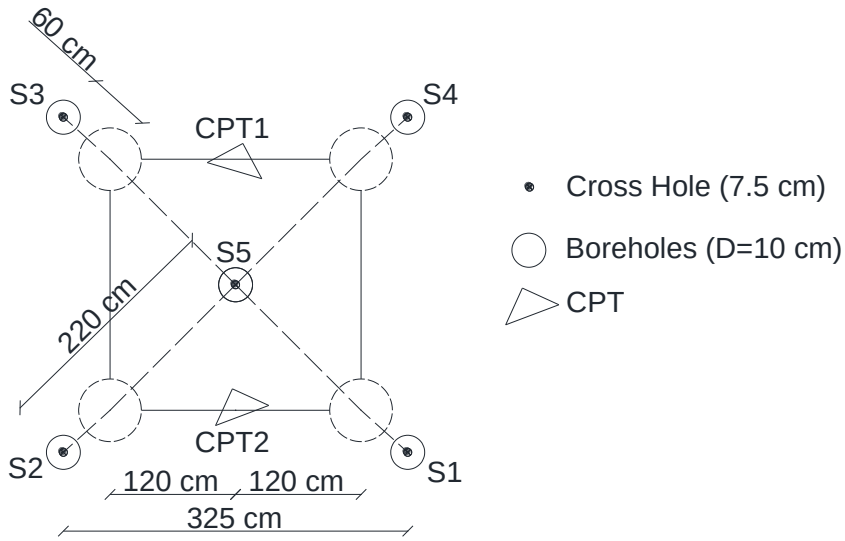

Figure 5.5 Testing for ground characterization

Figure 5.6 shows the construction of a general stratigraphic model of S1 borehole and the cone tip resistance (Q_c) corresponding to the soil resistance per unit area to penetration, obtained from CPT test. Ground conditions mainly consists of pyroclastic gravelly and silty sand underlying a layer of pumice of about 1m, above a deep groundwater level. In order to determine dynamic characteristics of the site, cross-hole tests were carried out, by putting a 3-component borehole geophone down central hole while lowering a source down adjacent

holes (on the vertex), firing the source at some prescribed depth interval. The source and geophone are always at the same elevation, and the energy from each shot is measured at a single depth in each receiver hole.

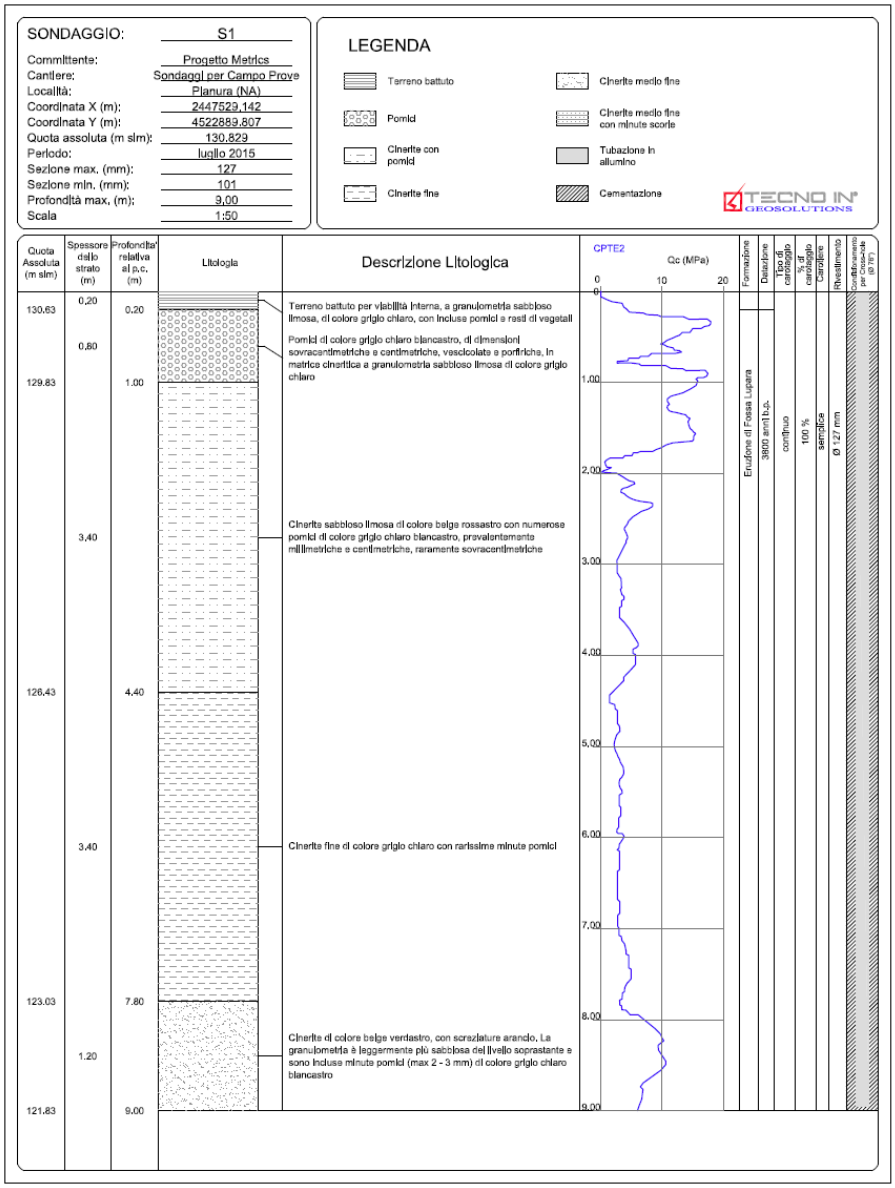

Figure 5.6 Stratigraphic model of S1 borehole and the cone tip resistance

These tests provide detailed seismic P- and S-wave velocity information between boreholes. The shear and compression wave velocity profiles were demonstrated in Figure 5.7.

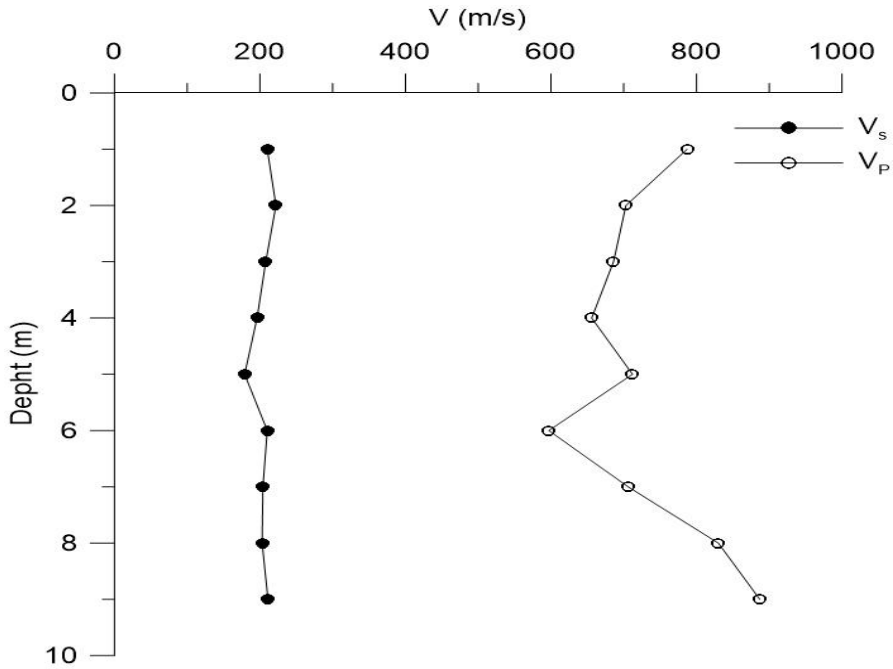

Figure 5.7 Shear and compression wave velocity profiles of the site

The properties of the idealized soil profile obtained from CPT and cross-hole test are summarized in Table 5.1.

Table 5.1 Properties of the soil profile

Material	φ (°)	E (kN/m^3)	G(kN/m^3)	V_s (m/s)
Layer 1	37	211558	72818	213

Layer 2	30	114700	62252.1	187.5
Layer 3	32	151900	68558.4	207

Later, a column made by SAP material was realized between boreholes S5 and S3 (Figure 5.8), in order to verify the influence of the SAP column on the wave propagation.

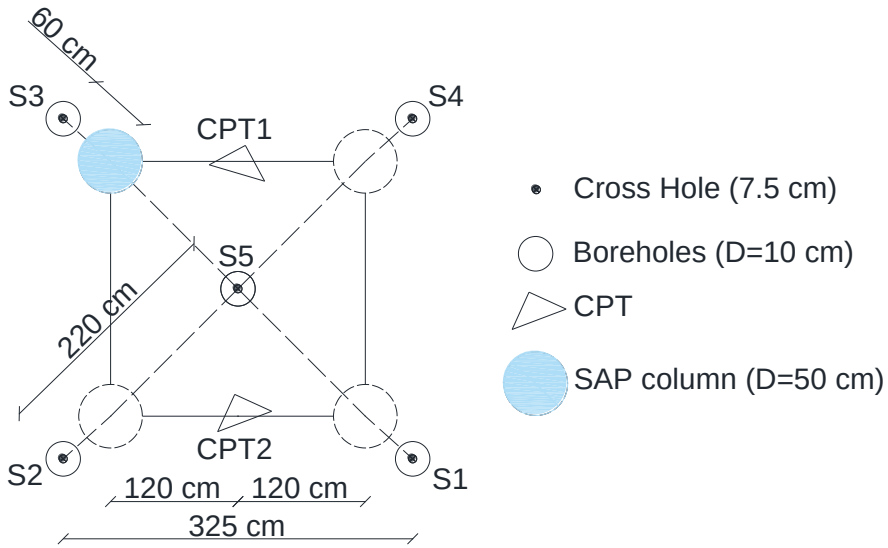

Figure 5.8 Testing for characterization of SAP column

A cross-hole test was performed between S5 and S3, from which it was possible to evaluate the shear wave velocity of the SAP material equal to 27 m/s.

Then the impedance ratio (IR) calculated for such a barrier was equal to 0.08 that is an indicator of a very soft barrier.

5.4. Soil testing equipment for field applications

Although an open trench has been shown to give the best isolation performance, in practice an open trench could not be stable. One method to ensure its stability is to fill the trench with a material that is relatively soft compared with the surrounding soil, yet is sufficiently stiff to sustain the confining pressure of the soil. A SAP polymer is considered to fill the trenches, the properties of which are listed in Table 5.2 Properties of SAP polymer.

Table 5.2 Properties of SAP polymer

E (Mpa)	G (Mpa)	ν	ρ (kg/m^3)	V_S (m/s)	V_P (m/s)
2.2	0.729	0.49	1000	27	46

As mentioned before, two barrier were realized. The first barrier was created with inverted pyramid shape, with dimensions reported in *Figure 5.9*. After the excavation, the SAP material was put in bags, placed along the boundaries of the barrier. Finally, the excavation was filled with the soil (Figure 5.11 a, b).

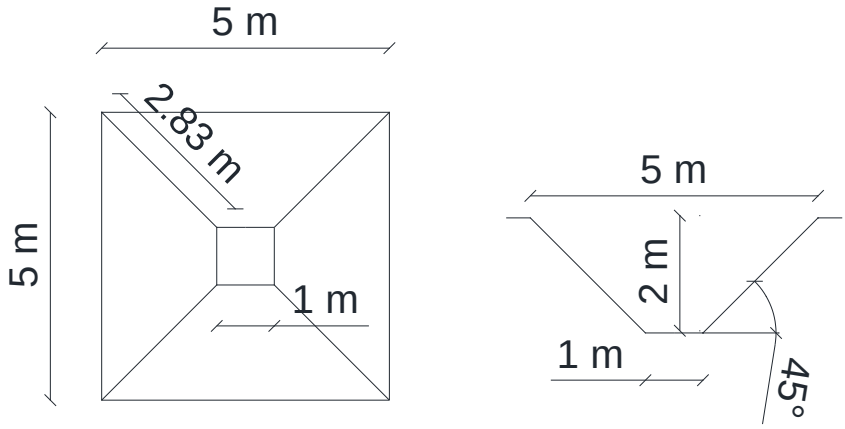

Figure 5.9 Layout of inverted pyramid barrier

The second barrier realized was an in-filled rectangular trench (Figure 5.10), placed at distance from the truncated conic barrier equal to 10 meters. In this configuration, the SAP material was placed directly (without bags) in the excavation (Figure 5.11 c, d). The source was placed between the barriers at small distance of both of them (5m), in order to use the barrier as an active isolation system.

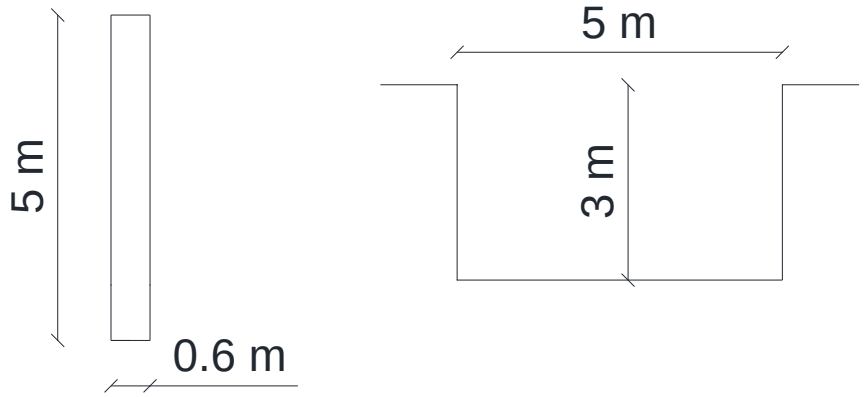

Figure 5.10 Layout of rectangular trench barrier

The amplitudes of vibrations were measured by highly sensitive accelerometers. Four accelerometers (#1 - #4) were placed in the field for different location plans. In Figure 5.13 were reported the layouts of the two models, with an indication of the instrumentation and of the distances. All the components of harmonic vibrations are recorded and stored in computer by using signal calculator program.

Vibrodyne shaker, which induces a sinusoidal motion, is used as a stationary vibration source to produce harmonic force of maximum amplitude of 710 N, in vertical direction, in a frequency range of practical importance of 10–20 Hz.

a) b)

c) d)

Figure 5.11 Photos of barriers: (a) (b) inverted pyramid barrier and (c) (d) rectangular barrier.

In the present study, continuous vibrations having frequencies of 10 Hz, 14 Hz and 20 Hz were generated to observe the effect of operating frequency. In the vibrodyne device, there is a spinning mass.

It can be express the amplitude and the frequency achievable as a function of the applied mass according to the equation:

$$P = A^2 \cdot \omega^3 \cdot M \qquad 5.3$$

where:

P is the power expressed in Watt

A is the amplitude of the sinusoidal signal expressed in meter

ω is the angular frequency

M is the mass expressed in kg.

The mass applied in these field tests is equal to 45 kg.

A concrete surface footing (0.80mx0.80mx0.80m) was constructed at distance of 5 m from both of the barriers, to guarantee an effective transmission of the waves (Figure 5.12).

The vibrodyne is mounted and placed centrically above the rigid square footing.

Figure 5.12 Photo of the vibration source

First of all, continuous vibrations were originated in designated frequencies and the amplitudes were measured at specific points in the absence of the wave barrier. Thus, attenuation characteristics of the site for different excitation frequencies could be determined independent from the wave barrier. Later, the barriers were excavated and filled with SAP polymer. Then, vibration tests were carried out in the same procedure as in case of no trench. Thereby, the effect of barrier could be observed in terms of screening effectiveness.

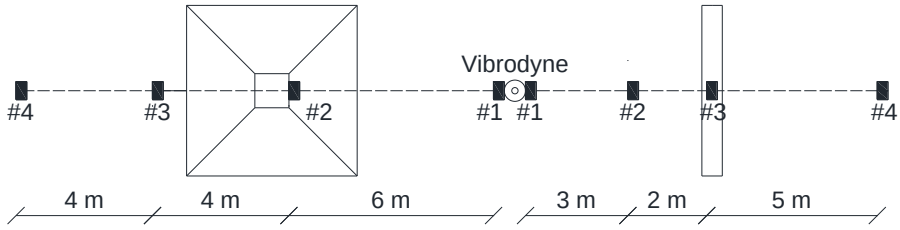

Figure 5.13 Layout of site experiments for different barriers

5.5. Input signals

The main properties of the input signals adopted in the field tests are summarized in Table 5.3.

Table 5.3 Characteristics of the applied shaking signal

Signal	Amplitude (N)	Frequency (Hz)	Dt (s)	Duration (s)
1	188	10.3	0.0005	90
2	348	13.8		
3	710	20.5		

The frequency of 20 Hz represents the maximum value achievable by the vibrodyne used. The three components of signal 1 (10.3 Hz), signal 2 (13.8 Hz) and signal 3 (20.5 Hz) recorded by the accelerometer located at the base of the square rigid footing, are shown in the following figures (Figure 5.14, Figure 5.15, Figure 5.16).

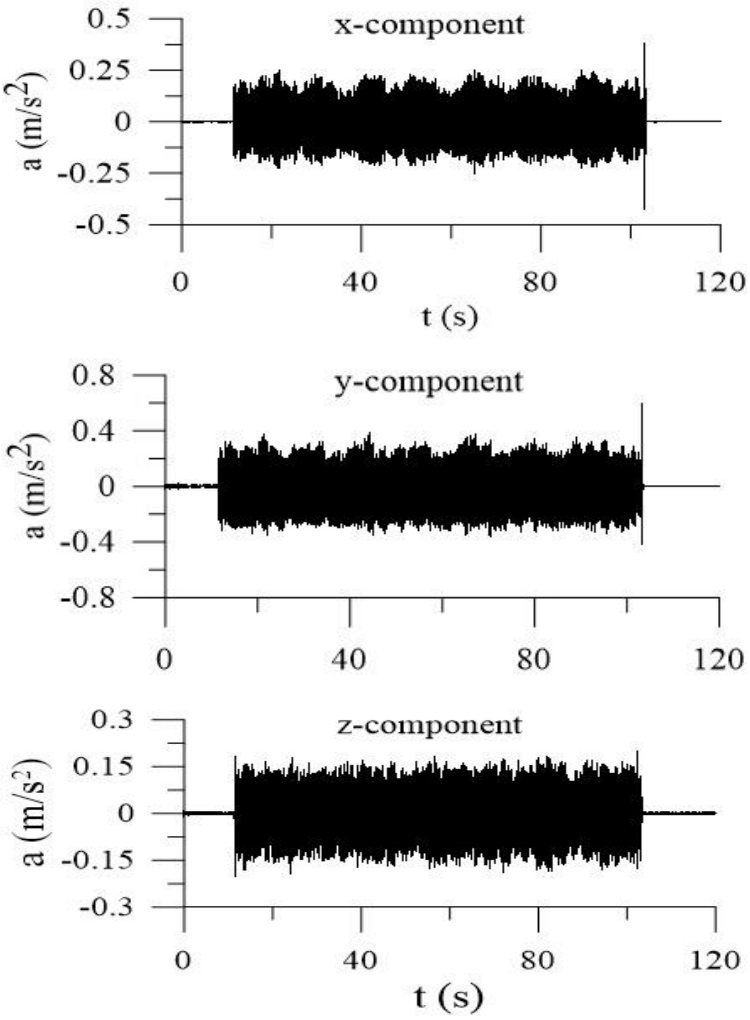

Figure 5.14 Components x, y and z of the signal 1

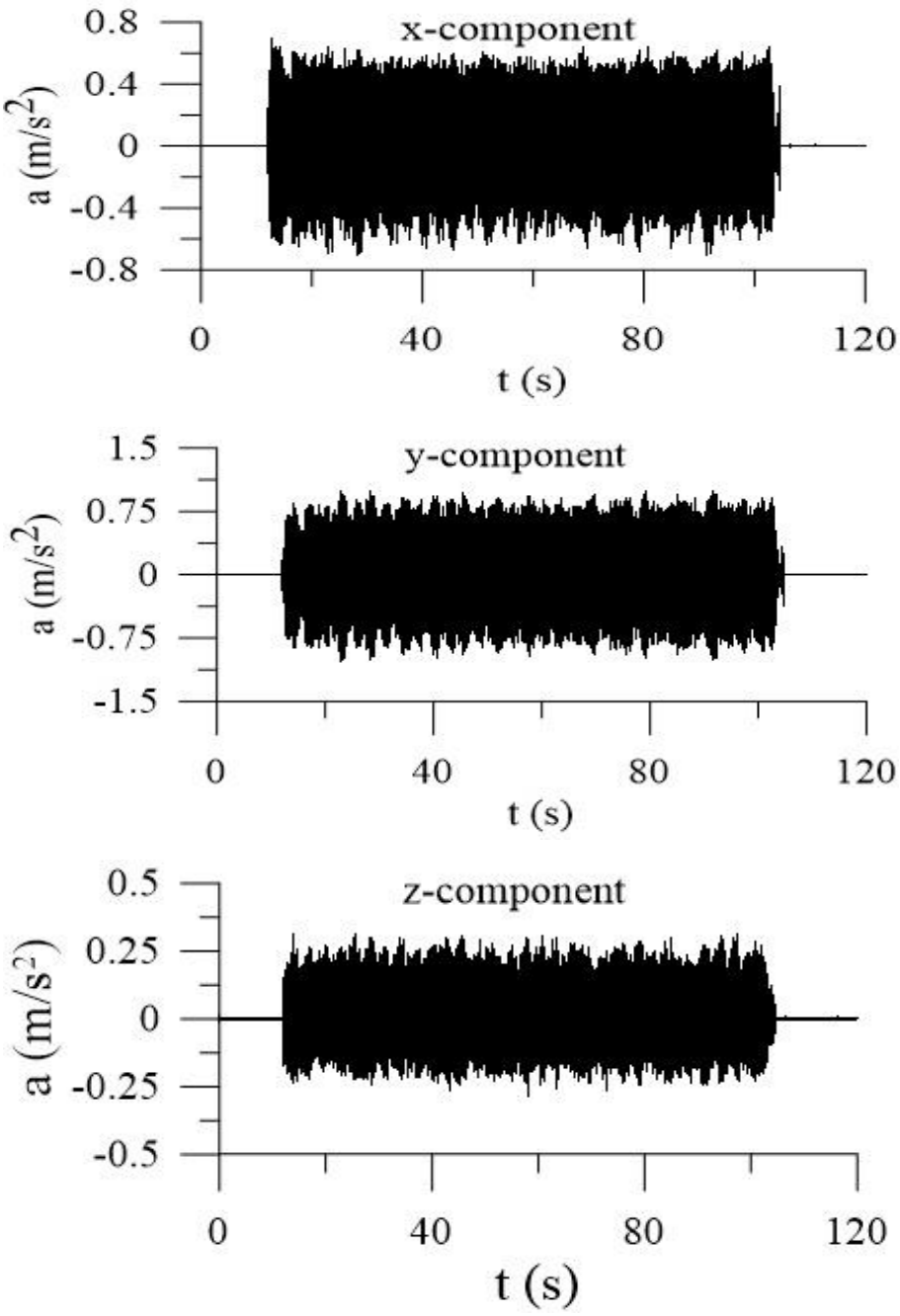

Figure 5.15 Components x, y and z of the signal 2

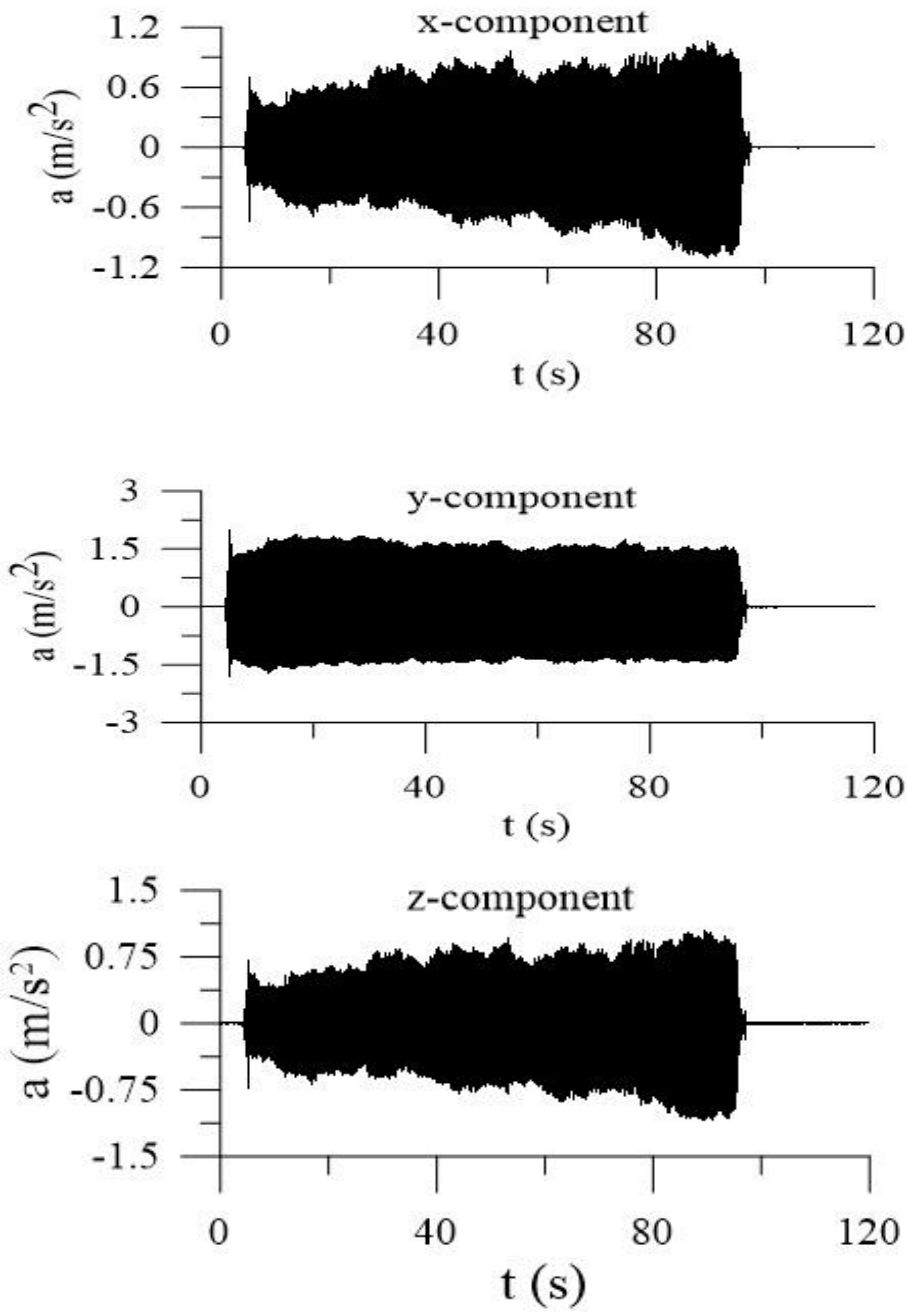

Figure 5.16 Components x, y and z of the signal 3

Since vibration isolation by a trench is primarily achieved by screening of surface (Rayleigh) waves, the depth, width, and distance of the trench from source are normalized with respect to the Rayleigh wavelength (H = Ht/λ_R, W = Wt/ λ_R, L=Lt/ λ_R where λ_R =Rayleigh wavelength) (*Table 5.4*). Using the data for soil reported in Table x, the Rayleigh wave velocity is

$$V_R = V_S \frac{0.87 + 1.12 \cdot \nu}{1 + \nu} \qquad 5.4$$

and the Rayleigh wave length is

$$\lambda_R = \frac{V_R}{f} \qquad 5.5$$

With reference to the rectangular barrier shown in Figure 5.10 the parameters summarized in *Table 5.4* are adopted.

Table 5.4 Trench dimensions normalized with Rayleigh wavelength (λ_R)

Frequency (Hz)	V_R (m/s)	λ_R (m)	H=H/λ_R	W=W_t/λ_R	L=L_t/λ_R
10.3	202.8	19.69	0.15	0.03	0.25
13.8		14.70	0.20	0.04	0.34
20		10.14	0.29	0.06	0.49

5.6. Field tests results

The efficacy of a barrier to mitigate the vibration is usually expressed in terms of amplitude reduction ratio A_r (section 5.2), which is the ratio of the vertical displacement amplitudes at the point in the presence and in

the absence of the barrier. All the components of the accelerations and displacements were considered here for both of the schemes, so the amplitude reduction ratio in terms of displacements was named $A_{r,i}$ while in terms of accelerations $\eta_{r,i}$, with i=x, y, z.

The amplitudes of vibrations were measured in terms of acceleration in the absence and presence of wave barrier. The displacement amplitudes are computed from the acceleration data. The noise in the signals recorded during the test was eliminated during signal processing by digital filtering with a high-pass filter.

5.6.1. Inverted pyramid barrier

The layout of the test with indication of the accelerometers (#1, #2, #3, #4) and their distance from vibrodyne source, is shown in figure.

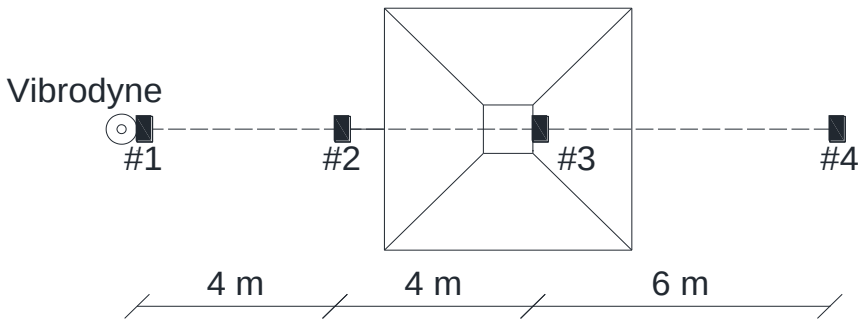

Figure 5.17 Layout of the test

The vertical component of the acceleration time histories recorded, with and without barrier, by accelerometer #4, for the three input signals, were shown in figure. It is evident the reduction of the amplitude of the acceleration recorded for all the input signals.

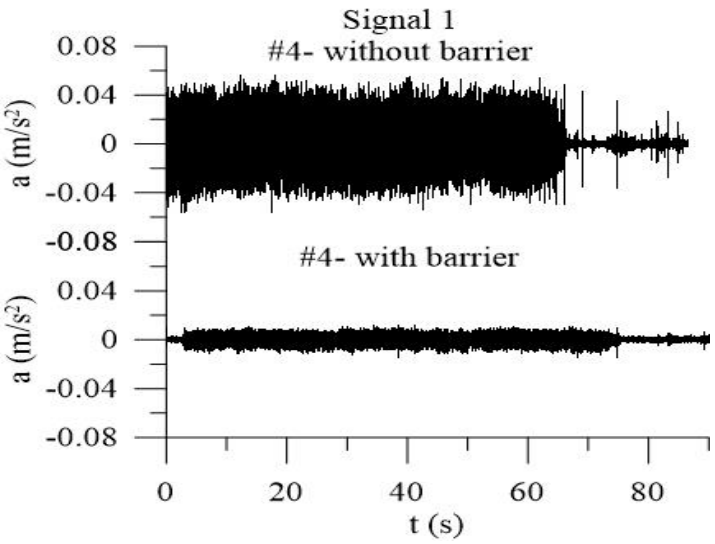

Figure 5.18 Vertical component of the acceleration time histories recorded by accelerometer #4 (Signal 1)

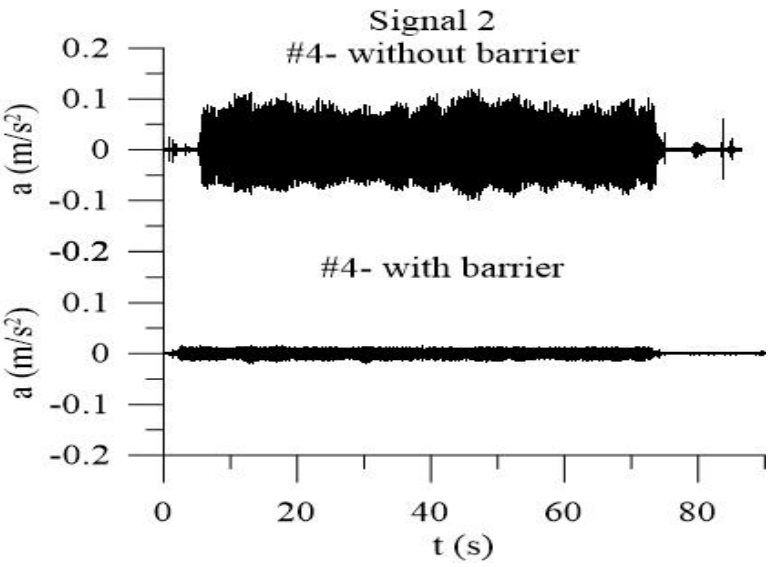

Figure 5.19 Vertical component of the acceleration time histories recorded by accelerometer #4 (Signal 2)

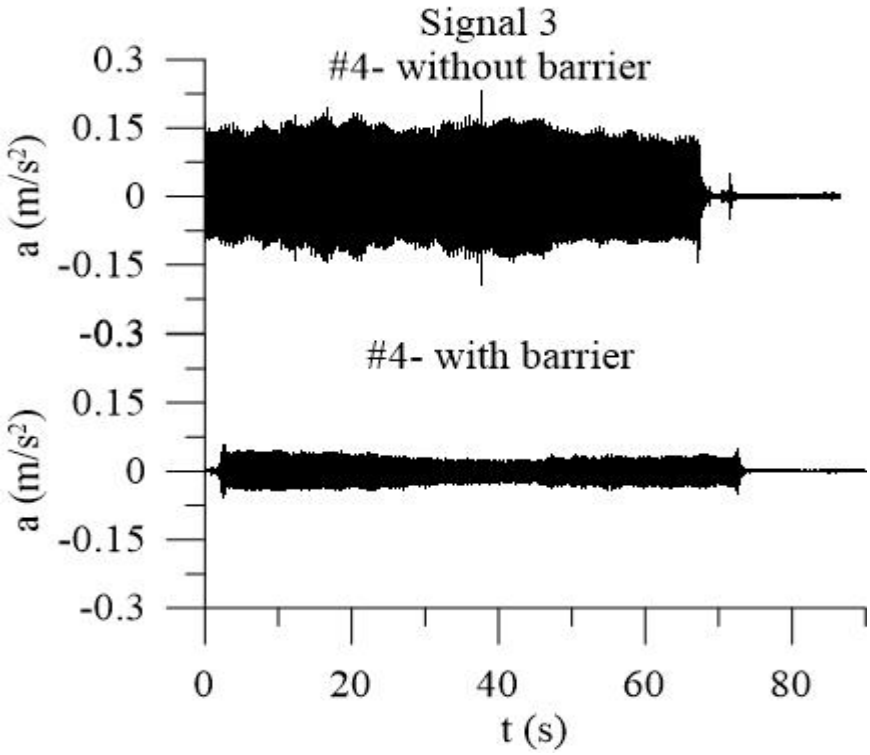

Figure 5.20 Vertical component of the acceleration time histories recorded by accelerometer #4 (Signal 3)

Attenuation of acceleration ($\eta_{r,i}$) and displacement ($A_{r,i}$) with distance from vibration source divided by the Rayleigh wavelength was demonstrated in Figure 5.21 and Figure 5.22. In this manner, it is possible to understand the evolution of the wave propagation. For all the components of the signals, there is an amplification effect before the barrier, more obvious for the vertical component, for which the amplification increases as the frequency of the signal increases, which

indicates the presence of strong reflected waves of similar wavelength traveling in the opposite direction of the incident Rayleigh waves.
Just inside the inverted pyramid barrier, the amplitude of the signals decreases until after the barrier.

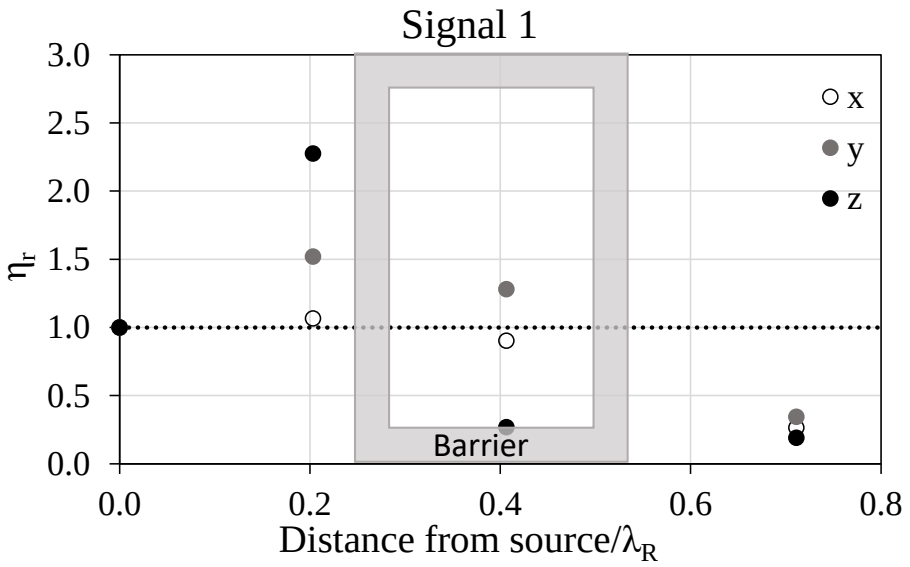

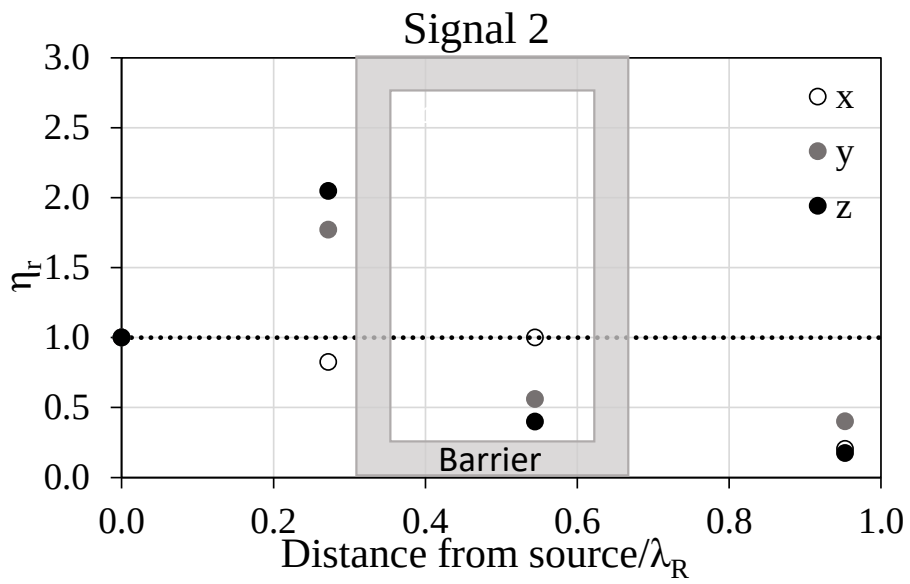

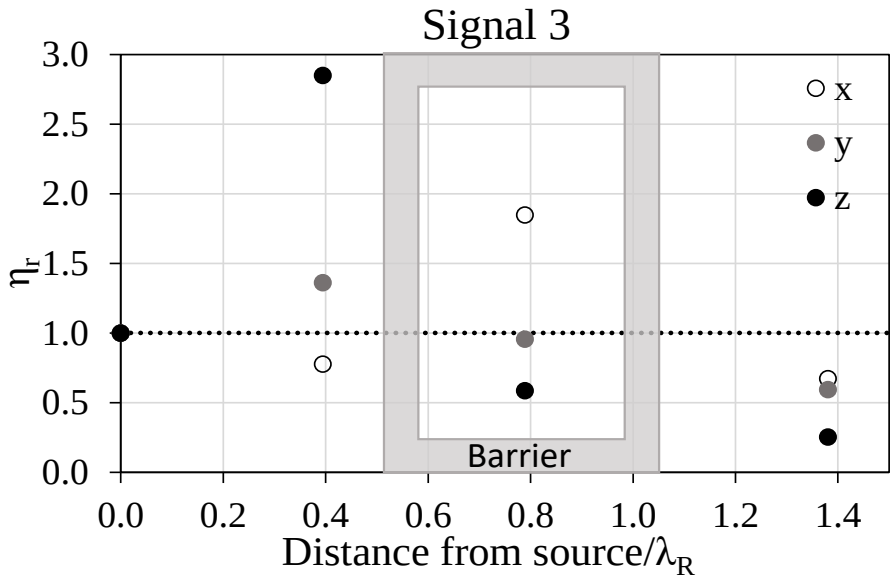

Figure 5.21 Attenuation of acceleration ($\eta_{r,i}$) with distance from vibration source divided by the Rayleigh wavelength for the three input signals

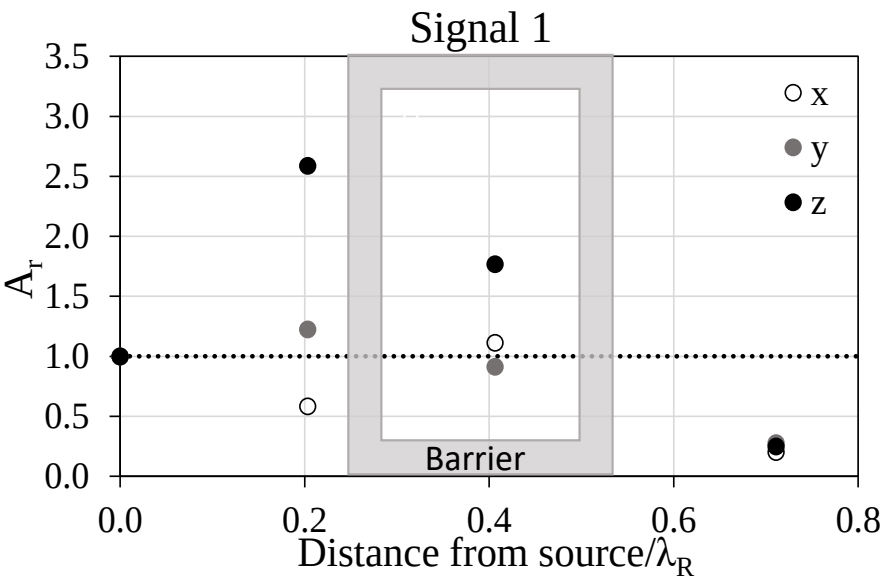

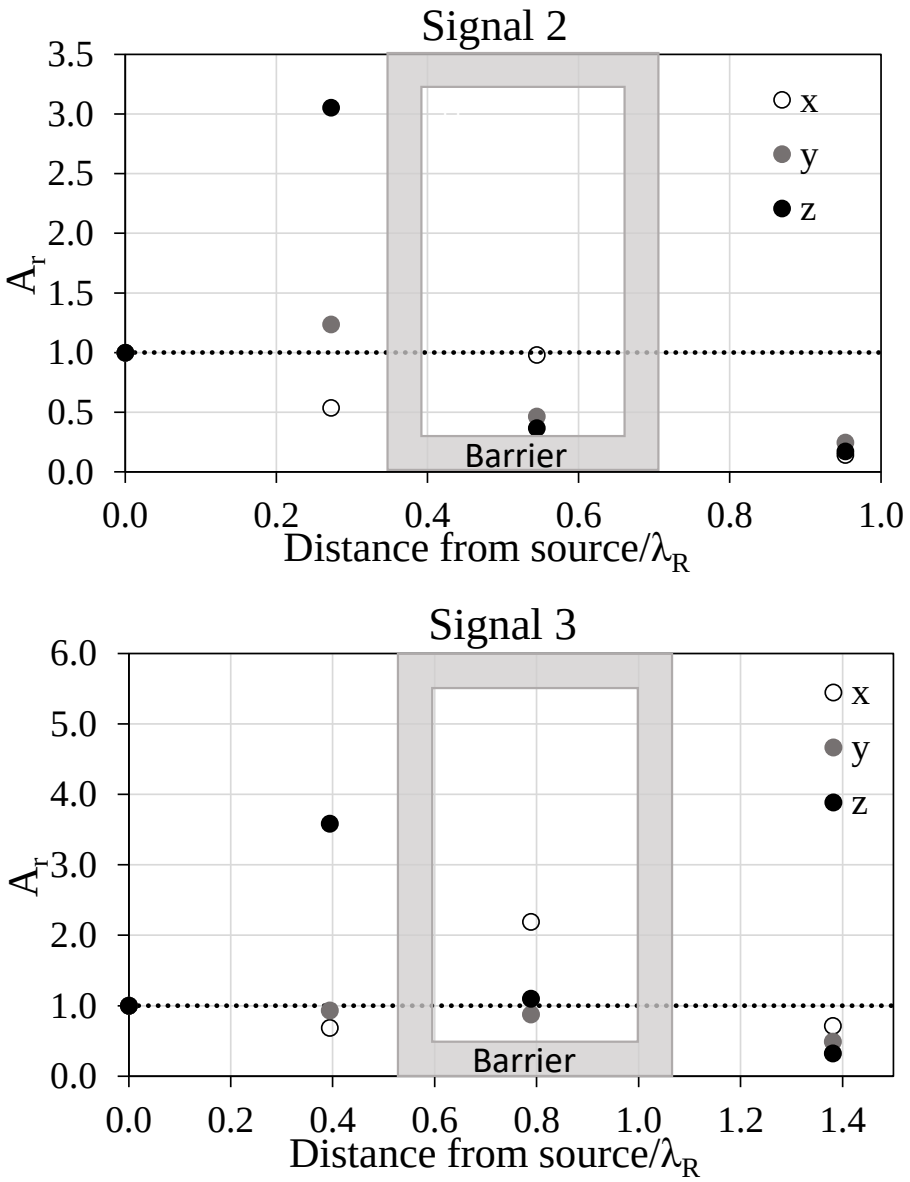

Figure 5.22 Attenuation of displacement ($A_{r,i}$) with distance from vibration source divided by the Rayleigh wavelength

At all considered source frequencies, the barrier causes significantly reduction of the soil vibrations, as shown in Table 5.5 where the amplitude reduction ratio was calculated.

Since vibration isolation was expected behind the trench, amplitude reduction ratios for each test series were calculated at points #4.

Table 5.5 Amplitude reduction ratios

Amplitude reduction ratio					
Signal	f (Hz)	#2	#3	#4	Average
1	10.3Hz	2.59	1.77	0.23	0.33
2	13.8Hz	3.05	0.37	0.17	0.26
3	20.5Hz	3.58	1.10	0.32	0.36

The values are between 0.17 and 0.32, that indicates a good isolation performance of the pyramid barrier given that the Wood criteria for the effectiveness of the open trench is Ar<0.25.

5.6.2. Rectangular barrier

The layout of the test with indication of the accelerometers (#1, #2, #3, #4) and their distance from vibrodyne source is shown in Figure 5.23.

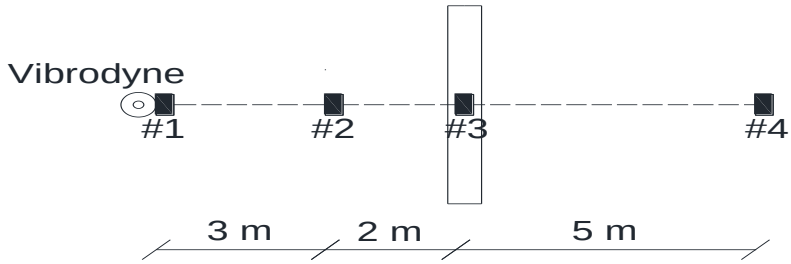

Figure 5.23 Layout of the test

The vertical component of the acceleration time histories recorded, with and without barrier, by accelerometer #4, for the three input signals, were shown in Figure 5.24

. It is evident the reduction of the amplitude of the acceleration recorded for all the input signals.

Attenuation of acceleration ($\eta_{r,i}$) and displacement ($A_{r,i}$) with distance from vibration source divided by the Rayleigh wavelength was demonstrated in Figure 5.25 and Figure 5.26. In this case, the effect of wave reflection is even more evident, causing a high amplification in the soil between the source and the barrier.

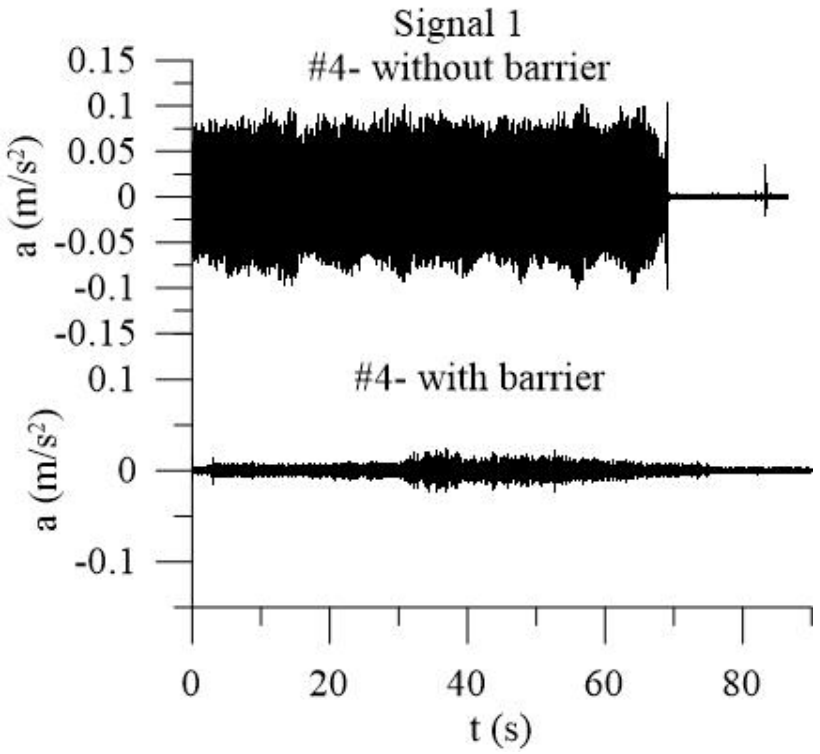

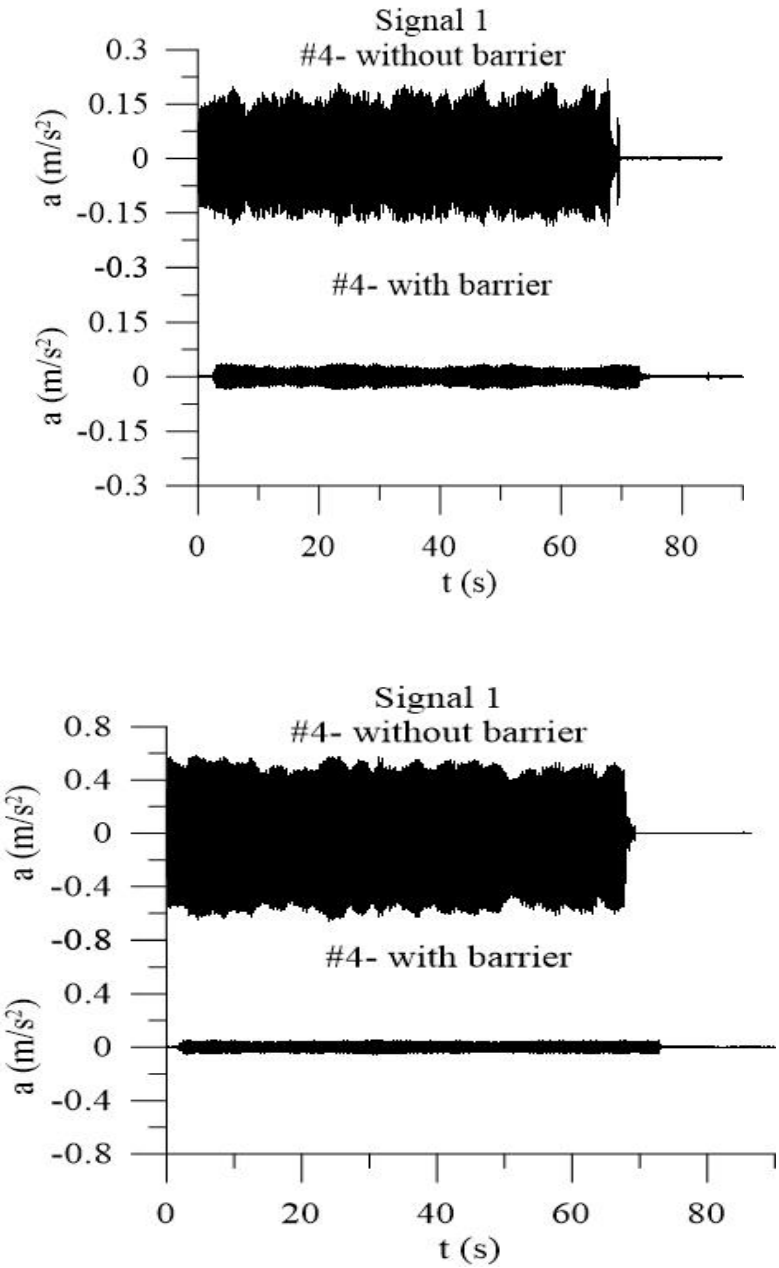

Figure 5.24 Vertical component of the acceleration time histories recorded by accelerometer #4 for the three input signals

In this case, all the three components of both acceleration and displacement seem to be highly reflected, while for the pyramidal barrier the z components were the ones having the highest reflection ratio. This may be related to the fact that the rectangular barrier is orthogonal to the radiating Rayleigh waves, thus causing a reflection angle of 180°, while the pyramidal barrier has sloping sides that generate a reflection angle<180°, thus moving the energy away from the surface. The instruments placed beyond the barrier measure accelerations and displacements much lower than the ones caused by the source in free field conditions, thus indicating a good screening efficiency.

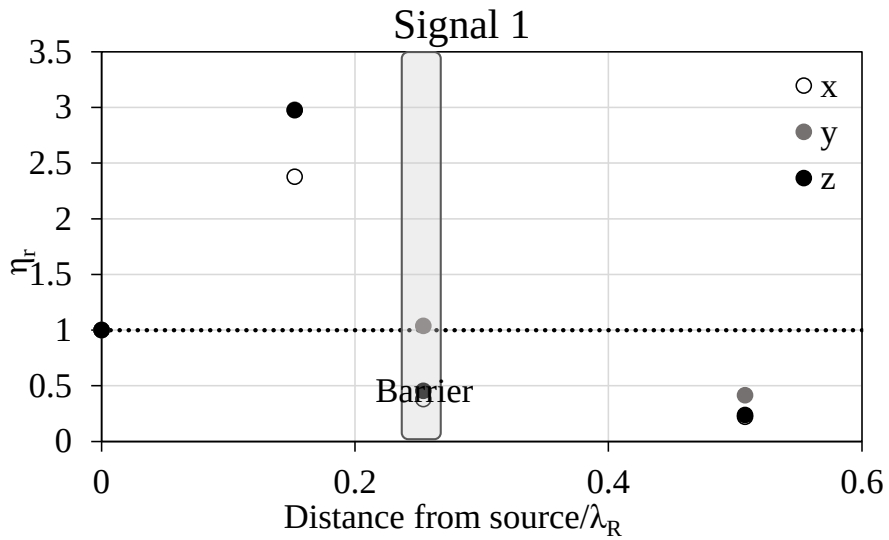

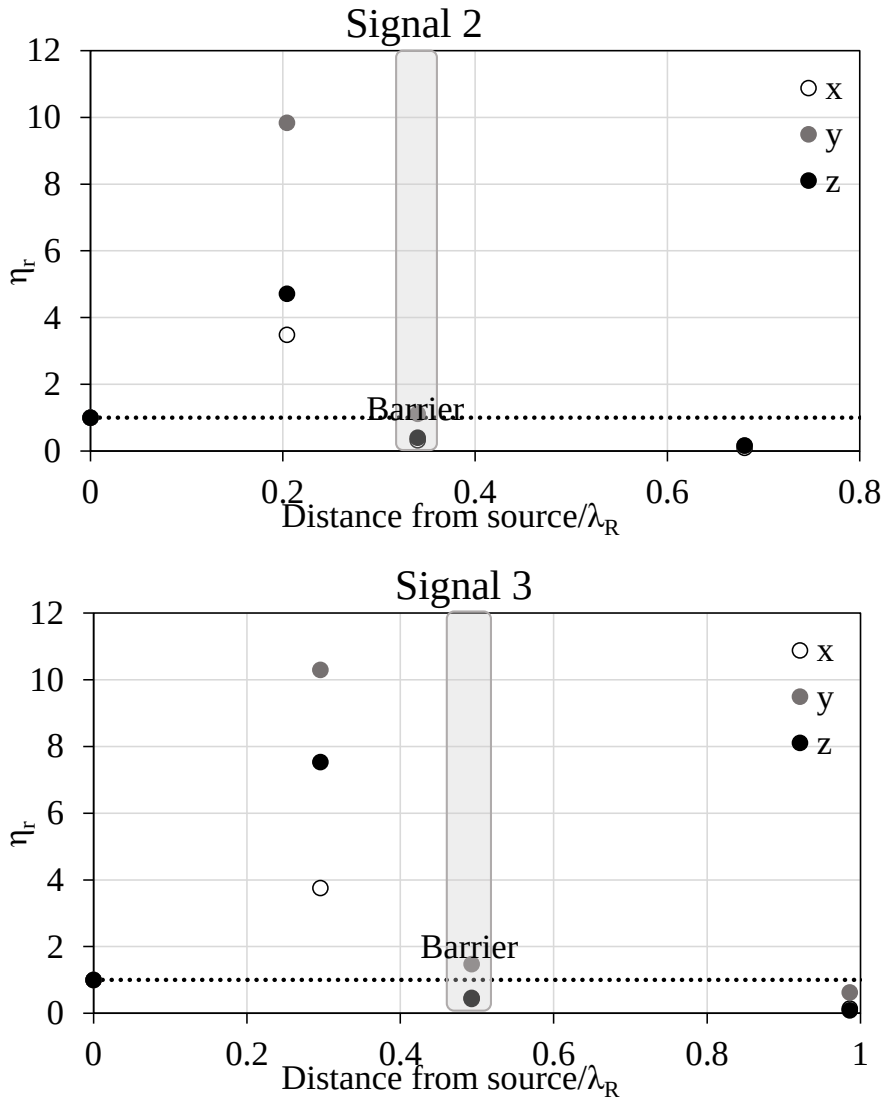

Figure 5.25 Attenuation of acceleration ($\eta_{r,i}$) with distance from vibration source divided by the Rayleigh wavelength

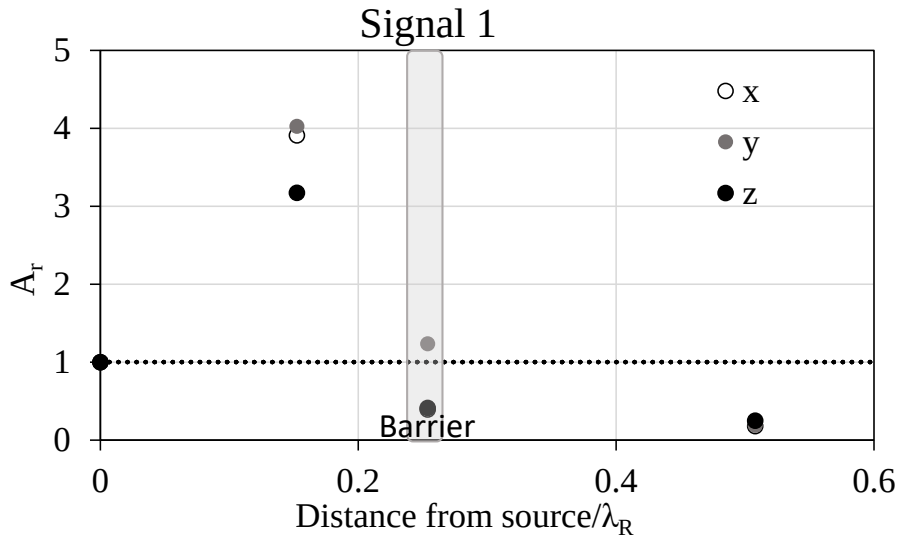
Signal 1
5
4
3
2
1
0
A_r
x
y
z
Barrier
0
0.2
0.4
0.6
Distance from source/λ_R

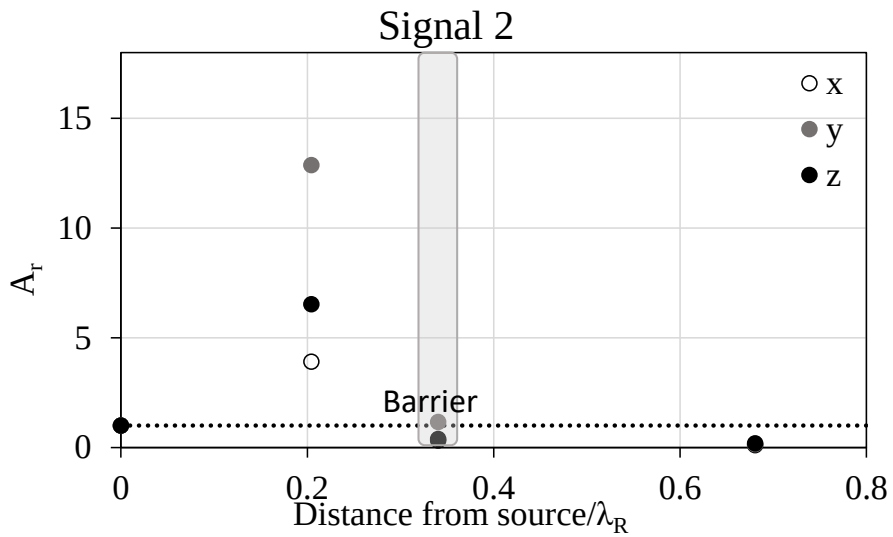
Signal 2
15
10
5
0
A_r
x
y
z
Barrier
0
0.2
0.4
0.6
0.8
Distance from source/λ_R

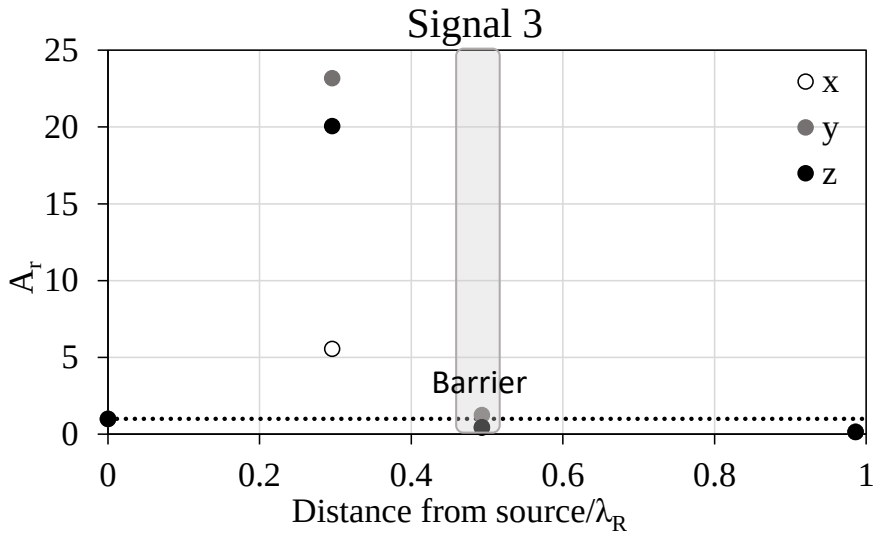

Figure 5.26 Attenuation of displacement ($A_{r,i}$) with distance from vibration source divided by the Rayleigh wavelength.

At all considered source frequencies, the barrier causes significantly reduction of the soil vibrations, as shown in Figure 5.26Table 5.6 where the amplitude reduction ratio was calculated.

Since vibration isolation was expected behind the trench, amplitude reduction ratios for each test series were calculated at points #4.

These values are between 0.29 and 0.33.

Table 5.6 Amplitude reduction ratio

Amplitude reduction ratio					
Signal	f (Hz)	#2	#3	#4	Average
1	10.3Hz	3.17	0.41	0.25	0.33
2	13.8Hz	6.53	0.38	0.19	0.29
3	20.5Hz	20.05	0.46	0.32	0.39

For open trench Woods (1968) and Dasgupta et al. (1990) suggested that the normalized trench depth should have been at least 0.6 for reasonable vibration isolation (Ar<0.25). The normalized trench depths of this in-filled barrier are 0.15, 0.20 and 0.29 (respectively for input signal of 10Hz, 14Hz and 20Hz), therefore smaller than 0.6. Despite that, the rectangular barrier shows a comparable screening perform.

5.7. Numerical simulation of the field tests

3D numerical simulations of the two field tests were performed by the FE code Plaxis (section §2.10.1) (Brinkgreve et al, 2007). The soil was modelled with an elastic perfectly plastic constitutive model. The value of the model parameters were selected consistently with the results of the site characterization. A small-strain damping of the sand (D_0) was modelled through the Rayleigh formulation, through the coefficients α_R and β_R, estimated using the "double frequency approach" suggested by Park and Hashash (2004), are calibrated on the basis of the field tests. The adopted values of parameters are summarized in Table 5.7.

Table 5.7 Parameters adopted in the numerical analyses

Material	φ (°)	E (kN/m^3)	G(kN/m^3)	V_s (m/s)
Layer 1	37	211558	72818	213
Layer 2	30	114700	62252.1	187.5
Layer 3	32	151900	68558.4	207

The soft barrier was modelled as an elastic-perfectly plastic Mohr-Coulomb material. The adopted values of parameters are summarized in Table 5.7. In the field tests, the barriers were built simultaneously, hence in the calibration phase this aspect was considered by modelling both barriers in the model. *Figure 5.27* depicts the model in Plaxis3D with the two configurations of the barrier.

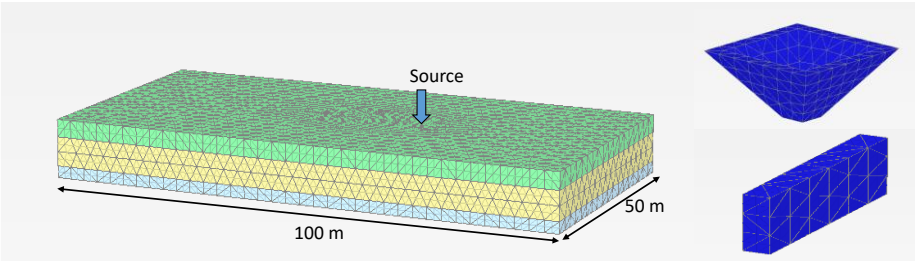

Figure 5.27 Geometry of the model in Plaxis3D, (a) inverted pyramid barrier, (b) rectangular trench barrier

The mesh generated is refined in proximity of the barriers and on the source. The recorded signals at the base of the concrete footing (accelerometer #1) were used as the input motion applied at the top boundary of the FE mesh, to generate surface waves. Bottom and right dynamic boundaries of the model are set to be *viscous*.

The results of the calibration phase are reported in Figure 5.28 for the signal 1 (10Hz) for both of the barrier in terms of attenuation of acceleration (η_r).

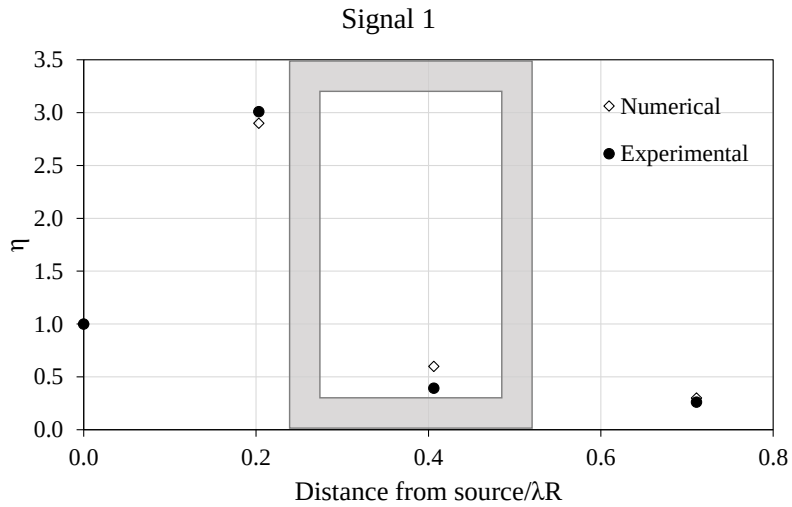

Figure 5.28 Results of the calibration for the inverted pyramid barrier

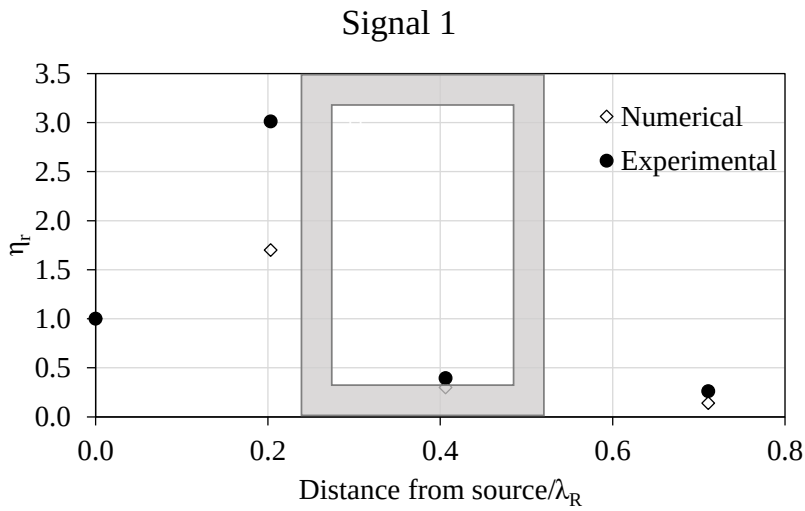

Figure 5.29 Results of the calibration by considering only the presence of the one barrier

After calibration, the same analysis was carried out by activating one barrier and differences were observed (Figure 5.29).

It is evident that the simultaneous presence of the two barriers determines a greater amplification effect between the barriers, so the realistic use of a single barrier seems to be more efficacy.

5.7.1. Effect of the geometrical configuration

Since the inverted pyramid barrier seems to show a better performance in terms of attenuation of accelerations and displacements, its geometrical configuration was varied to be able to study the influence of different parameters (inclination of the side, extension of the barrier…). The results are presented in terms of attenuation of acceleration and are reported only for the Signal 3 (20Hz), for which the maximum amplification effect before the barrier was observed. All the results are compared with the original scheme (inverted pyramid barrier) to observe the differences. The schemes investigated are shown in Figure 5.30.

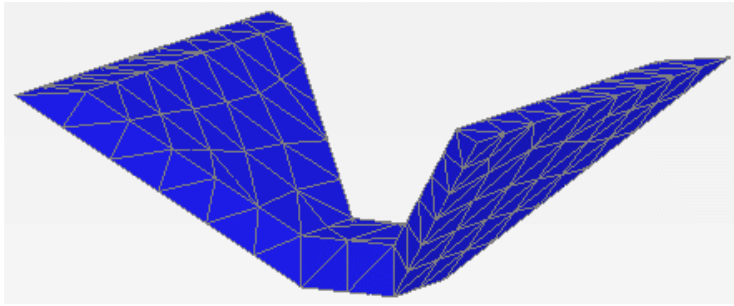

a)

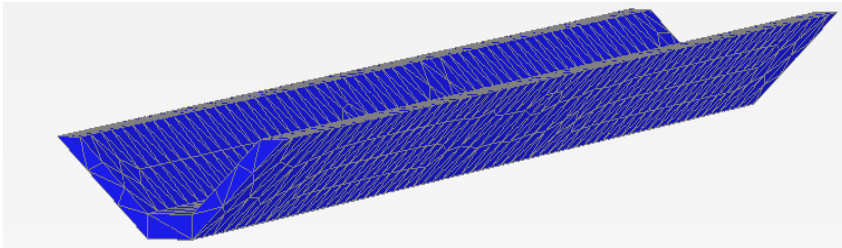

b)

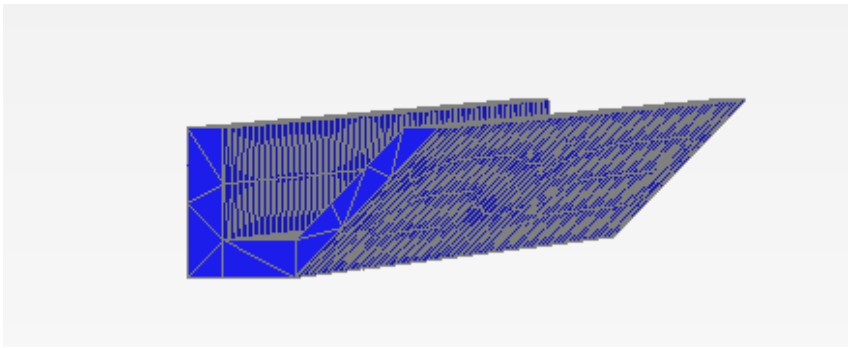

c)

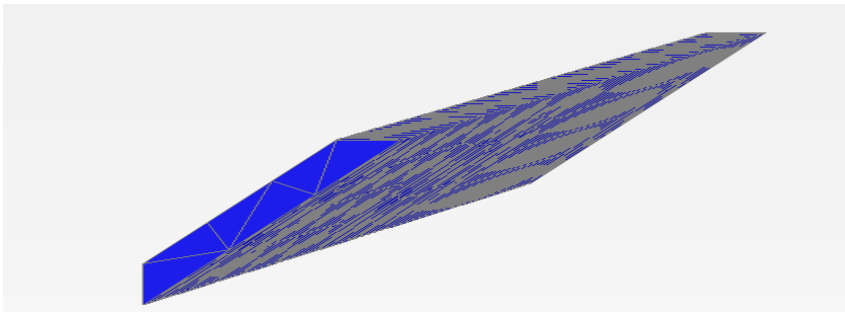

d)

Figure 5.30 Geometries studied in the numerical analyses a)Model 1; b)Model 2; 3) Model 3;4) Model 4

In the *Model 1* two sides of the inverted pyramid were removed. The effect respect to a complete pyramid is in reduction of the attenuation ratio η_r inside the barrier due to a minor reflection of the waves (*Figure 5.31*). In the *Model 2*, the sides of the pyramid are simply extended to all the width of the domain. The differences between the results for the different geometries can be seen to be fairly small (Figure 5.32). In the *Model 3*, the side near the source was kept inclined while the other side was assumed to be vertical. This geometrical configuration determines a deamplification before the barrier and an amplification inside the barrier due to a major waves reflection on the vertical side.

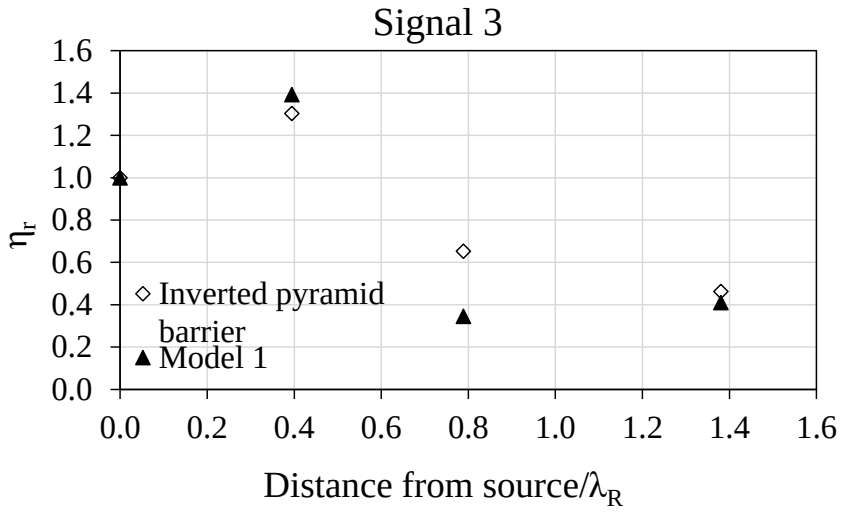

Figure 5.31 Attenuation ratio calculated for the Model 1compared with the original scheme

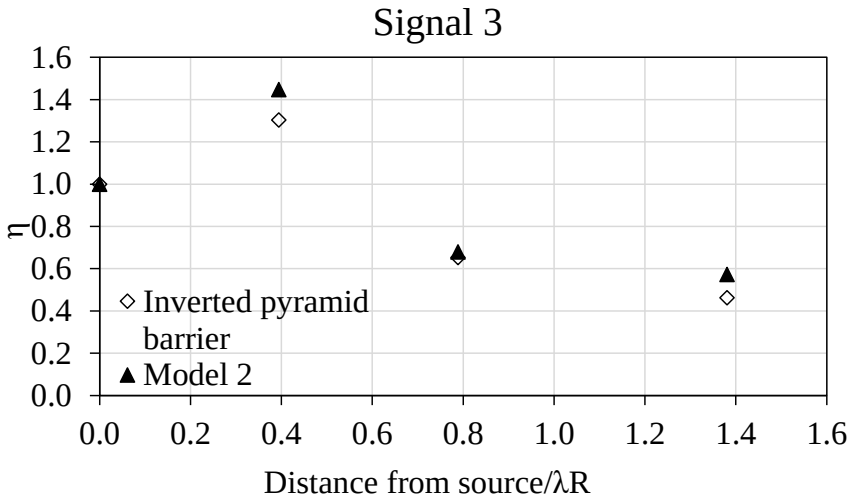

Figure 5.32 Attenuation ratio calculated for the Model 2 compared with the original scheme

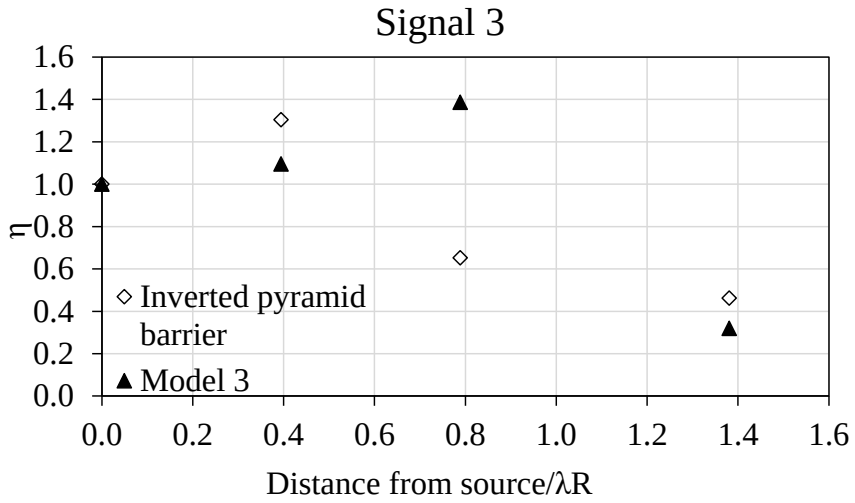

Figure 5.33 Attenuation ratio calculated for the Model 3 compared with the original scheme

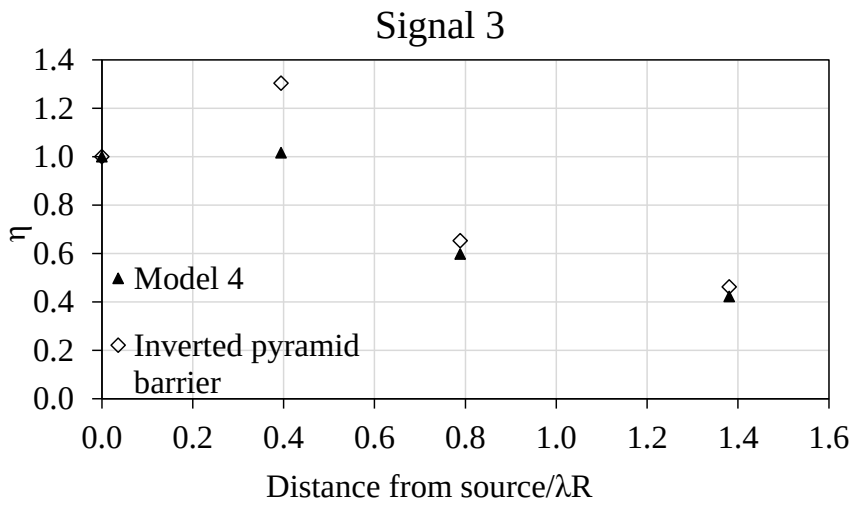

Figure 5.34 Attenuation ratio calculated for the Model 4compared with the original scheme

Finally, the barrier was reduced to only one side inclined (*Model 4*).

This change implicates that the amplification before the barrier was totally eliminated while after the barrier the behaviour was truly similar to the original scheme (inverted pyramid barrier) (Figure 5.34). Finally, the reduction efficiency of the barrier calculated as the percentage of reduction in terms of accelerations in the point #4 (after the barrier) was determined for all the scheme. The major reduction was obtained for the model 3 (one side inclined and one side vertical) and was of about 70% (Table 5.8).

Table 5.8 Reduction efficiency for the Model 1-4

Reduction efficiency				
Inverted pyramid	Model 1	Model 2	Model 3	Model 4
53.8%	58.9%	42.7%	68.0%	57.8%

5.8. Final remarks

The effectiveness of using barriers filled with a polymer (SAP) as a measure to reduce the surface vibrations has been investigated through a field trial. Using soft backfill material increases the effectiveness of in-filled trench and allows for larger trench depth with no supporting measures of the vertical walls of the trench. Field measurements of soft-filled trenches were presented. Vibrodyne is used to produce shear waves in the certain frequency range and seismograph is used to acquire generated values. Two geometrical configuration of the barriers were considered, in the first one the barrier was constructed with an inverted pyramid shape, while in the second one a rectangular trench was created.

The efficacy of the barriers to mitigate the vibration was evaluated by the amplitude reduction ratio in terms of displacements and accelerations. The inverted pyramid barrier have shown a better isolation performance than the rectangular barrier with values of A_r between 0.17 and 0.32. However, an amplification effect was recorded before the barrier.

For this reason, the experimental results were compared with FE numerical analyses of the same models. By validating the FE modelling via the comparison with the experimental results, a robust model has been built. This model has been used for carrying out a wider parametric numerical analysis. Different geometrical configurations were analysed by starting from the inverted pyramid barrier. The performance of four different geometries are compared. A trench with the side furthest from the vibrodyne at 45° and the side nearest the vibrodyne vertical (*Model 3*), shows the better performance in terms of reduction of the acceleration calculated after the barrier 1(reduction of the accelerations of about 70%). Instead, the amplification effect before the barrier was eliminated by adopting a barrier made by only one inclined side (*Model 4*). The isolation performance of the wave barrier may vary depending on physical and dynamic characteristics of the site. Further analyses are necessary to investigate other parameters that play a role in the mitigation of the surface vibrations.

REFERENCES

Aboudi, J. (1973): Elastic waves in half-space with thin barrier. *Proc. ASCE, 99, J. Engng. Mechs. Dir., EMI, 69–83*

Ahmad S., Al-Hussaini T.M. (1991). Simplified design for vibration screening by open and in-filled trenches. *J Geotech Engng, ASCE, 117 (1), pp. 67-88*

Al-Hussaini TM, Ahmad S. (1996). Active isolation of machine foundation by in-filled trench barriers. *J Geotech Eng ASCE;122:288–94.*

Barkan, D. D. (1962). Dynamics of bases and foundations. *New York, N.Y., McGraw-Hill Book Co., Inc.*

Beskos DE, Dasgupta B, Vardoulakis IG (1986). Vibration isolation using open or filled trenches, Part l:2-D homogeneous soil. *Comput Mech1986; 1:43–63.*

Brinkgreve RBJ, Swolfs WM, Engine E (2011) PLAXIS user's manual, *PLAXIS bv the Netherlands*

Comina C., Foti S (2007). *Surface wave tests for vibration mitigation studies* .in: *journal of geotechnical and geoenvironmental engineering, vol. 133(10), pp. 1320-1324. - ISSN 1090-0241*

Dasgupta, B. (1986): Vibration isolation of structures on homogeneous soil. *Ph. D. Thesis, University of Minnesota, Minneapolis, Minnesota*

Dasgupta, G. , Beskos, D. E. , and Vardoulakis, I.G., (1988). 3-D analysis of vibration isolation of machine foundations. *Proc., lOth Boundary Elements Conv., Vol. 4, C.A. Brebbia, Ed., Springer-Verlag, Berlin, Germany, pp. 59- 73.*

Davies, M.C.R., (1994) Dynamic soil structure interaction resulting from blast loading *International Conference Centrifuge 94, 319-324.*

Dolling, H.J. (1965): Schwingungsisolierung von Bauwerken durch tiefe auf geeignete Weise stabilisierte Schlitze. *VDI-Ber. 88, 3741*

Dolling, H.J. (1970a): Die Abschirmung von Erschutterungen durch Bodenschlitze. *Bautechnik 47, 151–158*

Dolling, H.J. (1970b): Die Abschirmung von Erschütterungen durch Bodenschlitze. *Bautechnik 47, 194–204*

El Naggar MH and Chehab AG (2005), Vibration Barriers for Shock-producing Equipments, *Canadian Geotechnical Journal, 42(1): 297−306.*

Fuyuki, M., Matsumoto, Y. (1980): Finite difference analysis of Rayleigh wave scattering at a trench. *Bull. Seism. Soc. Amer. 70, 2051–2069*

Itoh, K., (2003). Physical modelling of wave propagation from ground vibration and vibration countermeasure. *PhD Dissertation, Tokyo Institute of technology.*

Itoh, K., Zeng, X.,Koda, M., Murata O. and Kusakabe, O., (2005). Centrifuge simulation of wave propagation due to vertical vibration on shallow foundations and vibration attenuation countermeasures. *Journal of Vibration and control. 11, 781-800.*

Kattis, S. E., Polyzos, D., and Beskos, D. E. (1999a). Modelling of pile barriers by effective trenches and their screening effectiveness. *Soil Dyn. Earthquake Eng., 18(1), 1–10.*

Kattis, S. E., Polyzos, D., and Beskos, D. E. (1999b). Vibration isolation by row of piles using a 3D frequency domain BEM. *Int. J. Numerical Methods Eng., 46(5), 713–728.*

Liao, S.; Sangrey, D.A. (1978): Use of piles as isolation barriers. *Proc. ASCE 104, J. Geotech. Engng. Dir., GT9, 1139–1152*

Luong, M P., (1994). Efficiency of a stress wave mitigation barrier. *Proceedings of the international Conference on Centrifuge Modelling (Centrifuge 94), Balkelma, Singapoore, 283-288.*

May, T.W., Bolt, B.A. (1982): The effectiveness of trenches in reducing seismic motion. *Earth. Eng. Struct. Dyn. 10, 195–210*

McNeill, R. L., Margason, B.E., Babcock, F.M. (1965). The role of soil dynamics in the design of stable test pads, pp 366–375. *Guidance and Control Conference, Minneapolis, Minnesota*

Miller, G.F., Pursey, H. (1955): On the partition of energy between elastic waves in a semi-infinite solid. *Proc. Roy. Soc. London, A 233, 55–69*

Neumeuer, H. (1963): Untersuchungen über die Abschirmung eines bestehenden Gebäudes gegen Erschütterungen beim Ban und Betrieb einer U-Bahnstrecke. *Baumaschine and Bautechnik 10, 23–29*

Richart, Jr., F.E.; Hall, Jr., J.R.; Woods, R.D. (1970): Vibrations of soils and foundations. *Englewood Cliffs, N.J.: Prentice Hall*

Segol G., Lee C.Y., Abel J.F.. Amplitude reduction of surface waves by trenches. *Journal of the Engineering Mechanics Division, 104(3):621-641, 1978*

Woods, R.D. (1967): Screening of elastic surface waves by trenches. *Ph.D. thesis, University of Michigan, Ann Arbor, Michigan*

Woods, R.D. (1968): Screening of surface waves in soils. *Proc. ASCE 94, J. Soil Mechs. Found. Engng. Dir., SM4, 951–979*

Woods, R.D.; Barnett, N.E.; Sagesser, R. (1974): Holography, a new tool for soil dynamics. *Proc. ASCE 100, J. Geotech. Engng. Dir.*, GT11, 1231–1247

Yang Y and Hung H (1997), Parametric Study of Wave Barriers for Reduction of Train-induced Vibrations. *International Journal for Numerical Methods in Engineering, 40(20): 3729−3747.*

Zeng, X., Rose, J. and Rice, J., 2001. Stiffness and damping ratio of rubber modified asphalt mixes: potential vibration attenuation for high speed railway track beds. *Journal of vibration and control 7 (4), 527-538.*

Zhong, X., Zeng, X. and Rose, J., 2002. Shear modulus and damping ration of rubber modified asphalt mixes and unsaturated subgrades soils. ASCE Journal of materials in civil Engineering, 14 (6) 496-502.

CONCLUSIONS

This thesis is a part of a comprehensive research program on the study of an innovative ground treatment approach for the mitigation of the seismic risk of existing structure, by means of the creation of a continuous thin layer of grouted soil at a convenient depth.

The motivation of the research was the observation of the damage suffered by the historic buildings under earthquakes. In countries like Italy, with a high seismic hazard and old or very old towns, where many buildings are hundreds of years old, this is one of the most relevant problems for the protection of both population and cultural heritage (Costanzo et al., 2007). Few historic buildings meet current code seismic requirements for life safety, and most have architecturally significant elements that are threatened by future earthquakes. The use of the isolation system conceived for new structure could be in conflict with the respect of the iconic, historical and material integrity of the monuments.

The present work provides guidance on the use of the soft barriers to seismic isolate the existing buildings, highlighting pros and cons based on experimental and numerical results.

Centrifuge tests were carried out based on the progress made in the initial stages of the research program (Lombardi, 2014). Two reduced scale models of soft barriers in a sand layer underwent a series of ground shaking. The aim of the study was to get experimental evidence of the capability of such soft barriers to isolate a volume of soil thus reducing amplification of ground motion induced by earthquake loading. The two

models tested in centrifuge at 50 and 80 g consisted each in a layer of dense Hostun sand, free to be shaken along its main horizontal axis thanks to the adopted container (a laminar box). In the first model a thin horizontal layer made of latex balloons filled with a cross-linked gel was created at about mid-height of the sand layer. In the second, the same balloons were installed to form a V-shaped barrier aimed at isolating a relatively shallow volume of sand. The experimental results confirm the effectiveness of such soft barriers to reduce amplification in the isolated volume during seismic events, although V-shaped isolating barriers are less effective than a full horizontal barrier. The latter is however rather unfeasible and should only be considered as a reference condition. The experimental results were compared with FE numerical analyses of the same models, carried out also in free field conditions (without barrier) to have a benchmark condition. By validating the FE modelling via the comparison with the experimental results, a robust model has been built, that can be used for carrying out a wider parametric numerical testing.

A parametric numerical analysis is reported using elastic–plastic with hardening and small strain overlay constitutive model, with reference to two geometrical schemes (named rectangular and V-shaped barrier). A simple mechanical analogy is adopted to estimate the natural frequency of the soil mass bounded by the soft barrier, used to assess in a more general way the beneficial effects of such an isolating system. The effect of the insertion of a soft barrier made by different SAP-sand mixtures in the soil, in both static and dynamic conditions was analysed. The time histories of acceleration used as base input motions at the bottom boundary of the FE mesh are obtained from different databases. The

results of the dynamic analyses are evaluated in terms of maximum accelerations recorded at the top of the model, Arias Intensity and pseudo spectral acceleration. The V-shaped barrier is less effective than the rectangular one having the same depth, since the isolated mass is smaller and the filtering effect of the grouted layer is influenced also by the bulk stiffness. Therefore the use of the V barrier is not recommended. The volumetric stiffness K of the grouted layers plays a relevant role on the effectiveness of the isolating barrier. In the case of a rectangular caisson, the best solution is to have an extremely low value of K on the vertical sides, and a higher one at the base. So doing, the static settlements induced by the creation of the barrier would be reduced. The optimum scheme (both in static and dynamic conditions) is made by two different materials (100% SAP at the base and 60% SAP or 70% SAP along the sides of the rectangular caisson). In all cases, the reduced value of the shear strength angle in the grouted layers must be considered, to check if it may affect the load bearing capacity of the structure to be protected in an unacceptable way.

Significant results have also been obtained with the calibration of a macro-element able to give an insight on the static performance of soft buried barriers made of a mixture of soil and a Super Absorbing Polymer (SAP). It is assumed that it is possible to formulate directly a relationship between external forces and displacements of a foundation by considering the generalised stress and strain variables, respectively.

The calibration of macro-element parameters requires specific numerical simulation. The system response under static loads was studied, varying the geometry of the barrier. The surfaces of the ultimate

load of the systems, with and without soft barriers, were obtained, by performing numerical displacement controlled test. From the construction of the failure loci it is evident that this kind of seismic isolation is adapt only for the structures having a very large load bearing capacity safety factors, for which such a reduction may in some cases be not critical.

This new approach to the seismic risk mitigation appears a potentially valid alternative to other more conventional and invasive solutions, such as the structural reinforcement and the base isolation, and can result suited for the historical constructions for which integrity has to be preserved but it is still far from ready to be realized.

In the future, it is expected that the dynamic performance of the soft barriers might be interpreted with higher detail by macro-element approach, to better simulate also the soil-structure interaction.

The effectiveness of using barriers filled with a polymer (SAP) as a measure to reduce the surface vibrations has been investigated through a field trial. Two geometrical configuration of the barriers were considered, in the first one the barrier was constructed with an inverted pyramid shape, while in the second one a rectangular trench was created. The efficacy of the barriers to mitigate the vibration was evaluated by the amplitude reduction ratio in terms of displacements and accelerations. The inverted pyramid barrier has shown a better isolation performance than the rectangular barrier. However, an amplification effect was recorded before the barrier.

For this reason, the experimental results were compared with FE numerical analyses of the same models. By validating the FE modelling via the comparison with the experimental results, a robust model has been built. This model has been used for carrying out a wider parametric numerical analysis. A trench with the side furthest from the vibrodyne at 45° and the side nearest the vibrodyne vertical, shows the better performance in terms of reduction of the acceleration calculated after the barrier. Further analyses are necessary to investigate other parameters that play a role in the mitigation of the surface vibrations.

APPENDIX A
GEOTECHNICAL CENTRIFUGE MODELLING

A.1. Principles of centrifuge modelling

A centrifuge is essentially a sophisticated load frame on which soil samples can be tested. Geotechnical materials such as soil and rock have nonlinear mechanical properties that depend on the effective confining stress and stress history. A special feature of geotechnical modelling is the necessity of reproducing the soil behaviour both in terms of strength and stiffness. In geotechnical engineering there can be a wide range of soil behaviour relevant to a particular problem. There are two principal reasons for this: (i) soils were originally deposited in layers and so it is possible to encounter different soil strata in a site which may affect a particular problem in different ways; and (ii) in situ stresses change with depth and it is well known that soil behaviour is a function of stress level and stress history. The centrifuge applies an increased "gravitational" acceleration to physical models in order to produce identical self-weight stresses in the model and prototype. Soil models placed at the end of a centrifuge arm can be accelerated so that they are subjected to an inertial radial acceleration field, which, as far as the model is concerned, acts like a pseudo-gravitational acceleration field. By controlling the spinning velocity, gravitational fields much stronger than Earth's gravity. The one to one scaling of stress enhances the similarity of geotechnical models and makes it possible to obtain accurate data to help solve complex problems such as earthquake-induced liquefaction, soil-structure interaction and underground transport of pollutants such

as dense non-aqueous phase liquids. Centrifuge model testing provides data to improve our understanding of basic mechanisms of deformation and failure and provides benchmarks useful for verification of numerical models.

Scaling laws are relationships that relate the behaviour of the centrifuge model and the prototype. If the same soil is used in the model as in the prototype and if a careful model preparation procedure is adopted whereby the model is subjected to a similar stress history ensuring that the packing of the soil particles is replicated, then for the centrifuge model subjected to an inertial acceleration field of AT times Earth's gravity the vertical stress at depth h_m (where m indicate the model) will be identical to that in the corresponding prototype at depth h_p (where p indicate the prototype) where $h_p=Nh_m$. This is the basic scaling law of centrifuge modelling, that stress similarity is achieved at homologous points by accelerating a model of scale N to N times Earth's gravity. These are required to relate the observed behaviour of the scale model in the centrifuge experiment to the behaviour of a prototype. Some of the scaling laws come directly from the principle of centrifuge modelling, making use of dimensional analysis.

If an acceleration of N times Earth's gravity (g) is applied to a material of density ρ, then the vertical stress σ_v, at depth h_m in the model is given by:

$$\sigma_{vm} = \varrho N g h_m \qquad \text{A.1}$$

In the prototype, indicated by subscript p, then:

$$\sigma_{vp} = \rho g h_p \qquad \text{A.2}$$

Thus for $\sigma_{vm} = \sigma_{vp}$ then $h_m = h_p N^{-1}$ and the scale factor (model: prototype) for linear dimensions is 1: N. Since the model is a linear scale representation of the prototype, then displacements will also have a scale factor of 1: N.

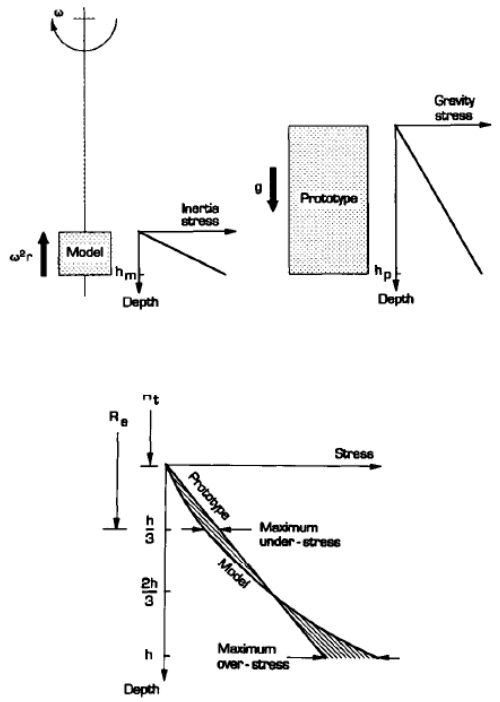

Figure A.1 a) Inertial stresses in a centrifuge model induced by rotation about a fixed axis correspond to gravitational stresses in the corresponding prototype ,b) comparison of stress variation with depth in a centrifuge model and its corresponding prototype (Taylor, 1995)

The distributions of vertical stress in the model and corresponding prototype are shown in Figure A.1a. These distributions of vertical stress

are compared directly in Figure A.1b where they are plotted against corresponding depth.

In the prototype, the vertical stress at depth $h_p = h_m N$ is given by:

$$\sigma_{vp} = \rho g h_p = \rho g N h_m \qquad \text{A.3}$$

Dynamic events such as earthquake loading or cratering require special consideration in order to define appropriate scaling laws. For such problems, it is simplest to consider the basic differential equation describing the cyclic motion x_p in the prototype:

$$x_p = A_p sin(2\pi f_p t_p) \qquad A.4$$

where A_p is the amplitude of the motion of frequency f_p.

Differentiating equation (2.4) gives:

$$\frac{dx_p}{dt_p} = 2\pi f_p a_p \, cos(2\pi f_p t_p) \qquad A.5$$

$$\frac{d^2 x_p}{dt_p^2} = (2\pi f_p)^2 a_p \, cos(2\pi f_p t_p) \qquad A.6$$

Using an analogous expression for motion in the model, the following expressions can be derived:

- displacement magnitude: A_m
- velocity magnitude: $(2\pi f_m)A_m$
- acceleration magnitude: $(2\pi f_m)^2 A_m$

In the model, linear dimensions and accelerations have scale factors 1: N and 1: N^{-1}, respectively, in order to retain similarity. From the above,

it is clear that this can be achieved if $A_m = N^{-1}A_p$ and $f_m = Nf_p$. An important consequence of this is that the velocity magnitude will then be the same in the model and the prototype. The time scaling factor for dynamic events is therefore 1: N in contrast to the 1: N^2 time scale factor for diffusion or seepage events. The most common scale laws (Schofield, 1980) are summarized in Table A. 1.

Table A. 1 Scaling laws

	Parameter	Scaling law model/prototype	Units
General scaling laws	Lenght	1/N	m
	Area	$1/N^2$	m^2
	Volume	$1/N^3$	m^3
	Mass	$1/N^3$	$Nm^{-1}s^2$
	Stress	1	Nm^{-2}
	Strain	1	-
	Force	$1/N^2$	N
	Bending moment	$1/N^3$	Nm
	Work	$1/N^3$	Nm
	Energy	$1/N^3$	J
	Seepage velocity	N	ms^{-1}
	Time (consolidation)	$1/N^2$	s
Dynamic events	Time (dynamic)	1/N	s
	Frequency	N	s^{-1}
	Displacement	1/N	m
	Velocity	1	ms^{-1}
	Acceleration	N	ms^{-2}

Geotechnical centrifuges can be sub-divided into two main classes: beam centrifuges and drum centrifuges. The beam centrifuge generally comprises a central spindle supporting a pair of parallel arms which hold the platform on which the test package is placed.

Beam centrifuges traditionally rotate in a horizontal plane. The acceleration field acting on the model is the resultant of the centrifuge acceleration field and the Earth's gravitational field. The behaviour of the model will depend on the orientation of the model on the centrifuge platform to this resultant acceleration field. Beam centrifuges can be subdivided into three platform types (fixed, restrained and swinging) as depicted in Figure A.2.

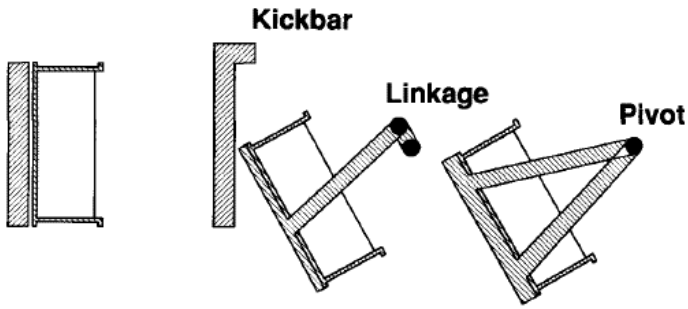

Figure A.2 Types of beam centrifuge platform: left, fixed, centre, restrained, right, swinging.

On the fixed platform the test package is attached to the vertical face plate. On the centre-line, the resultant acceleration is always effectively inclined to the platform at n: 1, where n is the centrifuge acceleration at the platform. When the centrifuge is started or stopped, restraints are

necessary to retain the soil and low shear modulus materials, such as fluids, in the test package.

The most important aspect of a geotechnical soil model is the effective stress profile. The effective stress history, the current effective stress state and the effective stress path followed during the test will dictate the behaviour of the model. Centrifuge model tests can be performed on undisturbed soil samples, if the effective stress conditions in the sample are representative of the prototype. Macro-fabric present in the undisturbed model sample, such as structure, fissures, inclusions and potential drainage paths, may not scale to be representative of the conditions in the prototype. Remoulded granular soil models can be prepared by tamping and pluviation techniques. The soil models are generally too large to be compacted on vibrating tables. Tamped samples can be prepared moist or dry for most grain size distributions. The sample is placed in layers which are then compacted by tamping to achieve the required overall density. There may be a variation of density within the tamped layers. Dry pluviation techniques can be used for uniformly graded dry sands. The density of pluviated samples can be accurately controlled by the energy imparted to the sand particles: dense samples are created by pouring the sand slowly from a height whereas loose samples are created by slumping the sand quickly into the model container. Centrifuge model test behaviour can be monitored by a variety of instrumentation. Available instrumentation includes not only a wide range of transducers but also visual techniques. Transducers in contact with the centrifuge model should be small and rugged enough to resist not only their increased self-weight but also mechanical handling

during test preparation and disassembly. Solid-state transducers are particularly suitable. The operating principle of the transducer must be considered. Normally, the transducer is required to be capable of continuous monitoring throughout the centrifuge test, such as pressure transducers. More infrequent monitoring may be acceptable such as deformations before and after an event. For continuous monitoring, the transducer should have an adequate frequency response, which is normally one or two orders of magnitude higher than that required in the prototype. Displacements can be measured with potentiometers or linearly variable differential transformers. Both these transducers require contact with the model.

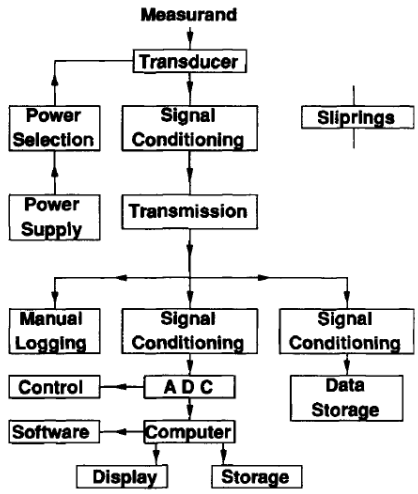

Figure A.3 Typical data-acquisition system

A typical outline of a data-acquisition system is shown in Figure A.3. In the centrifuge environment, failures of the data-acquisition system do occasionally occur. The system architecture should be modular to permit

faults to be easily traced and rectified. The data obtained from the acquisition software should be suitable for input to the data processing, analysis and reporting software to streamline the procedure of model test reporting.

A.2. Beam centrifuges

A beam centrifuge consists of horizontal structural beams that carry the payload at one end and a counterweight at the other end. The horizontal beams are all attached together either by welds or bolts and act as a single structural beam. There is usually a vertical shaft that supports the horizontal beams. The vertical shaft is mounted on bearings so that it is able to spin freely along with the horizontal beams. The power to drive the centrifuge is derived from electrical motors that are normally housed below the centrifuge chamber. The Turner beam centrifuge was designed by Philip Turner and was built in the workshops of the Department of Engineering at the University of Cambridge. It became operational in the late 1970s. Schofield (1980) describes the specifications of this machine and the operation of this centrifuge in detail. It has a nominal diameter of 10 m and the payload capacity is 1 ton at an operational g level of 150 times earth's gravity. A view of this centrifuge is presented in Figure A.4. The two ends of this machine are color coded blue and red. Although both ends are nominally identical, in regular operations the red end carries the centrifuge models while the blue end carries the counter weight made from steel plates. During earthquake tests the ends are reversed, that is, the blue end carries the

earthquake actuator and the centrifuge model while the red end carries the counterweight.

Figure A.4 A view of the Turner beam centrifuge at Cambridge

A.3. SAM actuator

The Stored Angular Momentum (SAM) is an earthquake actuator developed at Cambridge University (Madabhushi et al.1998). A schematic diagram of the SAM actuator and a view of the same are presented in Figure A.5. In this actuator the energy required for the earthquake is stored in a set of flywheels which are rotated by a simple three-phase motor. The main component of this actuator is a fast-acting hydraulic clutch that engages rapidly to commence earthquake motion of the centrifuge model. The SAM actuator is able to operate in 100-g centrifuge tests and fire earthquakes of desired sinusoidal frequency and duration. The user is able to choose the magnitude and duration of the earthquake and can change them in-flight between successive earthquakes.

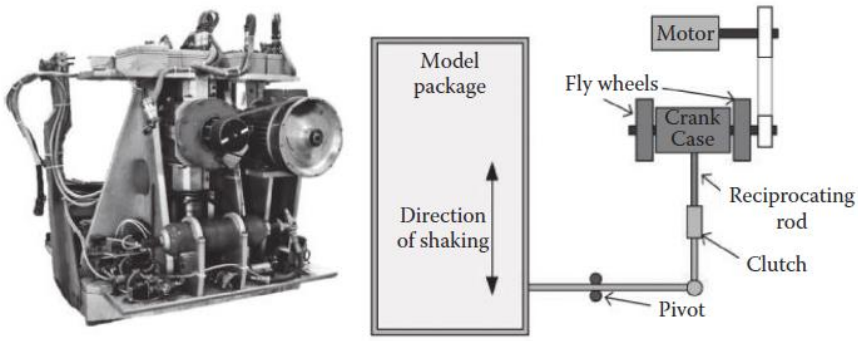

Figure A.5 Schematic diagram and a view of the SAM earthquake actuator

A.4. Laminar box

The tests are performed using a Laminar Box. The concept of the laminar model container is that it has zero lateral stiffness of its own and therefore its deformation is driven by the soil deformation. This concept has been around for a long time (e.g., Scott, 1994). The laminar model container is built by having individual laminas that are separated by cylindrical bearings and therefore can move freely relative to one another. A view of the laminar model container is presented in Figure A.6.

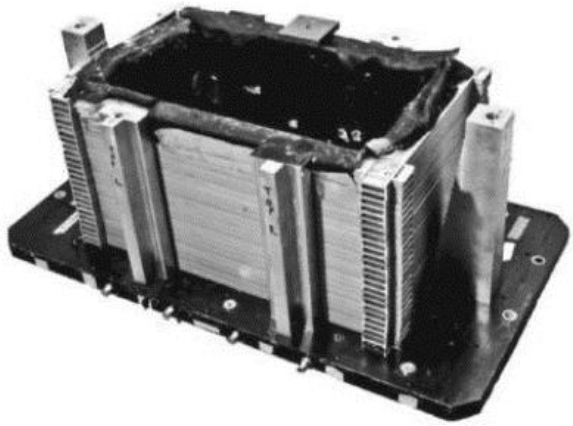

Figure A.6 A view of the laminar model container (Madhabhushi,2014)

The model container has inside dimensions of 500x250x300 and has a weight of 93.5 kg. A plate is put at the base of the box to connect the container with the SAM actuator and fire the earthquake on the model. The weight of the plate is 58 kg.

A.5. Instrumentations

A.5.1 Piezoelectric accelerometers

Measurement of acceleration plays an important role in many centrifuge tests where dynamic loads are present, such as when earthquake, wind, or wave loading is modeled. Traditionally accelerations are measured using miniature piezo-electric devices. These work by converting the mechanical stress induced in the piezo crystal into an electric charge. The electric charge is converted into a voltage by a simple charge-

coupled amplifier. A view of the piezo-electric accelerometer is shown in Figure A.7. These devices are calibrated before use in a centrifuge test using a specially designed calibrator that can apply precisely ±1 g acceleration. A calibration factor for the accelerometer is obtained in the units of g/V. These accelerometers can also be used directly in the soil body to measure soil accelerations at that location. The frequency response of these accelerometers is very good, in the range of 5 Hz to 2 kHz. Below 5 Hz they do not give good response. Another point to remember is that the piezo devices do not record constant accelerations, that is, the acceleration due to gravity in a centrifuge model is not recorded by these devices.

Figure A.7 Piezoelectric accelerometer

They require changing mechanical stresses acting on the piezo element to produce an electric charge and hence they only record time-varying accelerations.

A.5.2 Micro-Electrical-Mechanical Systems accelerometers (MEMS)

MEMS accelerometers are very small, measuring only a few millimeters. They have a tiny inertial mass suspended on a spring and their displacement is used to determine the spring force and hence the

acceleration of the device. A view of the MEMS accelerometer is shown in Figure A.8. These devices are able to measure both constant and time-varying accelerations. As a result they can be calibrated by just turning the device upside down and reversing the 1 g component due to the earth's gravity. The main advantage of using MEMS accelerometers is that they are very inexpensive.

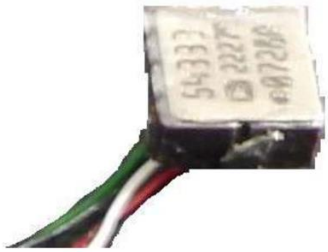

Figure A.8 MEMS accelerometer

A.5.3 Air Hummer

Another method of characterizing the soil models in a centrifuge test is by measuring the shear wave velocity V_S. Knowing the shear wave velocity, the small strain shear modulus G_0 can be obtained using the following equation:

$$V_S = \sqrt{\frac{G_0}{\rho}} \qquad 0.7$$

where ρ is the density of the soil. An air hammer is a small brass tube with a metal pellet inside it Figure A.9. By applying high-pressure air on alternative ends, the pellet is made to accelerate and strike the end of the tube causing a shear wave to be set up at the base of the model, which will propagate upward towards the soil surface.

Figure A.9 Air Hammer for inducing shear waves in model

The outside of the air hammer has glued sand to improve its coupling with the surrounding soil body. Accelerometers placed at different but known elevations will record the arrival times of the shear waves from which the shear wave velocity between adjacent accelerometers can be determined.

A.5.4 Displacement measurements

Displacement measurement in a centrifuge test is carried out traditionally by using contact devices such as linearly varying differential transformers (LVDTs). A view of a typical LVDT is presented in Figure A.10. They generally consist of two detached coil windings and a rod in a cylindrical casing.

The rod, whose tip is attached on the surface where the displacement is to be measured, couples the magnetic field in one coil with the other as it moves between them.

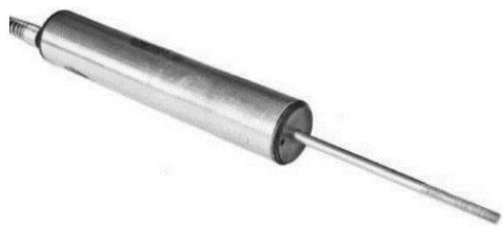

Figure A.10 A view of a linearly varying differential transformer